DEVELOPMENT OF WATERJET TESTING TECHNIQUES

ERIC THORNHILL

INFORMATION TO USERS

This manuscript has been reproduced from the microfilm master. UMI films the text directly from the original or copy submitted. Thus, some thesis and dissertation copies are in typewriter face, while others may be from any type of computer printer.

The quality of this reproduction is dependent upon the quality of the copy submitted. Broken or indistinct print, colored or poor quality illustrations and photographs, print bleedthrough, substandard margins, and improper alignment can adversely affect reproduction.

In the unlikely event that the author did not send UMI a complete manuscript and there are missing pages, these will be noted. Also, if unauthorized copyright material had to be removed, a note will indicate the deletion.

Oversize materials (e.g., maps, drawings, charts) are reproduced by sectioning the original, beginning at the upper left-hand corner and continuing from left to right in equal sections with small overlaps.

Photographs included in the original manuscript have been reproduced xerographically in this copy. Higher quality 6" x 9" black and white photographic prints are available for any photographs or illustrations appearing in this copy for an additional charge. Contact UMI directly to order.

Bell & Howell Information and Learning
300 North Zeeb Road, Ann Arbor, MI 48106-1346 USA
800-521-0600

DEVELOPMENT OF WATERJET TESTING TECHNIQUES

by

©Eric Thornhill, B. Eng.

A Thesis Submitted to the School of Graduate Studies

in Partial Fulfillment of the Requirements for the Degree of

Master of Engineering

Faculty of Engineering and Applied Science

Memorial University of Newfoundland

June 1999

St. John's, Newfoundland, Canada

ABSTRACT

In the last decade, waterjet propulsors have found increasing acceptance as an alternative to marine screws and other propeller types. Over the same interval, waterjets have evolved from relatively small, simple propulsors for small recreational craft, to sophisticated engineering systems appropriate for high speed and high power vessels. The continuing development of propulsors for such vessels is aided by research for improvement and evaluation of designs. The development of research capabilities in this field is in progress at the Institute for Marine Dynamics. It has been focusing on the ability to perform experiments of vessels and their propulsors at model scale in order to evaluate the performance of the integrated system.

Model testing techniques for waterjet propelled craft are reviewed and discussed from various relevant works on the subject. Several types of waterjet propulsors as well as some of the common vessel types are identified with respect to the scope of the testing capabilities of the facility. Two phases of experiments were prepared for a model of a 12 metre recreational craft with simple model jets. The phases consisted of bare hull resistance tests and self-propulsion tests. The experiments were intended as trials for testing techniques and instrumentation since results could be compared with the full scale performance of the vessel. One conclusion drawn from the tests was that a model waterjet propulsor would have to be designed and instrumented specifically for such experiments.

An experimental waterjet propulsor test platform was then developed to accommodate the requirements derived from the initial test phases. The platform housed a model which employed a modular design allowing variation of internal geometry of the waterjet design

if required. The platform was fully instrumented to measure flow speeds and pressures in the nozzle and near the impeller. A transparent impeller region was designed to observe possible cavitation phenomena. Thrust, torque, shaft speed and volume flow rate were also measured. The design, instrumentation, test program and test results of the model waterjet and platform are presented and discussed.

ACKNOWLEDGEMENTS

I would like to thank my supervisors Dr. Brian Veitch and Dr. Neil Bose for their advice and consultation throughout the tenure of this degree program. I would also like to thank the Institute for Marine Dynamics (IMD) for providing the facilities and resources used for this project. I am grateful for the financial support provided by the Natural Sciences and Engineering Research Council (NSERC), Bombardier Inc., Memorial University of Newfoundland (MUN), and the Society of Naval Architects and Marine Engineers (SNAME).

Special thanks go to Dr. Brian Veitch who initiated this project at IMD and did much of the preliminary work in finding potential partners and reviewing previous research work in waterjet propulsion.

I would also like to acknowledge the efforts of the design department at IMD including: John Bell, Mike Kilfoil, Trent Slade, Tony Randell and Andy Wallace. The fabrication shops at both IMD and technical services at MUN performed much of the construction of the various models and apparatus used for the experiments. Invaluable technical support was provided by: the IMD electronics shop, computer center personnel, Jim Everard (assembly and outfitting), Shane Mckay (with the LDV), and by David Day, a work term student who assisted with many of the experiments.

TABLE OF CONTENTS

APPENDIX C: Dynamic Instability at Model Scale

APPENDIX D: Resistance at Model and Full Scale

LIST OF FIGURES

LIST OF TABLES

NOMENCLATURE

Symbols and definitions are for model scale unless otherwise stated.

A_{i1}	Projected area of the Pitot tube rake at the inlet
A_{i2}	Projected area of the Pitot tube rake at the nozzle
A_j	Cross-sectional area of flow at Station j
A_{PM}, A_{PS}	Projected area of the hull above the waterline for model and ship
A_s	Projected area of the studs
b_1	Width of rectangular cross-section of flow at Station 1
C_{ARM}, C_{ARS}	Coefficient of resistance due to air resistance for model and ship
C_D	Coefficient of drag of the hull above the waterline
C_{Di}	Coefficient of drag for the Pitot tube rakes
C_{Ds}	Coefficient of drag for the studs
C_{FM}, C_{FS}	Coefficient of frictional resistance for model and ship
C_{instr}	Coefficient of resistance due to instrumentation such as Pitot tube rakes at the inlet and nozzle
C_{pj}	Static pressure coefficient at Station j
C_R	Coefficient of residual resistance (wavemaking)
C_{TM}, C_{TS}	Total resistance coefficient of model and ship
C_{Turb}	Coefficient of resistance caused by turbulence stimulators
E_j	Energy flux at Station j
F_D, F_{DM}	Tow force in x-direction
G	Acceleration due to gravity
h_1	Height of rectangular cross-section of flow at Station 1
H_{35}	Increase of the mean total head across the pump
h_j	Height of jet above undisturbed surface
L_{mM}, L_{mS}	Mean wetted length of model and ship
L_{wc}	Wetted chine length
L_{wk}	Wetted keel length
M_j	Momentum flux at Station j

n_s	Number of wetted studs
p_0	Static pressure in undisturbed flow
P_{DM}, P_{DS}	Delivered power of model and ship
P_{ELEV}	Power needed to elevate water to a height above undisturbed surface
p_j	Static pressure at Station j
P_{JSE}	Effective jet system power
P_{PE}, P_{PES}	Effective pump power for model and ship
Q_J	Volume flow rate of jet (model scale)
R_J	Radius of jet
Rn_M, Rn_S	Reynolds number for model and ship
R_S	Effective full scale resistance
S_M, S_S	Wetted surface area of model and ship
$u_{7\phi}$	Tangential velocity at Station 7
u_{xj}, u_j	Fluid velocity in x-direction at Station j
V, V_M	Model velocity of carriage speed
V_A	Air velocity measured underneath the carriage
V_{Ej}	Energy velocity at Station j
V_J	Mean jet velocity
w_{inlet}	Width of inlet
Z	Sinkage
ΔM_M, ΔM_S	Change in momentum flux at model and full scale
η_{inst}, η_{InstS}	Pump installation efficiency at model and full scale
η_P, η_{PS}	Pump efficiency at model and full scale
η_{WJ}	Waterjet efficiency
λ	Scale factor
ρ_M, ρ_S, ρ	Water density at model scale and full scale. $\rho=\rho_M$
τ	Running trim
υ_M, υ_S	Kinematic viscosity of water for model and ship
ζ_{ij}	Loss coefficient between Stations i and j

CHAPTER 1

INTRODUCTION

1 INTRODUCTION

In response to high speed transportation requirements, marine waterjet propulsion has grown rapidly during the past decade. At the small end of the size scale are recreational watercraft propelled by single jet units of less than 100 kW. At the other end are high speed commercial passenger ferries with multiple jets absorbing installed powers of over 70 MW. While current waterjet propulsion applications are concentrated on passenger transport and other special purposes, there is growing interest in high speed marine transportation of general cargo, such as containerised goods (e.g. Giles, 1997). As these concepts are realised, the already high growth rate in waterjet propulsion will likely continue, or be exceeded.

As marine waterjet systems have grown in size and complexity, more rigorous engineering support has been required, such as improved design guidelines by computational methods and experimental techniques.

Predictions of powering requirements for waterjet propelled vessels can be made with the aid of physical model tests of the vessel, equipped with scale model jets, in a towing tank. Development of model self propulsion test techniques has progressed along with the analytical methods used to make the predictions. These began using the same basic concepts applied to screw propeller vessels, but as a waterjet is an integral part of the hull, some of the traditional concepts, such as thrust deduction, do not apply to waterjet propelled ships in a physically obvious way. Further, measurement of some basic quantities, particularly thrust, is difficult in practice and requires instead an indirect measurement based on flow rates.

In response to the growing interest in waterjet propulsion, the Institute for Marine Dynamics (IMD) and Memorial University of Newfoundland (MUN) initiated a project to develop waterjet related model testing and measurement techniques, guided by the report of the 21st International Towing Tank Conference (ITTC) on the momentum flux method. This work was supported in part by Bombardier Inc. and the Natural Sciences and Engineering Research Council (NSERC).

The project consisted of several phases. The first two phases consisted of tests of a model of a waterjet propelled vessel. The first test series of the model was a bare hull resistance test series without thrusters or inlet openings. The results of this series were used as a baseline reference of the model's performance. A self propulsion test series was then performed which incorporated small model waterjet thrusters in the model. These tests were used to evaluate testing methods and measurement techniques needed to acquire data for performance analysis using the momentum flux method.

The last phase involved the design, fabrication, and commissioning of a waterjet test platform. The stationary platform housed a model waterjet of modular design with integrated instrumentation. It was used to further evaluate measuring techniques and instrumentation and provided a tool for evaluating thruster performance and for calibration of jet flow rate of the propulsor, which could be used in self propulsion tests.

This thesis first presents a brief summary of related research work in the area of waterjet propulsion. The types and functions of various instruments used in the project for measurements are then presented and discussed. As the experiments involved scale models, an analysis is given of the modeling and similitude laws for waterjet propulsion systems. The momentum flux method used for the analyzing experimental results is then presented as outlined by the 21st ITTC. The remaining chapters discuss the design, fabrication, and instrumentation of the models used in experiments as well as a presentation of the test results. Conclusions are drawn and recommendations for future work are discussed.

CHAPTER 2
LITERATURE REVIEW

2 LITERATURE REVIEW

Research work in the field of waterjet propulsion has progressed over the past decade as the understanding of the principles of waterjet operation, efficiency and hull interaction effects increase. Even in the light of recent progress with numerical simulations involving fluids, model testing serves an essential role in the investigation of fluid systems and validation of numerical codes. Published research in this field establish the foundation for which present research can be based. The remainder of this chapter gives a brief summary of the published research related to experimental work in the area of marine waterjet propulsion over the last decade. A more detailed review has been published by Terwisga (1996a).

Etter et al. (1996) presents a method for defining the propulsion terms for waterjet propelled craft and the experimental methods for their determination. A review of the

experimental methods for determining propulsion coefficients for conventional propellers is first presented along with their corresponding tests with waterjets. A brief description of the primary differences between conventional propellers and waterjets is given including their dimensionless parameters. A control volume approach applied to the momentum flux theory is discussed for waterjets. Drag is defined as the resultant of all external surface forces, and thrust as the resultant of all internal surface forces. The paper describes the benefits of different test arrangements in various facilities such as:

- a free surface variable pressure facility
- wind tunnel tests
- direct thrust measurement in a test stand
- towing tank model techniques such as bare hull resistance tests
- tests with inlet fairing with a tare block
- tests with inlet without tare block.

Equations for calculating performance parameters are given. A complete test program should include:

- inlet appendages (such as fairings) on the hull
- the operating inlet and initial ducting
- the ducting up to the pump inlet flange
- pump and nozzle
- steering and reversing gear
- propulsion system/vehicle interaction

Moon et al. (1997) describe a computational method developed to predict waterjet performance. They also describe model tests used to validate their computational work. The test arrangement was, in essence, an open water test boat for waterjets similar in concept to apparatus used for conventional screws propellers. The model consisted of a 4-

bladed 118mm diameter impeller with a 1mm tip clearance, a five bladed 120mm diameter stator, a 73.8mm diameter jet nozzle, and a 110mm diameter pitot type inlet. The platform was attached to a tow carriage and was tested at speed with the nozzle 306mm above the free surface and the inlet 364mm below. The transition between the inlet and impeller was circular in section and had a fairing around it to avoid excessive flow disturbance. Likewise, the pitot inlet was fitted into a faired cylindrical body. Power was supplied by a 5000 rpm servo drive motor with 8 Nm torque capacity.

Torque was measured with a Kempf & Remmers R46-IV propeller dynamometer (max. shaft speed = 3000 rpm, max. torque = ±40 Nm, max. thrust = 70 N). Flow rate was determined in the steady state bollard condition in two ways: directly, by collecting and weighing the discharge in an auxiliary tank over a measured time interval; and indirectly, by measuring the pressure change across the nozzle venturi and applying the Bernoulli and continuity equations. In the first case, the flow rate Q_j through the nozzle outlet area was used to calculate the mean jet velocity V_{jQ}. The jet velocity determined from the pressure measurements, V_{jp}, was then compared to V_{jQ} to give a correction factor to be applied to the pressure based measurements that were made in non bollard test conditions where direct measurement of flow was difficult. Pressure measurements were made with 8 taps at each of three stations: at the nozzle outlet, immediately downstream of the stator, and immediately upstream of the impeller. Pressure changes across the first two were used to calculate velocity, and changes across the latter two were used to calculate the impeller head, H.

The performance characteristics of the impeller were presented in terms of flow rate, pressure head, torque coefficient, and efficiency as:

$$J_Q = \frac{Q_j}{n \cdot D^3} \quad [2.1]$$

$$K_H = \frac{g \cdot H}{n^2 \cdot D^2} \quad [2.2]$$

$$K_Q = \frac{Q_t}{\rho \cdot n^2 \cdot D^5} \quad [2.3]$$

$$\eta_p = \frac{\rho \cdot g \cdot H \cdot Q_j}{2 \cdot \pi \cdot n \cdot Q_t} = \frac{J_Q \cdot K_H}{2 \cdot \pi \cdot K_Q} \quad [2.4]$$

Hoshino and Baba (1996) described several experimental methods used to determine waterjet propulsive performance, including cavitation tunnel tests and self propulsion tests for several types of vessels.

A cavitation tunnel arrangement was used to quantify inlet losses and impeller section wake fields by using a piping system in parallel with the tunnel's closed loop. The setup consisted of a ram jet type inlet mounted through a window in the tunnel's test section. The duct from the inlet passed through the window and into the impeller section, all of which were made from clear plastic to allow for observations and measurements. Downstream of the impeller section, where scaling was no longer a requirement, there was a diffusing length of pipe followed by a constant cross section pipe with an installed flow meter. No impeller or stator was fitted: water was drawn through the inlet, duct, impeller section and remaining piping by a pump located downstream. To close the loop,

the water was discharged back into the tunnel along the bottom leg upstream of the tunnel impeller.

Flow was measured with a flow meter, and static pressures were measured at the inlet and upstream of the impeller section, presumably with pressure transducers in taps. Wake surveys across the impeller section were performed with an LDV (see Section 3.9) for a range of inlet velocity ratios ($0.4 < IVR < 1.0$). The intake velocity ratio, IVR, is the ratio of the mean intake velocity to the free stream velocity of the flow. Losses were quantified by an inlet duct coefficient ζ_i given by:

$$\zeta_i = \frac{p_i - p_f + \frac{1}{2}\rho \cdot \left(V_i^2 - V_f^2\right)}{\frac{1}{2} \cdot \rho \cdot V_i^2} \qquad [2.5]$$

where,

V_i, V_f are the velocities at the inlet and impeller section, respectively

p_i, p_f are the static pressures at the inlet and impeller section, respectively.

In describing self propulsion tests for different types of ship, the authors mention several measuring techniques. For example, in tests with a semi-displacement ship, flow rate was measured by collecting the discharge in an auxiliary tank via a flexible hose positioned aft of the nozzle outlet. As pointed out by Moon et al. (1997) this inconvenient measuring system can be avoided by calibrating the measured flow rate with pressure measurements while in bollard conditions so that the pressure measurements can be used in running conditions.

Another example was for a pitot, or ram type inlet for a hydrofoil catamaran model. The general arrangement for this test was similar to the open water test boat setup used by Moon et al. (1997), although in the present case tow force was measured. Thrust was determined in two ways: directly by measuring the reaction force on a calibrated load transducer that was positioned in way of the jet discharge; and indirectly by measuring the pressure change across the nozzle venturi from which a velocity, flow rate, and then thrust can be calculated as:

$$T_{gross} = \rho \cdot Q_j \cdot (V_j - V_o) \qquad [2.6]$$

where,
Q_j is flow rate,
Vj is jet velocity,
Vo is free stream velocity fwd of inlet

Both ways were calibrated in bollard conditions and the authors noted that while they were in good agreement, the pressure measurements were used in the subsequent analysis which suggests that the pressure measurements were more effective. The number of pressure gauges at the two sections across the venturi was not reported.

Using the gross thrust T_{gross} calculated from self propulsion tests and measured resistance R from bare hull tests (with inlets closed), the inlet drag D_i was calculated as shown below. These were found for a range of inlet velocity ratios ($0.3 < IVR < 1.0$) for each of several test speeds.

$$D_i = T_{gross} - R \qquad [2.7]$$

The authors also gave details of a power prediction method that incorporates the results of resistance, self propulsion, and cavitation tunnel experiments.

Kruppa (1997) reported on a set of pump experiments that were done to investigate the effects of inflow disturbances on pump performance. The idea was to quantify the effects of typical features of waterjet installations, such as upstream shafting and non-uniform piping, compared to pump performance evaluated in ideal test bed conditions. Detailed internal flow measurements were made with an LDV. The author showed that for the pump tested, the different inflow disturbances all resulted in a peak efficiency drop of about 4% compared to ideal test condition results. It was also noted that high speed pumps, (e.g. axial flow) would suffer greater losses than lower speed pumps.

Minsaas (1997) described tests done in a free surface cavitation tunnel (at the Technical University of Berlin) to measure inlet losses and pressure and energy distributions in a pitot type inlet waterjet. Water was drawn into the inlet, through the duct, and into the impeller section by a downstream pump (no impeller was fitted). Axial wake was measured with a pitot rake fitted at the impeller section. The orientation of the rake in the impeller plane was controlled to step through 30 angular positions and pressures were measured at 6 radii. Static pressure was measured using pressure taps fitted at several locations between the inlet and impeller section, including 6 taps in the same plane as the pitot rake. Several different inlet lip geometries were tested. Cavitation patterns at the inlets were recorded and measurements were made over a range of inlet velocity ratios

and cavitation numbers. External drag on the inlet was measured with a six component balance.

The author presented two ways of calculating the inlet loss coefficient: one was based on the wake survey measurements, and the other on static pressure measurements. The results showed considerable differences, with the loss coefficient approximately 10% to 20% lower for the static pressure based on mean flow rate calculation. This was attributed to the fact that the surveyed velocity profile shows a non-uniform velocity profile, rather than a mean flow rate.

Terwisga (1997) presented a theoretical framework for the treatment of waterjet powering that dealt with each system component and the propulsor-hull interaction. While the scope of this work is outside the range of the present review, Terwisga (1997) provided a working definition of a waterjet-hull control volume that has practical use in laboratory measurements. Specifically, he proposed that one of the control volume's non material boundaries was conveniently defined as being in the vertical plane at a distance 1.1L forward of the inlet ramp's tangency point. L is the length of the inlet defined as the longitudinal distance between the leading and trailing tangent points. The limits of this boundary are set by the material boundary of the hull, or inlet ramp, and the point in the flow where there are no hull effects. This latter point can be approximately determined with measurements of the fluid velocity profile with, for example, an LDV or pitot rake.

Svensson (1997) gave a qualitative description of KaMeWa's power prediction methods. The measurement accuracy required to make reliable power predictions for waterjet

propelled vessels from self propulsion tests is very difficult to achieve. KaMeWa has taken a different approach which consists of using a combination of cavitation tunnel test experience, full scale data based corrections, and model resistance tests to predict full scale flow rate and shaft speed for a given power and ship speed.

Arén et al. (1996) reviewed the various waterjet test methods used at the KaMeWa free surface and conventional cavitation tunnels. Complete waterjet systems are tested in a free surface cavitation tunnel with a dummy hull. Construction of the waterjet is in clear plastic. Torque, Q_T, is measured by a shaft dynamometer and flow rate is determined from static pressure measurements across the nozzle venturi. Flow rate determined from static pressure measurements is calibrated with pitot tube measurements of the flow profile in the discharge jet. Waterjet efficiency η_u (uncorrected for modeling) is calculated using the mean jet velocity V_j and the mean velocity of the flow approaching the inlet V_{in} from:

$$\eta_u = \frac{\rho \cdot Q_j \cdot V_{in} \cdot (V_j - V_{in})}{P_{D.m}} \qquad [2.8]$$

where,

$P_{D.m}$ is delivered power at model scale

Q_j is volume flow rate

V_j and V_{in} are velocities at the jet and inlet respectively

Full scale power calculations are then based on resistance and self propulsion test results, including hull efficiency. Other measurements are made for various purposes, such as determining blade stresses, noise and vibration, and hull loads.

Inlet tests are done in a conventional cavitation tunnel with an arrangement similar to that described by Hoshino and Baba (1997). In addition to observations of cavitation and pitot rake wake surveys, the inlet loss coefficient, ζ, is determined based on measurements of velocity profiles at the inlet and outlet.

$$\zeta = \frac{E_{in} - E_{out}}{\frac{1}{2} \cdot \rho \cdot Q_j \cdot V_{in}^2} \qquad [2.9]$$

where,

E_{in} - E_{out} is the loss of power at the inlet

The terms in the numerator represent the energy loss. Given the fact that the measurements include surveyed profiles, an integral approach to the efficiency calculations may improve the accuracy.

Dyne and Lindell (1994) gave a comprehensive description of the standard power prediction method and corresponding model tests used at SSPA. They then criticized some elements of their work and proposed some improvements. This work is clearly reflected in the power prediction method given by the 21st ITTC Specialist Committee (of which Dyne was a member) and as such it is instructive to review it in some detail.

The standard self propulsion test consists of a towed model free to pitch and heave, but restrained in yaw, surge and sway. It is possible to use stock pumps, but the inlet and nozzle geometry must be scaled. Where stock pumps are used, they must be operated at or near their design point. Tests are done at a series of steady model forward speeds and pump speeds. At each test, the tow force, shaft speed and torque, model speed, fore and

aft drafts, flow rate, and static pressures at the intake and upstream and downstream of the pump are measured. Photographs and video are also used, and presumably atmospheric pressure and water temperature are measured regularly.

Flow rate is determined with either a paddle wheel in the jet, or with static pressure measurements across the nozzle venturi. Either way, the flow rate is first calibrated in the bollard condition by collecting and weighing the discharge in an auxiliary tank. Using the flow rate determined from these measurements, the mean speed at any station of known cross sectional area can be calculated from the continuity requirement. In this case, the mean velocity at stations 7, 5, 3 and 1 are required (see Figure 2.1). Stations 3 and 5 have material boundaries that define the cross sectional area. The stream tube area of the flow upstream of the intake, however, has non material boundaries and is estimated using an assumed width of $1.3b_1$, where b_1 is the width of the intake, and either a measured or calculated boundary layer velocity profile so that the thickness h_1 of the stream tube can be calculated from

$$Q_j = 1.3 \cdot b_1 \cdot \int_0^{h_1} u_{1x}(z) \cdot dz \qquad [2.10]$$

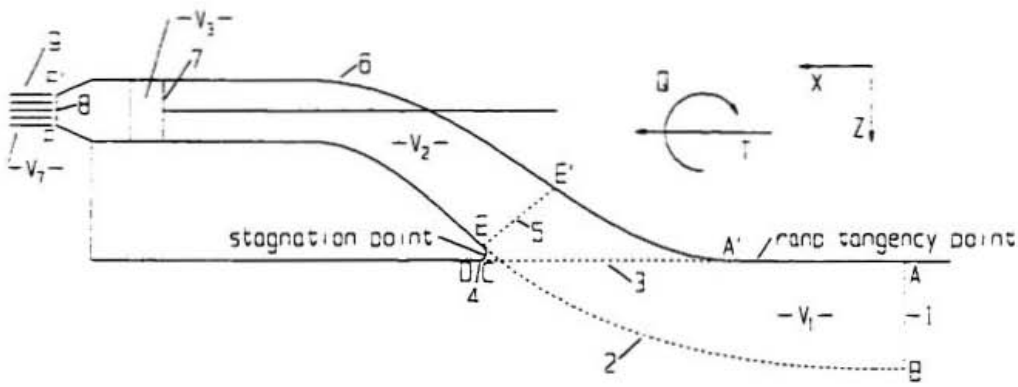

Figure 2.1 – Definition of waterjet system control volume

Station 9 is a second non material boundary. When the discharge forms a vena contracta at station 9 behind the nozzle outlet, the jet velocity should be determined based on the measured cross sectional area of the vena contracta. The mean velocities at the intake V_1, pump inlet V_3, pump outlet V_5, and jet V_7 can all be calculated. The power prediction then proceeds through the following steps:

Model thrust:

$$T = \rho \cdot Q_j \cdot (V_7 - V_1) \qquad [2.11]$$

Model wake:

$$w = \frac{(V_0 - V_1)}{V_0} \qquad [2.12]$$

where V_0 is the free stream or ship velocity

Thrust deduction:

$$t = \frac{T - (R - R_a)}{T} \qquad [2.13]$$

where,

T is the thrust

R is the total resistance

R_a is the air resistance

Model hull efficiency:

$$\eta_H = \frac{1 - t}{1 - w} \qquad [2.14]$$

Model shaft power:

$$P_D = 2 \cdot \pi \cdot Q \cdot n \qquad [2.15]$$

where,

Q is the shaft torque

n is the shaft speed [rotations per second]

Model total efficiency:

$$\eta_T = \frac{(R - R_a) \cdot V_0}{P_D} \qquad [2.16]$$

Model pump efficiency:

$$\eta_P = \frac{\eta_T}{\eta_{jet} \cdot \eta_R \cdot \eta_H} \qquad [2.17]$$

or,

$$\eta_P = \frac{Q_j \cdot \left(p_5 + \frac{1}{2} \cdot \rho \cdot V_5^2 - p_3 - \frac{1}{2} \cdot \rho \cdot V_3^2 \right)}{P_D} \qquad [2.18]$$

where p_i is the pressure at station i

Inlet loss coefficient:

$$\zeta_{13} = \frac{p_1 - p_3 + \frac{1}{2} \cdot \rho \cdot \left(V_1^2 - V_3^2 \right) - \rho \cdot g \cdot \Delta h}{\frac{1}{2} \cdot \rho \cdot V_1^2} \qquad [2.19]$$

where Δh is the jet's height above the water surface

Outlet loss coefficient:

$$\zeta_{57} = \frac{p_5 - p_7 + \frac{1}{2} \cdot \rho \cdot \left(V_5^2 - V_7^2 \right) - \rho \cdot g \cdot \Delta h}{\frac{1}{2} \cdot \rho \cdot V_7^2} \qquad [2.20]$$

Waterjet efficiency:

$$\eta_{jet} = \frac{2 \cdot \frac{V_1}{V_7} \cdot \left(1 - \frac{V_1}{V_7}\right)}{1 + \zeta_{57} - \frac{V_1^2}{V_7^2} \cdot (1 - \zeta_{13}) + \frac{2 \cdot g \cdot \Delta h}{V_7^2}} \qquad [2.21]$$

The resistance values in the calculation of thrust deduction are measured from resistance tests, p is static pressure, and Δh is the height between the free water surface and impeller's centerline. To predict full scale power, velocities and flow rate are scaled according to Froude scaling, thrust deduction is the same in model and full scale, and the ship wake is calculated in the same way as the model wake, by estimating the velocity profile forward of the intake. Knowing the hull efficiency, and using special pump tests to determine the pump efficiency η_P and relative rotative efficiency η_R, the ship shaft power required can be predicted:

Ship shaft power:

$$P_D = \frac{P_E}{\eta_{jet} \cdot \eta_H \cdot \eta_R \cdot \eta_P} \qquad [2.22]$$

or.

$$P_D = P_{Dm} \cdot \lambda^{3.5} \cdot \frac{\rho_s}{\rho_m} \cdot \frac{\eta_{Pm}}{\eta_P} \qquad [2.23]$$

where λ is the model scale
(the subscripts s and m are shown explicitly to denote ship and model)

The authors went on to discuss a new proposed method in which net thrust is calculated from momentum considerations, without recourse to a thrust deduction factor. The basic

concept is similar to the method proposed by the 21st ITTC, which is described in Chapter 5.

18th ITTC Waterjet Test Procedures (1987) describe methods which are based on using a theoretical model of overall system performance. This theoretical model is based on examining element performance and then using a system to account for the interaction effects. Bare hull resistance tests are performed on a vessel equipped with the inlet fairing. The experimental bare hull resistance is then used with statistics provided by waterjet producers to determine the gross thrust.

This method will yield a design thrust within an accuracy of about ± 5-7%. It is noted that the thrust deduction is mainly due to differences in trim and lift forces in the inlet from towed to propelled conditions.

English (1994) describes the elements of waterjets with flush intakes, the problems often associated with them, and some possible techniques for improving performance. Design variables are identified as well as some basic considerations such as choice of ramp angle and selection of impeller speed. Suggestions are made on methods to improve waterjet performance such as: boundary layer exclusion or re-energization, using impeller blades with swept leading edges and the use of pre-stage supercavitating pumps/inducers with rotary flow homogenizes.

CHAPTER 3
INSTRUMENTATION

3 INSTRUMENTATION

This chapter is dedicated to describing the operating principles of many of the types of instruments used in the various experiments discussed in this thesis.

3.1 Pitot Tubes

Pitot tubes are used to make measurements of fluid velocity. They are probes which face the flow stream, creating a stagnation point just ahead of the probe face. The pressure measured at this location can then be used with a reference static pressure to calculate the average local velocity at the probe.

The pitot tubes used in the experiments discussed in this thesis measured both the pressure at the stagnation point at the tip of the tube and the static pressure in the fluid. The pitot-static tube shown in Figure 3.1 consists of a small tube inside a slightly larger tube. The inner tube extends to the tip facing the flow stream and is exposed to the

pressure at the stagnation point. The outer tube contains small holes parallel to the flow which are used to measure the static pressure in the fluid. The diameters of the tubes can be chosen from a wide selection depending on the application. At the top of a pitot-static tube are two connections for tubing that can be attached to manometers or other pressure measurement devices. The experiments in this thesis used electronic pressure transducers as discussed in Section 3.2. Pitot tubes are intrusive measurement instruments in that they cause disturbances in the system they are measuring.

The flow velocity can be determined by using Bernoulli's energy equation:

$$\frac{p_0}{\gamma} + \frac{u^2}{2 \cdot g} = \frac{p_s}{\gamma} \qquad [3.1]$$

where,

p_0 = static pressure in fluid

p_s = pressure at stagnation point

u = local average fluid velocity

γ = specific weight of water

g = acceleration due to gravity

which can be expressed as:

$$u = \sqrt{2 \cdot g \cdot \left(\frac{p_s}{\gamma} - \frac{p_0}{\gamma} \right)} \qquad [3.2]$$

Often with pitot-static tubes there can be small errors introduced by imperfections in the tube or in the locations of the piezometer holes measuring static pressure. To account for any discrepancies a coefficient of instrument C_I, may be included in Equation 3.3. The value of C_I can be supplied by the manufacturer or determined during calibration tests.

$$u = C_1 \cdot \sqrt{2 \cdot g \cdot \left(\frac{p_1}{\gamma} - \frac{p_0}{\gamma} \right)} \qquad [3.3]$$

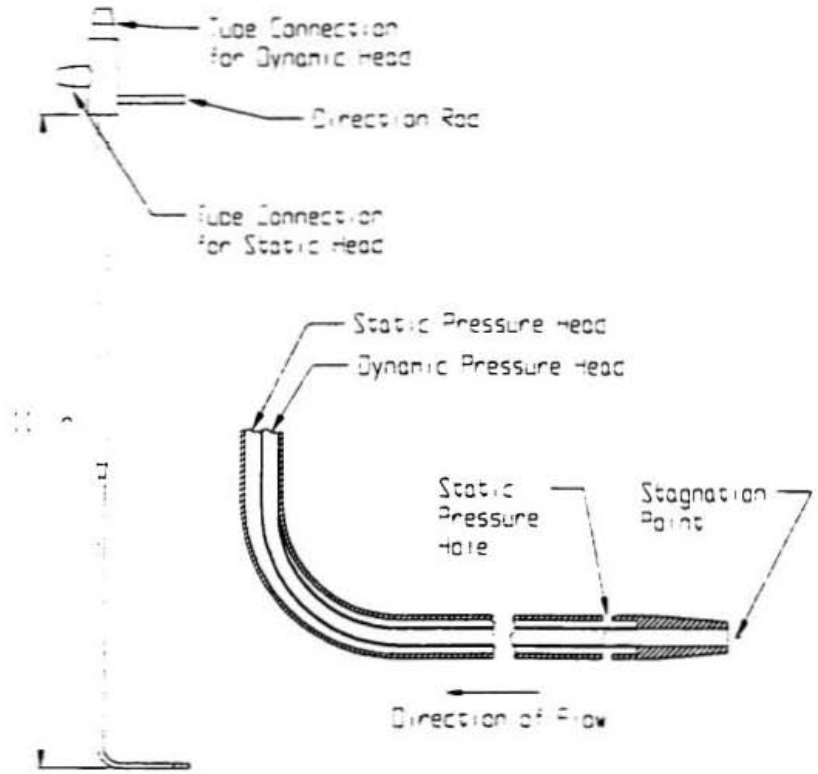

Figure 3.1 – Pitot Tube Measurements

3.2 Pressure Transducers

Pressure transducers are instruments that are able to translate pressure in a fluid to a proportional output voltage that can be sampled and acquired with a data acquisition system. Calibrations are used to determine the pressure to output voltage relationships for specific sensors. Two types of pressure transducers were used in the experiments discussed in this thesis: gauge pressure transducers and differential pressure transducers.

The gauge pressure transducer, shown on the right in Figure 3.2, measures the pressure in a fluid relative to atmospheric pressure. It operates by measuring the mechanical strain on a sensing diaphragm: one side of the diaphragm is exposed to the fluid, the other to the atmosphere. The sensing elements of the diaphragm incorporate four piezo-resistive silicon elements. These tiny strain gauge elements are designed to change their electrical resistance in proportion to applied mechanical stress. The diaphragm is located at the end of a threaded probe. At the top of this probe is a hexagonal cap with a rubber O-ring seal used to insure water tight installation. At the top of the housing are wires for the electrical connections and a small tube used to vent one side of the diaphragm to atmosphere.

A differential pressure transducer, shown on the left in Figure 3.2, operates under essentially the same principles except that each side of the sensing diaphragm is exposed to fluids of different pressures. The transducer therefore measures only a pressure difference. Differential pressure transducers are often used with pitot-static tubes since it is the difference between the stagnation pressure and static pressure that is of interest. The sensing elements are enclosed in a robust metal housing with a threaded hole in each end for tubing connections.

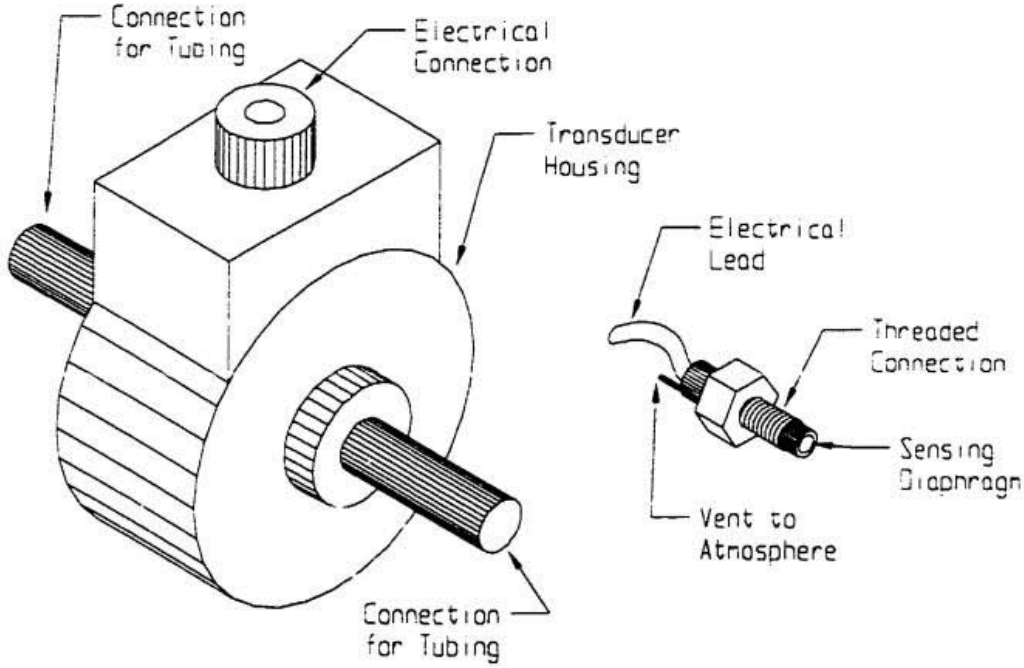

Figure 3.2 – Pressure Transducers

3.3 Displacement Transducers

A displacement transducer measures linear motion and position. This type of transducer was used to track the change in vertical position of the towed model discussed in Chapters 6 and 7. The transducer, shown in Figure 3.3, works on the principle of a linear variable differential transformer (LVDT). The LVDT consists of a primary winding, two secondary windings and a soft iron core. An alternating current is passed through the primary winding to produce a magnetic field which is concentrated in the soft iron core. The core then induces a voltage in each of the two secondary windings. When the core changes position, one secondary winding will receive more magnetic flux than the other to produce a measurable voltage difference. This voltage difference can then be calibrated against the linear position of the core.

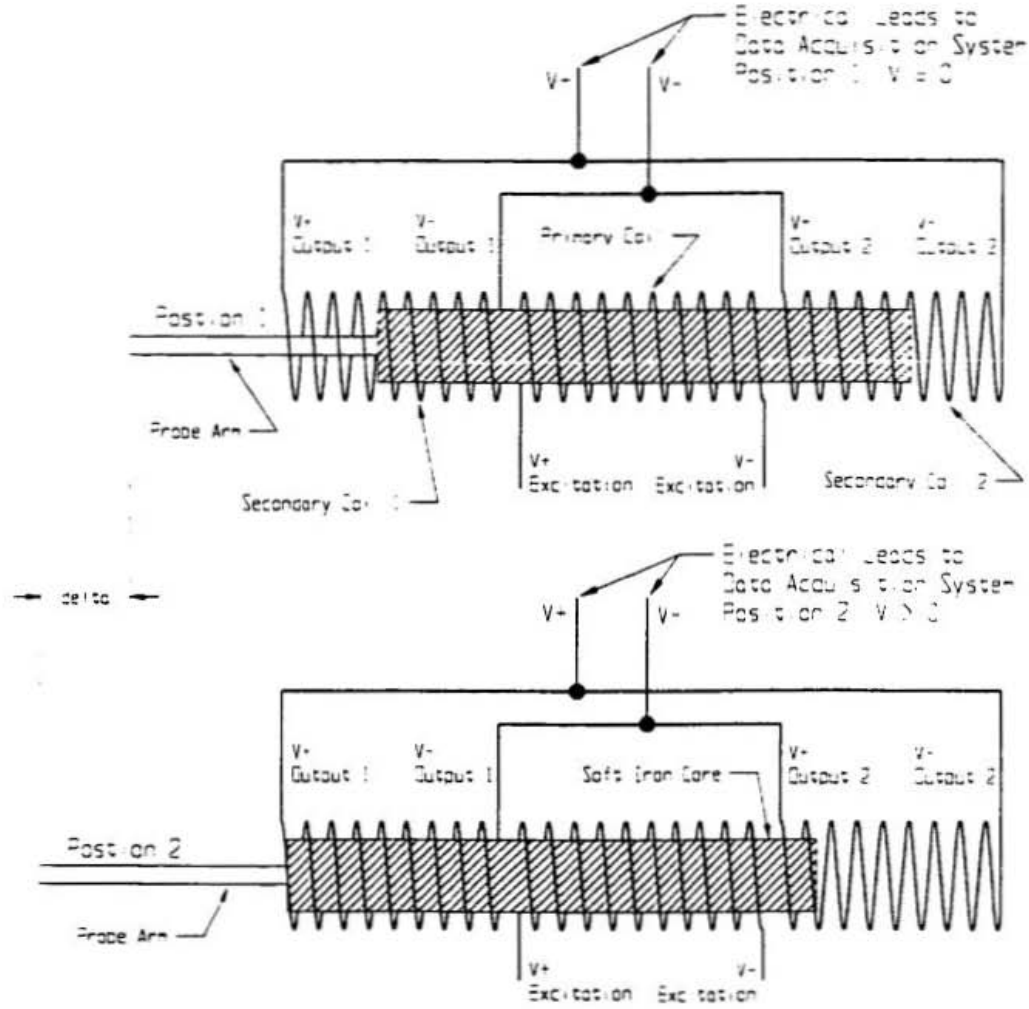

Figure 3.3 – LVDT Diagram

3.4 Force Transducers

Force transducers or load cells apply similar principles as pressure transducers in that they have internal gauges which change their electrical resistance when stressed. Force transducers are available in a variety of designs. The experiments discussed in this thesis used S-beam load cells. This transducer, shown in Figure 3.4, is designed to measure axial force in tension or compression. It consists of a metallic S-shaped body, usually

steel, with a cavity in the center. Four strain gauges are fixed to the internal surface of the cavity. These gauges change their electrical resistance in response to mechanical deformation. The four gauges form a Wheatstone bridge from which a voltage reading can be sampled with a data acquisition system and converted to physical units based on calibration results.

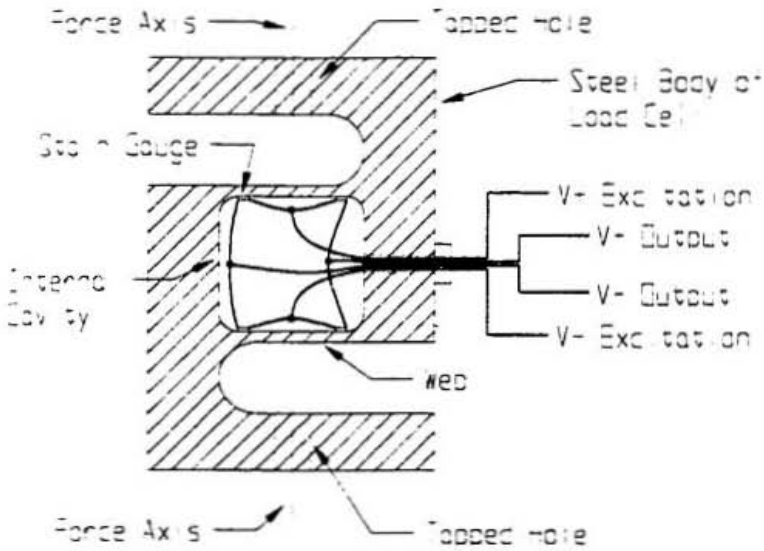

Figure 3.4 – S-Beam Load Cell

3.5 Torque Transducers

Torque transducers are used to determine the applied load on a waterjet system by the motor during operation. These measurements give an indication of the unit's performance and can be used for estimations of full scale power requirements. Kempf & Remmers dynamometers are often used for measuring torque on model propeller shafts at IMD. However, this method could not be used for tests with model waterjet thrusters since the required shaft speeds are much higher than rated for these dynamometers. In order to make torque measurements at these high shaft speeds, two approaches were taken.

The first approach involved a pair of small DC electric motors which had maximum shaft speeds exceeding 10,000 rpm. These motors were used for the self-propulsion tests described in Chapter 7. The motor was mounted to a housing which contained a bearing. A second section connected the bearing to a rigid flange such that the motor section was free to rotate. An extension arm was attached to the rotating section containing the motor and fixed to a small load cell. This arrangement can be seen in Figure 3.5. During operation, the load cell measured the reaction torque from the motor, and gave an output proportional to the torque on the shaft.

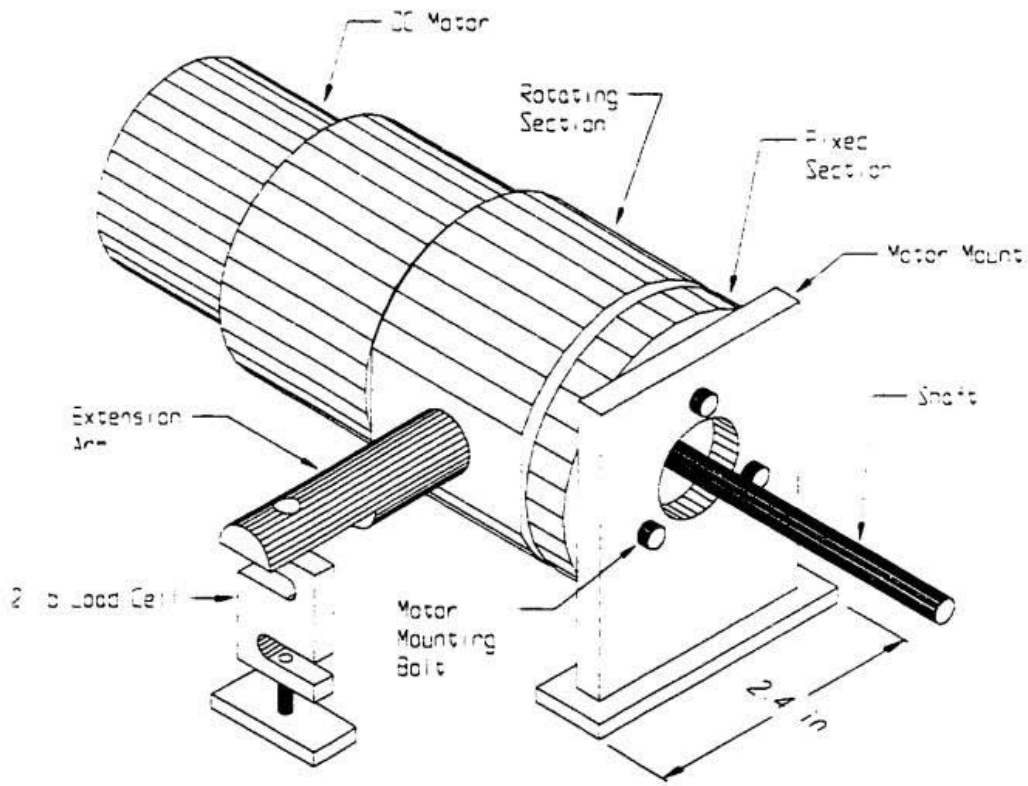

Figure 3.5 – Small Motor Reaction Torque Arrangement

The second approach was used for the larger AC brushless motor used in the waterjet test platform discussed in Chapter 8. This motor also had a high shaft speed (7000 rpm),

making the use of slip rings on a gauged shaft impractical. Again the alternative was to measure the reaction torque from the motor. The size and weight of the motor, coupled with irregular results from the smaller torque measuring arrangement, lead to a customized design of a reaction torque transducer for this application.

The transducer was designed as single unit with three main components: the motor mount, the mounting flange, and four gauged webs. The motor was bolted to the motor mount which was suspended in the mounting flange by the four webs as shown in Figure 3.6. Included in the mounting flange were holes for attachment to the support frame as well as four sets of overload stop screws which limited the rotation of the motor mount as a safety mechanism to prevent damage to the webs from high loads. A front view of the transducer can be seen in Figure 3.7.

The majority of the transducer was machined out of aluminum using traditional techniques. The web sections were cut using a wire electric discharge machining (EDM) technique. Sometimes called spark erosion machining, the process involves using tiny sparks which arc between the cutting wire and the part material causing erosion. The process is slow but coupled with computer numerically controlled movement for the cutting wire, can produce very small and accurate cuts.

The suitability of the web shape was examined using finite element techniques. Extensive effort went into designing the webs such that the stress distribution across the webs was even, and concentrations were minimized. The T-shape web shown in Figure 3.7 was seen to have the best stress properties for gauge mounts regardless of the direction of the applied torque.

The four webs were fixed with strain gauges on each side for a total of eight gauges. During operation one side of each web was under tension and the other under compression. This can be see in Figure 3.7 given a counter-clockwise applied torque ('C' for compression, 'T' for tension). The gauges were wired together to form a Wheatstone bridge shown in Figure 3.8. This arrangement was intended to minimize possible load anomalies experienced by the webs, such as supporting the weight of the motor. The equation for the transducer's output voltage is given below.

$$\frac{E_o}{E} = \frac{(C_1 + C_3)}{(C_1 + C_3) + (T_2 + T_4)} - \frac{(T_1 + T_3)}{(T_1 + T_3) + (C_2 + C_4)} \qquad [3.4]$$

E_o = output voltage

E = excitation voltage

C_{1-4}, T_{1-4} = resistance of strain gauges as labeled in Figure 3.8

Since the webs and gauges were sensitive to temperature variations, fiberglass washers were placed between the motor face and the motor mount in an effort to impede the heat transfer from the motor during operation. The natural frequency of the transducer was another concern and design effort went in to ensuring that it was outside of the frequency range induced by the motor at speed.

A special calibration rig was designed for this torque transducer. IMD does not have the capability for dynamic calibration for torque. A static calibration was therefore used which used weights with a known moment arm to apply loads to the transducer. A dummy weight was used to simulate the cantilever load on the transducer caused by the

motor. Static calibration of this type cannot account for, or determine, the effects caused by RF noise generated by the motor.

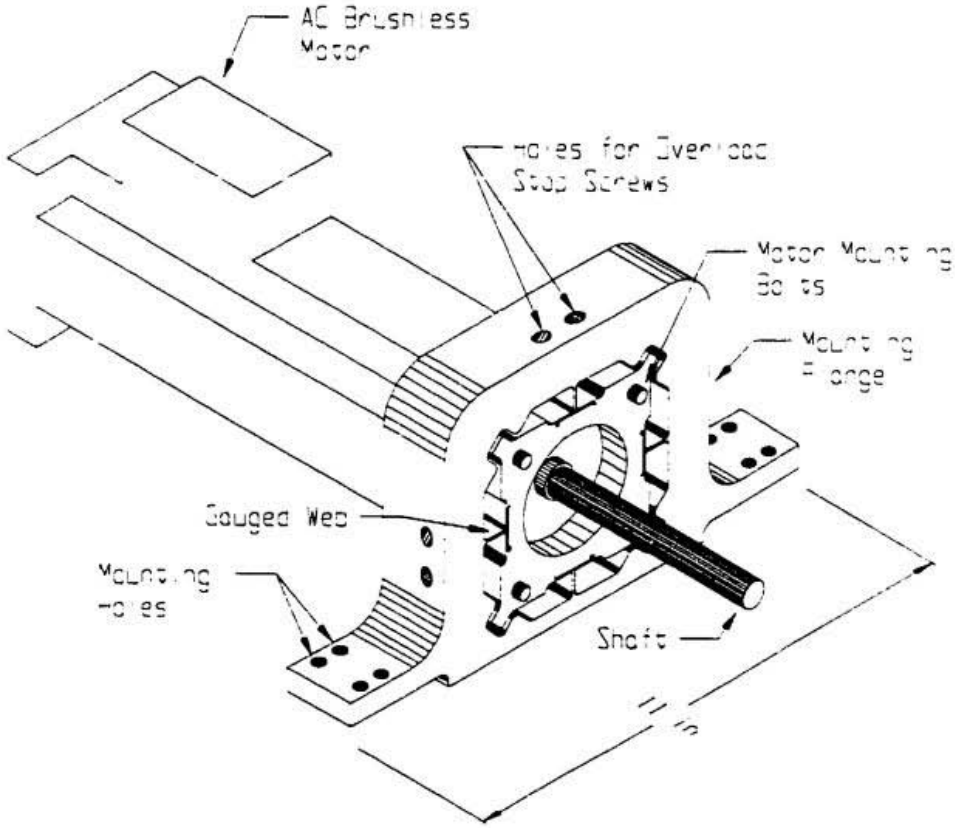

Figure 3.6 – Large Motor Reaction Torque Arrangement

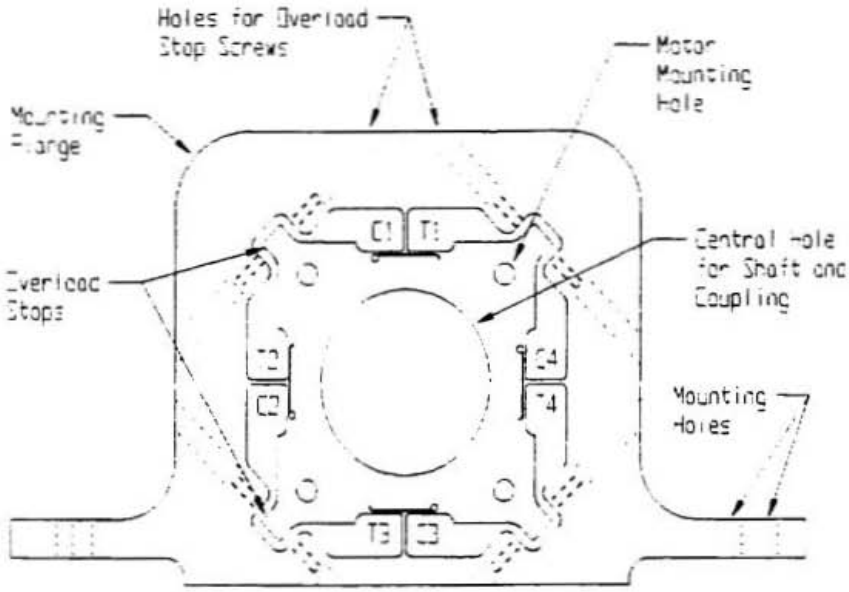

Figure 3.7 – Reaction Torque Transducer

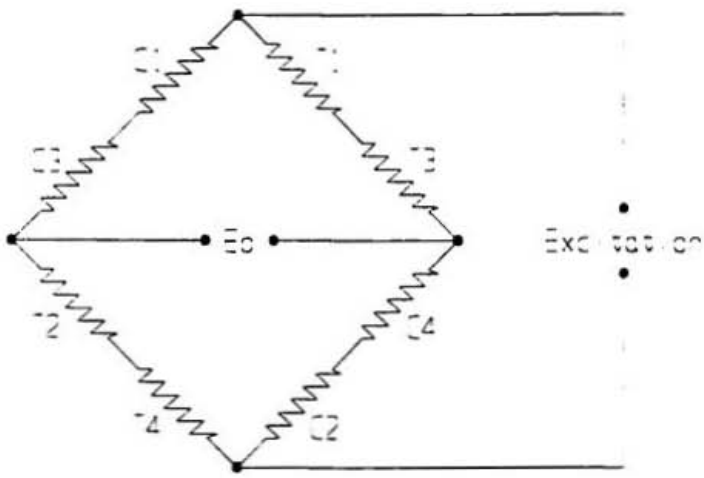

Figure 3.8 – Wheatstone Bridge for Torque Transducer

3.6 Tachometers

Tachometers are used to measure the rotational velocity of mechanical components. The tachometer operates under the same principles as a generator, the basic design of which is similar to a small DC motor. A magnetic core is surrounded by a primary winding. As the

core rotates, it induces a current flow and a corresponding voltage in the winding. This voltage, which is proportional to rotational velocity, can then be sampled by a data acquisition system. Tachometers were used to measure the impeller speeds of the model waterjets in Chapters 8 and 10.

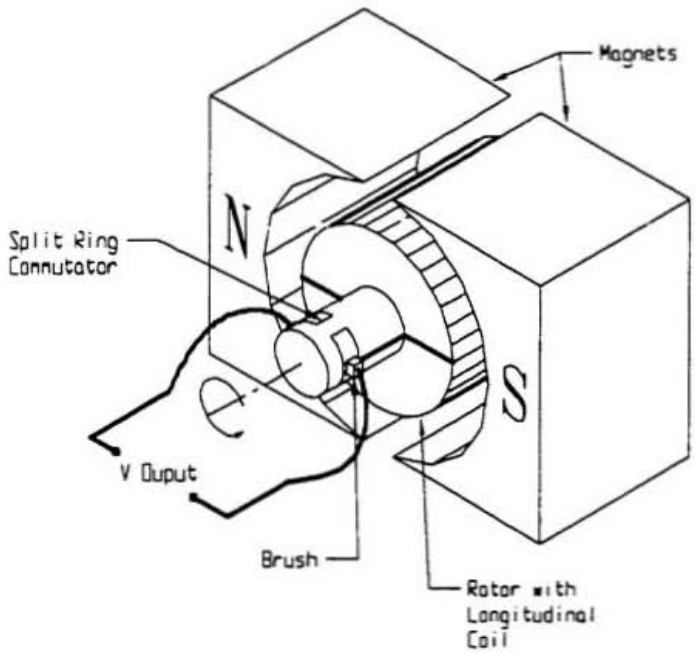

Figure 3.1 – Simplified Tachometer

3.7 Inclinometers

An inclinometer was used to measure the running trim of the towed model discussed in Chapters 6 and 7. The inclinometer used in these experiments employed a torsional flexure suspension system housed in a fluid. The basis of operation is a small DC torque motor which maintains the position of a pendulum whose pivot point is a thin member that can flex torsionally.

A torque motor is a variation of other motors designed specifically to hold stalled or very low speed conditions for long periods of time without burning out or releasing the applied torque. Normal motors apply approximately 150% of the rated torque at zero speed, which can cause them to burn out. Torque motors can act as a spring by continuously applying a certain torque or pressure although not always moving.

When the inclinometer is tilted, the pendulum moves under the force of gravity which causes a sensor to send a signal to a servo amplifier. The amplifier then adjusts the torque motor until the pendulum has returned to its original position. The current used to drive the torque motor passes though a stable resistor developing a voltage proportional to the tilt angle. This voltage can then be recorded by a data acquisition system. The inclinometer arrangement, shown in Figure 3.9, is surrounded by a semi-viscous fluid which acts to dampen shocks or vibrations. The entire unit is enclosed in a rectangular steel housing with a female connector on one side.

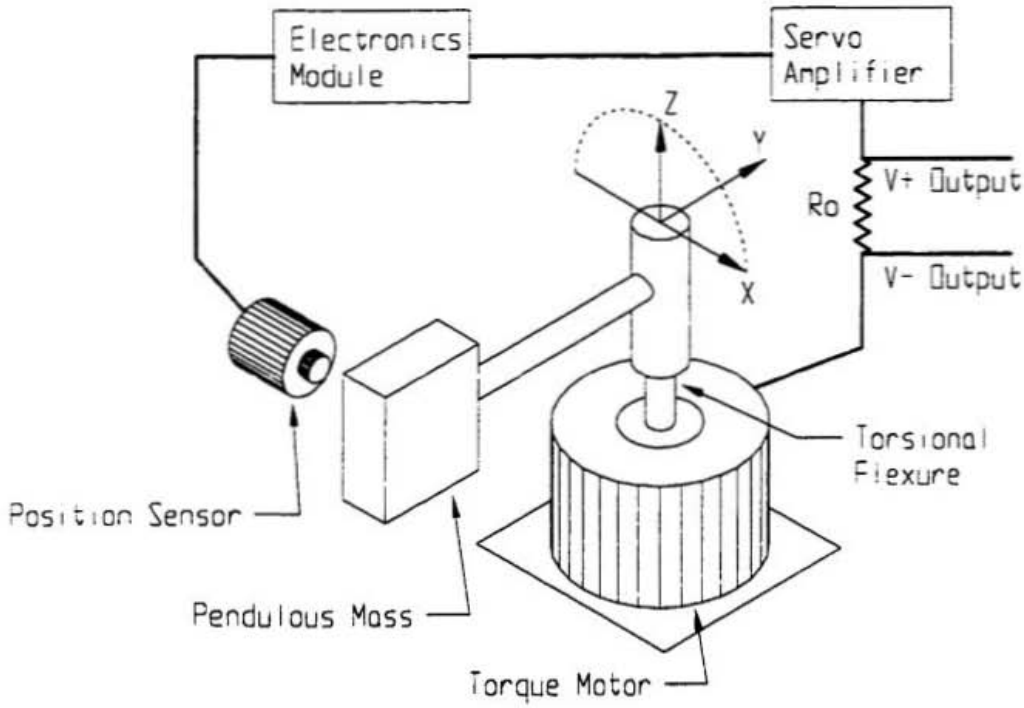

Figure 3.9 - Inclinometer

3.8 Data Acquisition

Measurements made by the electronic transducers were recorded with a standard data acquisition system used by IMD. Most transducers give continuous or analog output. For example, as a strain gauge deforms in a force transducer, the resistance change is smooth and continuous (within its design limits). In the data acquisition system, the analog output first passes through a signal conditioner which can amplify it and electronically filter out unwanted signals, if necessary. The signal conditioner also supplies the required excitation voltages needed for some transducers. The output signal then passes from the conditioner to an analog to digital converter. The A/D converter repeatedly takes discrete measurements or samples of the signal at set time intervals. A sampling frequency of 50 Hz was used for the experiments discussed in this thesis. The data acquisition system had

several channels and recorded the output from all the transducers simultaneously. Calibrations for converting voltages to physical units were performed through the same data acquisition arrangement as used for the experiments. This was necessary to avoid possible errors that can be caused by small differences in the behaviour of electronics from different signal conditioners, channels, and A/D converters. The sampled data can then be analyzed with software to extract the required information.

The output history of the channels was viewed graphically by computer which allows several time periods to be selected for analysis. All of the individual data points in a given selection were used to calculate: a maximum value, a minimum value, a mean value, and a standard deviation. In most of the tests discussed in this thesis, two selections were made. The first selection was taken of data recorded before the experiment was started and used as a reference. The second selection was taken of data recorded during the steady phase of the experiment. The values used in calculations, called tared values, were the differences between the steady state means and the reference means. A sample time history of a transducer's output is shown in Figure 3.10 along with example calculations in Table 3.1. The analysis software does not limit the number of selections that can be made and many other forms of analysis are available depending on the application.

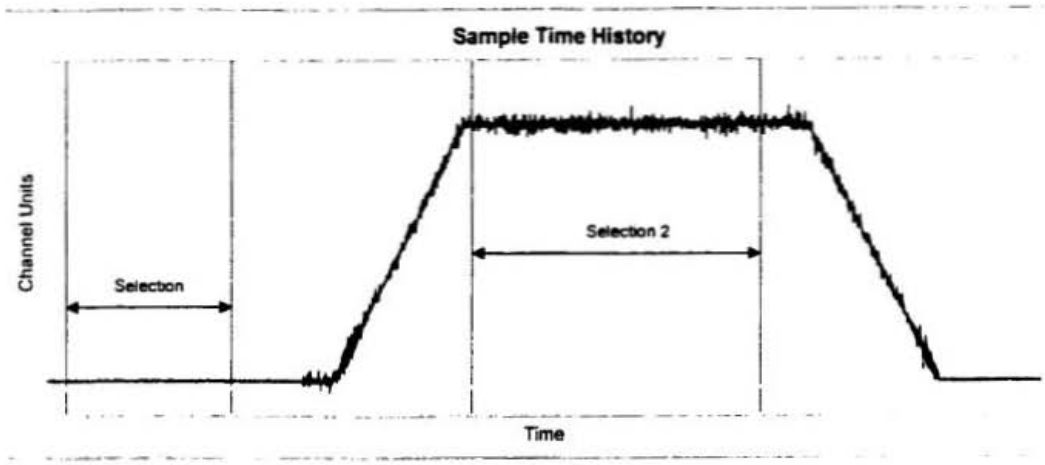

Figure 3.10 – Sample Channel History

Selection 1	**Selection 2**
Maximum Value x_{max}	Maximum Value y_{max}
Minimum Value x_{min}	Minimum Value y_{min}
Mean $\bar{x} = \frac{\sum_{i=1}^{n} x_i}{n}$	Mean $\bar{y} = \frac{\sum_{i=1}^{m} y_i}{m}$
Standard deviation $\sigma_1 = \sqrt{\frac{\sum_{i=1}^{n} (x_i - \bar{x})^2}{n-1}}$	Standard deviation $\sigma_2 = \sqrt{\frac{\sum_{i=1}^{m} (y_i - \bar{y})^2}{m-1}}$
x_i = measured values in selection 1	y_i = measured values in selection 2
n = number of values in selection 1	m = number of values in selection 2
Reference Value $\bar{x}$	
Steady State Value $\bar{y}$	
Tared Value $\bar{y}' = \bar{y} - \bar{x}$	

Table 3.1 – Example Calculations

3.9 Laser Doppler Velocimetry

Experimental measurement of the velocity distribution in a flow field can be a difficult task since most common measurement techniques involve instruments which, to some extent, invade or disrupt the flow they are measuring. Pitot tubes, hot wire anemometry, hot disk anemometry, etc., all require a probe to be located in the flow field and only measure an average flow velocity over the probe's measurement area. Since there are limits on how small these probe's can be made, measurement resolution is limited. The magnitude of the disruption a probe causes in the flow can vary, but cannot be eliminated completely. The use of a laser Doppler velocimeter or LDV, which relies on optics for flow measurement, can provide a means for making accurate non-intrusive measurements with high resolution.

An LDV does not measure the speed of the flow directly. Instead, it uses laser light to measure the velocity of tiny particles in the flow stream which are assumed to travel at the same speed as the flow itself. These particles are usually of the order of about 1 micron in diameter and the number of particles in the fluid, or the seeding density, is usually small enough to have virtually no effect on the flow characteristics. The primary components of an LDV system are: the laser(s), optic system, computer controlled indexer(s), probe(s), photo-detector(s), data acquisition, and processing software.

The principle of operation of an LDV is based on the behaviour of two intersecting laser beams. Laser light has the special property of being coherent. That is, all of the photons are travelling in phase so that laser light has a constant frequency. When two identical lasers intersect, they will interfere in the volume of intersection causing a stable pattern

of constructive and destructive interference. An illustration of this is given in Figure 3.11. A pair of identical beams are shown intersecting. The light is modeled as a sine wave fluctuating through maximum and minimum values. In the diagram, part of the sine wave of each beam is replaced by alternating thick and thin lines that represent the maximum and minimum values of their waves respectively. The constructive interference produced by intersecting maximum and minimum values causes brightly illuminated bands or fringes. Destructive interference produced by maximum values intersecting minimum values causes poorly illuminated bands between the fringes. The fringe spacing can be calculated with the known wavelength of the lasers and their angle of intersection, as shown in Equation 3.5.

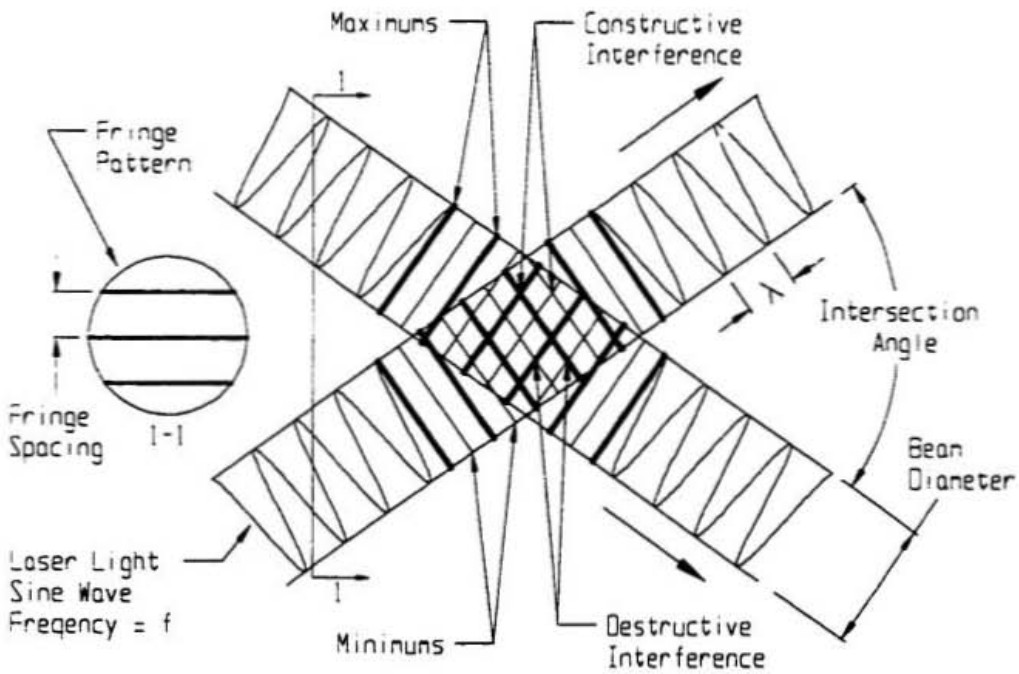

Figure 3.11 – Laser Interference Pattern

$$p = \frac{\lambda}{2 \cdot \sin(\theta / 2)} \qquad [3.5]$$

p = fringe spacing

λ = laser wavelength

θ = angle of intersection

The actual intersection point is an ellipsoidal volume whose size depends on the diameter of the beams and their angle of intersection. In this volume, the fringes can be thought of as disks. A particle travelling through this point is illuminated in pulses as it passes through each fringe. The reflected light from the particle can be measured by a photo-detector, an analog device which can respond almost instantaneously to changes in light intensity to give a proportional output voltage. A sample photo-detector output of a particle passing through a fringe pattern can be seen in Figure 3.12. The analog output voltage then passes through an analog to digital converter such as described in Section 3.8. The signal information can then be processed by computer. The shape of the Doppler burst shown in Figure 3.12 is caused by the Gaussian light intensity distribution which the intersection volume has in all three dimensions (i.e. the light is brightest at the center of the fringes).

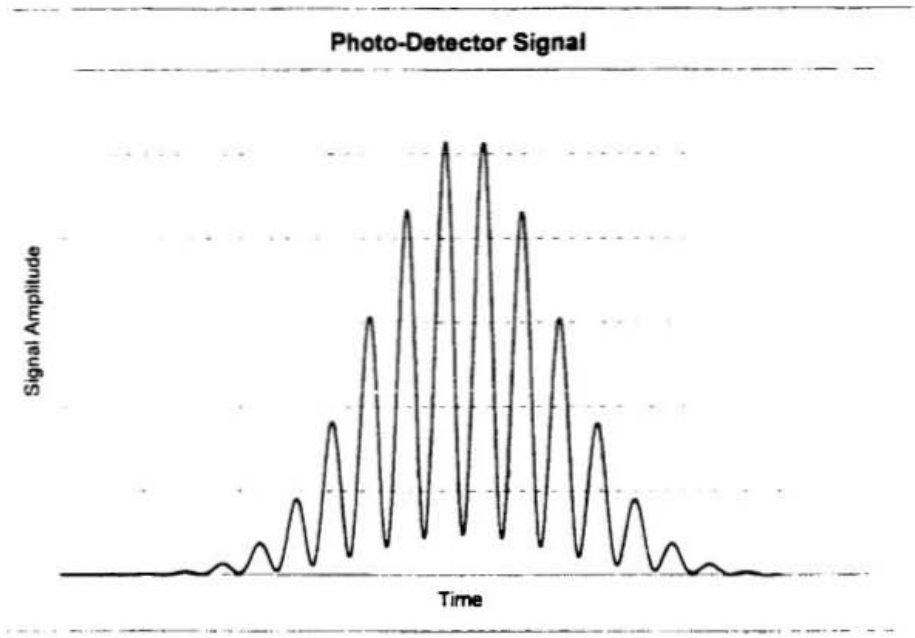

Figure 3.12 – Photo-Detector Signal from a Particle

Processing the photo-detector signals into velocities is performed in real time by the LDV software. It first filters usable signals from background noise and then transforms the Doppler bursts to the frequency domain by a Fourier transform. The predominant frequency for a given signal represents the average time the particle took to travel across each fringe spacing. The particle velocity can be then determined with the known fringe spacing by Equation 3.6. Since fringes are parallel in the intersection volume, this velocity only represents the component of a particle's absolute velocity which is normal to the fringe disks.

$$v_i = p \cdot f_i \qquad [3.6]$$

v_i = particle velocity component perpendicular to fringe lines

p = fringe spacing

f_i = signal frequency

Many particle signals are needed to accurately determine the flow velocity at a given point. Each particle contributes to a velocity distribution from which the mean, maximum, minimum and standard deviation can be used in subsequent analysis of the flow field. The number of particles required by the LDV for a given flow velocity measurement can be chosen to suit the experiment.

The LDV system at IMD, referred to in Chapter 8, can measure flow velocities in two orthogonal directions with a single probe. The system consists of an argon-ion laser which produces a single beam, which after entering the optical unit, passes through a Bragg cell. A Bragg cell is essentially a block of glass that is excited by an electro-mechanical transducer. Oscillations from the transducer produce acoustical waves which propagate through the glass to generate a moving pattern of high and low density. The incident light beam hits the series of travelling wave fronts which act as a thick diffraction grating. By adjusting the incident angle of the cell and the acoustic frequency, the beam can be divided by the cell between its zeroth and first order of diffraction. The original beam can therefore be split into two beams, one of which is phase shifted. These beams then travel though prisms which split each of them into two colors: green (λ = 514.5 nm) and blue (λ = 488 nm). The four beams travel through manipulators which direct them into fiber optic cables and then lead them to the probe. At the probe the beams are directed through a focusing lens which cause them to intersect. The planes formed by the pairs of intersecting beams are situated at right angles to each other. A particle passing through the intersection volume is illuminated by fringes in two orthogonal directions simultaneously. The reflected light (back scatter) is collected by the probe and focused into a fiber optic cable which sends it to the receiving optics. The light

is then divided by color and sent to two separate photo-multipliers. The resulting signals can then be processed into velocity data. A diagram of this set-up can be seen in Figure 3.14.

The direction, positive or negative, of each velocity component can also be determined in this system. Since one beam in each pair is phase shifted by the Bragg cell, in this case by 40 MHz, the interference pattern of fringes roll at this constant known frequency. This means that even a stationary particle produces a Doppler burst. Particles travelling in the same direction as the fringe roll produce lower signal frequencies while particles travelling against the fringe roll produce higher signal frequencies. The processing software accounts for this frequency shift while using it to assign directions to the velocity signals.

Measuring velocities in several locations requires precise movement of the probe's position. The experiments discussed in Chapter 8 use a computer controlled indexer with traverse ranges in three dimensions. This indexer, shown in Figure 3.13, is controlled by the LDV software so that measurements can automatically be made in an array of locations set by the operator.

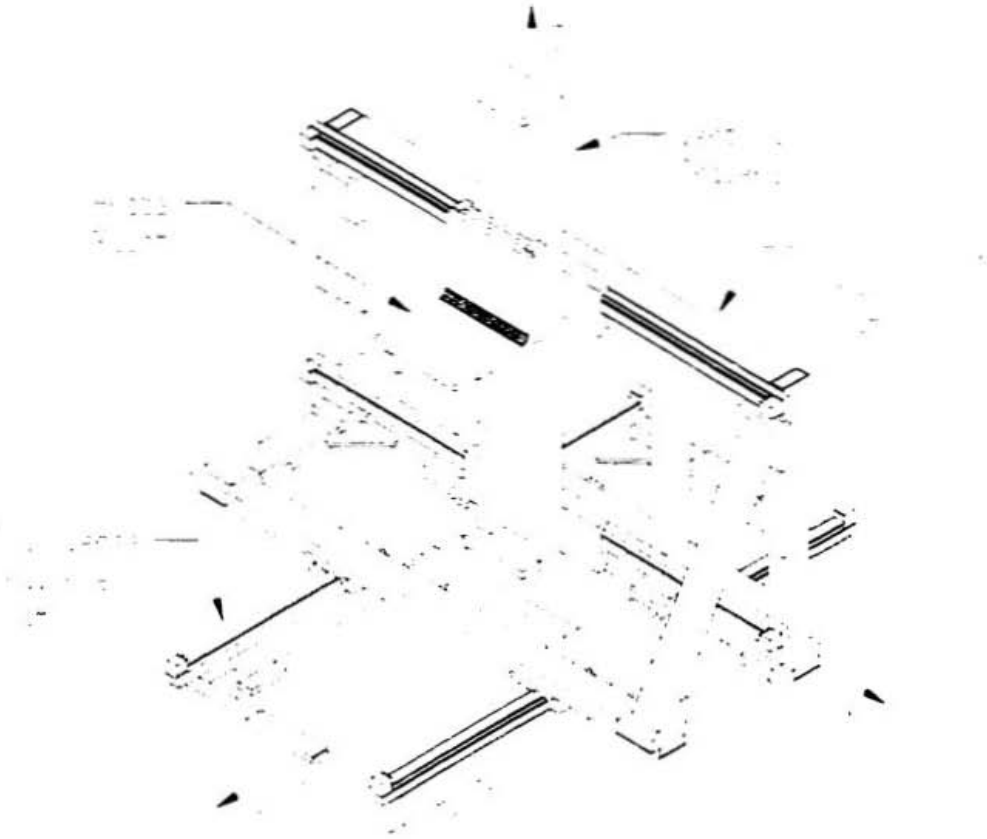

Figure 3.13 – LDV Indexing Frame

There are certain operational concerns with an LDV system which can inhibit its use in experiments. These include optical problems associated with particle seeding, and refraction and reflection in the measurement environment. Seeding is necessary to produce signals. However, too many particles can confuse the detectors if multiple particles pass through the measurement point at the same time. These signals would be rejected by the software. Insufficient seeding will produce low data rates which can lead to velocity values based on too few measurements. It is much easier to control the seeding density when performing tests in air, such as in a wind tunnel, than in water. There is sometimes enough particulate matter already present in water to achieve

readings, but additional particles are often needed. The tests discussed in this thesis used silver coated glass micro-balloons. Though these particles can easily be added to the system, assuring even distribution can be difficult as they are slightly heavier than water and tend to settle out of solution. Another seeding issue associated with water which can cause problems is entrained air. Except in a cavitation tunnel where the majority of the air can be removed from the test water, most tank water contains air. Depending on the conditions at the surface, this air can circulate as bubbles large enough to interfere with the lasers. An air bubble, when passing through the intersection volume, does not reflect much light back to the sensors but instead refracts it in all directions creating optical noise and interference with particle signals.

Refraction of the laser beams can also hinder the effectiveness of the tests. The refractive index of the testing environment affects the focal point of the lasers. When the probe is completely submerged in water, the longer focal length increases relative to that in air. Tests where the beams must pass through a viewing window, such as for cavitation tunnel tests, also affect the focal point. Reflected light from particles are also distorted slightly by the refraction characteristics between the probe and the measurement point.

Since the laser beams do not stop at the intersection volume, surfaces behind the measurement point must be considered when testing. Reflected light from these surfaces can swamp the sensors with light making recognition of particle reflections impossible. Background surfaces should be angled to direct the reflected beams away from the probe.

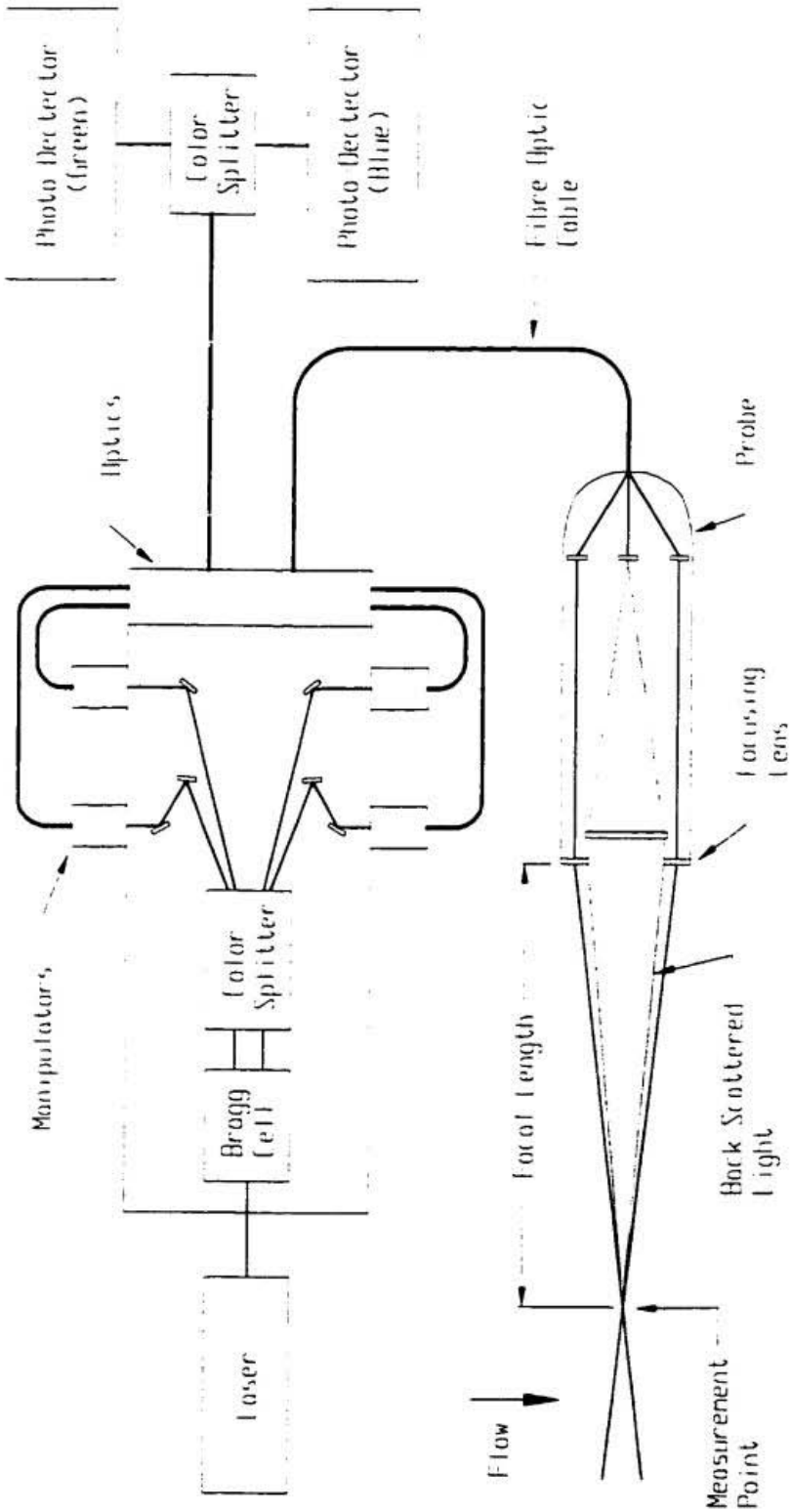

Figure 3.14 – LDV Probe and Laser

CHAPTER 4
SIMILITUDE ANALYSIS

4 SIMILITUDE ANALYSIS

For any experimental program involving scale models, similarity between the full or prototype scale and the model scale is required. It is not usually possible to have complete similarity between the two systems, but by using dimensional analysis, a set of model laws can be determined. These laws can then be used to ensure similarity of the most significant elements of the system and provide insight into the error that may arise from incorrect scaling of other elements. This chapter presents a dimensional analysis of the waterjet system using the method of synthesis. A set of model laws are identified and discussed in relation to the proposed experiments.

4.1 Method Of Synthesis

When performing experiments at model scale it is important to understand the relationships between phenomena occurring at this scale to those occurring at the full or prototype scale. Insight into these relationships can often be determined using dimensional analysis.

The first step in the analysis is the identification of the relevant variables and parameters that can affect the system and then define their units in terms of fundamental dimensions. Units are either fundamental or derived. The nature of the fundamental unit can be somewhat arbitrary though it is widely accepted in engineering systems that mass 'M', length 'L', and time 'T', are fundamental. Derived units such as velocity or density are defined as combinations of the fundamental units (Yuan, 1967).

e.g.	Variable	Derived units	Fundamental units
	mass	kg	M
	pressure	Pa	$\frac{M}{T^2 \cdot L}$

The next step in the analysis is to form the system variables in groups such that the fundamental units of the variables in the group are eliminated. An example of this process is given below. These dimensionless groups, called π terms, become the parameters of the analysis. It is the premise of dimensional analysis that two geometrically similar systems are kinematically and dynamically similar if each of the dimensionless parameters in one system is equal to the corresponding parameter in the other system, regardless of the

difference in scale. Relationships between model and prototype scale can therefore be made by equating the π terms formed for each system.

e.g. $$\pi_1 = \frac{V}{\sqrt{g \cdot D}} \quad \rightarrow \quad \frac{[M \cdot T^{-1}]}{\sqrt{[L \cdot T^{-2}] \cdot [L]}} = 1$$

$$(\pi_1)_{prototype} = (\pi_1)_{model} \qquad \therefore \frac{V_p}{\sqrt{g_p \cdot D_p}} = \frac{V_m}{\sqrt{g_m \cdot D_m}}$$

The number of π terms required to accurately define the system is given in the π theorem developed by Buckingham. It states that if there are 'm' variables with 'n' fundamental dimensions, then a correct analysis will result in (m-n) dimensionless parameters (Sharp, 1981).

There are several methods for creating dimensionless parameters. This analysis uses the method of synthesis developed in the late 1960's. In this method, groups of system variables are first formed such that the fundamental units form a length unit 'L'. A complete list of these groups, called linear proportionalities, are formed by combining each variable one at a time with every other variable in the system. The exception is density, ρ, which is only used when a variable has a mass dimension. Variables that are already in terms of a length dimension are left unchanged.

e.g. Combining velocity 'V' and RPM, 'N' gives: $$\frac{V}{N} \rightarrow \frac{[L \cdot T^{-1}]}{[T^{-1}]} = [L]$$

Combining pressure 'p' and gravity 'g' gives: $$\frac{p}{\rho \cdot g} \rightarrow \frac{[M \cdot T^{-2} \cdot L^{-1}]}{[M \cdot L^{-3}] \cdot [L \cdot T^{-2}]} = [L]$$

Diameter 'D' would be left unchanged: $$D \rightarrow [L]$$

The form of a linear proportionality is dependent only on the variable units and not on the system being analyzed. This means that proportionalities for common variables can be determined beforehand and listed for convenience. Finding a linear proportionality for two given variables then becomes a matter of simply checking that list or table. An example table of linear proportionalities for common variables used in fluid systems can be found in Sharp (1981).

The π terms for the system are formed by creating ratios of the linear proportionalities. Since all the proportionalities have units of length 'L', a ratio between any two proportionalities will be dimensionless. The number of ratios needed to define the system is given in the π theorem discussed previously. It is a requirement of the analysis that every system variable appear at least once in the final list of π terms. The ratios must also be linked by one or more of the linear proportionalities.

The total number of π terms that can be formed by all the possible ratios of all of the possible linear proportionalities will usually be considerably higher than the number of π terms that are necessary to define the system correctly. It is not enough that the dimensional analysis yields a correct solution; a convenient solution is required for the results to be useful. The surplus of possibilities offered by the method of synthesis gives the opportunity to direct the analysis to a convenient solution.

4.2 Waterjet System

The method of synthesis will now be applied to the waterjet system. Table 4.1 gives a general list of the variables and parameters which are considered necessary to describe the system. These can be combined in terms of a function as shown in Equation 4.1.

Variable or Parameter	Symbol	Units	Fundamental Units
Thrust	T	N	$[M][L][T]^{-2}$
Velocity	V	m/s	$[L][T]^{-1}$
Shaft speed	N	rad/s	$[T]^{-1}$
Density	ρ	kg/m^3	$[M][L]^{-3}$
Gravitational acceleration	g	m/s^2	$[L][T]^{-2}$
Pressure	p	Pa	$[M][L]^{-1}[T]^{-2}$
Dynamic viscosity	μ	kg/(m·sec)	$[M][L]^{-1}[T]^{-1}$
or kinematic viscosity	ν	m^2/sec	$[L]^2[T]^{-1}$
Characteristic length	L	m	[L]
Surface tension	φ	m/sec^2	$[M][T]^{-2}$

Table 4.1 - Waterjet Variables and Parameters

The functional expression of system variables is given by:

$$\phi(T, V, N, \rho, g, p, \mu, L, \varphi) = 0 \qquad [4.1]$$

Linear proportionalities of the variables can be formed by systematically combining the groups of variables as follows:

$$\left(\frac{T}{\rho \cdot V^2}\right)^{1/2}, \left(\frac{T}{\rho \cdot N^2}\right)^{1/4}, \left(\frac{T}{\rho \cdot g}\right)^{1/3}, \left(\frac{T}{p}\right)^{1/2}, \left(\frac{V}{N}\right), \left(\frac{\nu}{V}\right), \left(\frac{V^2}{g}\right),$$

$$\left(\frac{\nu}{N}\right)^{1/2}, \left(\frac{g}{N^2}\right), \left(\frac{p}{\rho \cdot N^2}\right)^{1/2}, \left(\frac{p}{\rho \cdot g}\right), \left(\frac{\nu^{2/3}}{g^{1/3}}\right), \left(\frac{\nu \cdot \rho^{1/2}}{p^{1/2}}\right), \left(\frac{\varphi}{\rho \cdot g}\right)^{1/2},$$

$$\left(\frac{\nu^2 \cdot \rho}{\varphi}\right), \left(\frac{\varphi}{p}\right), \left(\frac{\varphi}{\rho \cdot V^2}\right), \left(\frac{\varphi}{\rho \cdot N^2}\right)^{1/3}, \left(\frac{T}{\varphi}\right), L \qquad [4.2]$$

With 9 variables and 3 fundamental dimensions, the π theorem requires that 6 π terms are needed to describe the system.

Choosing 6 proportionalities and combining with the length term, L, yields:

$$\phi\left(\left(\frac{T}{\rho \cdot N^2 \cdot L^4}\right)^{1/4}, \left(\frac{V}{N \cdot L}\right), \left(\frac{\nu}{V \cdot L}\right), \left(\frac{V^2}{g \cdot L}\right), \left(\frac{p}{\rho \cdot N^2 \cdot L^2}\right)^{1/2}, \left(\frac{\varphi}{\rho \cdot V^2 \cdot L^2}\right)\right) = 0 \qquad [4.3]$$

These can be arranged in a more familiar format:

$$\phi\left(\left(\frac{T}{\rho \cdot N^2 \cdot L^4}\right), \left(\frac{V}{N \cdot L}\right), \left(\frac{V \cdot L}{\nu}\right), \left(\frac{V}{\sqrt{g \cdot L}}\right), \left(\frac{\Delta p}{\rho \cdot N^2 \cdot L^2}\right), \left(\frac{\rho \cdot V^2 \cdot L}{\varphi}\right)\right) = 0 \qquad [4.4]$$

These π terms are recognized as:

Thrust coefficient: $$K_T = \left(\frac{T}{\rho \cdot N^2 \cdot D^2}\right) \qquad [4.5]$$

Advance coefficient: $$J = \left(\frac{V_A}{N \cdot D}\right) \qquad [4.6]$$

Reynolds number: $$R_N = \left(\frac{V \cdot L}{\nu}\right) \qquad [4.7]$$

Froude number: $$F_N = \left(\frac{V}{\sqrt{g \cdot L}}\right) \qquad [4.8]$$

Cavitation number: $$\sigma = \left(\frac{\Delta p}{\rho \cdot N^2 \cdot L^2}\right) \qquad [4.9]$$

Weber number: $$W_N = \left(\frac{\rho \cdot V^2 \cdot L}{\varphi} \right) \quad [4.10]$$

where, $\Delta p = p_0 - p_v$ [4.11]

The 'L⁴' term in the thrust coefficient was replaced with the impeller diameter 'D' as the geometric parameter. The 'V' term in the advance coefficient is replaced with the advance velocity 'V_A' and the 'L' term is defined as the impeller diameter 'D'. The pressure term 'p' in the cavitation number is expressed as 'Δp' or the difference in the static pressure and the vapor pressure of water.

A thrust coefficient can be expressed as a function of the other π terms.

$$K_T = \phi\left(F_N, J, R_N, \sigma, W_N\right) \quad [4.12]$$

Assuming that the efficiencies of the motor and gearing at model and full scale are similar, the same process of analysis can be performed for expressions involving power 'P', shaft torque 'Q_S', and volume flow rate 'Q'. The system variables for these expressions are the same as given in Table 4.1.

$$P = \phi(V, N, \rho, g, p, \mu, L, \varphi) \quad [4.13]$$

$$Q_S = \phi(V, N, \rho, g, p, \mu, L, \varphi) \quad [4.14]$$

$$Q = \phi(V, N, \rho, g, p, \mu, L, \varphi) \quad [4.15]$$

The method of synthesis can then be applied to these functions as was done above. The resulting lists of linear proportionalities are similar but each include terms specific to that

expression. Choosing convenient π terms yields many of the same coefficients named above with the addition of a π term containing the parameter being sought.

Power:

$$K_P = \phi\left(F_N \,.\, J \,.\, R_N \,.\, \sigma \,.\, W_N\right) \qquad [4.16]$$

where, $K_P = \dfrac{P}{\rho \cdot N^3 \cdot D^5}$ is the power coefficient [4.17]

Shaft Torque:

$$K_{Q_S} = \phi\left(F_N \,.\, J \,.\, R_N \,.\, \sigma \,.\, W_N\right) \qquad [4.18]$$

where, $K_{Q_S} = \dfrac{Q_S}{\rho \cdot N^2 \cdot D^5}$ is the shaft torque coefficient [4.19]

Volume Flow Rate:

$$K_Q = \phi\left(F_N \,.\, J \,.\, R_N \,.\, \sigma \,.\, W_N\right) \qquad [4.20]$$

where, $K_Q = \dfrac{Q}{N \cdot D^3}$ is the volume flow rate coefficient [4.21]

4.3 Discussion of π Terms

In practice, it is not usually possible to equate all the dimensionless parameters in model and prototype scale simultaneously; compromises must therefore be made. In many fluid systems, sufficient similarity may still be achieved to make the method useful. It is often the case that only certain dimensionless parameters are important for a given system and not all the parameters need to be satisfied to achieve meaningful results. In the case of

waterjets, it is not possible to satisfy all of the π terms simultaneously. Each π term defined by the dimensional analysis is discussed below.

Reynolds Number:

$$R_N = \left(\frac{V \cdot L}{\nu}\right) \qquad [4.22]$$

Reynolds number can be thought of as a ratio of the inertial and viscous forces in the fluid. Reynolds number can be used to indicate flow regime. Fluids can behave in one of three fairly distinct regimes: laminar, transitional, and turbulent. When modeling, it is important that the fluid is operating in the same flow regime of flow in both scales, otherwise significant scaling errors may occur. Matching Reynolds number between model and prototype ensures matching flow behaviour with respect to viscous effects, but is not usually practical as it can result in prohibitively high model velocities.

e.g. If $\frac{L_p}{L_m} = \lambda$ is the scale, then by matching Reynolds number:

$$R_{N_{prototype}} = R_{N_{model}} \rightarrow \frac{V_p \cdot L_p}{\nu_p} = \frac{V_m \cdot L_m}{\nu_m}$$

$\therefore V_m = \lambda \cdot V_p$ i.e. Model velocities are λ times larger then prototype velocities

Waterjets have high speed flow and operate in the turbulent flow regime with correspondingly high Reynolds numbers. If Reynolds number is not matched at model scale, it is a requirement that it is at least operating in the turbulent flow regime as indicated by an adequately high Reynolds numbers. Typically, provided values of

Reynolds number are higher than 10^6 in both model and prototype, the scale error is expected to be negligible (Harvald, 1983).

Froude Number:

$$F_N = \left(\frac{V}{\sqrt{g \cdot L}} \right) \qquad [4.23]$$

Froude Number can be thought of as the ratio of inertial forces to gravitational forces in the system. Waterjet systems perform work on the water by lifting it through an elevation in order to expel it above the water surface. Froude number is therefore significant and needs to be matched at model and prototype scales. Froude number is also significant in studies of hull resistance where gravity is a factor in the surface waves produced by a moving vessel.

Advance Coefficient:

$$J = \left(\frac{V_A}{N \cdot D} \right) \qquad [4.24]$$

Advance coefficient can be thought of as the ratio of the axial velocity of flow into the impeller, to the tangential velocity of flow relative to the impeller tips. This condition of kinematic similarity is essential for modeling flow characteristics and impeller performance. The nature of the testing arrangement for waterjets discussed in Chapter 8 did not allow an accurate simulation of the behaviour of an actual waterjet unit, since there was no forward speed component ($V_A = 0$). This is called the bollard condition. Waterjet units rarely operate in the bollard condition; only briefly during start-up. Instead

they are designed to operate at high speeds and with correspondingly high advance speeds. This limitation of this experimental arrangement is recognized.

Cavitation Number:

$$\sigma = \left(\frac{\Delta p}{\rho \cdot N^2 \cdot L^2} \right) \qquad [4.25]$$

Another common form of cavitation number can be expressed with a velocity term by compounding terms 2 and 5 from Equation 4.3 and then adding a ½ term so that the denominator will represent stagnation pressure:

$$\sigma_V = \left(\frac{\Delta p}{\frac{1}{2} \cdot \rho \cdot V^2} \right) \qquad [4.26]$$

The form of cavitation number in Equation 4.9 was chosen because, as discussed with the advance coefficient, there was no forward speed and therefore no convenient characteristic speed term to use in Equation 4.26.

Cavitation number can be thought of as the ratio of the difference between absolute ambient pressure and vapor pressure, to the free stream dynamic pressure. Matching cavitation number at both scales would require scaling the 'Δp' term since the scaling of velocity 'V' has already been set by matching Froude number. The proposed set-up for the experiments in this thesis does not allow variation of either the vapour pressure of water or the absolute ambient pressure. Cavitation is, however, an important aspect of waterjet performance and can be modeled in a cavitation tunnel. A cavitation tunnel, is an apparatus designed to operate with flows at a scaled absolute ambient pressure.

Weber Number:

$$W_N = \left(\frac{\rho \cdot V^2 \cdot L}{\varphi} \right) \qquad [4.27]$$

Weber number can be thought of as the ratio of inertial forces to free surface tension forces. It is included in order to assure similarity with regard to the surface stresses in the cavitation bubbles. Weber number, as with cavitation number, was not matched in the waterjet platform experiments.

4.4 Scaling Laws

Scaling laws allow the magnitude of a variable in one scale to be calculated from its value at a different scale. These laws can be formed by using the π terms defined in the preceding section. Since water was the fluid used in both scales and a centrifuge was not used to affect gravity, the parameters of density, viscosity and gravity were not scaled.

The scale of any quantity in the system is given in terms of the geometric scale λ.

$$\lambda \equiv \frac{L_p}{L_m} \qquad [4.28]$$

where, L is any similar linear measure of the systems, and subscripts 'p' and 'm' denote values in prototype and model scales respectively.

Velocity can be scaled by equating the Froude numbers in both model and prototype.

$$F_{n_p} = F_{n_m} \qquad [4.29]$$

$$\frac{V_p}{\sqrt{g \cdot L_p}} = \frac{V_m}{\sqrt{g \cdot L_m}} \quad \rightarrow \quad \frac{V_p}{V_m} = \frac{\sqrt{g \cdot L_p}}{\sqrt{g \cdot L_m}} \qquad [4.30]$$

$$\frac{V_p}{V_m} = \sqrt{\lambda} \qquad [4.31]$$

Next using the advance coefficient J, the scaling law for shaft speed can be determined:

$$J_p = J_m \qquad [4.32]$$

$$\frac{V_p}{N_p \cdot L_p} = \frac{V_m}{N_m \cdot L_m} \quad \rightarrow \quad \frac{N_p}{N_m} = \frac{L_m}{L_p} \cdot \frac{V_p}{V_m} \qquad [4.33]$$

$$\frac{N_p}{N_m} = \frac{1}{\sqrt{\lambda}} \qquad [4.34]$$

The scaling law for pressures can be found by using a form of the 5th π term in Equation 4.3.

$$\frac{p_p}{\rho \cdot N_p^2 \cdot L_p^2} = \frac{p_m}{\rho \cdot N_m^2 \cdot L_m^2} \quad \rightarrow \quad \frac{p_p}{p_m} = \left(\frac{N_p}{N_m}\right)^2 \cdot \left(\frac{L_p}{L_m}\right)^2 \qquad [4.35]$$

$$\frac{p_p}{p_m} = \lambda \qquad [4.36]$$

Scaling the thrust in the system is performed by satisfying the thrust coefficient in both the model and the prototype.

$$K_{T_p} = K_{T_m} \qquad [4.37]$$

$$\frac{T_p}{\rho \cdot N_p^2 \cdot A_{N_p}^2} = \frac{T_m}{\rho \cdot N_m^2 \cdot A_{N_m}^2} \quad \rightarrow \quad \frac{T_p}{T_m} = \left(\frac{N_p}{N_m}\right)^2 \cdot \left(\frac{L_p}{L_m}\right)^4 \qquad [4.38]$$

$$\therefore \quad \frac{T_p}{T_m} = \lambda^3 \qquad [4.39]$$

Scaling the power in the system is done by satisfying the power coefficient in both the model and the prototype.

$$K_{P_p} = K_{P_m} \qquad [4.40]$$

$$\frac{P_p}{\rho \cdot N_p^{\,3} \cdot D_p^{\,5}} = \frac{P_m}{\rho \cdot N_m^{\,3} \cdot D_m^{\,5}} \quad \rightarrow \quad \frac{P_p}{P_m} = \left(\frac{N_p}{N_m}\right)^3 \cdot \left(\frac{L_p}{L_m}\right)^5 \qquad [4.41]$$

$$\therefore \quad \frac{P_p}{P_m} = \lambda^{7/2} \qquad [4.42]$$

Scaling the shaft torque of the system is performed by satisfying the shaft torque coefficient in both the model and the prototype.

$$K_{Q_{S_p}} = K_{Q_{S_m}} \qquad [4.43]$$

$$\frac{Q_{S_p}}{\rho \cdot N_p^{\,2} \cdot D_p^{\,5}} = \frac{Q_{S_m}}{\rho \cdot N_m^{\,2} \cdot D_m^{\,5}} \quad \rightarrow \quad \frac{Q_{S_p}}{Q_{S_m}} = \left(\frac{N_p}{N_m}\right)^2 \cdot \left(\frac{L_p}{L_m}\right)^5 \qquad [4.44]$$

$$\therefore \quad \frac{Q_{S_p}}{Q_{S_m}} = \lambda^4 \qquad [4.45]$$

Scaling the volume flow rate of the system can be done by satisfying the volume flow rate coefficient in both the model and the prototype.

$$K_{Q_p} = K_{Q_m} \qquad [4.46]$$

$$\frac{Q_p}{N_p \cdot D_p^{\,3}} = \frac{Q_m}{N_m \cdot D_m^{\,3}} \quad \rightarrow \quad \frac{Q_p}{Q_m} = \left(\frac{N_p}{N_m}\right) \cdot \left(\frac{L_p}{L_m}\right)^3 \qquad [4.47]$$

$$\therefore \quad \frac{Q_p}{Q_m} = \lambda^{5/2} \qquad [4.48]$$

Summary of Scaling Laws:

Parameter	Ratio	Scale
Length	L_p / L_m	λ
Velocity	V_p / V_m	$\sqrt{\lambda}$
RPM	N_p / N_m	$1 / \sqrt{\lambda}$
Pressure	p_p / p_m	λ
Thrust	T_p / T_m	λ^3
Power	P_p / P_m	$\lambda^{7/2}$
Torque	Q_{s_p} / Q_{s_m}	λ^4
Volume Flow Rate	Q_p / Q_m	$\lambda^{5/2}$

Table 4.2 – Scaling Laws

CHAPTER 5
MOMENTUM FLUX METHOD

5 MOMENTUM FLUX METHOD

Early attempts to develop techniques for performing model tests of waterjet propulsors involved applying those used for conventional marine screw propellers. A waterjet, however, is an integral part of the hull making some of the traditional concepts, such as thrust deduction, difficult to apply to waterjet propelled ships in a physically obvious way. Measurement of some basic quantities, particularly thrust, is difficult in practice and requires instead an indirect measurement technique based on flow rates. In response to these issues, a different approach was taken for performing model tests on waterjets and waterjet propelled vessels. This approach, called the momentum flux method, is presented and discussed in this chapter.

The momentum flux method is described in the "Final Report and Recommendations to the 21st ITTC: Waterjets Group, Appendix A". The method was developed such that in principle, it agreed with the procedures used by most towing tanks and manufacturers

involved in waterjet testing. It is based on the laws of conservation of momentum, energy and continuity.

The method is used primarily in the analysis of the steady state behaviour of a waterjet. Transient operation such as during start-up, accelerations, or in waves, though important, are not considered part of the scope of this thesis. For reference purposes, the vessel is considered to be stationary in a moving flow. All flow velocities used in momentum and energy calculations are made relative to the vessel.

Momentum flux is defined as the measure of the momentum in a quantity of fluid which crosses a unit area of a given surface in a unit of time. Energy flux, used to calculate power and internal losses, is similar but is the measure of the energy in the fluid. The locations where momentum and energy flux are measured correspond to the stations as defined in Figure 5.1.

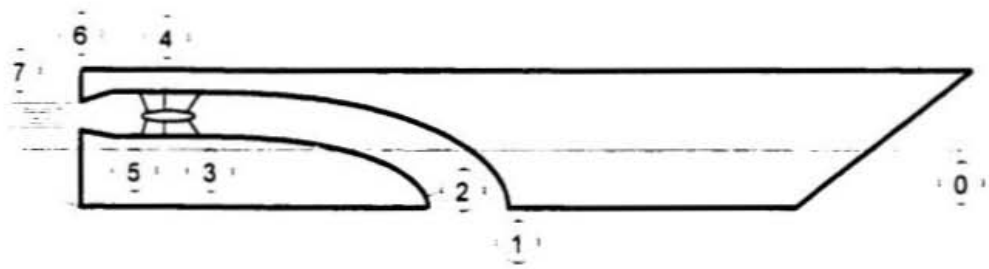

Station No.	Location
0	in undisturbed flow far ahead of the vehicle
1	far enough in front of the intake ramp tangency point, before inlet losses occur
2	Normal to the internal flow at the aft lip of the intake
3	just ahead of the pump

4	Between pump and stator or between stages
5	behind stator
6	at the nozzle outlet plane
7	behind the nozzle outlet plane where the static pressure coefficient in the jet is zero (vena contracta)

Figure 5.1 – Definition of Station Numbers

5.1 Station 1: Waterjet Intake

The intake momentum flux is measured at Station 1 (variables and parameters corresponding to the intake are denoted with the subscript 1). Measurements are made here to account for the fluid momentum due to the movement of the vessel itself. Given the example of a towed vessel moving at a given forward speed but without power to its thrusters, water is forced through its jet units due to the vessel's forward movement, or the fluid's motion aft when taken relative to the vessel. The velocity distribution of this flow is used to calculate the intake momentum flux. Since this flow is also present in an operating jet, it must be accounted for in calculations of thrust and power.

The 21st ITTC suggests that the intake momentum flux be measured at a rectangular plane area at Station 1. The flow into the jet is assumed to behave as shown in Figure 5.2. Streamlines moving at velocity V (the vessel or model speed) separate near the intake: some enter the intake while the rest continue along the hull. The distance from the hull bottom where the fluid is drawn into the intake defines the height of the rectangular area where the flux measurement is made. This is the theory; the actual method suggested for determining the area is to assume a width 30% larger than the width of the inlet intake.

The height is then determined from continuity, given that the flow rate through the system, referred to as the jet flow rate Q_J, is known.

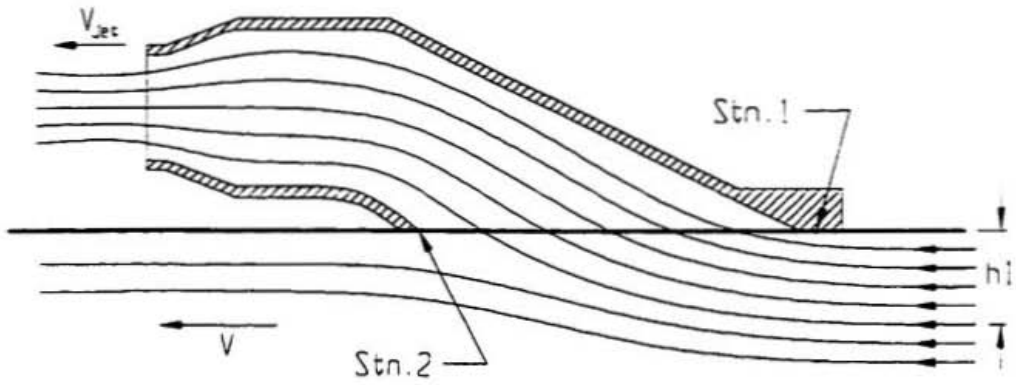

Figure 5.2 – Idealized Flow to Intake

Since the height of this area begins at the hull surface, it contains a vertical velocity distribution that includes the boundary layer from the hull in this region. This velocity distribution must be determined before the equations of continuity, momentum or energy can be applied. Figure 5.3 shows an illustration of the boundary layer in this region. The height h_1 would usually span the entire boundary layer and include a portion of the free stream which may have a constant distribution or may show variations due to the accelerations from the jet drawing in water. It should be noted that this flow is assumed to be two-dimensional or constant across the local y-axis as it would be oriented in Figure 5.3. It is realized by the ITTC that this flow has three-dimensional characteristics; the above method is suggested due to a lack of testing and measurement expertise in this area.

An illustration of the intake momentum flux area is given in Figure 5.4. The figure shows the bottom of the model planing hull used for self propulsion experiments in Chapter 7.

The starboard waterjet's intake is shown with three pitot tubes. The intake area is cross hatched with its dimensions noted. The pitot tubes were used to determine information about the velocity distribution in the flow.

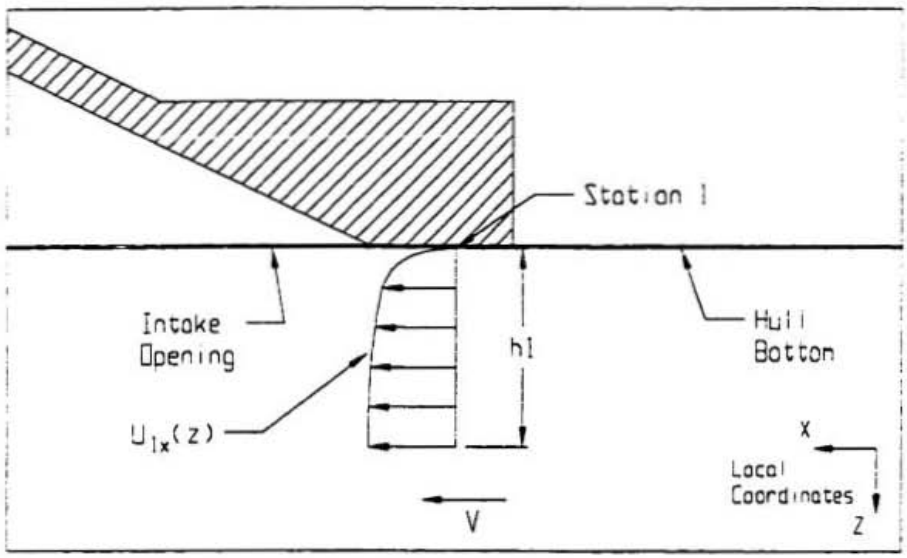

Figure 5.3 – Boundary Layer Ingestion to Intake

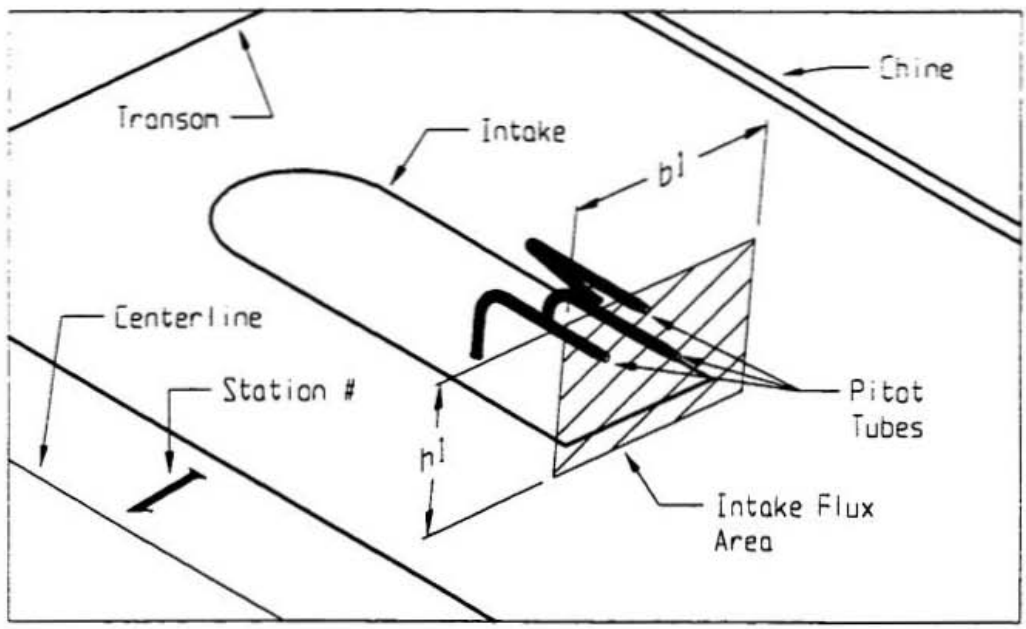

Figure 5.4 – Area for Intake Momentum Flux

The following outlines the method for calculation:

From continuity,

$$Q_J = \int_{A_I} u_{Ix}(A) \cdot dA_I \qquad [5.1]$$

where,

Q_J is the volume flow rate of jet (known)

A_I is the intake flux area

$u_{Ix}(A)$ is the velocity distribution across A_I

Applying the assumption of 2-D flow yields:

$$Q_J = \int_{A_I} u_{Ix}(z) \cdot dA_I \qquad [5.2]$$

A rectangular cross-sectional area with width 30% larger than intake width is used:

$$b_I = 1.3 \cdot w_{inlet} \qquad [5.3]$$

The height h_I can then be determined implicitly from:

$$Q_J = b_I \cdot \int_0^{h_I} u_{Ix}(z) \cdot dz \qquad [5.4]$$

Since this method is based on several broad assumptions of the flow, other approaches that can provide greater accuracy are needed. Simple variations on the above include changing the size of b_I, and using a half-elliptic intake flux area. The effects of these variations should be determined with a sensitivity analysis. Tests mentioned in the 21st ITTC showed that an error of 20% in the choice of b_I resulted in only a 1% error in predicted power and that the influence of section shape was small. More complex variations would require greater knowledge of the three dimensional inflow effects of the jet during operating conditions, from both physical experiments and numerical modeling.

The momentum and energy flux for Station 1 are sensitive to the velocity distribution and area used in their calculation and are influenced by the same reservations expressed above. The equation for momentum flux at Station 1 is given by:

$$M_1 = \rho \cdot \int_{Q_1} u_1(Q) \cdot dQ \qquad [5.5]$$

where in general,

$$dQ = u_{1x} \cdot dA \qquad [5.6]$$

yielding:

$$M_1 = \rho \cdot \int_{A_1} u_{1x}^2 \cdot dA \qquad [5.7]$$

which further simplifies to:

$$M_1 = \rho \cdot b_1 \cdot \int_{h_1} u_{1x}^2 \cdot dz \qquad [5.8]$$

It may be desirable in some cases to express the momentum flux in the following form:

$$M_1 = \rho \cdot \int_{Q_1} V_{E1} \cdot dQ_1 \qquad [5.9]$$

where V_{E1} is the local velocity energy component of the flow;

$$V_{E1} = V \cdot \sqrt{\left(\frac{u_1}{V}\right)^2 + C_P} \qquad [5.10]$$

and C_P is the static pressure coefficient obtained from the difference in the static pressure p_1 at Station 1 and the static pressure p_0 in the undisturbed flow, given by:

$$C_P = \frac{(p_1 - p_0)}{\frac{1}{2} \cdot \rho \cdot V^2} \qquad [5.11]$$

The energy flux at Station 1 is calculated in a similar manner as the momentum flux.

$$E_1 = \frac{1}{2} \cdot \rho \cdot \int_{Q_1} u_{x1}^2 \cdot dQ \qquad [5.12]$$

which can be expressed as:

$$E_1 = \frac{1}{2} \cdot \rho \cdot b_1 \cdot \int_{h_1} u_{x1}^3 \cdot dz \qquad [5.13]$$

The local energy velocity V_{E1} can also be used in this calculation.

$$E_1 = \frac{1}{2} \cdot \rho \cdot \int_{Q_1} V_{E1}^2 \cdot dQ \qquad [5.14]$$

5.2 Intermediate Stations: Waterjet Unit

The intermediate stations defined in Figure 5.1 are used in calculations relating to efficiency components of the model waterjet. Determining momentum and energy flux inside the waterjet ducting requires detailed knowledge of the velocity profiles at the various stations. Accurate measurement of these profiles, especially near the impeller and stator, may be exceedingly difficult during some tests. Special test rigs with a larger scale waterjet may be needed to determine the behaviour of the flow inside the thruster. This, in conjunction with numerical simulations, may be used to develop greater understanding of the dynamics of a given waterjet design. The equations for momentum and energy flux for the internal stations are:

$$M_j = \rho \cdot \int_{Q_j} V_{Ej} \cdot dQ \qquad [5.15]$$

$$E_j = \frac{1}{2} \cdot \rho \cdot \int_{Q_j} V_{Ej}^2 \cdot dQ \qquad [5.16]$$

where the subscript j denotes a given station number.

In the undisturbed flow ahead of the vehicle, Station 0, the energy flux is:

$$E_0 = Q_J \cdot \frac{1}{2} \cdot \rho \cdot V^2 \qquad [5.17]$$

5.3 Station 7: Vena Contracta

The decreasing cross sectional area of the nozzle forces the velocity of the flow to increase, providing the necessary thrust. It also causes the streamlines in the jet to converge and they tend to continue converging beyond the nozzle exit until they become parallel, usually about half the nozzle diameter from the nozzle face. This point, shown in Figure 5.5, is called the vena contracta and is the region of the free jet stream with the minimum cross sectional area. Beyond the vena contracta the streamlines tend to diverge due to frictional effects. The vena contracta is useful for calculations because as the static pressure coefficient in this region is zero, all of the fluid's energy is kinematic.

Accurate knowledge of the velocity distribution across the vena contracta area, as with the intake flux area, is important to determining meaningful values for energy and momentum flux. If the flow rate of the jet, Q_J, is also determined from flow velocities in this region, then accuracy becomes even more significant. The 21st ITTC stresses the importance of correctly assessing the flow rate when it showed that a 1% error in Q_J can result in a 3-4% error in predicted power. Considerable efforts must therefore be made to use reliable methods of determining and checking the jet flow rate.

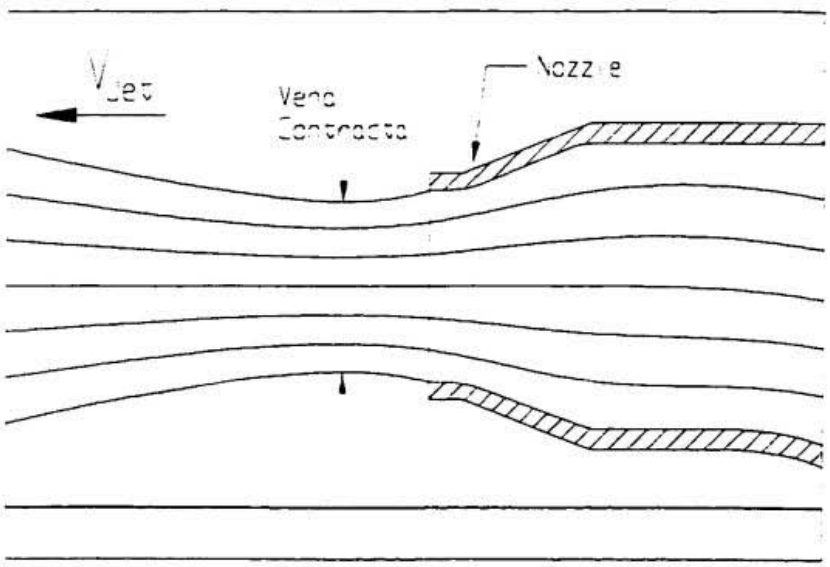

Figure 5.5 – Vena Contracta of Jet

If the jet velocity distribution is known, the volume flow rate can be determined from:

$$Q_J = \int_{A_7} u_{x7} \cdot dA \qquad [5.18]$$

The momentum flux equation differs slightly from those at other stations:

$$M_7 = \rho \cdot \int_{Q_J} u_{7x} \cdot dQ + \int_{A_7} (p_7 - p_0) \cdot dA \qquad [5.19]$$

where $(p_7 - p_0)$ is the pressure reduction caused by tangential or rotational velocities, $u_{7\phi}$, present in the flow:

$$(p_7 - p_0) = -\rho \cdot \int_{R_7} \frac{u_{7\phi}^2}{r} \cdot dr \qquad [5.20]$$

The energy flux at Station 7 is determined from:

$$E_7 = \frac{1}{2} \cdot \rho \cdot \int_{Q_J} V_{E7}^2 \cdot dQ \qquad [5.21]$$

which can be written as:

$$E_{7} = \frac{1}{2} \cdot \rho \cdot \int_{A_7} V_{E7}^{2} \cdot u_{7x} \cdot dA \qquad [5.22]$$

where V_{E7} is the local energy velocity at Station 7, intended to account for tangential velocities in the jet flow:

$$V_{E7} = \sqrt{u_{7x}^{2} + u_{7\theta}^{2} + \frac{2}{\rho} \cdot (p_{7} - p_{0})} \qquad [5.23]$$

The influence of moderate jet rotation is small but the change in momentum flux is affected. When it is difficult to determine the velocity components of the jet accurately, checks should be made to determine the strength of the jet rotation and the magnitude of axial jet velocity deviations to ensure that any simplifications are justified.

5.4 Calculations

Once momentum and energy flux are determined for each station, it is then possible to calculate other parameters that can characterize the performance of the propulsion system. These include:

- Jet thrust
- Effective jet system power
- Elevation power
- Internal losses
- Effective pump power
- Model shaft power
- Predicted full scale power

5.4.1 Jet Thrust

The change of momentum flux for corresponding stream tubes in resistance and self-propulsion tests, can be written as:

$$\Delta M_M = M_7 \cdot \cos(\alpha) - M_1 \qquad [5.24]$$

where,

α is the angle between the shaft line of the jet and the horizontal plane

ΔM_M is the change in momentum flux

The value of ΔM_M is the component of momentum flux produced by the waterjet. It is therefore equal to the effective thrust of the system (ΔM_M values for multiple jet units would be summed). Determination of the full scale resistance and thrust could then follow the same procedures described in Chapter 7.

The 21st ITTC, however, scales this value directly without accounting for variations in resistance components from model to full scale, computing the effective full scale resistance from:

$$R_S = \frac{\rho_S}{\rho_M} \cdot \Delta M_M \cdot \lambda^3 \qquad [5.25]$$

5.4.2 Effective Jet System Power

The effective jet system power, P_{JSE}, can be computed from the increase of energy between Station 1 and Station 7:

$$P_{JSE} = E_7 - E_1 \qquad [5.26]$$

5.4.3 Elevation Power

The power needed to lift the water to the height of the jet above the undisturbed water surface is computed from:

$$P_{ELEV} = \rho \cdot g \cdot Q_j \cdot h_j \qquad [5.27]$$

In cases where only part of the jet is above the undisturbed free water surface. P_{ELEV} is calculated as:

$$P_{EVEL} = \rho \cdot g \cdot \int_{Q_1} z \cdot dQ \qquad [5.28]$$

where the integration is performed only above the undisturbed free surface ($z \geq 0$).

5.4.4 Internal Losses

Power is also needed to overcome the inlet and outlet losses. The loss coefficients for the intake and diffuser ζ_{13}, and for the outlet nozzle ζ_{57}, can be expressed as follows:

$$\zeta_{13} = \frac{E_1 - E_3}{E_0} \qquad [5.29]$$

$$\zeta_{57} = \frac{E_5 - E_7}{E_7} \qquad [5.30]$$

Calculation of E_3 can be simplified if the velocity distribution just ahead of the pump is uniform. This is, however, almost never the case. In reality the velocity is quite non-uniform with large velocity variations.

The power associated with internal losses is given by:

$$P_{intloss} = \zeta_{13} \cdot E_0 + \zeta_{57} \cdot E_7 \qquad [5.31]$$

Since in many practical cases it is impossible to determine the velocity distributions at any station inside the waterjet system in self-propulsion tests, the conclusion is that internal loss coefficients must be determined in special tests with large models, permitting detailed velocity and pressure measurements to be performed. In these tests, which can be carried out either in a special test rig in a towing tank or in a cavitation tunnel, modeling of the boundary layer ahead of the intake is important for obtaining accurate results.

5.4.5 Effective Pump Power

The effective power P_{PE}, is the sum of the contributions described in Sections 5.4.2 to 5.4.4:

$$P_{PE} = P_{JSE} + \rho \cdot g \cdot Q_J \cdot h_J + \zeta_{13} \cdot E_0 + \zeta_{57} \cdot E_7 \qquad [5.32]$$

or where H_{35} is the increase of the mean total head across the pump:

$$H_{35} = \frac{1}{\rho \cdot g \cdot Q_J} \cdot \left[E_7 \cdot (1 + \zeta_{57}) - E_1 + E_0 \cdot \zeta_{13} \right] + h_J \qquad [5.33]$$

$$P_{PE} = \rho \cdot g \cdot Q_J \cdot H_{35} \qquad [5.34]$$

5.4.6 Model Shaft Power

If the pump efficiency (η_P) of the model, determined in a conventional pump test rig, and the pump installation efficiency (η_{inst}), accounting for the non-uniformity of the inflow to the pump in the waterjet system, are both known, then the delivered power (P_{DM}) needed to propel the model can be determined.

$$P_{DM} = \frac{P_{PE}}{\eta_P \cdot \eta_{inst}} \qquad [5.35]$$

One method suggested by the ITTC is to test the pump in a test rig to determine the pump efficiency and then repeat the tests with a special inlet, modeling the flow at Station 3 ahead of the waterjet pump. The difference in the results will then give the installation efficiency.

A more direct method would be to test the pump in the same rig as used for testing the internal losses. The flow into the pump is then modeled in a natural way and the scale effects caused by different boundary layers ahead of the intake in model and full scale could be clarified. The tests can be used either to determine the internal losses and the product of pump and installation efficiencies separately, or to give an effective jet system power plus the elevation power:

$$\eta_{WJ} = \frac{P_{JSE} + \rho \cdot g \cdot Q_J \cdot h_J}{P_{DM}} \qquad [5.36]$$

A practical problem with this procedure is that two waterjet systems must be manufactured, a smaller one for the self-propulsion tests and a larger one for the special tests.

The model shaft power can also be determined from torque measurements. If P_{DM} is not equal to $2 \cdot \pi \cdot Q \cdot n$, then the estimate of internal loss coefficients (ζ_{13}, ζ_{57}) or efficiency values (η_P, η_{inst}) should be reconsidered.

A check of the model shaft power can only be used to estimate the total error in efficiencies and loss coefficients and not specific details. It is also limited to calculation of the effective jet system efficiency at model scale.

5.4.7 Predicted Full Scale Power

The calculation of full scale power requires full scale values of volume flow rate, size of intake area, and energy velocities at Stations 1 and 7. Due to the scale effects of the boundary layer profile at the intake, these quantities can not be conveyed directly from corresponding model values. However, the following procedure can used indirectly to determine the required values.

Firstly, the full scale boundary layer thickness and velocity profile at the inlet are predicted using boundary layer theory, including effects of a certain hull roughness at full scale. The static pressure coefficient is assumed to be the same as in the model test.

Full scale values of Q_J, M_1, h_1 and M_7 are then computed from the momentum theorem, using the full scale velocity profile and maintaining the change of momentum flux. Inlet and outlet shapes must be geometrically similar for model and full scale.

$$\Delta M_S = R_S \qquad [5.37]$$

$$\Delta M_S = \frac{\rho_S}{\rho_M} \cdot \Delta M_M \cdot \lambda^3 \qquad [5.38]$$

Full scale values of E_1 and E_7, appropriate internal loss coefficients ζ_{13S} and ζ_{57S}, as well as pump and installation efficiency figures h_{PS} and h_{instS}, are to be estimated.

If the special tests mentioned above have been carried out with a large waterjet system, it would be possible to convert the results to full scale with some confidence, especially if the tests have been performed with a full scale boundary layer at the inlet.

Using the figures estimated in Section 5.4.7, the full scale effective pump power P_{PES} is computed as described in Sections 5.4.2 to 5.4.5 together with the increase of mean total head across the pump H_{35S} as shown in Section 5.4.5. The pump shaft power can then be computed from:

$$P_{DS} = \frac{P_{PES}}{\eta_{PS} \cdot \eta_{instS}} \qquad [5.39]$$

5.5 Stock Waterjet Pumps

For practical reasons the self propulsion tests are often carried out with stock pumps rather than with geometrically similar models of the full scale pumps. If this is the case the prediction procedure is as follows:

a) Although the pump is not to scale, the inlet and outlet configurations must be.

b) The methods described under Sections 5.1 to 5.4.3 are the same. However, the model pump should not be operated far from its optimum in order to avoid strong rotation and large axial velocity variations in the jet.

c) The internal losses and the efficiency values at model scale are of no interest so the procedure continues with Section 5.4.7.

d) To be able to determine the internal losses and the different pump efficiencies in full scale it is necessary to carry out the special tests mentioned above with a large waterjet system with scaled pump and internal ducting.

e) If results from such tests are not available the predictions will have to depend on the accuracy of estimating internal losses and pump efficiencies.

5.6 Summary

The methods for waterjet testing discussed in this chapter are from the "Final Report and Recommendations to the 21st ITTC: Waterjets Group, Appendix A" (1996). The momentum flux method is a clear improvement on the original attempts involving techniques developed for screw propellers, but still has room for improvement. The method relies heavily on knowledge of velocity profiles in various sections of the waterjet. There are many practical difficulties with accurately determining this information experimentally as is discussed in later chapters. Certain assumptions about the nature of the flow, used for simplifications, as well as the need to make estimations of many efficiency parameters are also drawbacks of the method which tend to decrease confidence in the full scale predictions. The work discussed in this thesis is directed primarily at developing expertise at IMD in making the experimental measurements required by this method. This type of expertise is necessary before performance evaluations of jets, improvements in methodology, or any research focused on specific areas of waterjet propulsion, can be performed.

CHAPTER 6
BARE HULL RESISTANCE TESTS

6 BARE HULL RESISTANCE TESTS

The first phase of testing consisted of a series of bare-hull resistance tests. These were used to determine characteristics of the hull at speed including: resistance, running trim, and heave. Though this was a waterjet propelled vessel, the model hull for these tests did not contain the inlet holes for the waterjets. There has been some debate (ITTC, 1996) over the usefulness of performing bare hull resistance tests on waterjet propelled vessels, since the action of the jets and inlets significantly changes the behavior of the flow near the hull which can affect vessel performance. As this was a development project focused on testing and measurement techniques, it was decided to perform the bare hull tests as a baseline for results achieved by other testing methods.

The vessel tested was a 1:8 scale model of the *Niagara Jet Boat* by MetalCraft Marine Incorporated. The *Niagara* is a recreational craft which operates in rivers and lakes

giving day tours for up to 36 people with 2 crew. There are several Niagara type vessels currently in operation. The particulars of the vessel are given in Table 6.1.

LBP	11.8 m
Beam	4.3 m
Displacement (Loaded)	18 tons
Propulsion	3 x Hamilton 291 waterjets
Max. Speed	40 knots

Table 6.1 – Particulars for Niagara Jet Boat

6.1 Model Construction

The model was constructed in three steps. A block of polyurethane foam was first machined to the shape of the hull minus a thickness to accommodate a layer of fiberglass. This was done with a Liné numerically controlled milling machine. The foam was hand finished to remove cutting steps, fiberglassed and polished. This hull form was used to fabricate a female mould of the hull shape, also out of fiberglass. The female mould was then used to construct the final model, which consisted of a layer of gelcoat and two layers of carbon fiber mat with epoxy resin. The carbon fiber was chosen over conventional E-glass to minimize the model weight while ensuring adequate strength. The model's structure was reinforced with: transverse stiffeners, longitudinal stiffeners, a watertight bulkhead near the stern, and a shear deck with coaming. The model, shown in Figure 6.1, was fitted with a plastic cover which acted as a splash guard during tests.

The interior of the model was designed to be open, allowing maximum flexibility when arranging instrumentation and ballast weights. The model was fitted with several Ren-

Shape™ pads which were machined flat with the Liné. These were used as mounting pads and references for instrumentation. The Liné was also used to make three holes in the hull which were either plugged or used for the installation of pitot tubes for flow measurements near the hull surface.

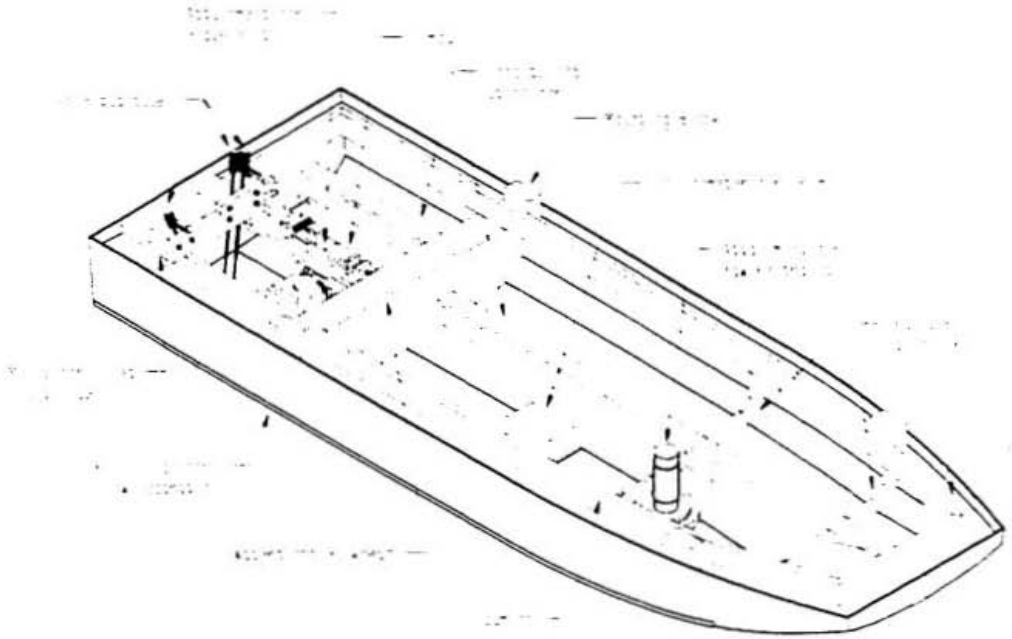

Figure 6.1 – Niagara Jet Boat Model

The hull surface was marked with station numbers on the bottom and port side. The port side was also marked with a grid used to determine the wetted surfaced area from underwater video taken during tests. The starboard side was marked with a smaller grid used to position flow visualization tufts. Outlines for the position of the waterjet inlet openings were marked on both sides. Two rows of turbulence stimulation studs were attached to the hull bottom and knife edges were fitted along the chines to promote flow separation (see Figure 6.2).

6.2 Turbulence Stimulation

As discussed in Chapter 4, flow regime is an important aspect of model testing. Full scale vessels usually have flows in the turbulent flow regime which means flow at model scale must also be turbulent. Depending on the scale used, it is possible for the model flow to be in any of the three regimes. In order to promote turbulence at model scale, devices were used to 'trip' the flow. Laminar flow near or in the transitional regime can be forced into turbulence by using obstacles which induce eddies in the flow which in turn generate the chaotic flow streamlines characteristic of the turbulence regime. Flow with sufficiently low Reynolds numbers may re-stabilize after a disruption or pass by it without change, so it is important to be aware of the specific Reynolds numbers involved in a given experiment. Several methods have been suggested for stimulating turbulence such as a trip wire, or some other form of roughness near the bow. IMD conventionally uses rows of 1/8" diameter by 1/8" high studs placed 1" apart center to center, fitted on adhesive tape for stimulating turbulence on its models (Hughes and Allan, 1951).

It is usually recommended that the studs be placed about 5% aft of the bow. Placing the studs too close to the bow may result in laminar flow re-establishing itself farther down along the hull; farther aft of the stem leaves the flow undisturbed over the portion of the hull forward of the studs. The location of 5% aft of the stem has been suggested to be the best compromise between these two situations. The line of studs should be placed parallel to the waterline at the bow.

Turbulence stimulation is complicated slightly when dealing with planing craft since the relative attitude of the hull with respect to the water changes significantly with forward

speed. Studs located near the bow may be submerged at lower speeds but may lift out of the water as the vessel trims with increasing speed. These higher speeds, and consequently higher Reynolds numbers, may result in natural turbulence over the hull eliminating the need for studs. If this is not the case, another row or rows of studs may be required farther aft to ensure turbulence over the full operating range of the model.

Another consideration with high speed models is the behavior of the flow at the chines. Planing craft often have V-shaped hulls with hard chines. At full scale, the flow hits these chines and sprays outward. At the lower Reynolds numbers of the model, the flow can cling to the surface of the model instead of separating from the hull as spray. This can result in a higher specific resistance. Separation can be promoted on the model with the use of knife edges along the chines. The knife edge extends about 1mm from the hull surface and can trip the flow causing it to separate from the hull. Full scale planing craft often have spray rails which perform a similar function, forcing the flow to separate from the hull in an effort to decrease wetted surface area.

The *Niagara* model was equipped with two rows of turbulence studs. The first set began at the centerline at station 9.5 (see Figure 6.2) and extended to the chines between station 8 and station 8.5. The second set began at station 6.5 and extended to the chines between station 5 and station 5.5. The angle of the stud rows relative to the centerline was intended to match the half angle of entrance of the waterline. Two rows were used to ensure stimulation at all speeds. Flow separation at the chines was achieved with knife edges extending from the transom to station 10. The positions of the turbulence studs and knife edges can be seen in Figure 6.2.

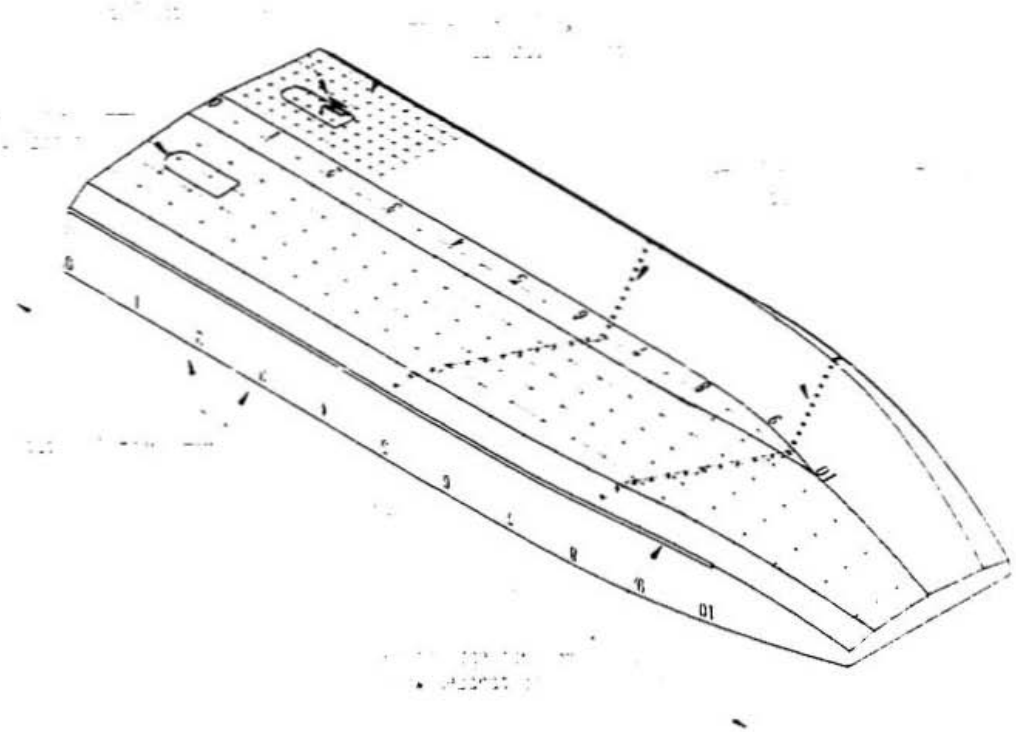

Figure 6.2 – Model Hull Markings

6.3 Model Ballasting

Since planing craft performance is sensitive to ballast condition, the bare hull resistance tests were performed over a range of displacements and locations of the longitudinal center of gravity (LCG). Three displacements each with three LCG positions for a total of nine ballast conditions were tested. A table showing the full scale and model scale ballast conditions is shown in Table 6.2 along with their naming codes. These were used to identify the ballast condition of the model. For example, ballast condition 'A2' had a displacement of 24.70 kg with an LCG of 0.534 m forward of the transom. The procedure used for ballasting the model for these conditions, as well as determining the VCG and model inertia, is given in Appendix A.

Full Scale Displacement	Model Scale Displacement	Naming Code
12,646 kg	24.70 kg	A
14,873 kg	29.05 kg	B
17,106 kg	33.41 kg	C

Full Scale LCG*	Model Scale LCG*	Naming Code
3.976 m	0.497 m	1
4.272 m	0.534 m	2
4.576 m	0.572 m	3

* LCG is referenced forward of transom

Table 6.2 – Ballast Conditions at Model and Full Scale

6.4 Description of Facility

The bare hull resistance test series was carried out in IMD's Clear Water Tank (CWT). The towing tank, shown in Figure 6.3 and Figure 6.4, is 200 m long, 12 m wide, 7 m deep and contains fresh water. The models are attached to a 14 m long tow carriage which spans the full width of the tank and weighs approximately 80 tons. The carriage moves along steel rails running the length of the tank. It is powered by eight electric motors with a total power of 1500 kW, which can give a maximum speed of 10.0 m/s with accelerations available in steps of 0.2 m/s^2 up to 1.2 m/s^2. Limitations on the tank length are imposed by the locations of the underwater video cameras, wave maker, and wave absorbing beach, which shorten the usable run length to about 160 m. The maximum practical acceleration and deceleration of the carriage has been found to be only about 0.8 m/s^2 in order to avoid wheel slippage on the steel rails. These restrictions limit the maximum carriage speed to approximately 8.5 m/s while still providing a few seconds of constant velocity.

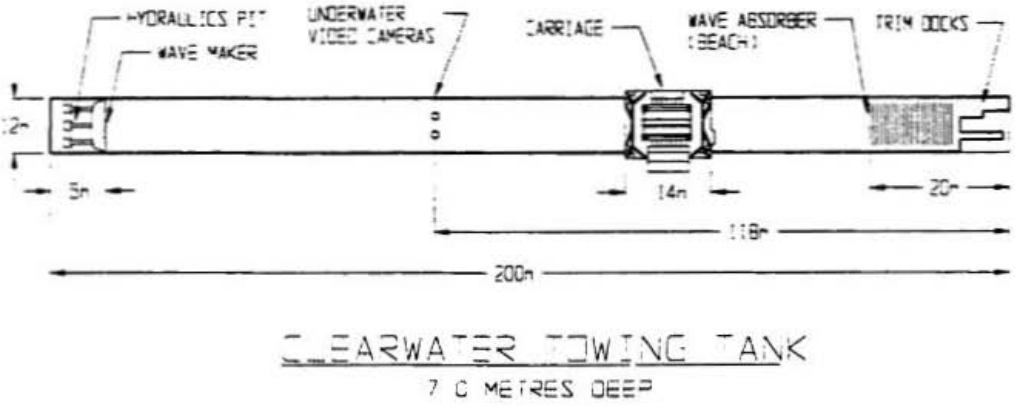

Figure 6.3 – Plan View of Clear Water Towing Tank

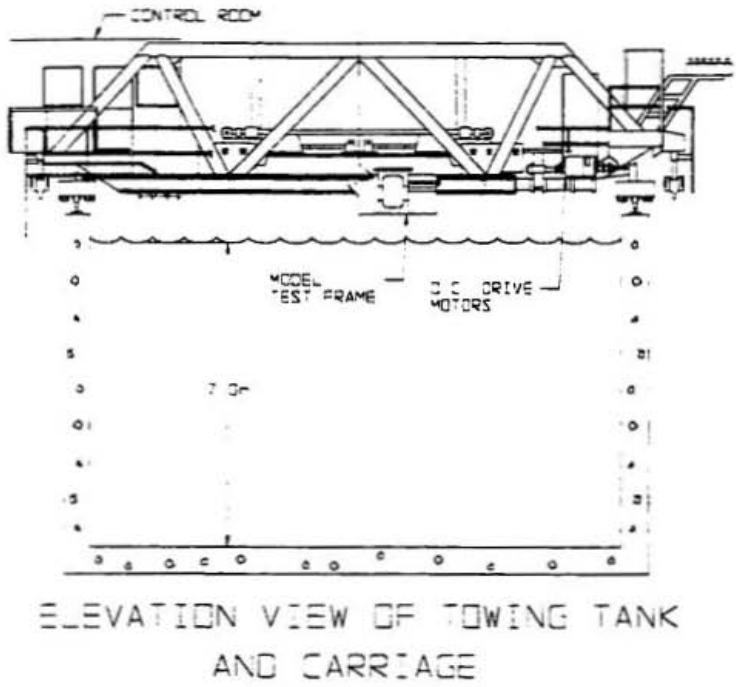

Figure 6.4 – Side View of Clear Water Towing Tank

6.5 Tow Arrangement and Instrumentation

The model was outfitted with instrumentation to measure running trim, heave and tow force. Pitot tubes through the hull were used for some tests to measure the flow velocity near the inlet locations. Flow visualization tufts were attached to the hull around the location where the port inlet opening would be when installed (see Figure 6.2). Model velocity was measured by the carriage and air velocity near the model was measured with an anemometer. Video was taken both above and below water during tests.

The model was fitted to the tow carriage with a gimbal and yaw restraint. The gimbal used in these tests, shown in Figure 6.5, was custom built for testing small models (under 2 meters in length). It consisted of a universal joint which attached to the model with a mounting plate. On top of the universal joint was a base plate on which a linear bearing or 'frictionless' table and load cell were located. The load cell was attached rigidly between the base plate and frictionless table with brackets. The tow force provided by the carriage was transmitted through the heave post which connected to the linear bearing. The bearing transmitted the tow force through the load cell and on to the model. The heave post applied a supporting moment to the frictionless table which forced the base plate to remain horizontal. The load cell therefore measured only the horizontal component of the applied load to the model which by definition was the model's resistance. The universal joint allowed the model to pitch and roll freely and the heave post was free to move vertically in the tow post arrangement.

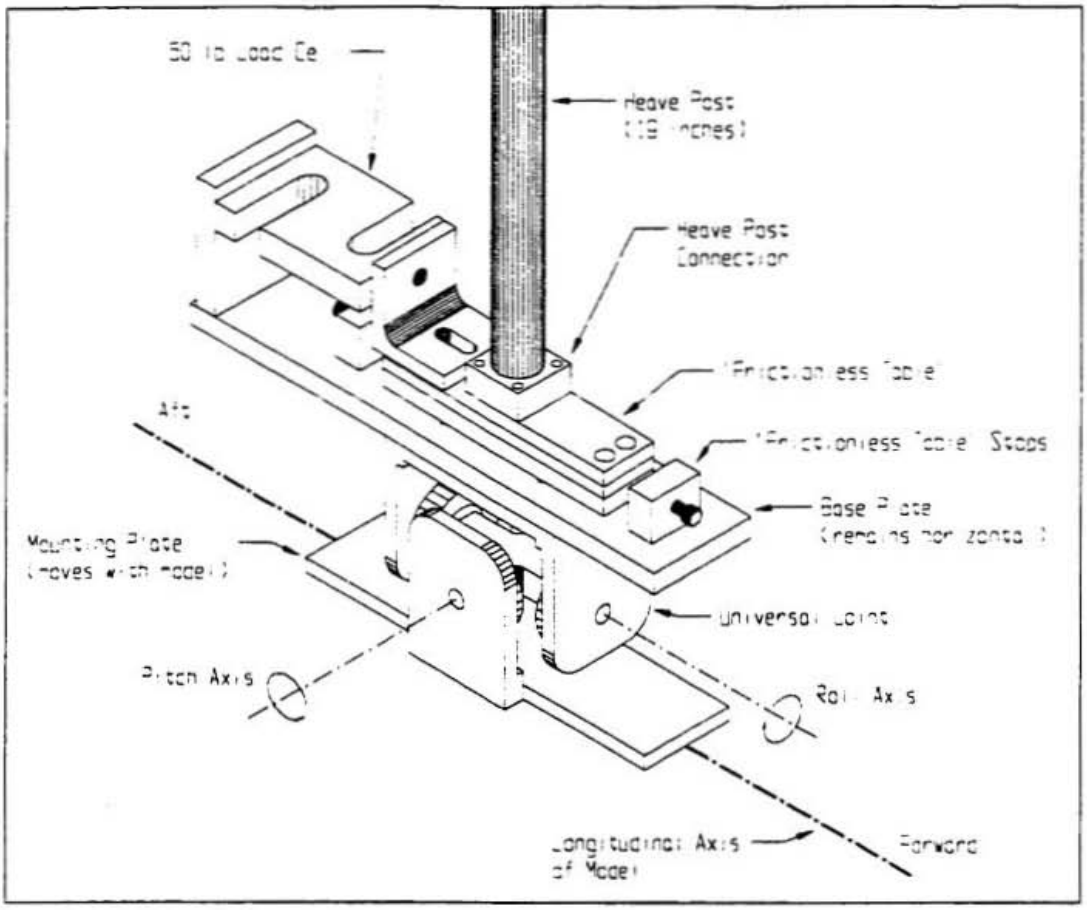

Figure 6.5 – Gimbal Arrangement

The tow post contained bearings for the heave post and a connection for a displacement transducer (see Section 3.3) which attached to the top of the heave post and measured its vertical movement and hence the vertical position of the model. At the top of the tow post were clamps which attached to the carriage tow post.

The gimbal was located near the aft of the model, as opposed to at its center of gravity, in order to better simulate the thrust produced by its waterjets. The location of the applied tow force or thrust to the model can affect running trim and therefore the behaviour of the

model. The gimbal should be placed as close as possible to the jet units in order to model the force system of a self propelled vessel.

The model was prohibited from rotating about the heave post by a yaw restraint shown in Figure 6.6. The yaw restraint was designed to provide only a reaction force against yaw. It was counterbalanced so that it did not affect the ballast, and its arrangement allowed the model to freely heave and pitch and roll.

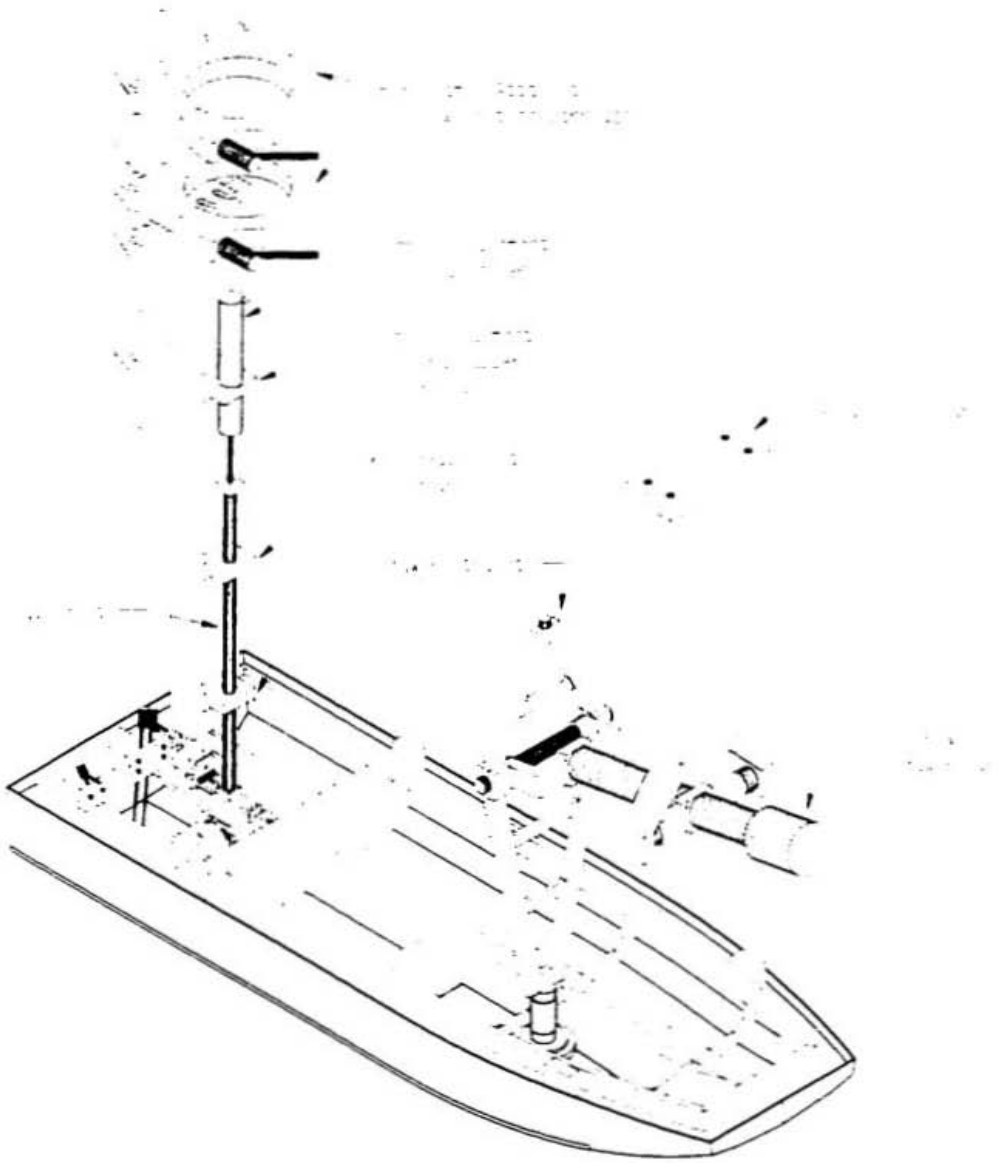

Figure 6.6 – Tow Arrangement

Running trim was measured with an inclinometer (see Section 3.7) that rested on a pad machined level to the hull baseline. Three pitot tubes, used for some tests to measure flow velocity near the hull, were held in place with a brace attached to the coaming. The tubes passed through holes in the hull and were positioned parallel to the hull bottom so that the heads of the tubes formed a plane just ahead of the beginning of where the

starboard inlet was located when the waterjets were installed. This arrangement is shown in Figure 6.7. Table 6.3 lists the locations of the pitot tubes used during tests. Pitot-1 and pitot-3 used differential pressure transducers while pitot-2 was attached to two separate absolute pressure transducers giving individual readings for the static and dynamic pressures (see Section 3.2). All of the pressure transducers used were placed in the model during testing and constituted a considerable part of the ballast weight (not shown in the figures).

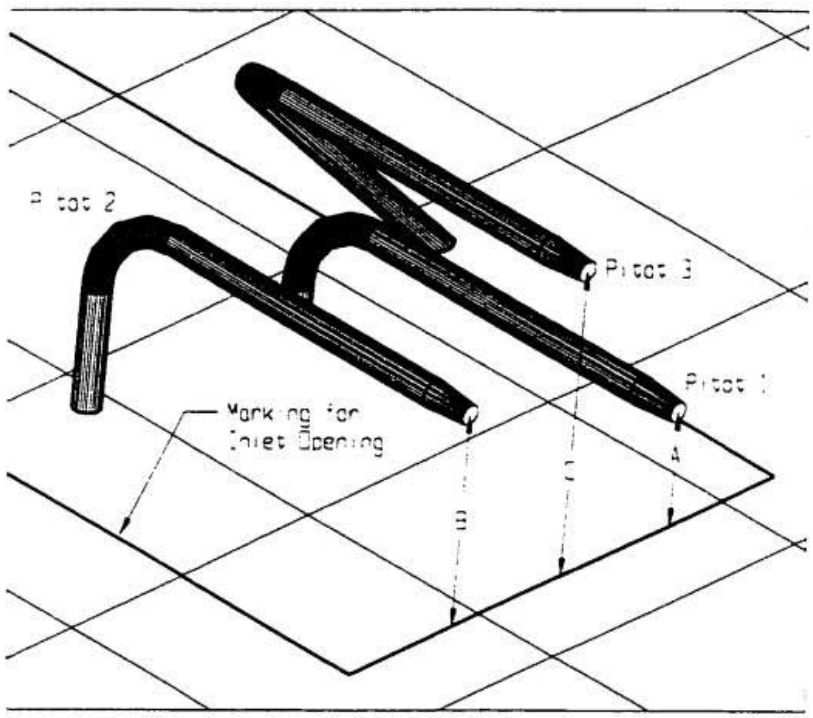

Figure 6.7 – Inlet Pitot Tube Locations (Starboard Side)

Name	Position 1	Position 2
Pitot-1	9.5 mm	3.0 mm
Pitot-2	17.5 mm	7.0 mm
Pitot-3	25.5 mm	9.5 mm

Table 6.3 – Inlet Pitot Tube Positions

Table 6.4 lists the measurements made during the bare hull resistance tests. The data acquisition system (see Section 3.8) sampled at a rate of 50 Hz for all channels. Other measurements, such as air and water temperature, as well as atmospheric pressure, were only made occasionally to ensure testing conditions remained constant. Measurements made from underwater video are discussed in Appendix B.

Measurement	**Units**	**Instrument**
Carriage speed	m/s	From carriage control
Thrust	N	50 lb. Load cell horizontal in gimbal
Heave	mm	LVDT connected to heave post
Running Trim	deg.	Inclinometer attached to hull
Fluid pressure just before inlet plane near hull	Pa	Three pitot tubes with pressure transducers
Air speed under carriage	m/s	Anemometer located near model under carriage
Wetted surface area	m^2	Still frames of underwater video taken at speed
Wetted lengths	m	Still frames of underwater video taken at speed
Flow visualization	-	Examining flow visualization tufts on still frames of underwater video taken at speed
Water and air temperature	°C	Digital thermometer (measurement recorded not acquired)
Ambient Atmospheric Pressure	Pa	Digital barometer (measurement recorded not acquired)

Table 6.4 - Bare Hull Resistance Measurements and Instrumentation

6.6 Test Program

The bare hull resistance test program was divided into four types of test series:

1. Bare hull without tufts or pitot tubes
2. Bare hull with tufts, pitot tubes in position 1
3. Bare hull with tufts, pitot tubes in position 2
4. Bare hull without tufts, pitot tubes in position 2

The test series spanned full scale velocities from 10 knots to 45 knots in 5 knot increments, or model speeds from 1.82 to 8.18 m/s as shown in Table 6.5. The velocity was scaled according to Froude number as discussed in Chapter 4.

Full Scale Speed	Model Scale Speed
10 knots	1.82 m/s
15 knots	2.73 m/s
20 knots	3.64 m/s
25 knots	4.55 m/s
30 knots	5.46 m/s
35 knots	6.37 m/s
40 knots	7.28 m/s
45 knots	8.18 m/s

Table 6.5 – Speeds at Full and Model Scale

All eight speeds with all nine ballast conditions were tested without flow visualization tufts and pitot tubes. These provided a baseline with regards to resistance, running trim and heave. The second test series was performed with tufts and pitot tubes in position 1 (see Table 6.3). These were intended to establish the behaviour of the boundary layer flow near the inlet under varied running conditions. The third series was run only in the

B2 ballast condition (design condition) with the pitot tubes in position 2. The last set of tests were performed with the pitot tubes but without the flow visualization tufts.

6.7 Bare Hull Resistance Test Results

The experimental results for the bare hull resistance tests were primarily used as a baseline reference for the self propulsion tests discussed in Chapter 7. The following sections present some of these results. Data in the figures refers to the tests without pitot tubes and flow visualization tufts, unless otherwise stated.

During some tests, particularly at the higher model speeds, the model experienced a form of dynamic instability called porpoising. A brief description of this phenomena is given in Appendix C. This behaviour affected some of the test results since measurements were not being taken with the model operating at steady state.

6.7.1 Resistance

In general, the resistance profile of planing vessels take on a characteristic shape. Resistance tends to increase with vessel speed until a critical value is reached. This is called the 'hump' speed and is a local resistance maximum where the vessel attempts to climb its own bow wave. As the vessel speed increases past this, the vessel begins to plane which results in reduced resistance until it reaches a local minimum. Beyond this, increasing speed results in a steady increase in resistance.

The model resistance profiles measured during tests followed this characteristic shape. Resistance was sensitive to both displacement and the position of the LCG. There was

also a significant effect produced by the presence of the inlet pitot tubes and flow visualization tufts.

Figure 6.8 shows the resistance results of the three LCG positions for the 'B' ballast condition. The effect of LCG on resistance was most predominant in the hump region of the resistance curve. Moving the LCG aft increased the resistance in this region. As the vessel reaches higher speeds, the effect of moving the LCG aft reduced resistance. An aft LCG was therefore a penalty at lower speeds but was beneficial at planing speeds.

Figure 6.9 shows the resistance results for the middle LCG over three displacements. There seemed to be a proportional upward shift of the resistance curve with increasing model displacement. The greatest difference was seen at the top of the resistance 'hump' where the heaviest displacement showed considerably larger resistance values.

The peak of the hump of the resistance curves occurred at about the same model speed for all ballast conditions, coinciding with the peak in running trim which also occurred at that speed, approximately 3.4 m/s.

The instrumentation also had an effect on the resistance curves. Figure 6.10 shows three test series of the B2 ballast condition with different levels of instrumentation in the flow. The added resistance of the pitot tubes and tufts increased with model speed. The middle curve is the resistance of the model fitted with the pitot tubes at the inlet but without the flow visualization tufts. Though only containing a few points, it lies about midway between the other curves showing that the effect of the pitot tubes was about the same as

from the tufts. These effects are also discussed in Section 7.4.1 along with results from the self propulsion tests.

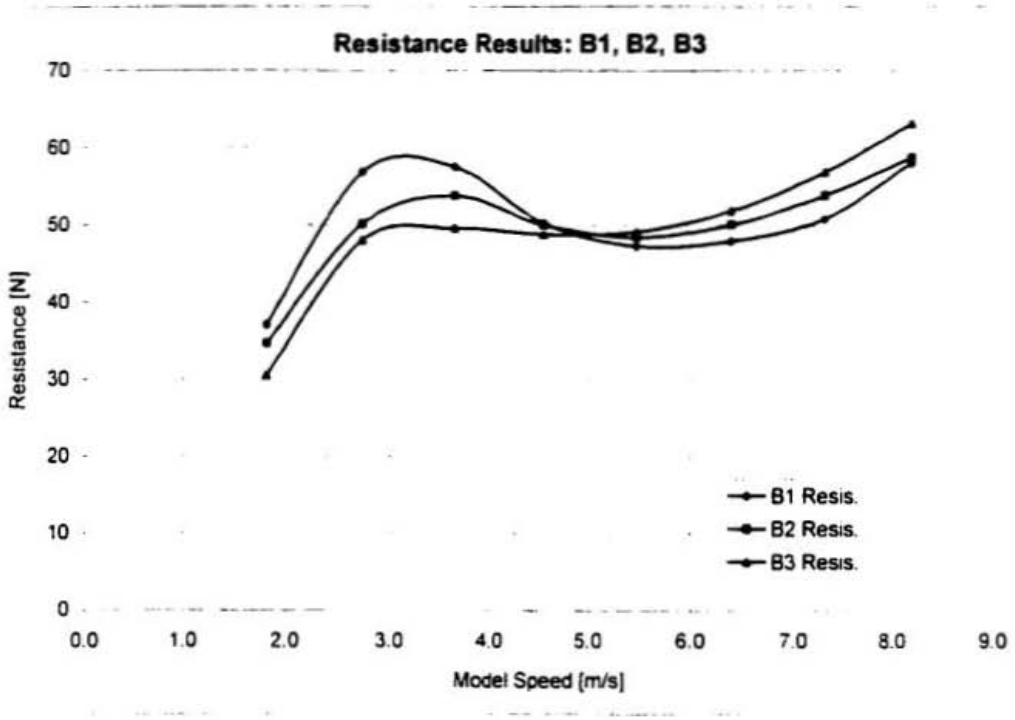

Figure 6.8 – Resistance Results: B1, B2, B3

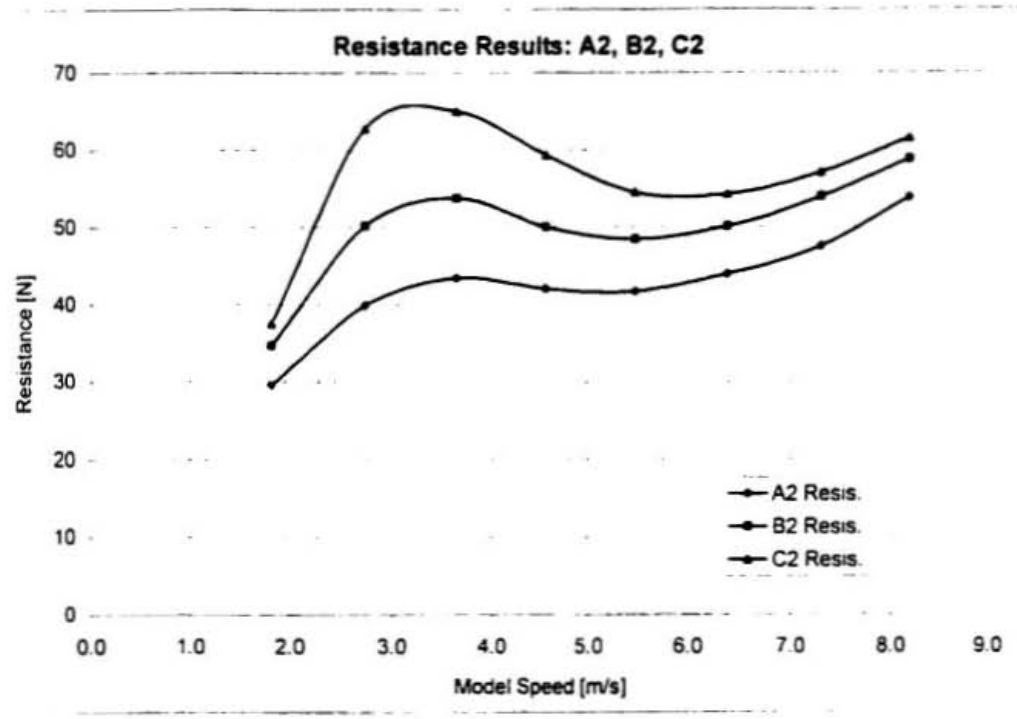

Figure 6.9 – Resistance Results: A2, B2, C2

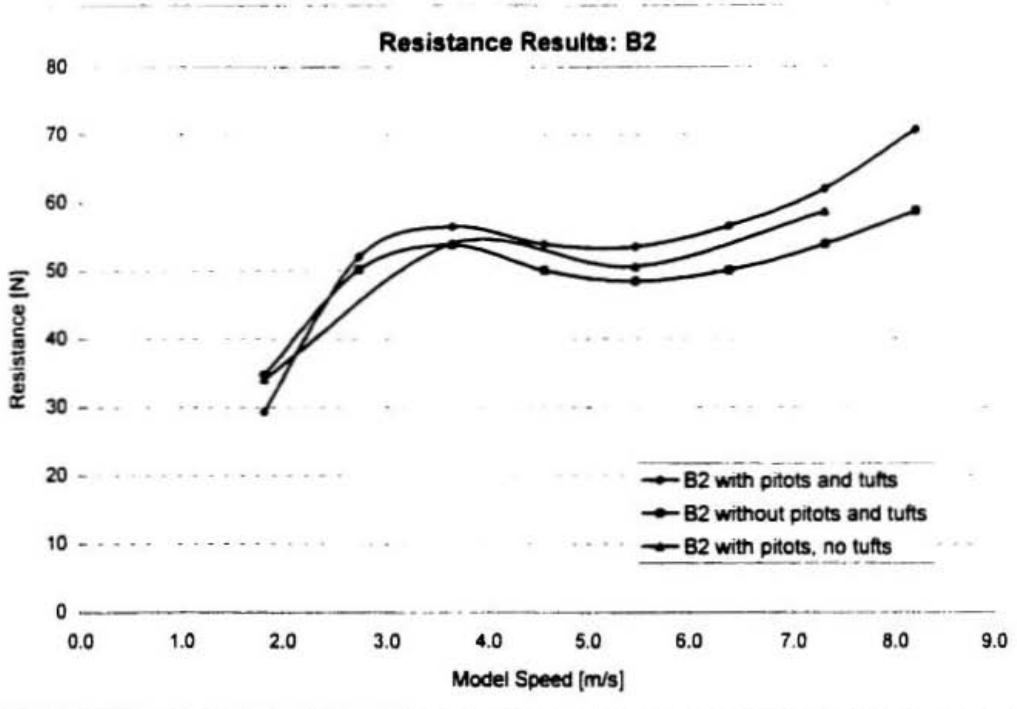

Figure 6.10 – Resistance Results: B2

6.7.2 Running Trim

The running trim of the model increased sharply as the model gained speed. It peaked at about the same model speed as the hump in the resistance curves, then gradually decreased as model speed was increased.

The running trim results followed similar trends in relation to ballast condition as the resistance curves discussed above. Figure 6.11 shows the running trim results for three LCG positions. As with the resistance curves, the aft LCG position produced higher trim angles at lower speeds but reduced the trim angle at planning speeds. The effect of displacement on running trim can be seen Figure 6.12. As with the resistance curves, increased displacement resulted in increased trim, which was most pronounced at the hump speed of about 3.4 m/s.

The pitot tubes and flow visualization tufts had little influence on the running trim profile of this model. Comparisons of the running trim of the model in various configurations can be seen in Section 7.4.2.

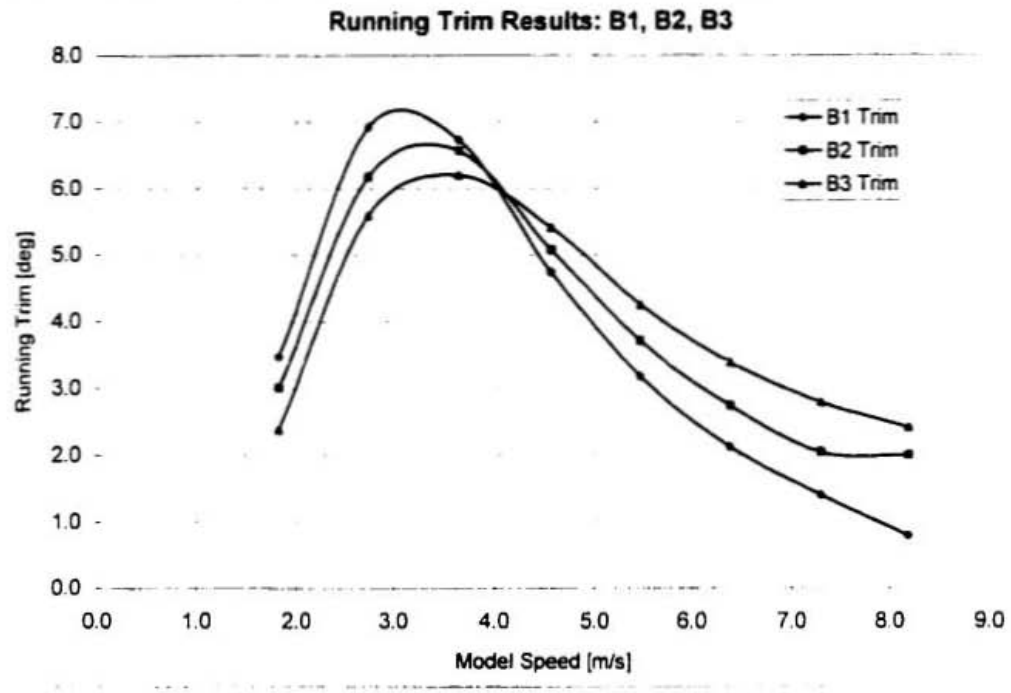

Figure 6.11 – Running Trim Results: B1, B2, B3

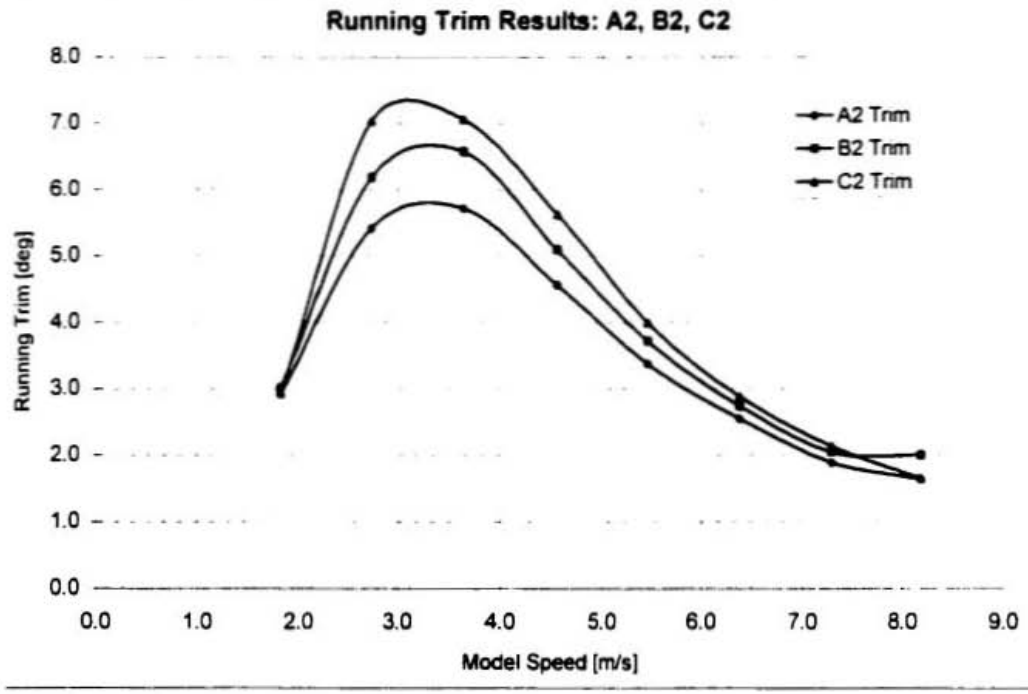

Figure 6.12 – Running Trim Results: A2, B2, C2

6.7.3 Heave

Heave or sinkage is the vertical change of the model's position while at speed. Generally, the model was seen to first rise as it approached planing speeds. Near the hump speed, the model would then be pulled down by pressure forces on the hull as model speed increased. This 'sinkage', as with running trim, showed signs of leveling off at higher speeds.

Figure 6.13 shows the effect of the LCG position on the heave profile of the model at speed. The effect was similar to those from displacement changes in the resistance and running trim profiles. As the LCG was moved forward, there was a proportional decrease in the magnitude of the measured sinkage at the higher model speeds. This effect was not as pronounced at the lower model speeds.

The effect of changes in displacement on the heave profile is shown in Figure 6.14. Lighter model weights produced smaller changes in heave at speed, while the heavier displacements showed proportionally larger changes in values of heave. The zero value was the position of the model at rest.

As with running trim, the presence of the inlet pitot tubes and flow visualization tufts had little effect on the heave profiles of this model. Comparison of heave from different model configurations can be seen in Section 7.4.3.

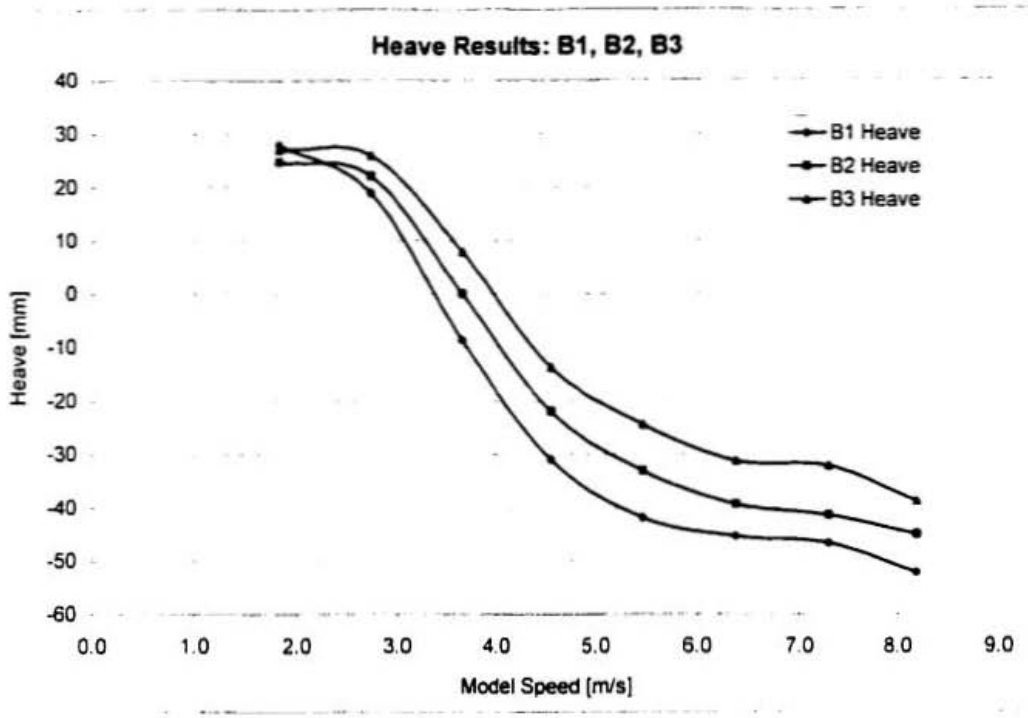

Figure 6.13 – Heave Results: B1, B2, B3

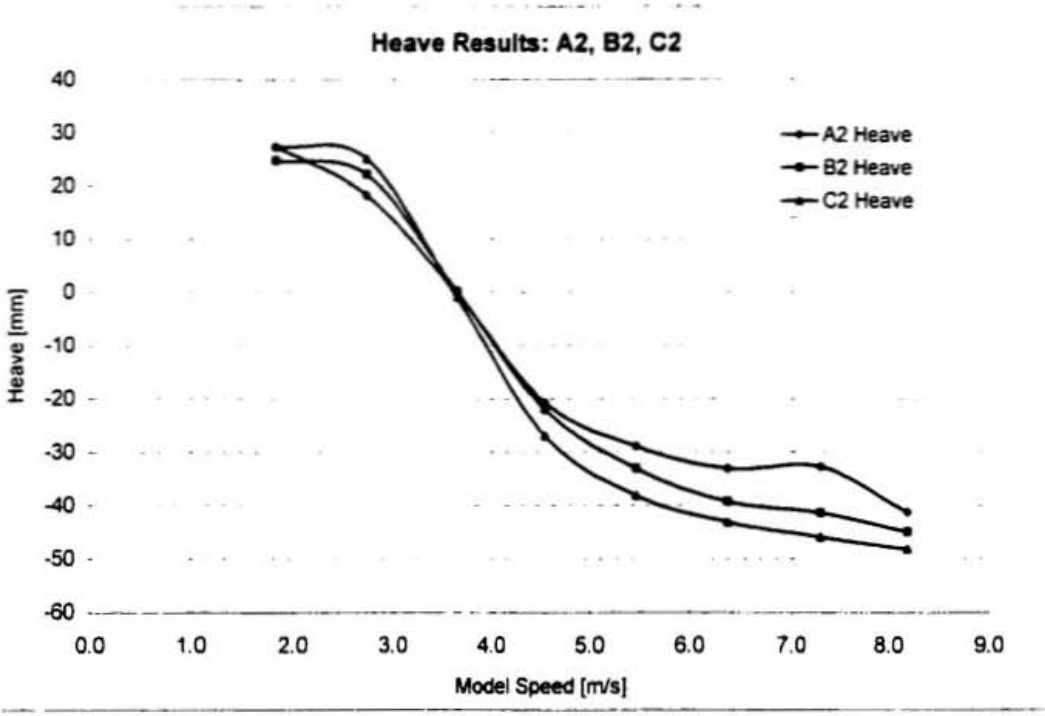

Figure 6.14 – Heave Results: A2, B2, C2

6.7.4 Wetted Areas and Lengths

The procedure for converting the model scale data determined in these tests to full scale data requires certain characteristics of the model at speed. These include the wetted area of the hull, and the wetted lengths of the centerline or keel, and chines. Underwater video was taken during tests to determine these values. The profiles of the curves for wetted area and length depend directly on the heave and trim of the model. An example of measured results from the video analysis is given in Figure 6.15.

The analysis procedure for the video and sample pictures of the underside of the hull at speed are presented in Appendix B. The conversion procedure for determining full scale data from model scale results as well as sample calculations are given in Appendix D.

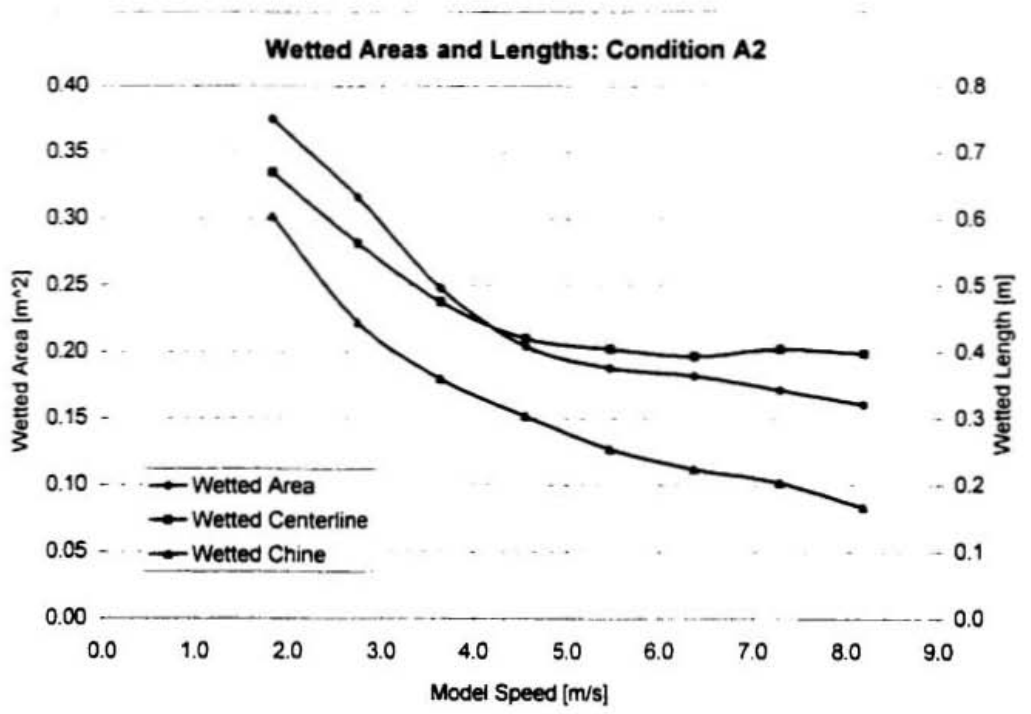

Figure 6.15 – Wetted Areas and Lengths: A2

6.7.5 Pitot Tube Measurements

The second and third test series were performed to determine the characteristics of the flow near the locations where the waterjet inlets would be when installed. This information was to be used in conjunction with similar data from the self propulsion tests discussed in Chapter 7 to help investigate the effect of the waterjets on this flow. The flow measurements were made using three pitot tubes oriented parallel to the hull bottom and pointing forward, at different distances from the hull (see Figure 6.7 and Table 6.3). Each pitot tube was intended to give a velocity measurement of the flow in its region of the boundary layer.

The thickness of the boundary layer can be estimated with equations developed from experiments with turbulent flow (Daugherty et al., 1985). An example of such a calculation is given below:

$$\frac{\delta}{x} = \frac{0.377}{Rn^{1/5}} \qquad [6.1]$$

where,

δ is the thickness of the boundary layer

x is the location of interest

Rn is the Reynolds number

Reynolds number, discussed in Chapter 4, was calculated by the following:

$$Rn = \frac{V \cdot L}{\nu} \qquad [6.2]$$

where,

V is the model speed

ν is the kinematic viscosity of water

L is the characteristic length

The characteristic length, L, was taken as the average of the wetted chine and centerline lengths as determined from the underwater video analysis (see Appendix B).

$$L = \frac{L_{chine} + L_{centerline}}{2} \qquad [6.3]$$

where,

L_{chine} is the wetted chine length

$L_{centerline}$ is the wetted centerline length

The theoretical boundary layer thickness at the location of the pitot tubes is shown in Figure 6.16 plotted against model speed. It ranged from about 2 to 11 mm depending on model speed.

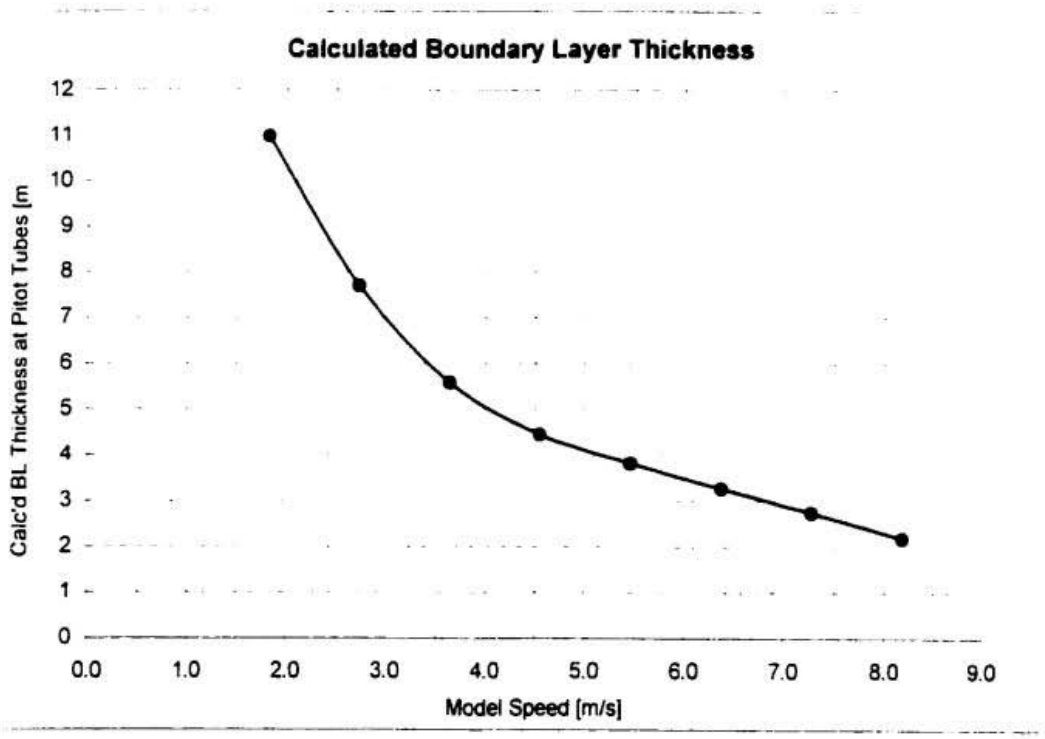

Figure 6.16 – Calculated Boundary Layer Thickness

The results from the pitot tube measurements did not provide much insight to the size or velocity distribution in the boundary layer. In the second test series, where the pitot tubes were in position 1 (see Section 6.5), the pitot tube closest to the hull consistently showed a slower flow speed than the mean. This suggested that it may have been located just inside the boundary layer envelope. Based on these results, the pitot tubes were moved closer to the hull, position 2, for test series 3. Only a few tests were performed with this arrangement and only for the B2 ballast condition.

Figure 6.17 shows the readings from the pitot tubes for test series 2, ballast condition B2 over the eight model speeds combined with the results from test series 3. The results from test series 3 show slightly lower velocities than those for test series 2, which was expected as the measurements were made closer to the hull. However, no clear velocity profile resembling boundary layer flow was evident in the data. The measurements, particularly those from test series 2, seem to be measuring the free stream velocity. This is shown in Figure 6.18 where the pitot tube results are plotted against model speed.

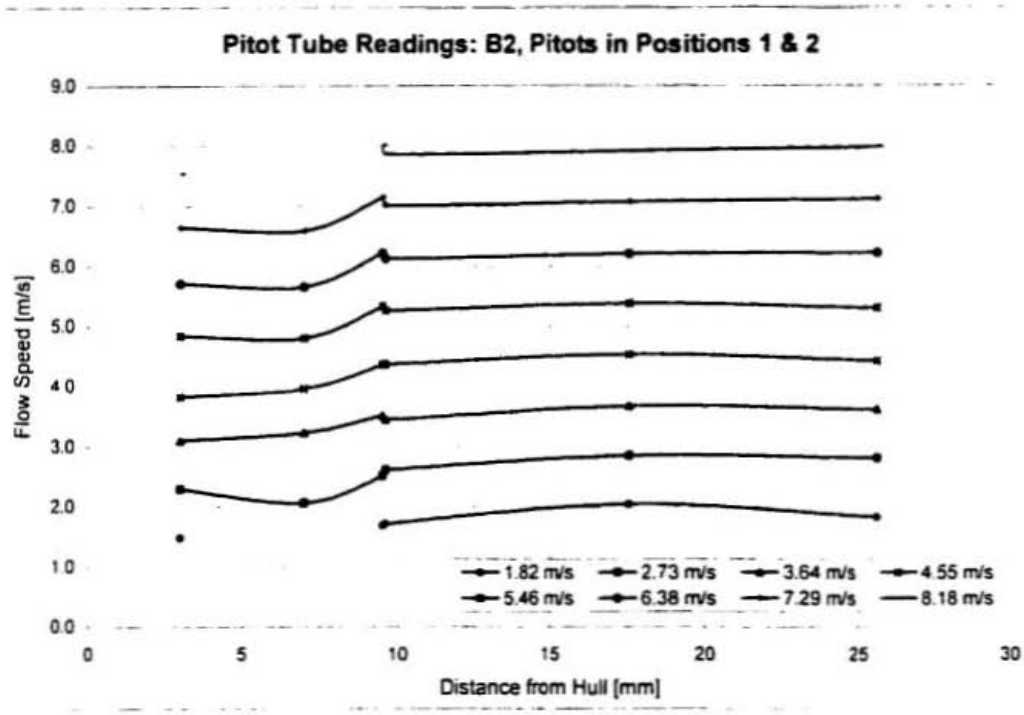

Figure 6.17 – Pitot Tube Readings

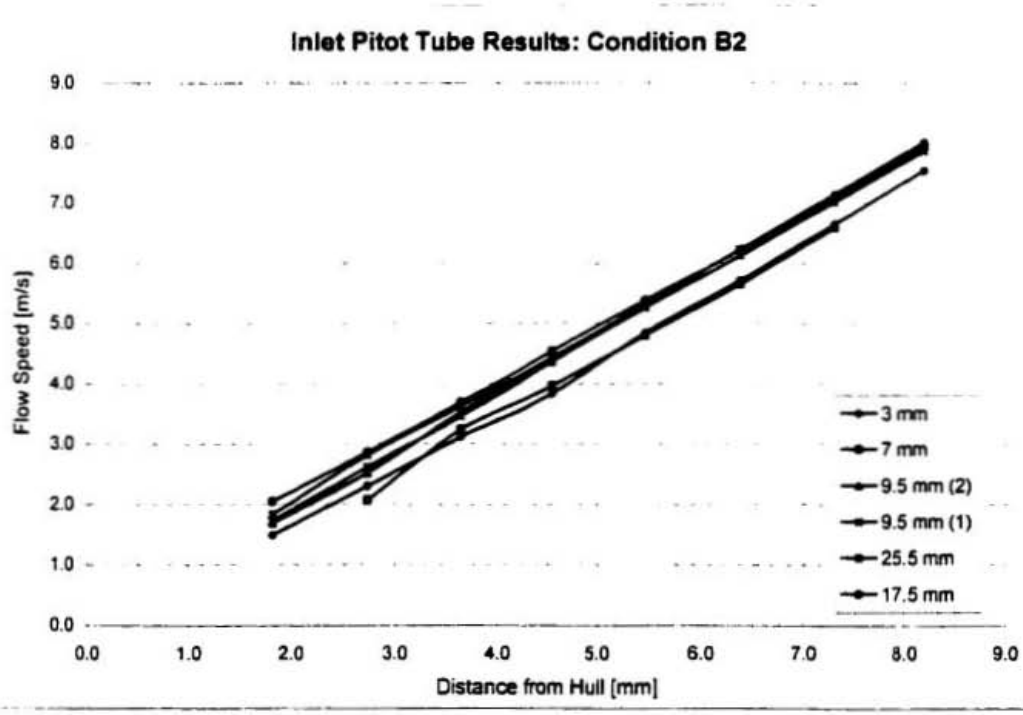

Figure 6.18 – Inlet Pitot Tube Results: B2

The thinness of the boundary at higher speeds presents measurement difficulties with the pitot tubes due to their size. Even at the lower speeds, the pitot tube and pressure transducer arrangement for measuring flow velocity did not seem have the sensitivity to provide the required level of resolution to distinguish a boundary layer profile. The use of pitot tubes for this type of measurement does not seem to be practical for a model of this size.

6.8 Conclusions

The bare hull resistance test series for this model followed established procedures for this type of experiment. The results provided a useful baseline for the self propulsion experiments of this model discussed in Chapter 7. The flow measurements near the hull, however, did not provide adequate resolution of the flow velocities in the boundary layer. More sensitive and less intrusive measurement techniques should be investigated for this type of experiment.

CHAPTER 7
SELF PROPULSION TESTS

7 SELF PROPULSION TESTS

The second phase of experiments consisted of self-propulsion tests. In this type of model test, the model is powered by its own propulsion system while being towed by the carriage. The *Niagara* model was fitted with a pair of small waterjet thrusters and DC electric motors. Instrumentation on the motors and the jets was used to make measurements needed to apply the momentum flux method discussed in Chapter 5. Self propulsion tests more closely model the behavior of the full scale vessel since the flow field induced by the waterjet units is present.

7.1 Model Preparation

After the completion of the bare hull resistance tests, the model was stripped of instrumentation and placed in the Liné CNC milling machine where the inlet and nozzle

openings were made, and attachment pads for the waterjets were machined. The model waterjet units were then installed as shown in Figure 7.7.

7.1.1 Model Waterjet Units

The waterjet thrusters used in these experiments were not scaled models of the propulsors found on the *Niagara Jet Boat*. Since the purpose of this project was to develop experience in testing methodologies and instrumentation, it was decided that the least expensive waterjets available would be used for this first attempt at this type of test. The units used came from a model hobby company which produces small waterjet units complete with motors and controllers for use in recreational radio controlled model boats. These jets were an appropriate size for the *Niagara* model and seemed to have the requisite power. The alternative was to have custom made jets designed and manufactured, which due to their size and components such as the impeller and stator, would have been prohibitively expensive.

The model jets, shown in Figures 7.1 and 7.2, were of a simple design for pure axial flow. The inlet opening was rectangular with a rounded aft section (see Figure 6.2). The internal ducting spanned the inlet to the circular section which contained a two bladed impeller. Directly behind the impeller, the ducting connected to a removable nozzle which contained four integrated stator blades. The impeller and nozzle are shown in Figure 7.3. The steel impeller shaft rested in a brass tube which passed from the outside of the unit through the inlet ducting to the impeller with a bearing at each end. The impeller, fixed to the end of the shaft, rested against this tube with a small Teflon washer. The body of the unit was plastic as was the nozzle/stator and impeller. It was powered

with a small DC motor which fitted to a flange on the unit. A small coupling was used in the transition from the motor shaft to the impeller shaft.

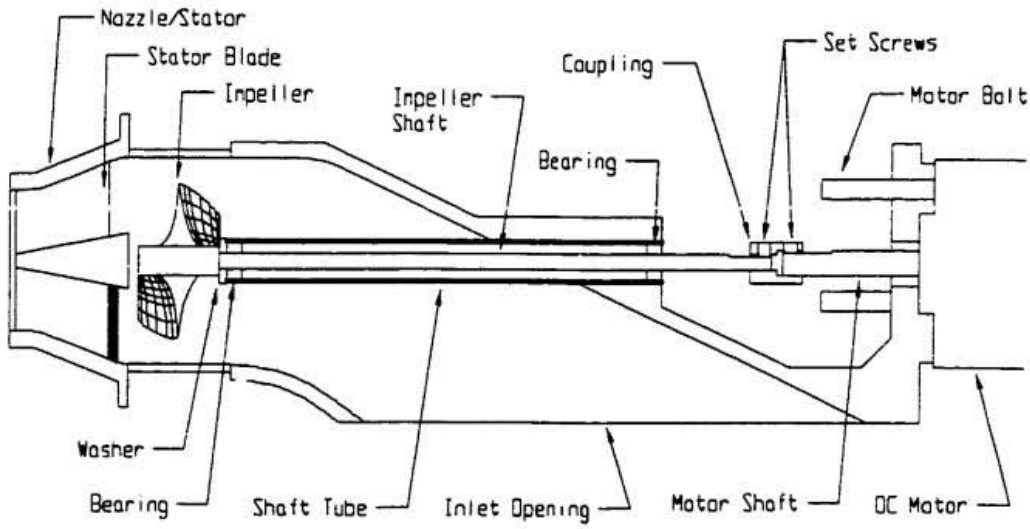

Figure 7.1 – Side View of Model Waterjet

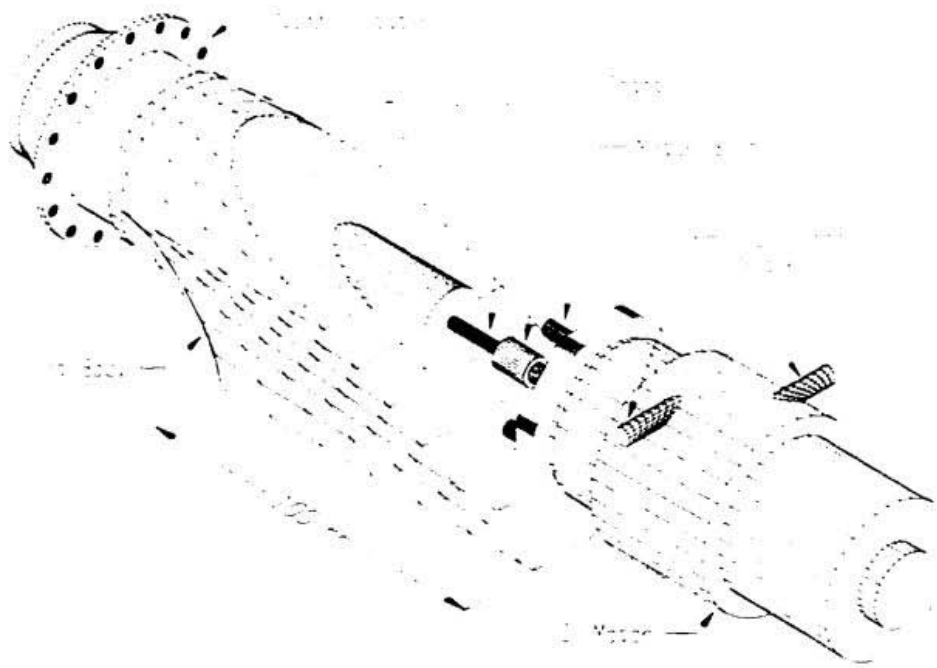

Figure 7.2 – Model Waterjet

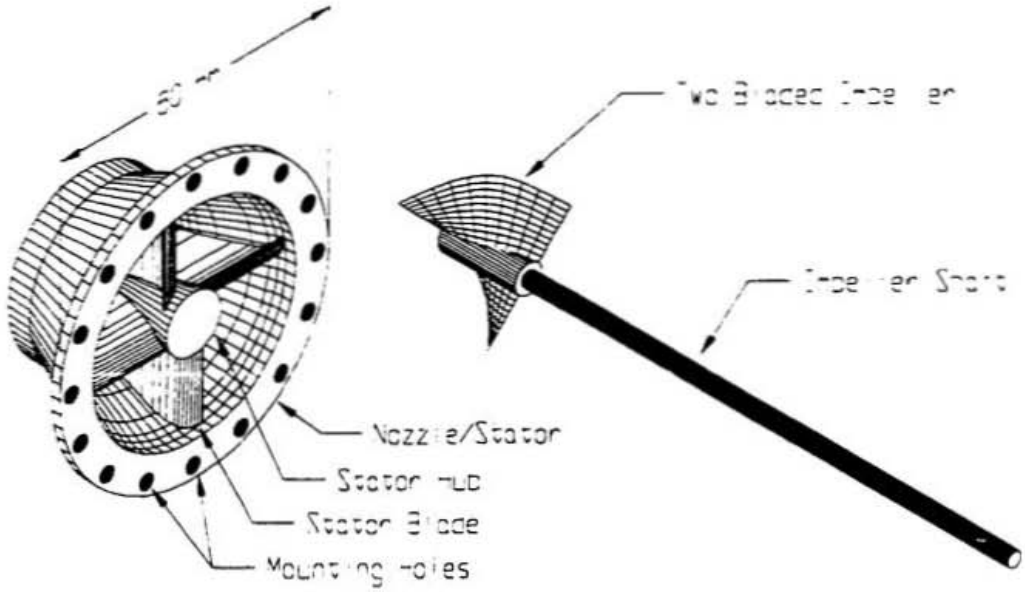

Figure 7.3 – Model Nozzle/Stator and Impeller

The motors used to power the model waterjets did not have a controller for accurately setting the shaft speed. However, the shaft speed was related to the motor's excitation voltage. Different shaft speeds could therefore be achieved by adjusting the motor voltage with digital power supplies. This method did not give tight control over the shaft speed as can be seen in Figure 7.4, which plots shaft speed versus motor voltage. This did not pose a significant problem since accurate shaft speed measurements were made independently with tachometers. The two motors produced slightly different shaft speeds for the same excitation voltage. Figure 7.5 shows a plot of the shaft speed difference between the two motors against excitation voltage. Since no clear relationship could be determined, this difference could not be adjusted for when testing. However, since the magnitude of the difference was usually within a few percent, mean shaft speeds for the two motors were used for calculations.

Another difficulty with these motors was their large current draw. The power supplies available were limited to 20 amps while the motors were rated for 25 amps. The power supplies therefore could not be used to develop the full motor power necessary at high model speeds. Full power was instead achieved with a 12 volt automotive battery connected to each motor for high speed tests. Since the data acquisition of motor voltage and current required the digital power supplies, these channels were not sampled in tests using battery power.

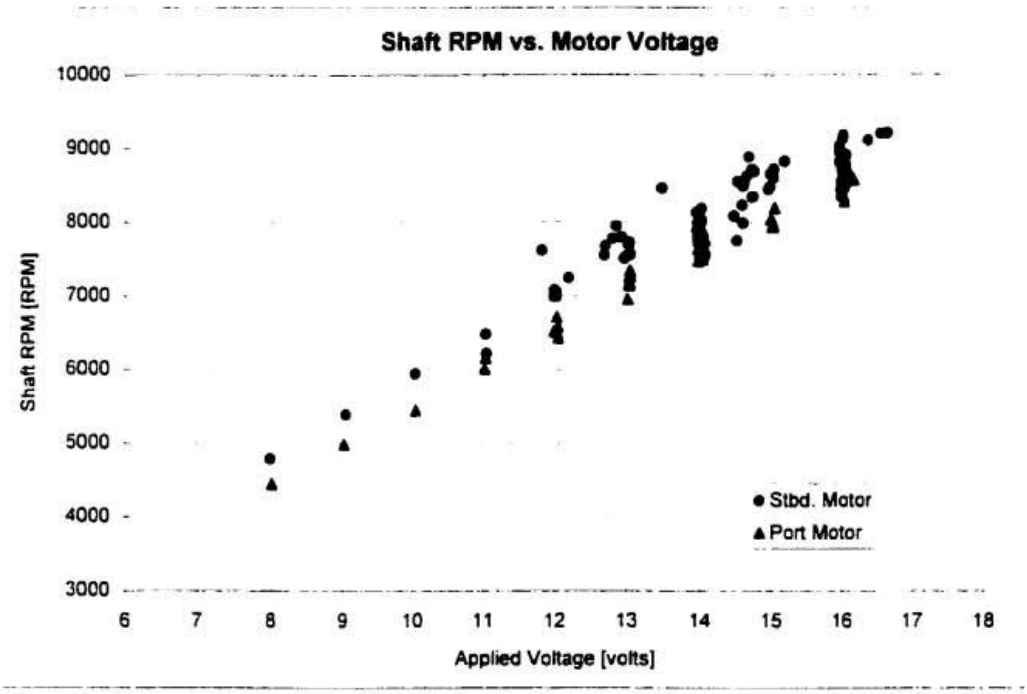

Figure 7.4 – Shaft RPM vs. Motor Voltage

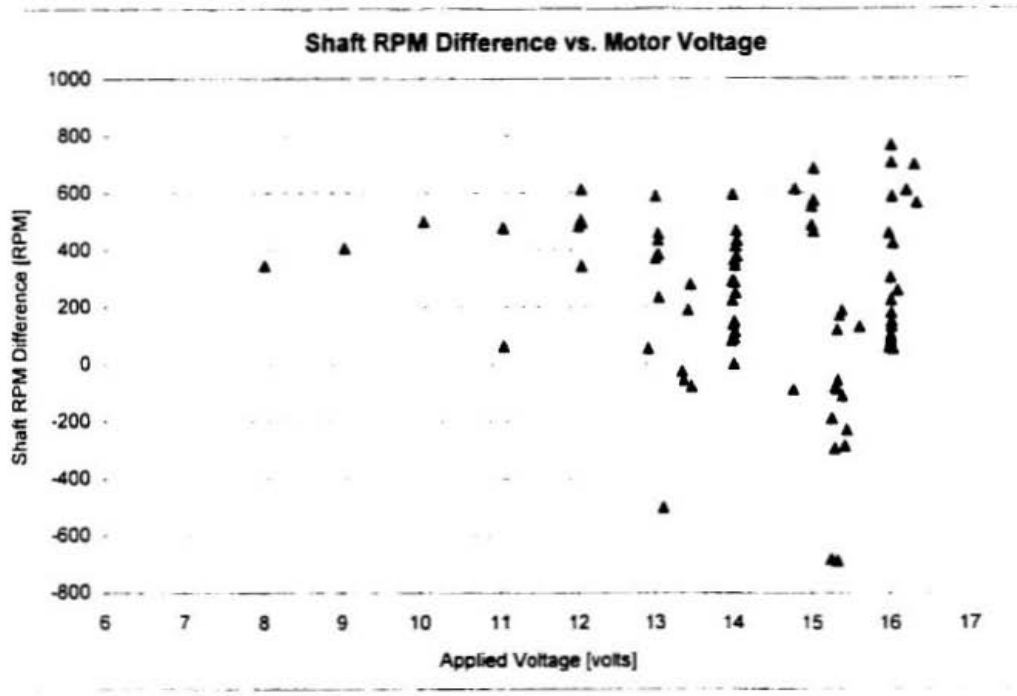

Figure 7.5 – Shaft RPM Difference vs. Motor Voltage

7.2.2 Model Outfitting

The model thrusters were mounted in the hull as shown in Figure 7.7 (some details are omitted for clarity). The small reaction torque gauges discussed in Section 3.5 were used with both motors and can also be seen in the figure. The port tachometer was mounted directly above the port motor while the starboard tachometer was mounted on the starboard longitudinal stiffener to accommodate the installation of the inlet pitot tubes, which are not shown in the figure. A small pump was used to circulate cooling water through the motors during testing.

The gimbal and tow arrangement for the self propulsion tests were the same as for the bare hull resistance tests and consisted of: an inclinometer, underwater and above water video, yaw restraint, inlet pitot tubes, flow visualization tufts, and turbulence stimulation.

Absolute running trim and heave data was taken during these tests. This differs from the bare hull resistance tests which measured only the changes in trim and heave of the model at rest to the model at speed. The running trim values were instead taken relative to a horizontal reference and heave values were taken relative to the waterline (zero heave meant the baseline of the model was at the water surface). At rest, the inclinometer measured the model's static trim, and the displacement transducer indicated the draft of the model at the heave post location. When comparing data with the bare hull resistance tests in later discussions, relative or tared values were used.

Three additional pitot tubes were used in these tests in an attempt to determine the flow rate at the port thruster nozzle. The stator, which was integrated in the nozzle, divided the nozzle area into four quadrants. Facing the nozzle, a pitot tube was located at the upper left quadrant, the lower right quadrant, and dead center (see Figure 7.6). The tubes were mounted with a bracket attached to the coaming and transom. The instrumentation used in the self propulsion tests is listed in Table 7.2.

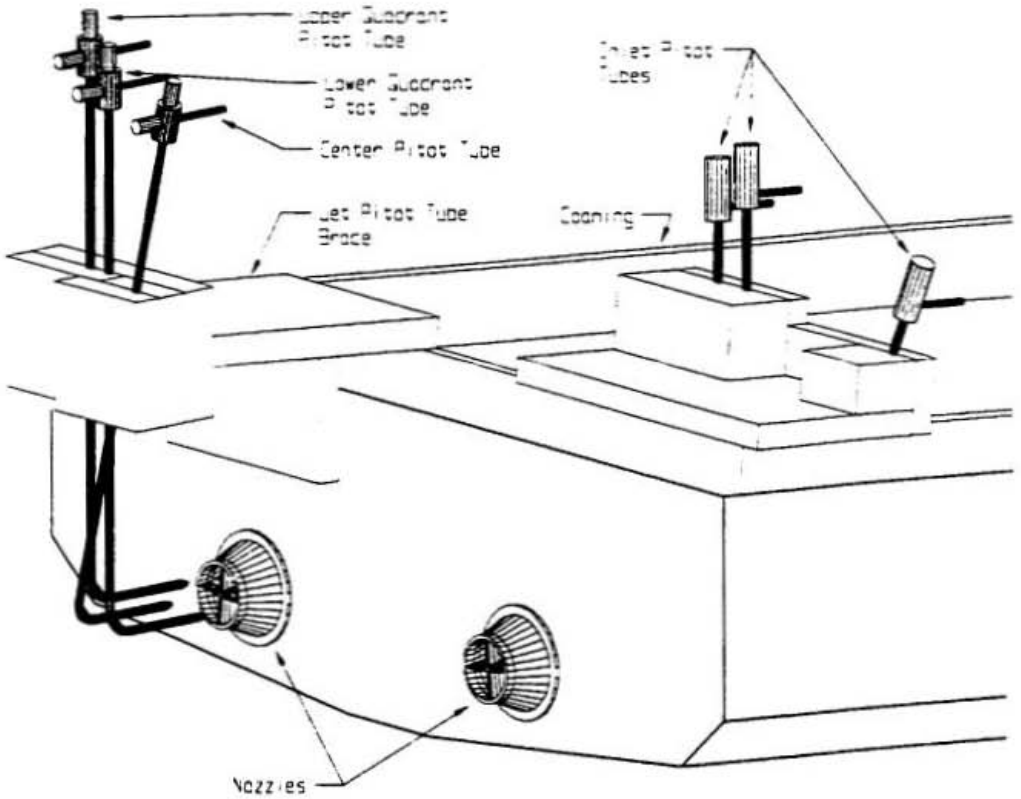

Figure 7.6 – Port Nozzle Pitot Tube Arrangement

Since the configuration of the model changed due to the added instrumentation, a new ballast plan was created in order to ensure that the same ballast conditions as the bare hull resistance tests were being used. The same procedure discussed in Appendix A was used with the addition of dummy weights sized and located to match the weight of the water inside the thruster units. The internal jet volume should be treated as lost buoyancy rather than added mass but since this volume was small, this method was adequate for these tests. The ballast conditions were the same as presented in Table 6.2. The model inertias, however, had changed as shown in Table 7.1.

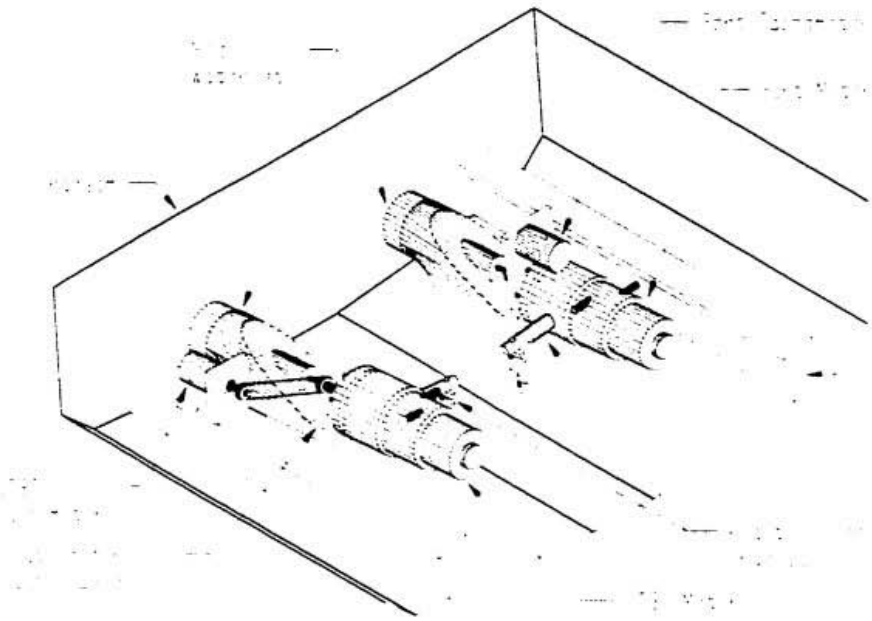

Figure 7.7 – Thruster Arrangement

	LCG 1	LCG 2	LCG 3
Displacement A	7.13 $kg \cdot m^2$	8.64 $kg \cdot m^2$	10.20 $kg \cdot m^2$
Displacement B	8.91 $kg \cdot m^2$	9.29 $kg \cdot m^2$	11.48 $kg \cdot m^2$
Displacement C	8.03 $kg \cdot m^2$	11.21 $kg \cdot m^2$	11.05 $kg \cdot m^2$

Table 7.1 – Model Inertias for Self Propulsion Tests

Measurement	Units	Instrument
Carriage speed	m/s	From carriage control
Thrust	N	50 lb. load cell in the gimbal
Heave	mm	LVDT connected to heave post
Running trim	deg.	Inclinometer attached to hull
Fluid pressure just before inlet plane near hull	Pa	Three pitot tubes with pressure transducers at stbd. Inlet
Air speed under carriage	m/s	Anemometer located near model under carriage
Wetted surface area	m^2	Still frames of underwater video taken at speed
Wetted lengths	m	Still frames of underwater video taken at speed
Flow visualization	-	Examining flow visualization tufts on still frames of underwater video taken at speed
Stbd. motor speed	RPM	Tachometer
Port motor speed	RPM	Tachometer
Stbd. motor torque	N·m	Reaction torque transducer
Port motor torque	N·m	Reaction torque transducer
Stbd. motor voltage	volts	Signal from power supply
Port motor voltage	volts	Signal from power supply
Stbd. motor current	amps	Signal from power supply
Port motor current	amps	Signal from power supply
Fluid pressure in jet	Pa	Three pitot tubes with pressure transducer in port jet
Water and air temperature	°C	Digital thermometer (measurement recorded not acquired)
Ambient atmospheric pressure	Pa	Digital barometer (measurement recorded not acquired)

Table 7.2 – Self Propulsion Measurements and Instrumentation

7.2 Test Program

The self propulsion tests consisted of two types of test series:

1. Self propulsion with tufts and pitot tubes
2. Self propulsion without tufts or pitot tubes

The same model velocities were used as listed in Table 6.5. As will be discussed, self propulsion tests of a towed model require several runs for each model velocity, while the impeller speed is varied. Tests were performed with the digital power supplies and some tests used battery power. The self propulsion tests did not include tests for all of the ballast conditions as used in the bare hull resistance tests. The increased number of runs per model speed limited the size of the test series that could be performed in the time allotted in the tow tank. The design condition, B2, was tested across its full range with and without flow measuring instrumentation.

7.3 Self Propulsion Point

As discussed in Chapters 4 and 6, the resistance of the model cannot be converted directly to full scale since Reynolds number was not matched at both scales. The effect of incorrectly scaling Reynolds number, which is related to the viscous or frictional component of resistance, can be estimated by calculating this resistance component at both scales using empirical formulas. Other resistance components which are not matched at both scales, such as the drag from instrumentation at model scale, can also be estimated. The total model resistance, expressed non-dimensionally, can then be corrected to represent the full scale resistance by subtracting unmatched resistance components at model scale and adding the appropriate components at full scale.

An example of this type of calculation was performed for the bare hull resistance test results in Appendix D. The net difference between the non-dimensional resistance at both scales should first be calculated in order to perform the analysis of the self propulsion test results.

Once the non-dimensional coefficients for the total resistance at model and full scale were determined, they were both expressed in terms of model scale units. These curves are shown for the B2 ballast condition in Figure 7.8 (Rtm is the measured model resistance, and Rts* is the total resistance corrected for full scale but expressed at model scale). Higher Reynolds numbers at full scale result in a lower frictional resistance component and hence lower overall resistance. The difference between these two curves, the resistance correction line, is also plotted in the figure.

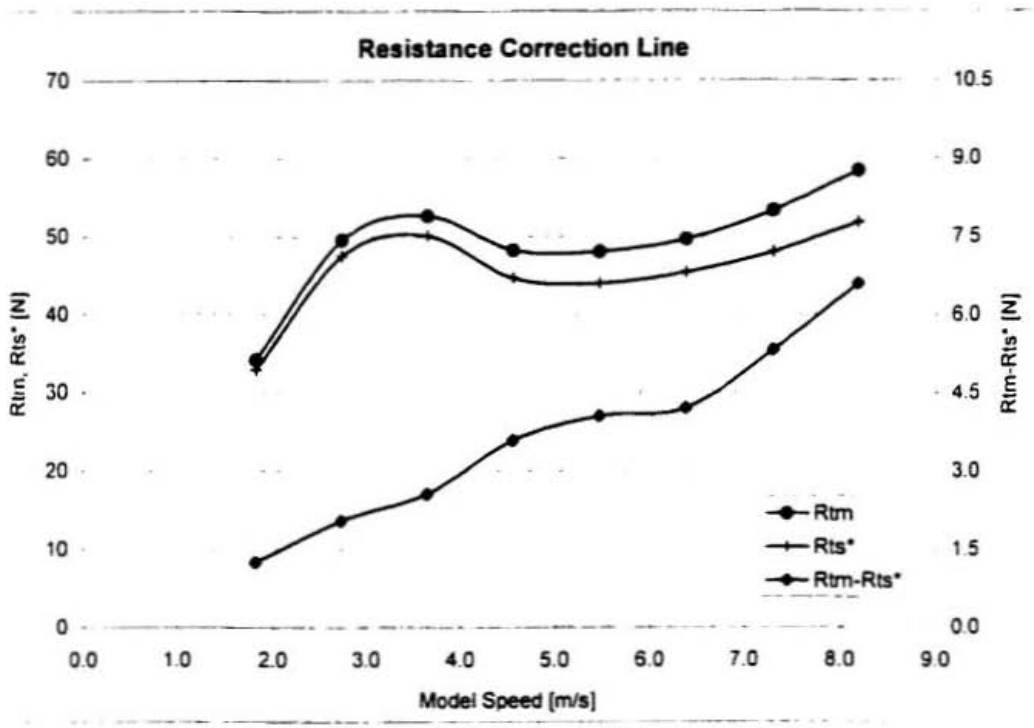

Figure 7.8 – Resistance Correction Line

The resistance correction line is needed to properly define the self propulsion points of the model during the self propulsion tests. The self propulsion point can be loosely thought of as the point where the model is being entirely propelled by its own power and is not being aided or hindered by the presence of the tow post and carriage. At model scale, the self propulsion point is when zero force is measured by the load cell in the gimbal. However, in order to adjust for the differences due to scale discussed above, the self propulsion point applicable to full scale results is the point at which the tow force equals the appropriate value on the resistance correction line.

This point is not generally achieved during a single test but is interpolated from data taken from several tests. The procedure involves systematically changing the thrust by varying the impeller speed while towing the model at a constant speed. The tow force

measured over a series of impeller speeds should contain both under-propelled (greater than the resistance correction) and over-propelled (less than the resistance correction) values for a given model speed. The self propulsion point is then interpolated from these measurements. For these tests, three to five points were considered sufficient for the interpolations.

Figure 7.9 shows the tow force measurements for the lowest and highest model speeds plotted against impeller speed (B2 ballast condition with pitot tubes and tufts). Also in the figure are lines representing the corresponding values for resistance correction discussed above. A self propulsion point is defined as the intersection of the appropriate resistance correction line with the linear regression line fit through the data (higher order regression curves could be used if suitable). The self propulsion points for each model speed are shown in the figure.

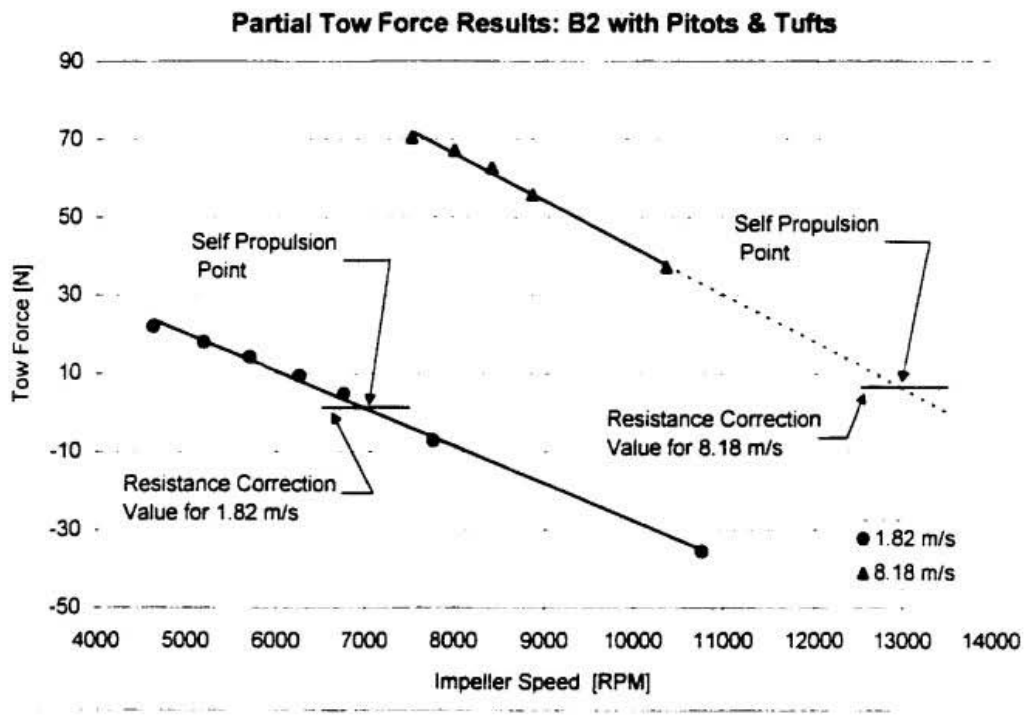

Figure 7.9 – Partial Tow Force Results: B2 with Pitots and Tufts

The data for the highest model speed in the figure (8.18 m/s) also illustrates a problem experienced for all of the ballast conditions tested: the model waterjets were unable to produce sufficient thrust at high speeds. It was therefore necessary to extrapolate the self propulsion points from the available data. The use of extrapolations affected the accuracy of the self propulsion values which were used in all subsequent calculations.

In order to simplify the analysis of the self propulsion results, the self propulsion point as defined above was not used in the remaining discussions. As these experiments were focusing on testing methods and instrumentation, comparing and evaluating data at model scale proved to be much less complicated. The self propulsion point referred to in the rest of this chapter refers to the model self propulsion point, or the point of zero tow force without the resistance correction.

Figure 7.10 shows the complete set of tow forces measured during tests at the B2 ballast condition with pitot tubes and tufts, along with the linear regression lines used to determine the model self propulsion points. These self propulsion points are plotted against model speed in Figure 7.11. The last three points in the curve were values calculated from extrapolations as shown in Figure 7.10 with dashed lines.

The curve for impeller speed shown in Figure 7.11 was the best of the ballast conditions tested. This was attributed to the number of runs performed at each speed for this condition. Fewer runs for the other conditions produced several clearly inaccurate self propulsion points at the higher speeds due to extrapolation error.

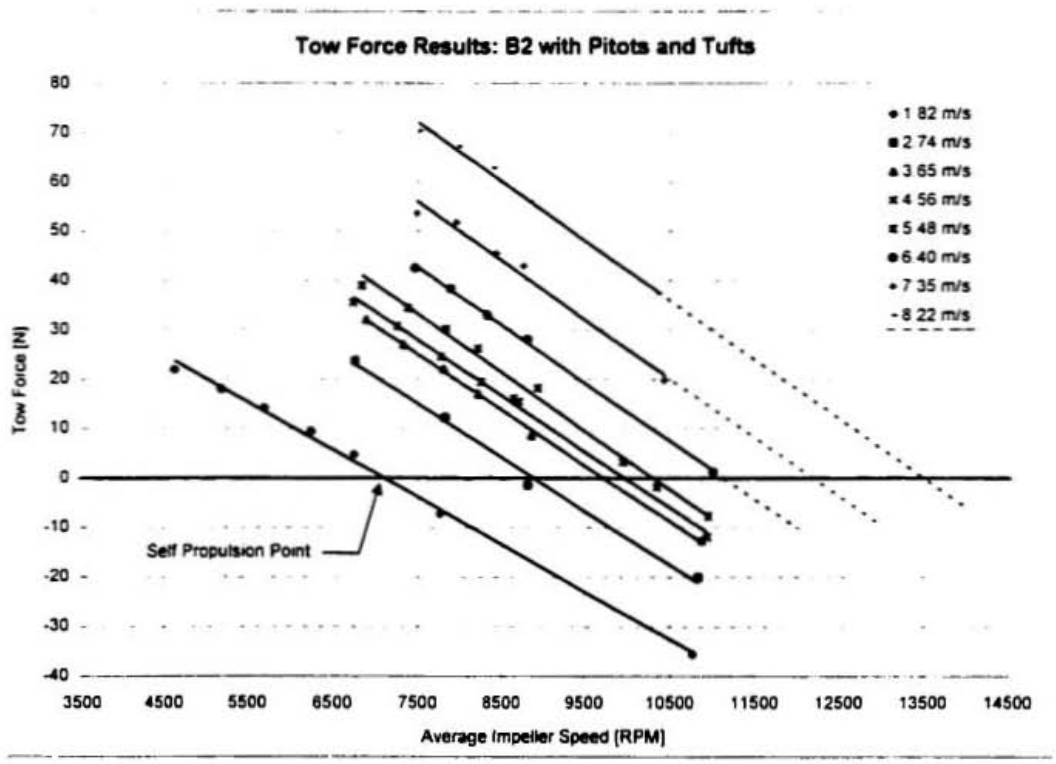

Figure 7.10 – Tow Force Results: B2 with Pitots and Tufts

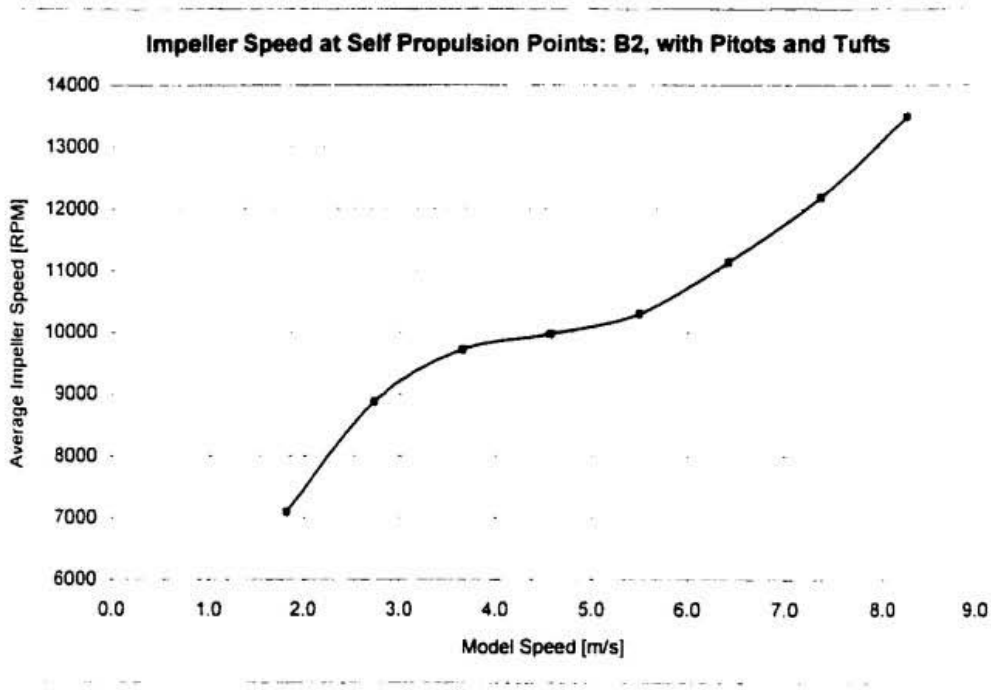

Figure 7.11 – Impeller Speed at Self Propulsion Points

The values of other measurements at the self propulsion points were calculated in a similar manner. Trim, heave, pitot tube results, wetted lengths and areas, were plotted with the tow force results and fitted with regression lines.

Figure 7.12 shows the results of running trim for the test series discussed in the above figures. These results show that running trim was not very sensitive to impeller speed or thrust. Running trim values were fairly constant throughout the range of impeller speeds at each model speed. The trim data at the two highest model speeds, 7.35 m/s and 8.18 m/s, showed more spread than measurements at the lower model speeds. This was a result of the porpoising behaviour discussed in Appendix C. Results for many of the higher model speeds of the self propulsion tests were affected by porpoising. Figure 7.13 shows the running trim values at the self propulsion points plotted against model speed. This

curve closely matches running trim curves determined during the bare hull resistance tests.

This procedure was repeated for the remaining measurements taken during the self propulsion tests including those from the underwater video analysis (discussed in Appendix A).

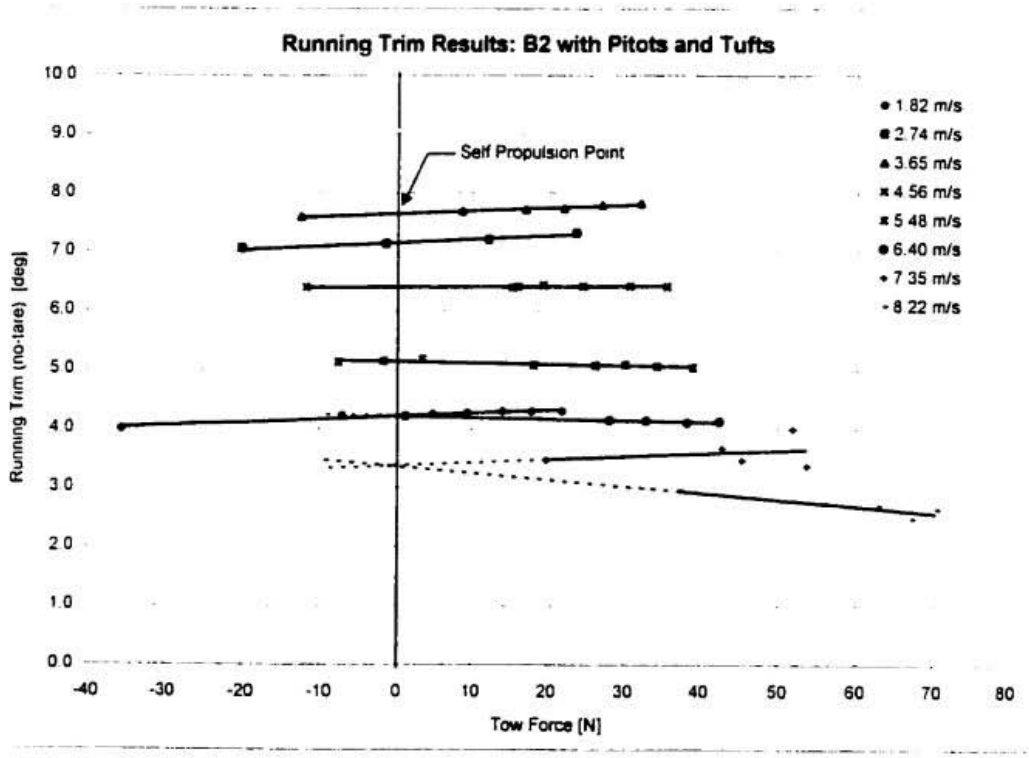

Figure 7.12 – Running Trim Results: B2_P1-P8

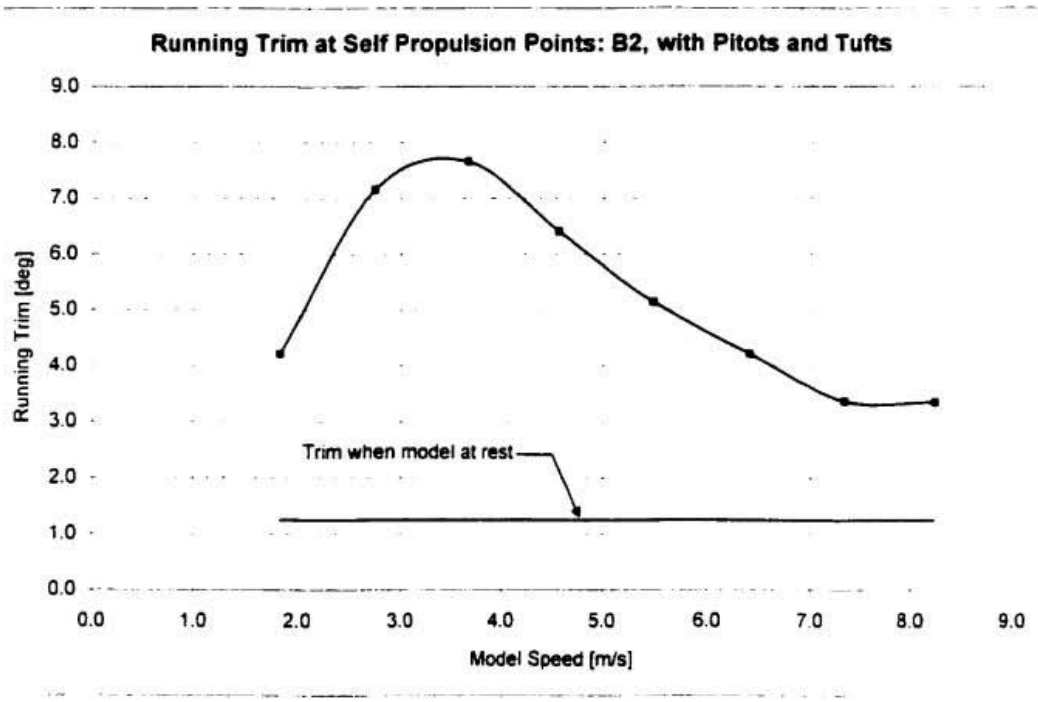

Figure 7.13 – Running Trim at Self Propulsion Points

7.4 Experimental Results

The self propulsion tests served several purposes; to develop experience at IMD in testing methods for waterjet propelled vessels, to compare relevant data with the bare hull resistance tests in order to evaluate the testing method, and to evaluate the use of the momentum flux method as outlined by the 21st ITTC.

7.4.1 Resistance and Impeller Speed

Significant differences in model resistance were observed for different testing configurations for the same ballast condition. Figure 7.14 shows the results of the tow force measurements made for various configurations of the B2 ballast condition from both the bare hull resistance tests and the self propulsion tests (no power to thrusters).

The influence of each change in the model's condition was significant, particularly at the higher speeds. The most predominant effect was the presence of the inlet openings which shifted the resistance curves upward by nearly 20% at the highest speed. The addition of the pitot tubes and tufts to the hull resulted in an upward shift of approximately 10% at the highest speed. Several tests were performed with the flow visualization tufts but without the pitot tubes (no inlet openings). Though the curve only has a few points, it shows that the influence of the pitot tubes was about the same as for the tufts, each responsible for about a 5% upward shift of the resistance at the highest model speed.

These results show considerable resistance penalties caused by the instrumentation. Increases in model resistance of such magnitudes, due to the use of these devices, show they were affecting the flow fields they were intended to measure. Less intrusive methods are needed to gather this information at this scale.

Figure 7.15 shows the average impeller speeds calculated at the self propulsion points for tests with and without the pitot tubes and tufts. Also plotted in the figure are the tow forces measurements made during the same test sets, but without power to the model thrusters. The impeller speed curves have a similar shape to the tow force or resistance curves. The upward shift in resistance caused by the pitot tubes and tufts is reflected in the impeller speed curves with a corresponding upward shift. This shows that the impeller speed curves respond proportionally to changes in model resistance for this model.

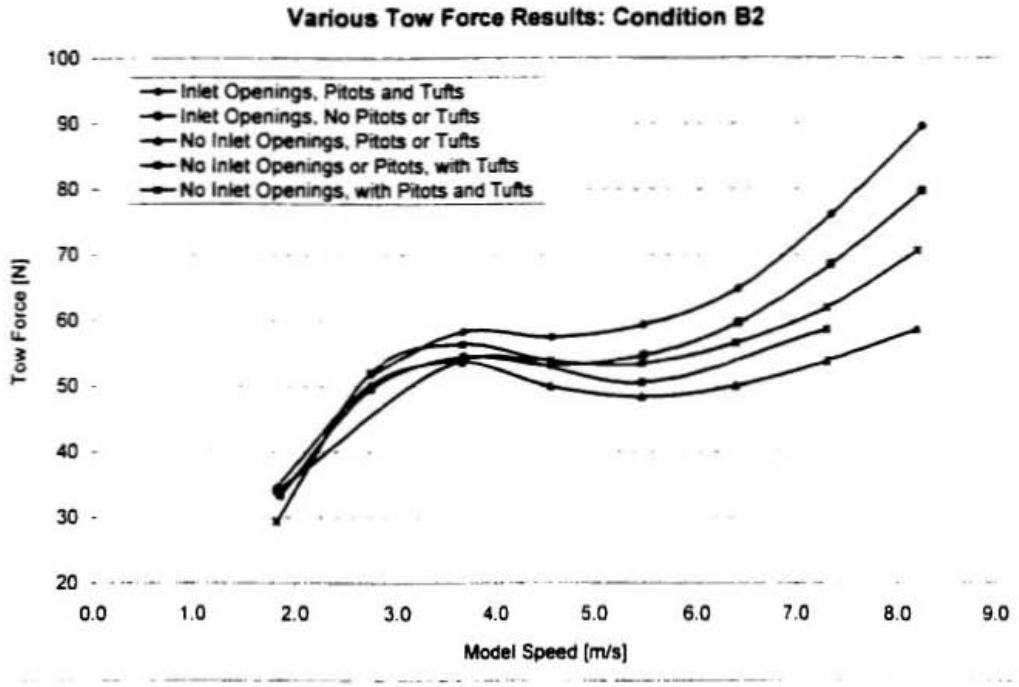

Figure 7.14 – Various Tow Force Results: Condition B2

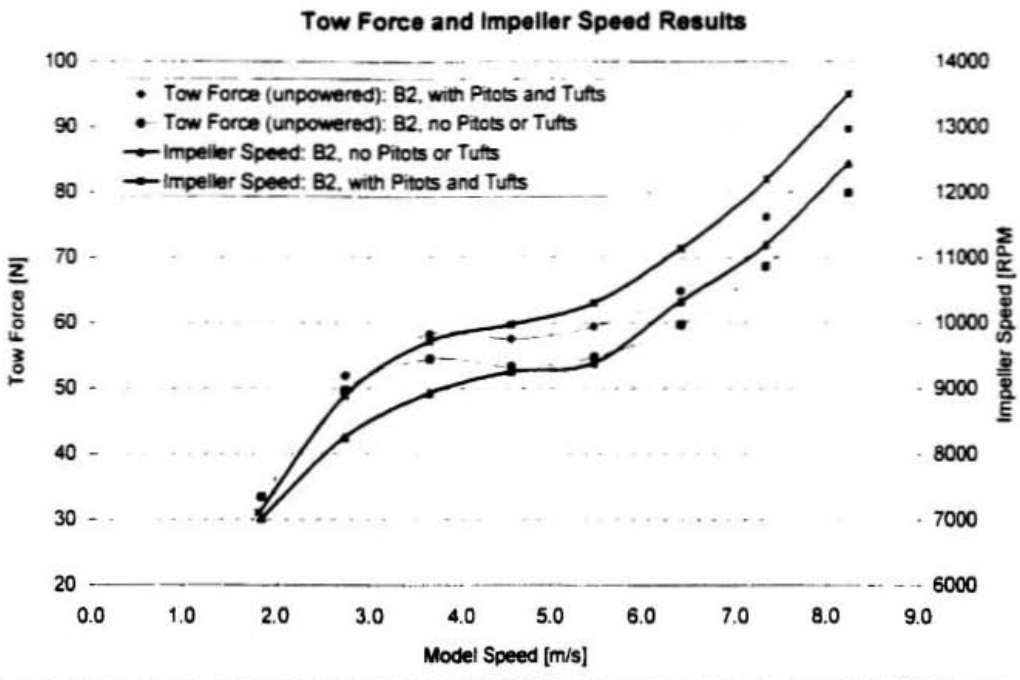

Figure 7.15 – Tow Force and Impeller Speed Results

7.4.2 Running Trim

The running trim of the model was not very sensitive to the presence of the jets or to the extent of their operation. Running trim was also unaffected by the presence of flow disturbing instrumentation such as the pitot tubes and tufts. As with the bare hull resistance tests, the running trim profiles were much more sensitive to changes in the position of the LCG and changes in model displacement. Figure 7.16 shows various running trim data for the B2 ballast condition from the self propulsion tests and from the bare hull resistance tests. The curves show that the model followed similar trim profiles regardless of the presence of instrumentation, inlet openings, or operating thrusters. Bare hull resistance tests could therefore be used to estimate the running trim profile of some vessel types. This profile can be used to estimate the vessel speed when the 'hump' in the resistance curve will occur. As discussed in Chapter 6, the peak in the running trim curve corresponds to the hump in the resistance curve and indicates the onset of planing.

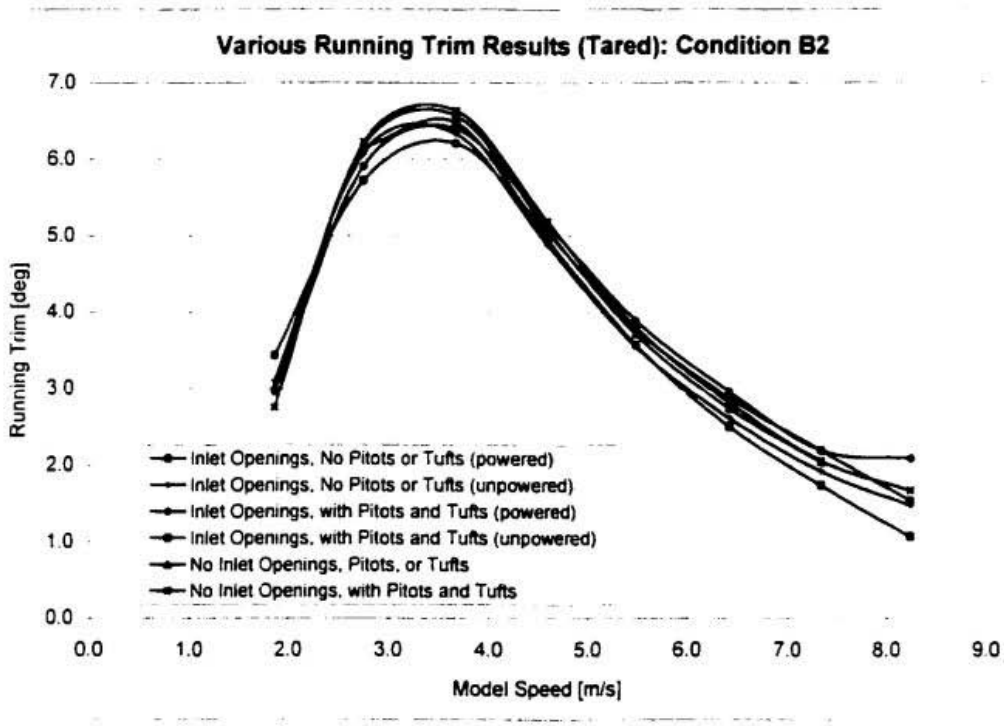

Figure 7.16 – Various Running Trim Results

7.4.3 Heave

Heave or sinkage is a measure of the change in the vertical position of the model's center of gravity when running at speed. Figure 7.17 shows various sinkage profiles for the B2 ballast condition from the self propulsion and the bare hull resistance tests. As with running trim, discussed in Section 7.4.2, the sinkage profile was not very sensitive to testing configurations. Sinkage, however, also similar to the running trim, was sensitive to changes in the ballast condition.

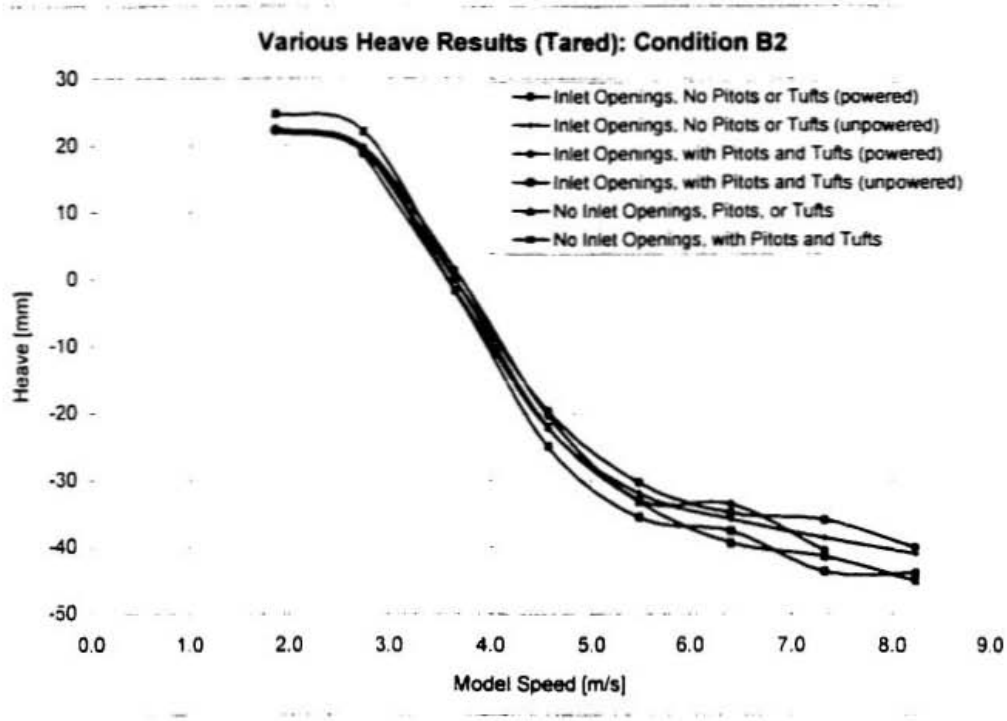

Figure 7.17 – Various Heave Results

7.4.4 Motor Current

The current level supplied to the motors was acquired by the data acquisition system from the digital power supplies used for most tests. The second powering configuration discussed in Section 7.2 involved using large batteries. It was not practical to include current and voltage meters with this arrangement so these channels were not acquired for these tests. This limited the accuracy of the self propulsion points for current since the regression lines lacked key data points.

Qualitatively, it is evident from Figure 7.18 which shows the current results for the B2 ballast condition, that the starboard motor was consistently drawing more current to operate than the port motor. This was due to a high degree of mechanical friction on this

shaft. Both shafts, considering their size, seemed to have exceptionally high mechanically losses, but the starboard shaft was particularly 'tight'.

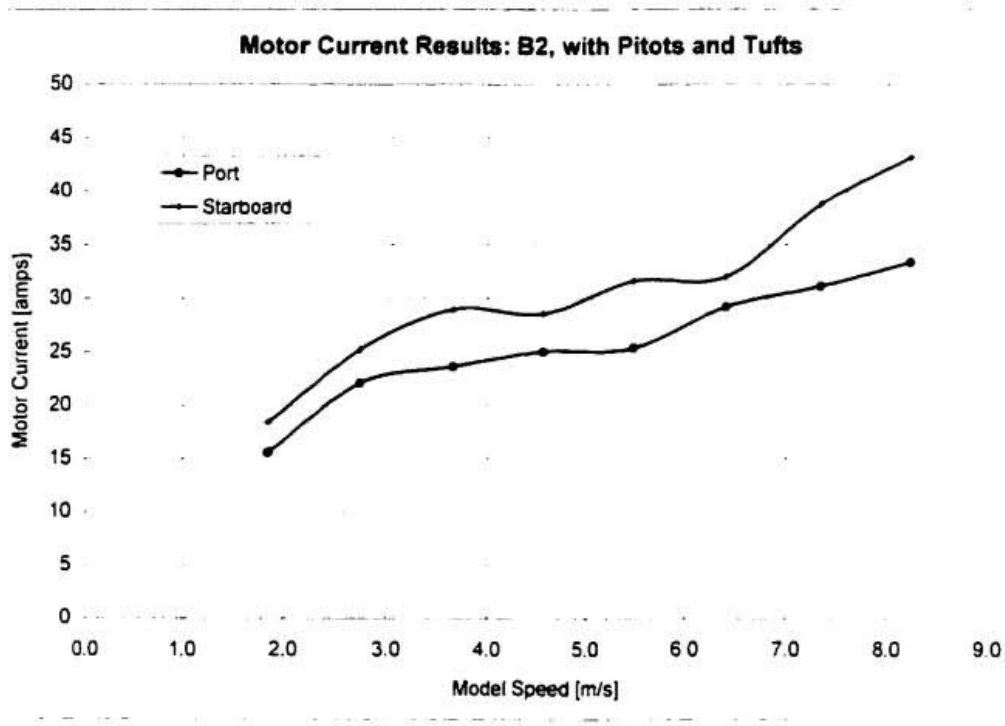

Figure 7.18 – Motor Current Results

7.4.5 Motor Torque

The torque produced by the motor was measured with custom reaction torque transducers discussed in Section 3.5. Figure 7.19 shows the measured torque profiles at the self propulsion points for the B2 ballast conditions with and without pitot tubes and tufts. The load cell for the starboard torque transducer failed part way through the testing program leaving many tests, such as the 'No Pitots and Tufts' series in the figure, without starboard torque data.

The motors were high speed and produced very little torque which made torque measurement a difficult task. The load cells needed to be sensitive and consequently produced noisy signals as the transducers responded to vibrations from the motors and the planing action of the model. Due to the spread found the torque data, it could not be used for calculations of power or efficiency.

The torque profiles did, qualitatively, match some previously made observations. The starboard motor produced higher torque than the port motor which agreed with the current measurements discussed in Section 7.4.4. Also, the starboard torque measured with pitot tubes and tufts was higher than those without. This corresponds to observations made in Section 7.4.1 concerning the added resistance due to the presence of pitot tubes and tufts in the testing configuration.

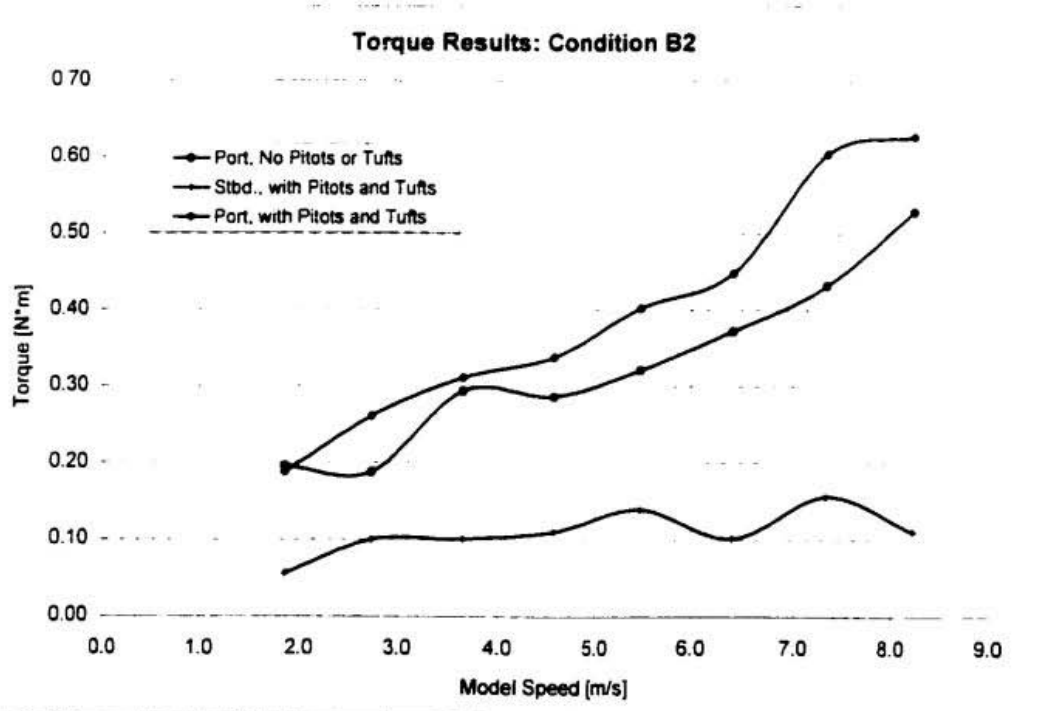

Figure 7.19 – Motor Torque Results

7.4.6 Inlet Pitot Tubes

The pitot tubes (see Section 3.1) located at the inlet, shown in Figures 6.2 and 6.7, were intended to measure the velocity distribution of flow just ahead of the inlet. This data would have been used in the calculation of the momentum intake flux discussed in Section 5.1 for the application of the momentum flux method. Figure 7.20 shows the fluid velocities measured by the three inlet pitot tubes for the B2 ballast condition for both the self propulsion tests and the bare hull resistance tests.

As can be seen in the figure, the results from each pitot tube from the bare hull resistance tests (labeled 'BH') and the unpowered self propulsion tests (labeled 'SP') are almost identical and closely correspond to the carriage speed. It was hoped for these tests that the pitot tubes would measure into the boundary layer at the hull, but this was not the case. They did, however, show consistent results measuring the free stream velocity of the flow. The inlet pitot tube measurements for the powered self propulsion tests were broadly scattered. It was expected that the flow during these tests would be accelerated above the free stream velocity due to the action of the jets and could be measured by the pitot tubes at their respective locations. The actual results were difficult to interpret and were not used in calculations.

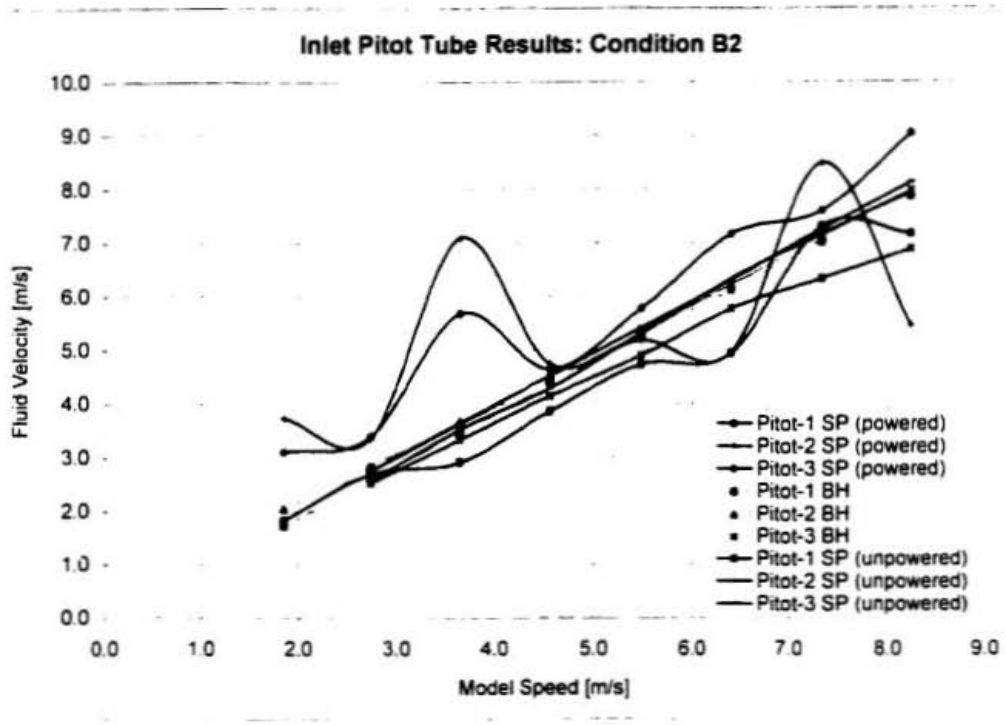

Figure 7.20 – Inlet Pitot Tube Results

7.4.7 Jet Pitot Tubes

The jet pitot tubes were located just aft of the port nozzle (see Figure 7.6). These pitot tube measurements were crucial for applying the momentum flux method since they were to provide data on the magnitudes and distribution of the velocities in the jet stream. The spread of the data, as shown in Figure 7.21, greatly hindered the accuracy of volume flow rate calculations, an important parameter in waterjet testing

However, as with several of the other results, certain observations can be made about the curves in general. Firstly, the lower pitot tube showed the highest overall velocities. The fluid travelling along the lower streamlines did not have as far to travel and did not need to be elevated like streamlines striking the upper pitot tube. The center pitot tube showed

the lowest overall velocities which was likely caused by its proximity to the stator hub which would have produced a wake affecting the measurement.

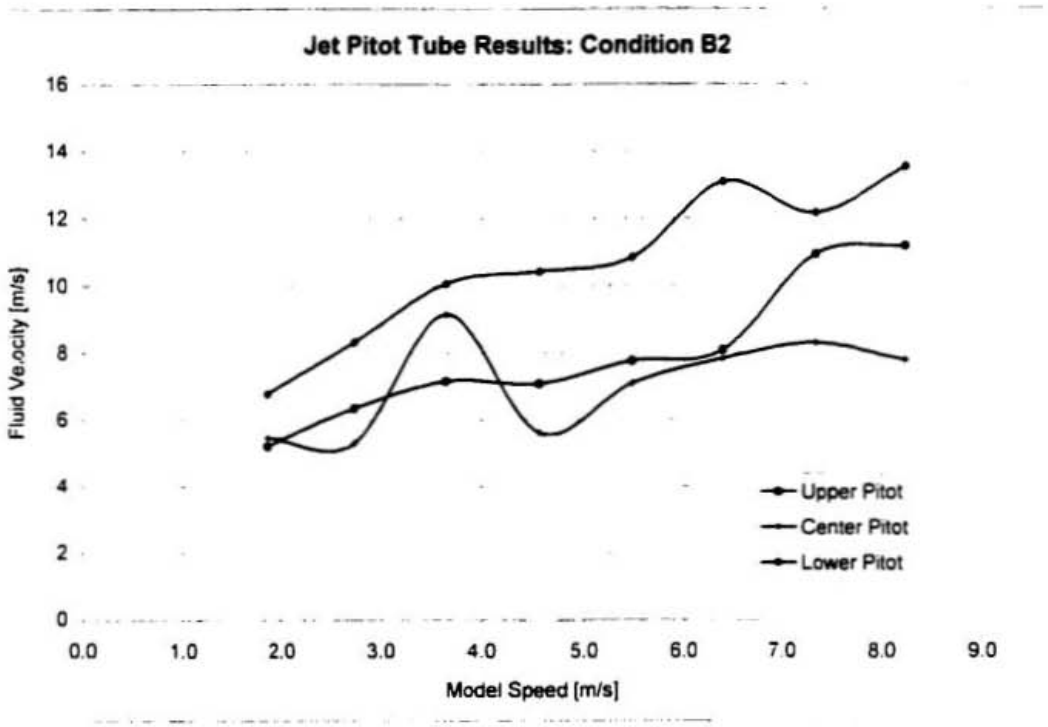

Figure 7.21 – Jet Pitot Tube Results

7.4.8 Mechanical Problems

During the course of the testing program, several mechanical problems were encountered which affected test set-up times and the accuracy of acquired data. Most of these problems were associated with the waterjet thrusters and motors. Among these were:

- Motors were under-powered
- Set screws in shaft couplings would often vibrate out of position disrupting torque transmission to impeller shaft
- Intermittent power interruptions to motors due to faulty electrical connections

- O-rings connecting the motor shaft with the tachometers were prone to breakage
- Impeller shafts leaked water that had to be removed between tests
- Poor connections between pitot tubes and pressure transducers resulted in air bubbles periodically forming in some tubes
- Calibration unit for pressure transducers exhibited leakage during calibration tests. Pitot tubes were not calibrated for flow velocities.

Many of these problems were addressed during the test program. Effort should be made in future to avoid these types of problems when performing similar tests.

7.4.9 Dynamic Instability

As mentioned in Section 7.9.1, tests of this model at certain ballast conditions and speeds resulted in the dynamic instability known as porpoising (see Appendix C). The model was more disposed to porpoising during the self-propulsion tests than during the bare hull resistance tests. This could be attributed to the different model inertias involved in these tests and/or the influence of the model thrusters.

7.5 Analysis of Results

Several problems were encountered during the course of this phase of testing, some of which directly influenced the test data. As a portion of the test data was consequently unusable, much of the desired analysis could not be performed. Therefore, the momentum flux method, discussed in Chapter 5, was not applied to these tests.

A notable observation was made during the analysis of the underwater video. Tests which employed the flow visualization tufts around the starboard inlet showed that there was

flow moving from the transom to the aft of the inlet. Figure 7.22 is an image from the underwater video of a self propulsion test (ballast condition A2, model speed 7.35 m/s, battery power to thrusters). The figure shows the aft tufts being drawn forward into the inlet. This contradicts the assumption made for these tests; that the inlet flow was ingested entirely from oncoming streamlines into the inlet. Similar flow patterns were seen for nearly all of the tests using the thrusters regardless of model or impeller speed. The flow reversal shown here presents difficulties for measurement and analysis of the intake momentum flux.

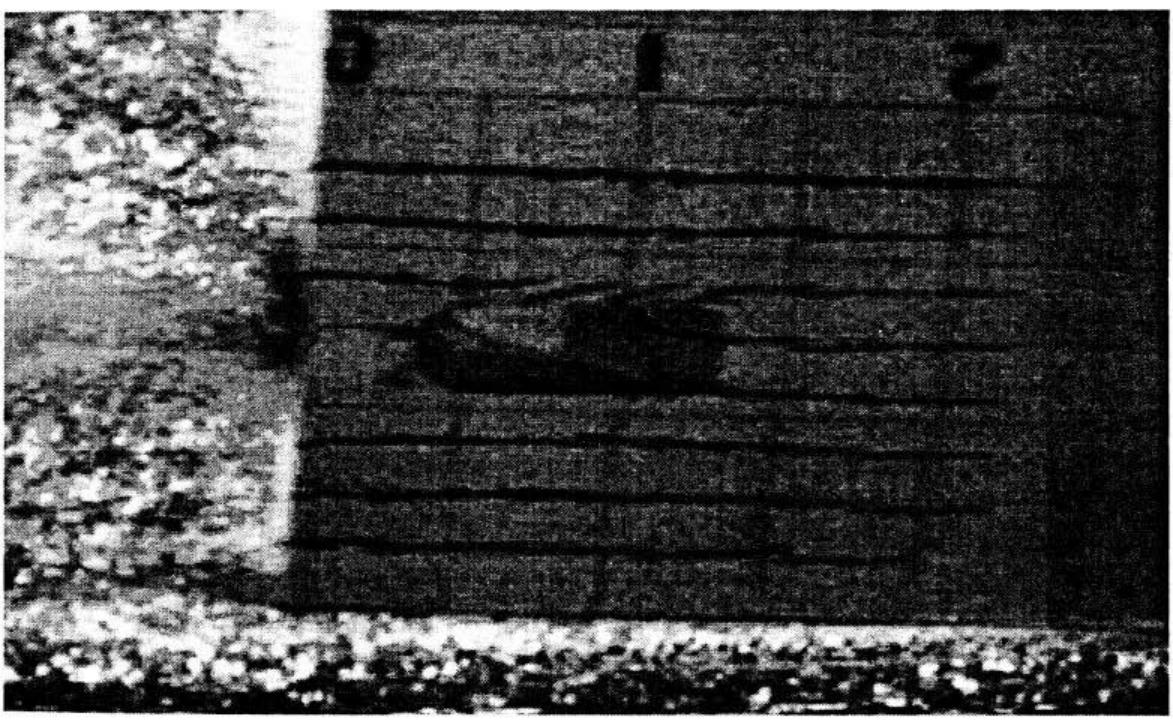

Figure 7.22 – Underwater Video of Inlet

7.6 Recommendations

This test phase provided much experience and knowledge in the practical aspects of these types of experiments which can be used in future endeavors. Certain general recommendations can be made:

- Toy waterjets cannot be used for experimental purposes. Effort should be put into designing and fabricating precision stock waterjets for use in experiments which incorporate instrumentation for measurements.
- The size of the model and propulsors made many measurements difficult and consequently gave poor results. Scale factors leading to larger model sizes should be employed.
- Motors used for waterjets should be chosen to have the requisite power with controllers able to accurately maintain a given shaft speed.
- Alternative methods for torque measurement should be investigated.
- Alternative flow measurement techniques should also be investigated. Pitot tubes could still be used, but more calibration and testing would be needed.
- Flow rate measurement of the jet is crucial. Methods for direct flow measurement or sufficiently calibrated indirect measurements should be developed.

CHAPTER 8
WATERJET TEST PLATFORM

8 WATERJET TEST PLATFORM

The next stage in the development of waterjet testing capabilities at IMD was the development of a waterjet test platform. Using experience gained during the self propulsion tests described in Chapter 7, and based on models from other research facilities (Dyne and Lindell, 1994), it was decided that a stationary platform capable of determining performance characteristics of an instrumented model waterjet unit should be developed. The model propulsor could then be used in self propulsion tests using the platform data to calculate items such as jet flow rate when running at speed.

Ideally, the platform should incorporate an inflow to the waterjet that would simulate the flow the inlet would experience when operating in a moving vessel. Testing in the bollard pull condition, though not ideal, does simplify the early stages of the development of the platform. The waterjet model discussed here was designed so that it could, in future, be

mounted to either the tow tank carriage or the cavitation tunnel in order to perform experiments incorporating a free stream velocity.

The platform was designed and built for a small trim tank at IMD. The trim tank is 7.3 m long, 2.4 m wide and 1 m deep. It has its own water filtration system and overhead crane. The platform housed a scaled waterjet propulsor of a size that would make measurements feasible but not so large that it could not be used in a towed model vessel. The waterjet model was designed to be modular, facilitating fabrication and allowing easy variation of components. As there was no pre-existing platform which could have been modified to accommodate a waterjet, the model thruster, platform, and supporting components were all designed and built specifically for this project.

8.1 Instrumentation

Flow measurements are both the most important and most difficult to make for these types of tests. Two types of flow measurement techniques were employed in the test platform. Firstly, jet flow rate was determined by direct measurement of the weight of discharged water collected over a timed interval. Flow velocities at various locations were then calculated from pressure measurements made just before the impeller, and at two positions in the nozzle. Attempts were also made to use the laser Doppler velocimeter (LDV) discussed in Section 3.9, to measure velocity profiles of the flow entering the inlet, across the nozzle, and in the vena contracta. Other measurements made in the test platform, such as thrust, shaft speed and torque are listed in Table 8.1.

Measurement	Units	Instrument
Thrust	N	50 lb. load cell in line with thruster
Shaft Speed	rev./sec	Taken from motor controller. Verified with laser tachometer
Shaft Torque	N·m	Custom-made reaction torque transducer
Motor Current	Amps	Taken from motor controller
Fluid pressure just before impeller	Pa	Four pressure transducers arranged concentrically around a station just before impeller and flush with internal surface
Fluid pressure at beginning of nozzle section	Pa	Four pressure transducers arranged concentrically around a station at the beginning of the nozzle and flush with internal surface
Fluid pressure at end of nozzle section	Pa	Four pressure transducers arranged concentrically around a station at the end of the nozzle and flush with internal surface
Ambient Atmospheric Pressure	Pa	Digital barometer
Water and air temperature	°C	Digital thermometer
Water collection time	sec	Inclinometer gauges position of test frame showing beginning and end of collection period
Collected water weight	kg	Collection tank weighed with 2000 lb. load cell from overhead crane
Fluid velocity mapping at inlet	m/s	LDV indexed through a fixed volume near inlet
Fluid velocity mapping in nozzle	m/s	LDV directed through a window in the nozzle and indexed across the internal diameter
Fluid velocity mapping in jet stream	m/s	LDV indexed across the diameter of the jet stream at the vena-contracta
Possible inception of cavitation	-	Visual inspection of impeller region with aid of strobe light

Table 8.1 – Test Platform Instrumentation

8.2 Sea-Doo™ Waterjet

It was decided to use the propulsor from a Sea-Doo™ (Explorer '94) personal watercraft as the model tested in the platform, largely because of the interest Bombardier Inc. expressed in the project. Personal watercraft (see Figure 8.1) are generally small, one or two person vessels, which operate at very high speeds with excellent maneuverability powered by a single waterjet with a gasoline engine. Bombardier Inc. agreed to provide the necessary geometry for fabrication of the model, as well as information on shaft speeds and powering used in their watercraft.

Figure 8.1 – Sea-Doo™ Watercraft

8.2.1 Scale Considerations

The model thruster was designed to a scale of 1:1.82, resulting in an impeller diameter of 3 inches. The choice of scale was a balance between the ability to install instrumentation, powering and weight considerations of available electric motors, and limitations imposed by the towing carriage. As mentioned, the platform was intended for testing a range of waterjets which could conceivably be used in self propulsion tests in the towing tank and

not just for this specific test set up. Certain compromises therefore had to be made with respect to the Sea-Doo™ model. Personal watercraft tend to be very highly powered relative to their size, much more so than a waterjet propelled yacht or high speed ferry. This fact, coupled with the relatively small physical size of personal watercraft, meant that a model sized for the towing carriage and for the power available at model scale would be too small to instrument. This arrangement would also restrict the testing range of the platform to only this type of vessel. The scale of the model was therefore increased to a size where it could be instrumented and where the platform could be used to test waterjets from other vessel types. This also meant that the testing range of the Sea-Doo™ model was limited. A reasonably sized electric motor could only provide enough power to span a portion of the model's operating range and tests involving the tow carriage would also be limited due to speed restrictions.

An illustration of the differences in the requirements of models of different vessels can be seen in Table 8.2. The Sea-Doo™ waterjet used in the platform and a waterjet used in a typical high speed ferry were scaled to the same physical model size with a given electric motor. The resulting power, shaft and vessel speeds, required and available at model scale are shown. Mechanical losses and other factors are not accounted for in this simplified example, but it does demonstrate that larger vessels with correspondingly larger scale factors, require considerably less power than the Sea-Doo™ model.

Vessel	Full Scale	Required at Model Scale	Available at Model Scale
Sea-Doo™ Watercraft	65 kW 7000 RPM 60 knots	8.0 kW 9500 RPM 23 m/s	3.36 kW 7000 RPM 8.5 m/s
High Speed Ferry	790 kW 2100 RPM 35 knots	0.25 kW 6640 RPM 5.7 m/s	3.36 kW 7000 RPM 8.5 m/s

Table 8.2 – Requirements at Scale

8.3 Model Waterjet Design

After the scale and motor were chosen for the given geometry, the next step in the design was to break up the thruster into components. A modular design provided the most flexibility in the test apparatus with regards to future work. It was also convenient with regards to fabrication and instrumentation. The model waterjet was separated into the following units as shown in Figure 8.2:

1. Bottom Plate
2. Grill
3. Inlet Section
4. Shafting & Seals
5. Impeller Housing
6. Impeller
7. Stator Section
8. End Plate
9. Stator Cone
10. Nozzle
11. Motor and Shafting Arrangement

A right hand rule coordinate system was used in the platform. The positive x-axis was oriented parallel to the impeller shaft and in the direction of flow. The positive z-axis pointed upward while the y-axis was oriented according to the right hand rule.

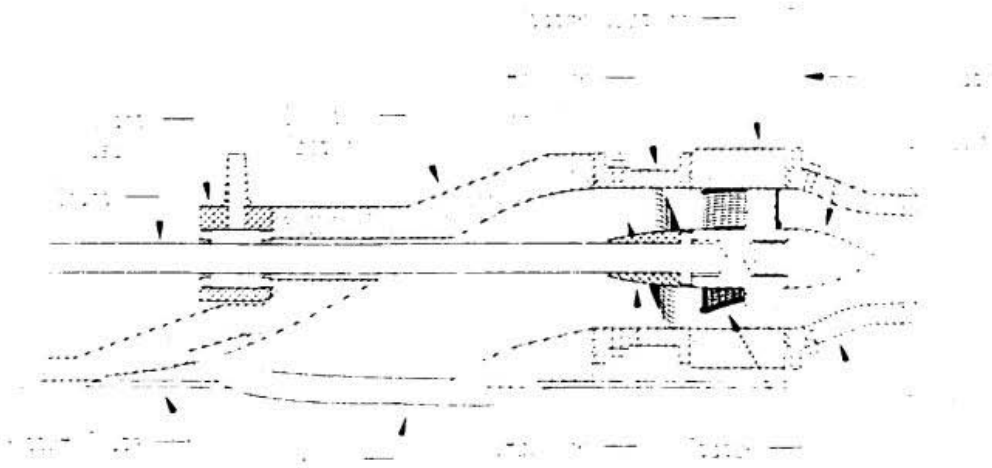

Figure 8.2 – Cross Section of Model Waterjet

8.3.1 Bottom Plate

Waterjets are usually fully integrated into the hulls of the vessels they power. This poses some difficulty when attempting to separate them as independent units. On the test platform the bottom plate acted as a replacement for the hull bottom. For this trial design, the bottom plate was flat and did not incorporate the geometry of the bottom of the Sea-Doo™.

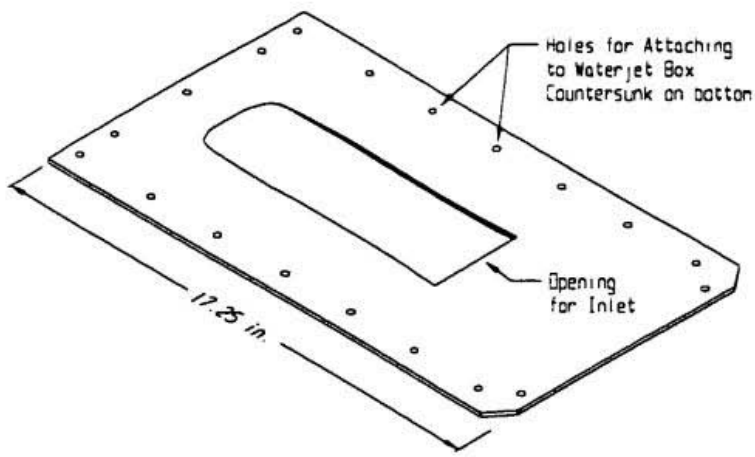

Figure 8.3 – Bottom Plate

8.3.2 Grill

The grill located at the bottom of the inlet is intended on the full scale craft to prevent foreign objects from entering the thruster and causing damage to the internal components. It is included in the model in order to match flow characteristics. Since the full scale grill is integrated with the hull as well as the inlet, the model grill was modified slightly to meet flush with the current flat bottom plate. Although small craft generally use grills, many larger applications of waterjet propulsors do not.

The grill was fabricated with the Stratasys FDM 1650 rapid prototyping machine at the Faculty of Engineering and Applied Science at Memorial University. The method involved constructing a 3-D computer model which was then 'sliced' by the prototyping software. The model was then built level by level by a small tube which extruded molten ABS plastic. Surface finishing and final fitting was done at IMD.

8.3.3 Inlet Section

The inlet section consisted of the transition in ducting from the opening in the bottom plate to just before the impeller where the interior of unit became circular in cross section. In the full scale craft, most of the inlet as defined here is fabricated as part of the hull. The model grill, though removable, was fully integrated into the design of the inlet since they must meet to form a smooth transition for the incoming flow. The inlet section was also made in the rapid prototyping machine out of ABS plastic, but had to be made in two parts because of its size. Figure 8.4 shows the assembly of the inlet, grill and bottom plate. The division line shown was the intersection of the two parts of the inlet which

were permanently fastened together. Surface finishing and machining of bolt holes and the shaft clearance hole was done at IMD.

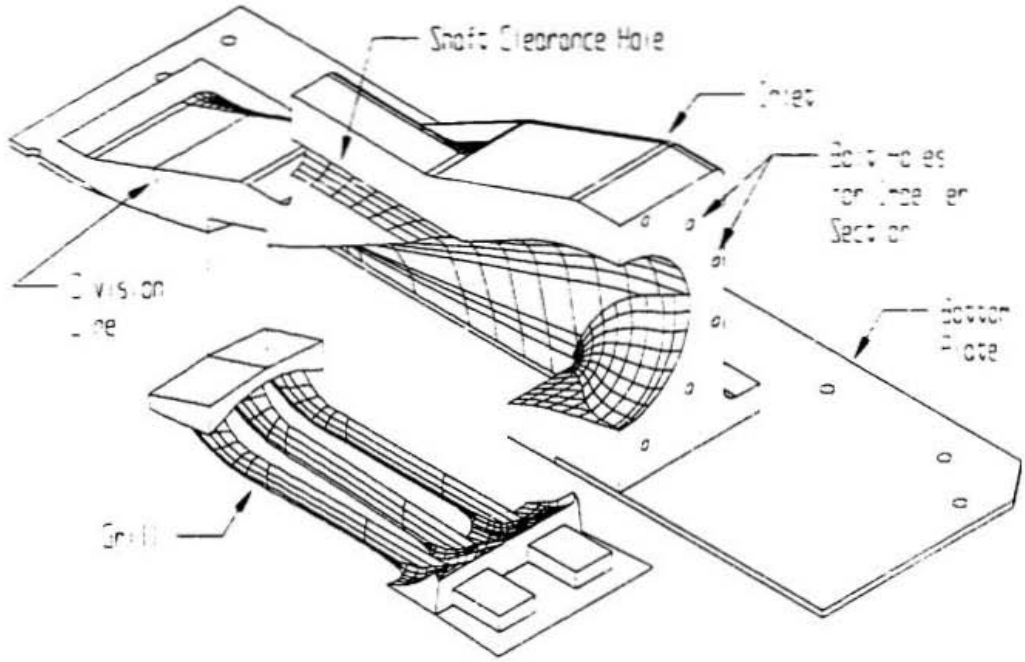

Figure 8.4 – Inlet and Grill

8.3.4 Impeller Housing

The impeller housing, shown in Figure 8.5, was a short cylindrical section of the waterjet ducting in which the impeller was located. This section was made optically clear so that visual inspection of the impeller could be made during testing. Four pressure transducers were placed at the forward end in order to measure the pressure just ahead of the impeller (Station 3 shown in Figure 5.1). The section was symmetrical and can be reversed in the set-up so that the pressure transducers read the pressure around the impeller itself. The impeller housing was machined at IMD out of a solid 4 inch diameter acrylic rod.

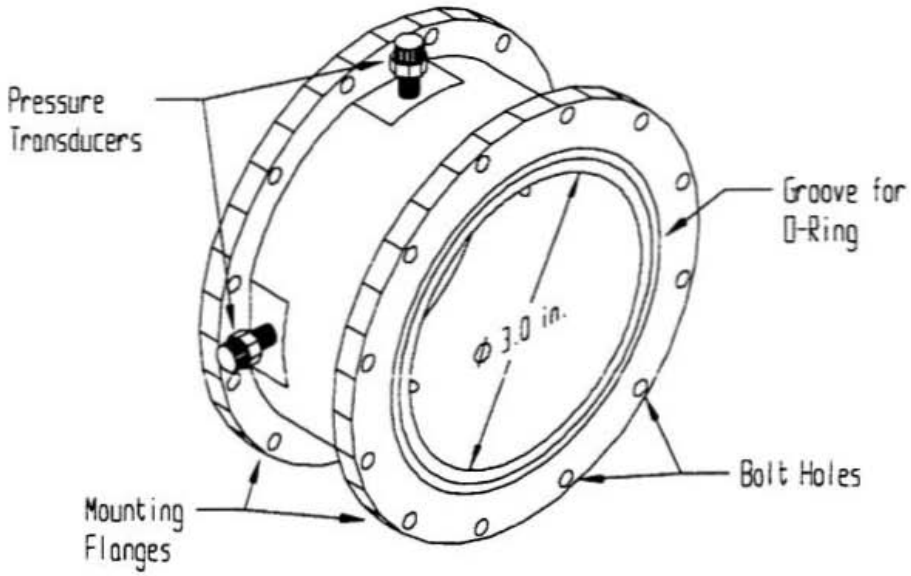

Figure 8.5 – Impeller Section

8.3.5 Impeller

The impeller is a important element in a waterjet thruster. Small changes in the impeller design can lead to significant changes in jet performance. The test platform could be used to make comparative studies of different impeller designs, provided model impellers of different designs are available. The Sea-Doo™ impeller consisted of three overlapping blades of constant pitch on a tapered hub. The shafting arrangement was different from full scale and was designed specifically for this model. The model impeller fitted to the shaft by sliding on from the shaft's fore-most end. A small flange was machined at the aft end of the shaft to fit into a recess in the aft of the impeller hub. Six screws and two positioning pins (not shown in figure) held the impeller in place. Just aft of this flange, the remaining end of the shaft was machined to a smaller diameter designed to rest in a needle bearing located in the stator hub (see Section 8.3.6). The impeller and shaft can be seen in Figure 8.6.

Fabrication of model impellers or propellers is usually an expensive process because the tolerances required for hydrodynamic testing are tight, often requiring the use of a multi-axis CNC milling machine to cut the model out of a solid piece of parent material. The model impeller used in the platform was fabricated using a considerably less expensive technique. A computer model was first created and a wax model was built with the rapid prototyping machine at MUN. The wax model was then sent to Skat-Trak Performance Products Inc., a company specializing in manufacturing full scale impellers for personal watercraft. They were able to cast a stainless steel impeller from the wax model as well as perform the surface finishing and additional machining of the hub interior. Future attempts could be used to further refine this method.

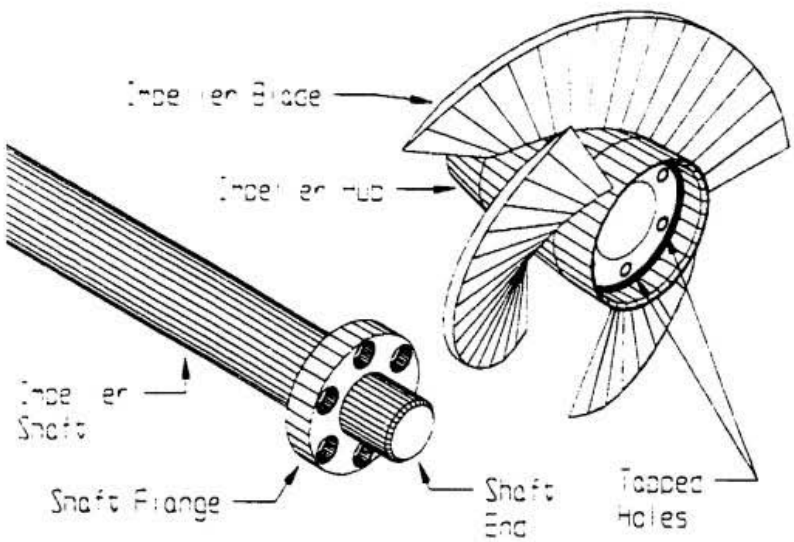

Figure 8.6 – Impeller and Shaft

8.3.6 Stator Section

The stator in a waterjet thruster is a set of fixed blades or vanes designed to 'straighten' the flow coming from the impeller. The impeller imparts a rotational energy to the flow. The stator transfers some of this energy into axial flow which is the only component producing the waterjet's thrust. The stator section is made up of the stator hub, blades, and outer cylinder or housing. In the full scale thruster, the entire section was cast as a single unit. The model stator however, was broken into three components. The stator housing consisted of two parts: top and bottom blocks which bolted together to form a circular internal section the length of the stator. The stator blades and hub were the third piece which fitted between the stator blocks. The outside edges of the stator blades were machined to exactly match the internal surface of the stator blocks so that when they were secured together, the unit became rigid with visually imperceptible seams between components. The forward end of the stator hub contained a needle bearing for the impeller shaft. The aft end contained a threaded hole for the tail cone which was used to provide a smooth transition at the end of the stator hub. The stator section components, as well as the tail cone were all CNC machined from aluminum.

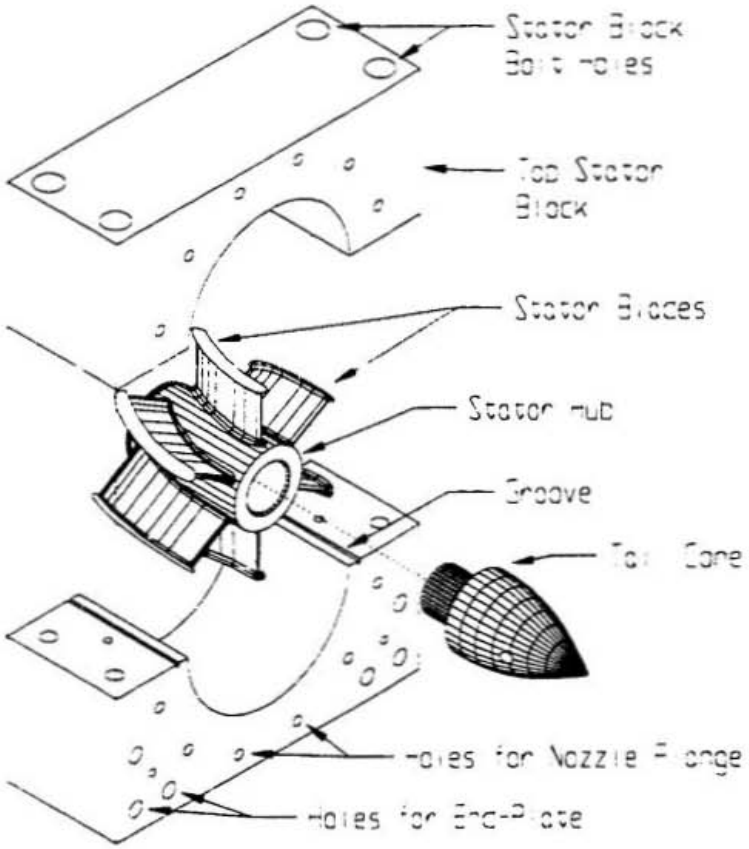

Figure 8.7 – Stator Section

8.3.7 End Plate

The end plate of the model represented the transom of the vessel. Often the transom of full scale craft is angled to provide a more favourable thrust angle for operation. For model tests, the jet was made horizontal to facilitate measurements. The end plate shown in Figure 8.8 was a removable component of the model set-up since changes of jet components may require different plate dimensions. The end plate connected directly to the structure of the housing for the model thruster (waterjet thruster box), discussed in Section 8.4.1. The bottom stator block bolted to the inside of the end plate and provided alignment for the shaft which rested in the bearing located in the stator hub.

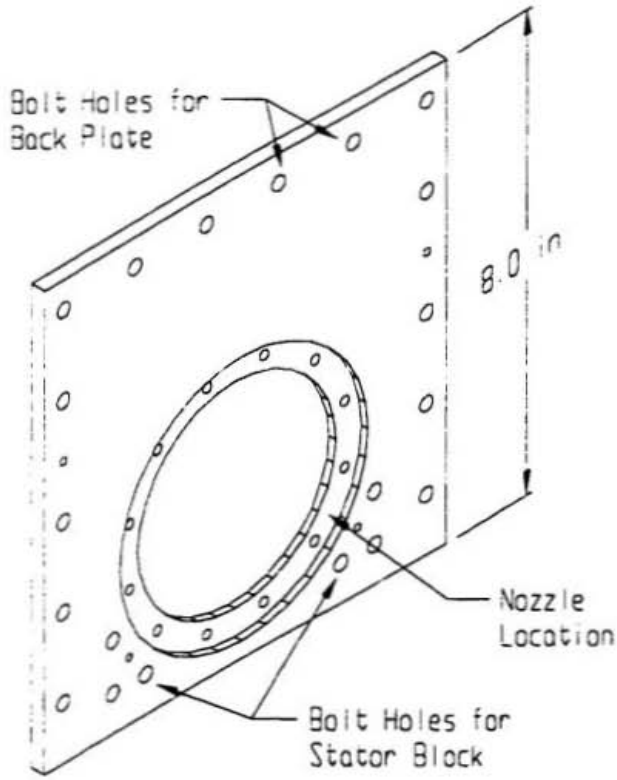

Figure 8.8 – End Plate

8.3.8 Nozzle

The nozzle shown in Figure 8.9 is also a key component of the waterjet design since it controls the conversion of pressure energy to kinetic energy of the flow as well as providing a higher pressure at the impeller which can help delay the inception of cavitation. It was designed to smoothly decrease the cross-sectional area of the flow giving a proportional rise in flow velocity. Four pressure transducers were placed around two locations in the nozzle. A small acrylic window was included in the side of the nozzle near the exit. The intention was to use the LDV (see Section 3.9) through this window to make velocity measurements across the diameter of the nozzle.

The model nozzle was machined on a CNC lathe from aluminum. On full scale craft the nozzle is often used to provide steering control either by redirection of the nozzle itself or in conjunction with a steerable secondary nozzle. Reversing can also be done at the nozzle with the use of a 'bucket' that diverts the jet forward, providing reverse thrust. This test program did not focus on vessel maneuverability or jet steering control so these features were not modeled.

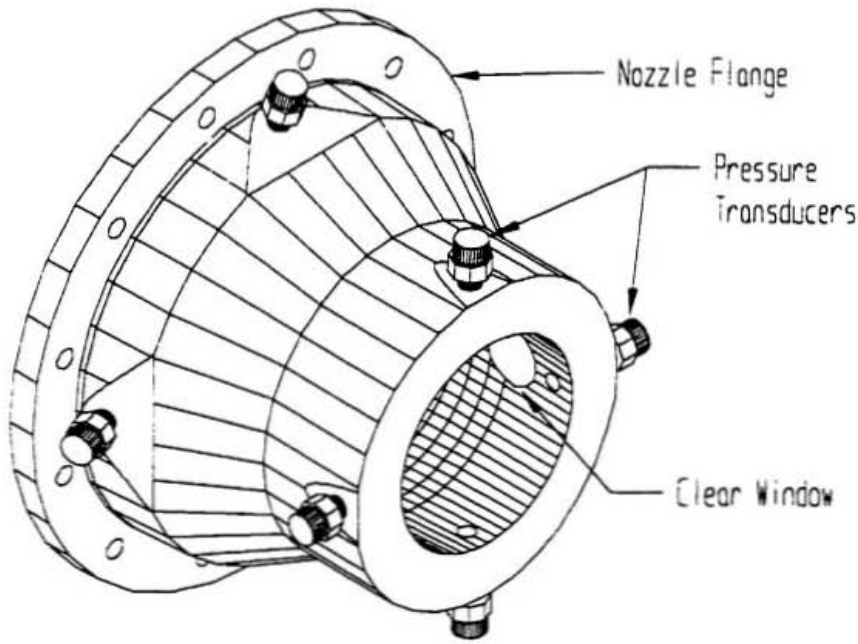

Figure 8.9 – Nozzle

8.3.9 Motor and Shafting Arrangement

The arrangement of the entire model thruster can be seen in Figure 8.11. The power for the waterjet was provided by a brushless 3.36 kilowatt electric motor mounted to custom-made reaction torque transducer (discussed in Section 3.5) secured to the structure of the waterjet thruster box. The motor shaft was connected to the impeller shaft with a zero backlash bellows coupling. The impeller shaft rested in a needle bearing at its aft end and

a self aligning bearing near the coupling. No thrust bearing was used; the forces from the impeller shaft were absorbed in the motor and torque transducer. As the shaft entered the inlet section it passed through a pressurized seal, shown in Figure 8.10. Two seals were placed back to back across a small cavity which was pressurized with water. At high shaft speeds, standard seals can often leak due to vibrations. The pressurized cavity produced stronger contact between the seals and the shaft, and acted as a barrier to prevent air ingestion. Air in the system causes performance to deteriorate and can affect pressure measurements. The shaft diameter of the model was slightly larger than dictated by the scale factor in order to meet the required strength for the system.

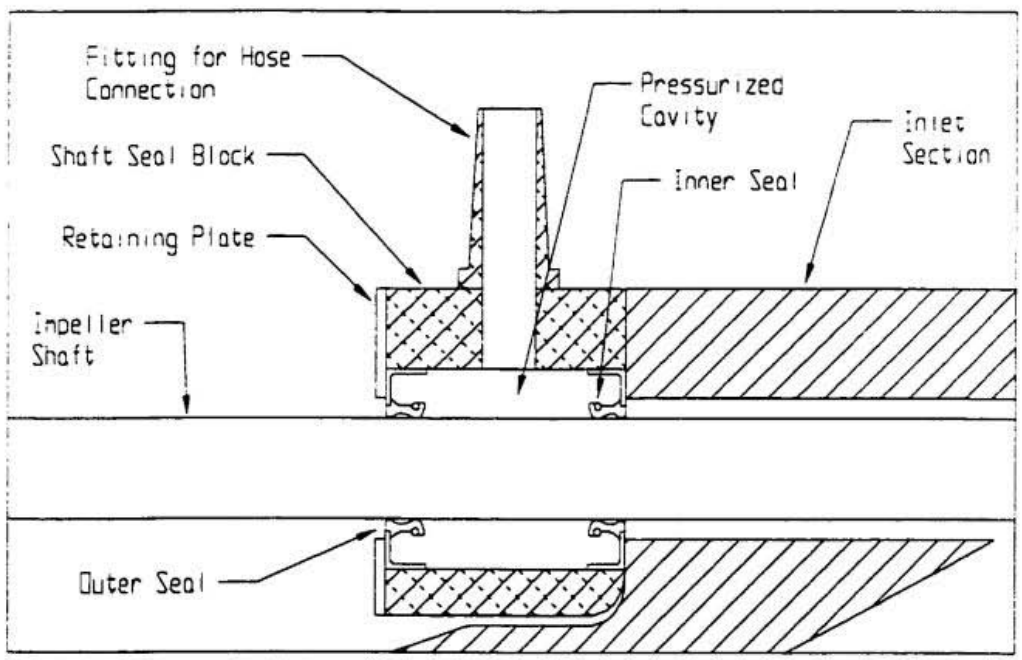

Figure 8.10 – Shaft Seal

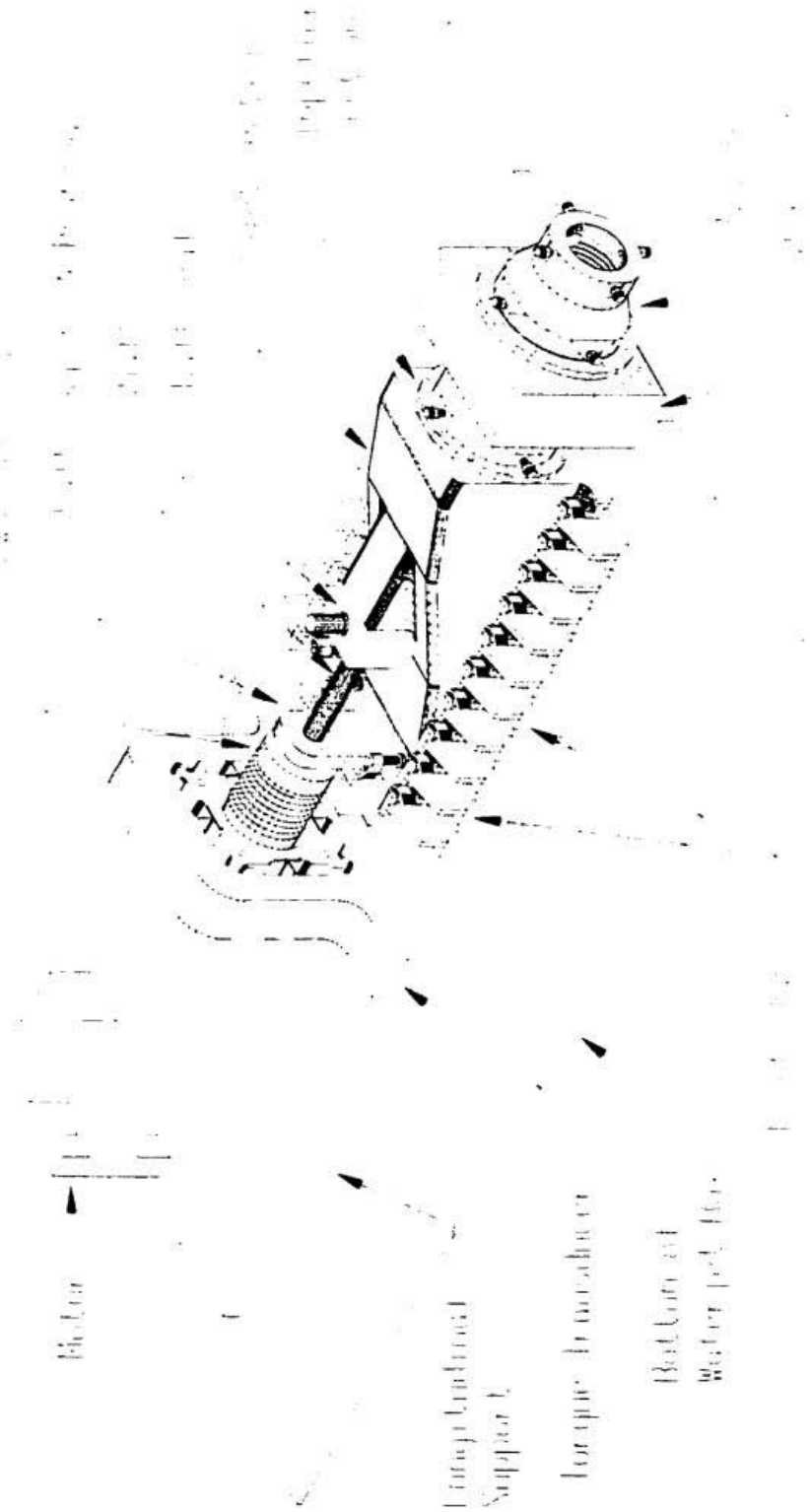

Figure 8.11 – Model Waterjet Arrangement

8.4 Test Platform Design

The test platform consisted of the structure and components needed to perform the experiments with the model thruster. These include:

- Waterjet thruster box
- Pivot frame
- Support frame and LDV Indexer
- Water collection tank

8.4.1 Waterjet Thruster Box

The waterjet thruster box was a watertight enclosure for the model. It had a clear plastic cover fitted with openings for wiring and access to the model. A small ventilation fan was also fitted to provide cooling for the motor. The waterjet box consisted of a frame made from aluminum box tubing fitted with an aluminum metal skin. Two longitudinal supports which ran the length of the bottom of the box were used for attachment of the model thruster components such as the many inlet clamps and the torque transducer. Brackets fitted to the outside of the box provided attachment points for the load cell and flexible linkages (or flexures) which were used in conjunction with the pivot frame to measure system thrust. Connection points in the waterjet box (or thruster box) for the torque transducer, end plate, flexures, etc. were all carefully machined after the unit was fabricated to ensure proper alignment of all components. Figure 8.12 shows the jet system installed in the waterjet box.

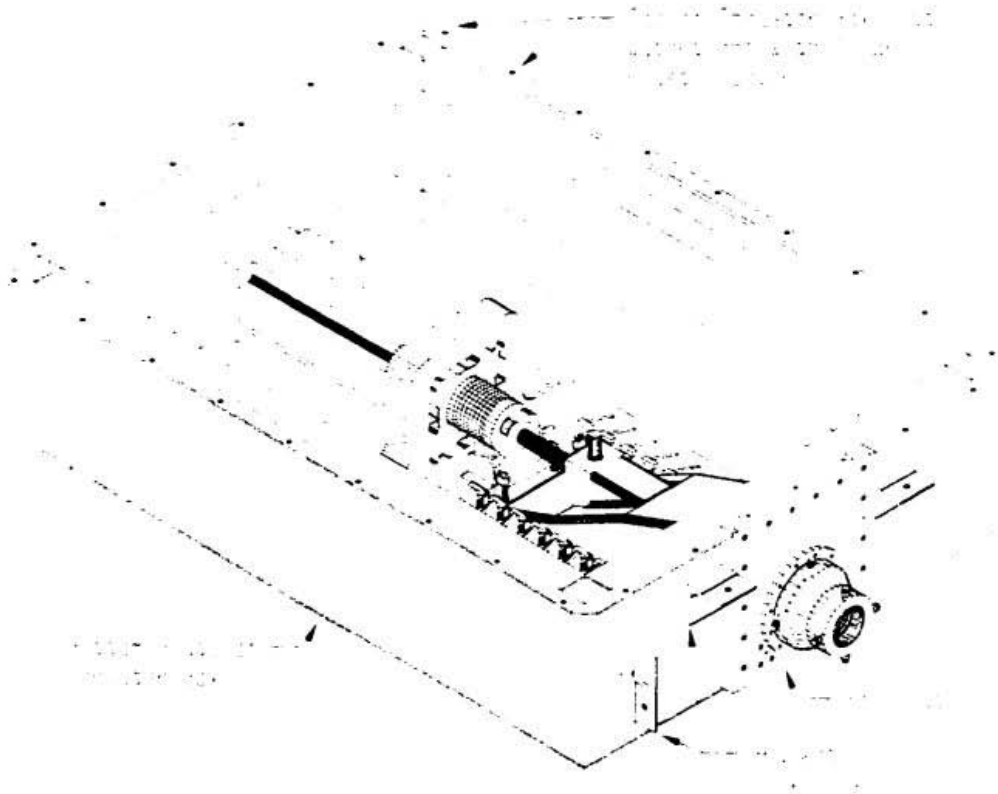

Figure 8.12 – Waterjet Thruster Box

There were six connection points on the exterior of the waterjet box for flexures. Flexures are rods which have sections with a very small diameter. This shape allows a flexure to be flexible for small deflection bending while at the same time being rigid along its axis. Figure 8.13 shows the type of flexure used with the thruster box. The flexure arrangement shown in Figure 8.14 was designed to rigidly connect the waterjet box with the pivot frame while allowing measurement of the unit's net thrust. Three flexures suspended the thruster box vertically while two flexures provided lateral support on the port side. The orientation of these flexures provided rigid support in all but the direction of thrust in which they were inclined to bend. The sixth flexure was located at the front of the waterjet box in line with the impeller shaft and the center of the nozzle. It transmitted the

thrust to a load cell attached to the pivot frame. Since the force measurements by the load cell only required very small deflections, the entire system, connected and aligned properly, was strong and rigid.

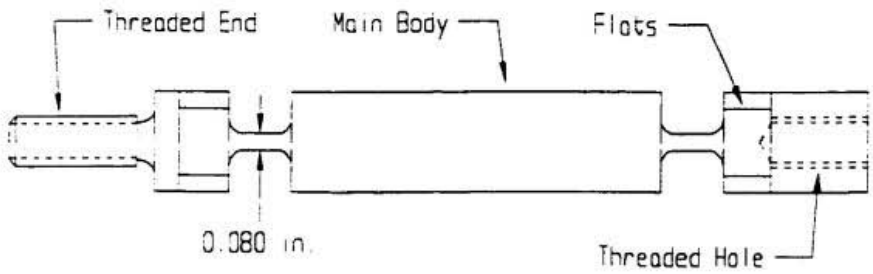

Figure 8.13 – Typical Flexure

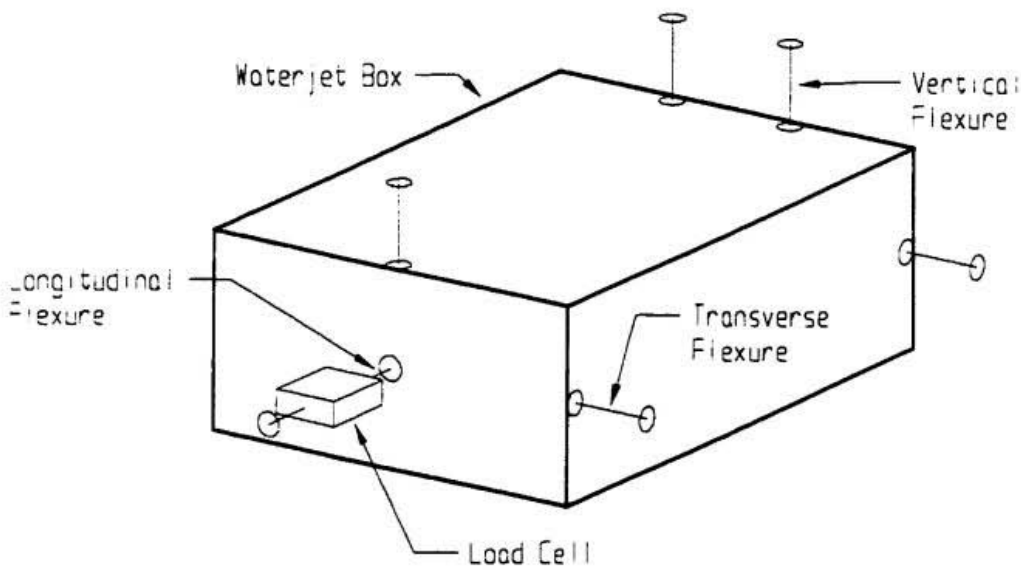

Figure 8.14 – Flexure Arrangement

The load cell used was a 50 lb. (200 N) S-shaped force transducer (discussed in Section 3.4) which was calibrated in position with the thruster box and pivot frame. Two eye bolts were attached to the thruster box an equal distance on each side and in plane with the load cell. Wires from the eye bolts ran together to a single wire which passed over a

pulley to a weight tray. The pulley location was adjusted until the wires were level and aligned with the load cell. Calibration was performed by adding a series of known weights to the to tray simulate model thrust. This in-situ method of calibration ensured greater accuracy for thrust measurement but accounting for system induced bias.

8.4.2 Pivot Frame

The pivot frame not only provided the supporting structure for the thruster box and flexures, but also enabled the thruster to be primed prior to testing. A side view of the pivot frame and waterjet box can be seen in Figure 8.15. For the thruster to act as a waterjet, the flow must be ejected from the nozzle above the water's surface. This means that when operating, the majority of the thruster must be above the waterline. However, the impeller cannot establish the flow unless it is at least partially submerged at start up. At full scale when the craft is at rest, the nozzle and impeller are submerged. As the impeller speed increases, it first acts as a ducted propeller with a fully or partially submerged flow. The vessel then gains speed, increasing the wake at the transom and providing a trough in which the nozzle can eject water into the air as a waterjet. Since the test platform was testing at the bollard condition, a different approach was needed for establishing flow at start up (priming). The pivot frame was used for this purpose by providing a means of manually submerging the impeller and nozzle until the flow was established, and then returning the nozzle above the water's surface as a full waterjet.

The shape of the pivot frame was designed primarily to accommodate the flexures attaching it to the waterjet box. The pivot frame was fabricated from structural aluminum with connection points machined for alignment. Two pillow block bearings were located

at the front end of the frame in which rested a shaft which acted as the pivot axis for the frame. Mechanical stops were used to keep the frame from being over rotated. One stop prevented the frame from rotating above its horizontal position while another prevented it from lowering more than 10 degrees. Figure 8.15 shows the pivot frame and thruster box in their horizontal and priming positions.

A rendered view of the pivot frame can be seen in Figure 8.17. A handle located at the aft pivot frame was used to manually raise and lower it. This was aided by a counterweight system not shown in the figure. A wire attached to the handle traveled by pulleys over the support frame to a weight tray suspended at the side of the trim tank. The weight was set to keep the pivot frame in its horizontal position when at rest. The unit was primed by lifting the weight tray, which lowered the pivot frame to its down position. Safety bolts on each side of the handle could lock the pivot frame in the horizontal position by sliding into matching holes in the support frame. An inclinometer attached to the pivot frame was used to determine the position of the frame when analyzing data.

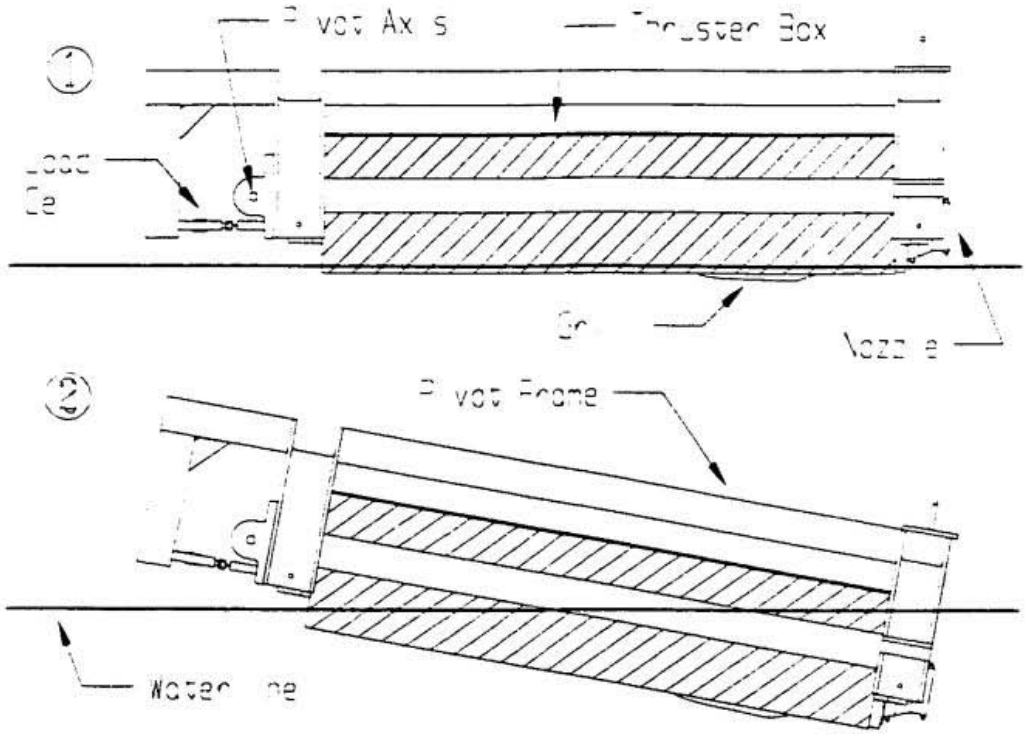

Figure 8.15 - Priming Position

Figure 8.16 shows the locks used to support the thruster box during maintenance of the thruster unit. These locks protected the flexures from adverse loads. such as those that might occur when thruster components were being repaired or replaced. Two locks on each side of the thruster box consisted of a threaded rod with a tapered end which traveled through blocks attached to the support frame to a hole in the side of the thruster box. The rod was moved in until the tapered end fitted tightly in the undersized hole in the thruster box.

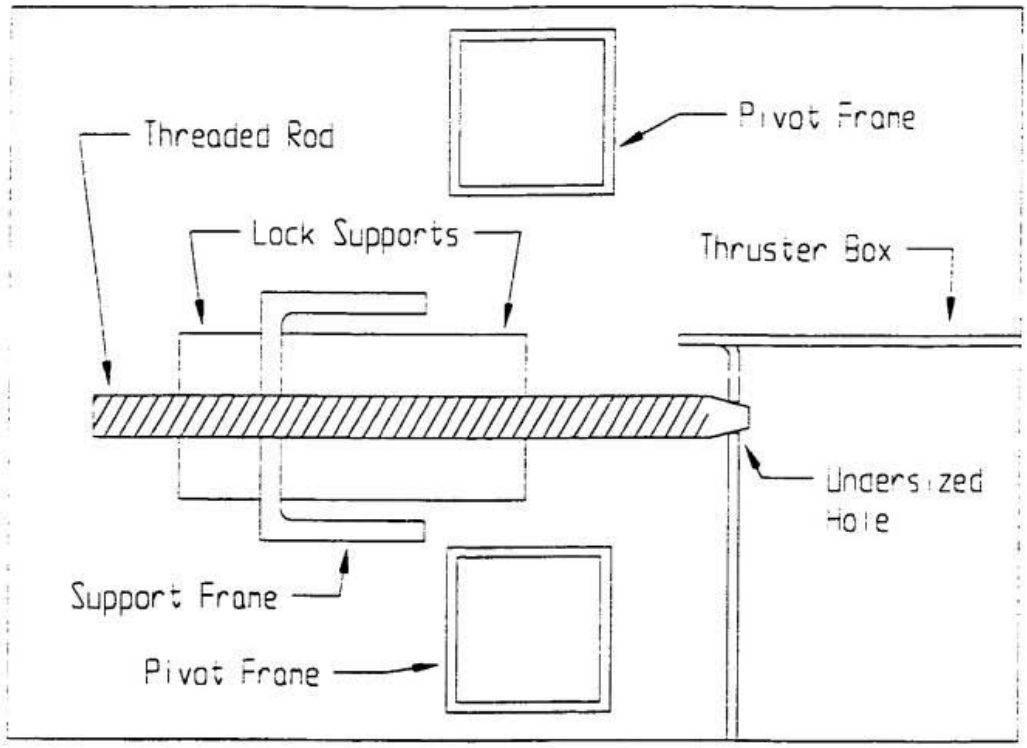

Figure 8.16 – Support Locks

Figure 8.17 – Pivot Frame

8.4.3 Support Frame and LDV Indexer

The support frame, shown in Figure 8.19, was made from structural aluminum and spanned the width of the trim tank. It supported the pivot frame and waterjet box, the LDV indexer, and had connections for the water collection tank used in the flow measurement tests discussed in Section 8.5.2. The pivot frame was supported by bearings for the pivot shaft at its forward end and by a counterweight system not shown in the figure at its aft end. The safety bolts locking the pivot frame in its horizontal position and the support locks for the waterjet box all used the support frame for connection points.

Mounted to the starboard side of the support frame, the LDV indexer (see Section 3.9) controlled the position of the LDV probe which was attached to the end of an extension arm. Attempts were made to make flow velocity measurements with the probe in three areas: under the inlet, in the nozzle, and in the free jet stream. Measurements under the inlet required that the probe be tilted at a slight angle (5 degrees) to allow clearance for the converging laser beams at certain measurement points. This was achieved with an angled spacer plate between the probe bracket and extension arm shown in Figure 8.23. Measurements in the nozzle and in the free jet required the probe to be level. These tests used a level spacer plate for the probe bracket, which could also be used to extend the range of the probe aft for some tests.

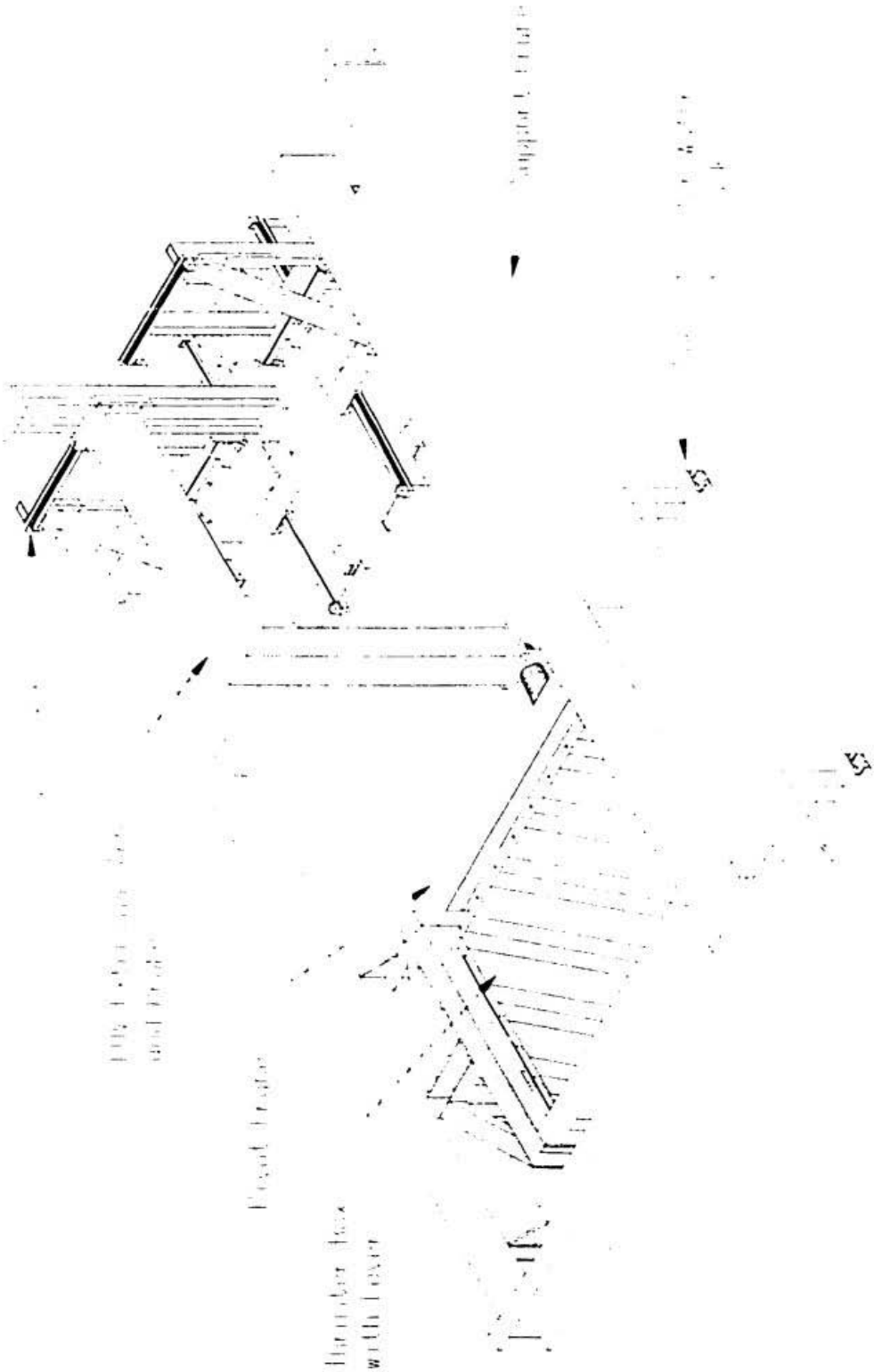

Figure 8.18 – Support Frame

8.4.4 Water Collection Tank

The water collection tank was used to determine the average flow rate through the waterjet by weighing the mass of water it ejected over a measured period of time. This is found to be an accurate and reliable method of flow rate measurement. The size of the trim tank posed a problem when first designing the collection tank. The limited water surface area of the trim tank meant that if water was collected from the jet without being replaced, then the water level in the trim tank would quickly drop below the level of the inlet, allowing air to enter the system. This was solved by allowing the collection tank to be free floating. As water entered the collection tank, the collection tank wound sink, displacing an equal volume of water and thereby maintaining the water level in the trim tank.

The collection tank, shown in Figure 8.19, was made from an aluminum box tubing frame with a sheet metal skin. The entrance hole was where the connection was made for the ducting used to direct the water from the jet to the tank. An air vent hole located at the top of the tank prevented pressure from building during collection and a valve at the tank bottom was used to drain water after tests. There was an access panel at the back of the tank for maintenance. Two rods on each side of the front of the tank were used to keep the tank in position during testing. These rods fitted into slots in the support frame and were held in with pins. During water collection, the tank rotated from a floating position to a mostly submerged position. The shape of the tank was designed to minimize the reaction forces on the support rods throughout its range of rotation during a test. Four eye bolts located at the corners of the top of the tank were reinforced with the tank's internal structure to provide lifting points for the overhead crane which was used for weighing

and draining. The empty tank weighed about 60 kg and held approximately 350 kg of water.

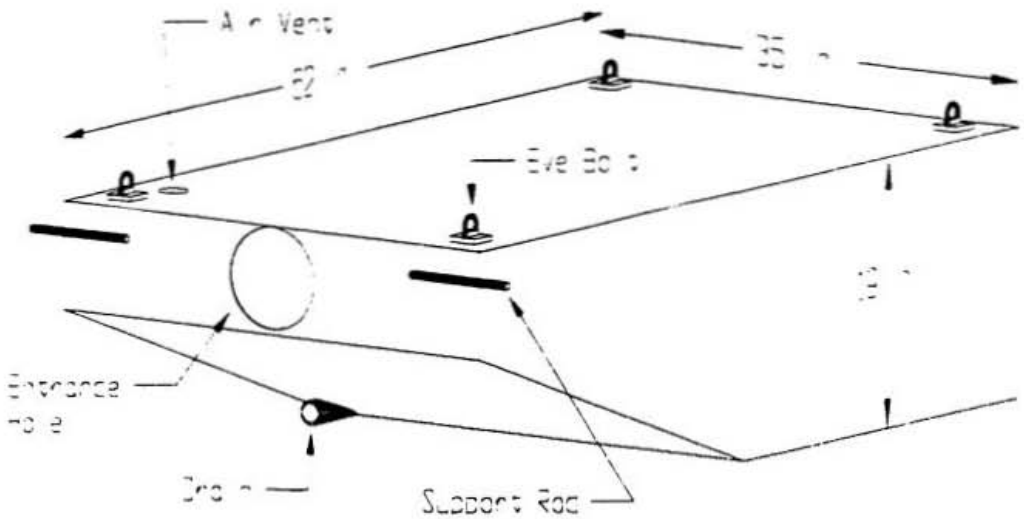

Figure 8.19 – Water Collection Tank

The ducting used to direct the water into the collection tank consisted of four parts. At the nozzle end, a short length of rigid three inch diameter tubing was fitted with a clamp which attached to the support frame. This tubing was made to fit as closely as possible to the nozzle without any physical contact while allowing room for priming. This separation was used to ensure that the ducting did not affect the nature of the flow or measurements such as thrust. The jet stream exited the nozzle with a diameter just under two inches and began to expand as it moved aft. The ducting likewise expanded with a sheet metal diffuser just behind the rigid tube attached to a length of five inch diameter flexible hose. This hose was required to flex and bend freely as the collection tank rotated from an empty to a filled position. Another sheet metal diffuser then connected the hose to the collection tank. This arrangement can be seen in Figure 8.20.

Figure 8.20 – Water Collection Arrangement

8.5 Test Program

The commissioning test program for platform was designed primarily to evaluate the platform's components, instruments and the methods used for testing. A rigorous series of shakedown tests were first performed to determine and correct unforeseen difficulties in the various systems. These tests were performed over a period of two months during which many components and methods were fine tuned. Tests were performed as needed, necessary modifications were made, and the tests re-done. This process continued until the testing methods were well defined and the results were accurate and repeatable.

Once the shakedown phase of testing was complete, three additional test phases were performed. They consisted of the following:

1. Flow tests
2. Water collection tests
3. Flow mapping tests
    - Flow mapping at inlet
    - Flow mapping in nozzle
    - Flow mapping in jet vena contracta

The experiments spanned impeller speeds ranging from 20 rps (1200 rpm) to 95 rps (5700 rpm) in increments of 5 rps. Speeds much below 20 rps were unable to maintain a waterjet and speeds in excess of 95 rps would have required a more powerful motor. Tests at impeller speeds of 70 rps and 75 rps were not performed due to excessive vibrations of the shaft, bearings and seals at this apparent natural frequency. Tests for each series were performed at least twice in order to check repeatability of the data.

Before testing began, the trim tank was equipped with wave damping lines (swimming lane dividers) at each end of the tank. These were used to dampen the waves and circulation caused by the jet. Spray walls were fitted at the aft end of the trim tank to prevent water spray from getting on the floor around the tank. The electronic equipment and computers on the starboard side of the tank were protected from spray with a clear plastic partition which allowed the operator to monitor the experiment.

8.5.1 Flow Tests

The flow tests were used to acquire pressure, thrust, torque and current data from the jet. Data acquisition began about 30 seconds before the motor was energized to establish references for the data channels. The jet was then primed as shown in Figure 8.15 and held until a steady flow had been achieved. The jet was then returned to its horizontal

position where the impeller accelerated to its set speed. Steady operation continued for about 2 minutes to allow sufficient data for establishing means. The impeller was then decelerated and the motor deactivated, ending the test. Acceleration and deceleration values (3 rps/s) were set by the motor controller to allow gradual transitions from stopped to running speeds in order to minimize stress on components.

The first series was performed with a standard jaw-type coupling between the motor shaft and the impeller shaft while the second two series employed a bellows-type shaft coupling. There was a significant decrease in noise and vibration when the second coupling was installed. The original bellows coupling sheared during the shake-down tests and since it took time to receive the replacement, a jaw-type coupling was used for the first few tests.

8.5.2 Water Collection Tests

The water collection tests were used to determine the mass flow rate of the jet. Thrust, pressure and current data were also acquired. Each test began by weighing the empty collection tank (discussed in Section 8.4.4) from the overhead crane with a 2000 lb. (9000 N) load cell. The tank was then fitted into slots in the support frame and secured with pins. Data was acquired for about 30 seconds before start up as a reference. The pivot frame was then lowered to its priming position and the impeller brought up to speed. The discharge from the nozzle during this acceleration phase was directed underneath the collection tank. Once the impeller reached its set speed, the pivot frame was quickly brought up to its horizontal position, where the flow was directed through ducting into the collection tank. As the tank filled, it rotated about its connection points to

the support frame. Once the tank was full, the pivot frame was quickly brought back to its priming position which stopped the flow into the collection tank. The impeller then decelerated to a full stop to end the data acquisition. The tank was disconnected from the support frame and weighed. After draining, the tank was re-weighed before the next test to account for any water that may still have been present. Figure 8.21 shows the positions of the pivot frame and collection tank at various points during a test.

The analysis of the test data was slightly different from the other tests discussed as three selections were taken. These selections can be seen in Figure 8.22 which shows a sample time history for both the pivot frame inclinometer and the impeller speed. The first selection was made before the test began and was used as a reference. The second selection was taken during the period when the jet was directed into the collection tank, shown by the pivot frame in its horizontal position. This gave the collection time. The third selection was used to determine the data means used for analysis. Marked 'Selection' in the figure, it consisted of a period of steady state operation that did not include sudden changes from underwater to above water flow.

The transition phase at the beginning and end of the collection period had the potential to cause errors in both the determination of the collection time and the weight of the collection tank. However, this unavoidable transition phase was brief enough not to have produced any significant error in the measured results (see Section 8.6.3).

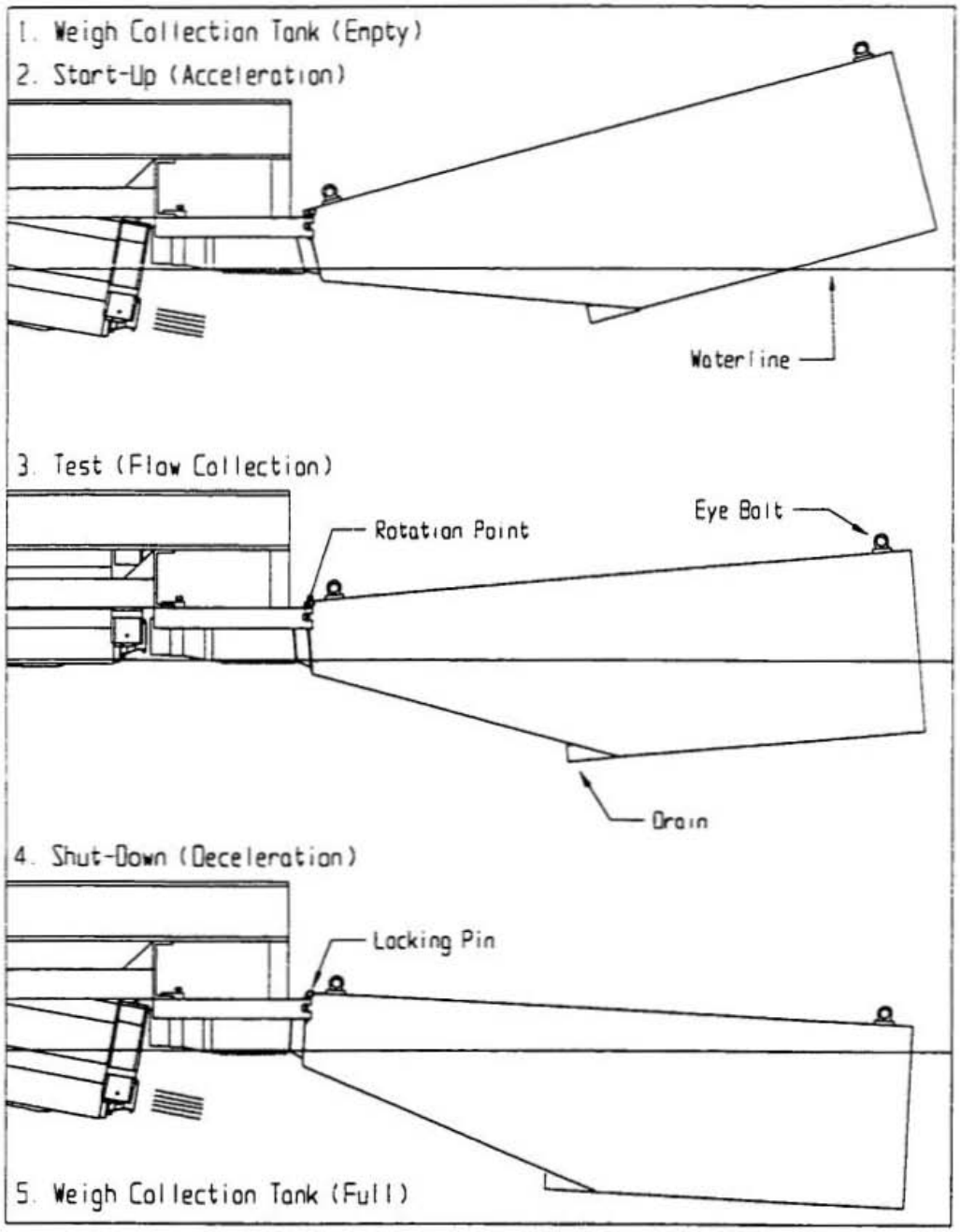

Figure 8.21 – Water Collection Test

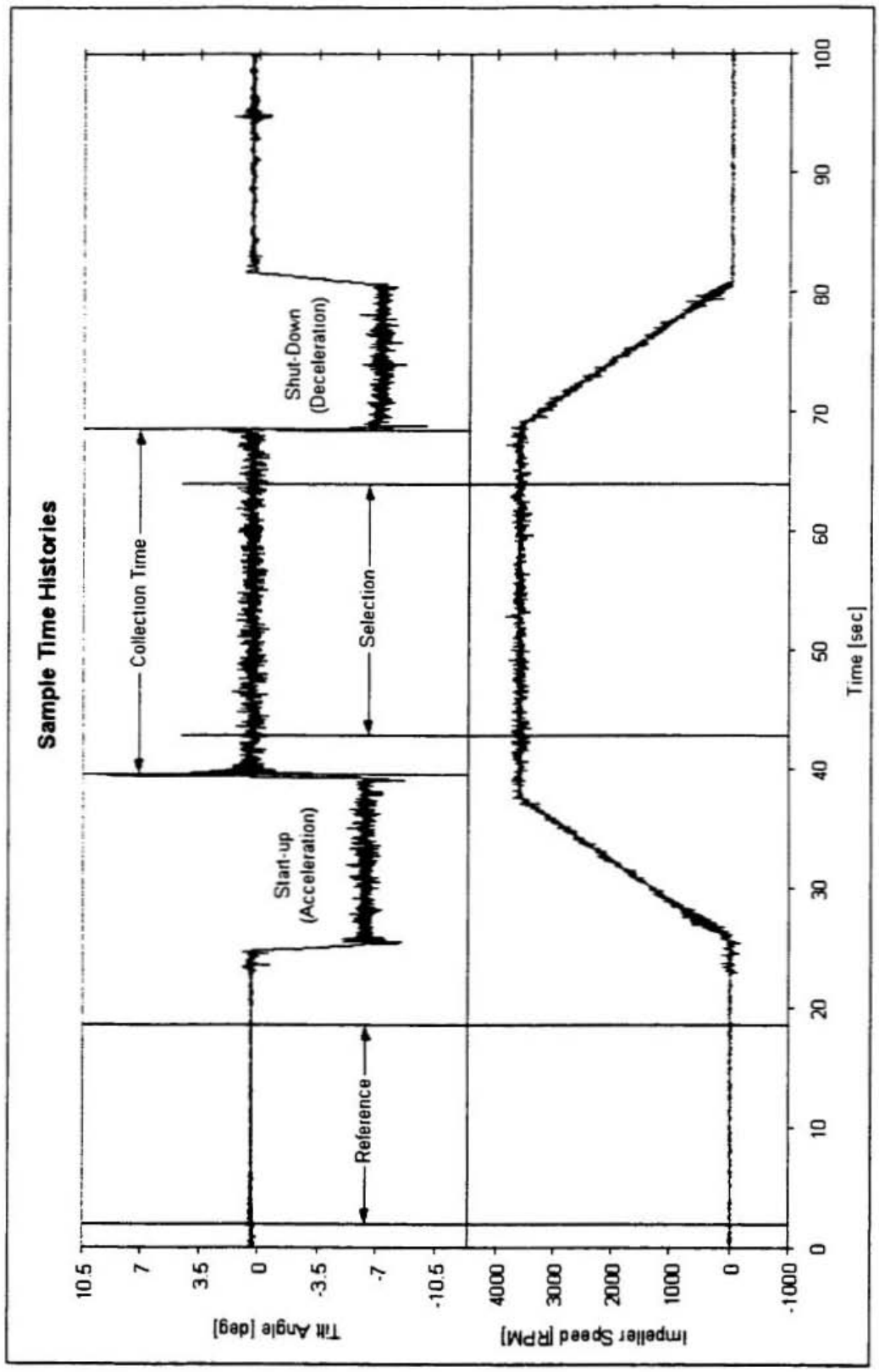

igure 8.22 – Sample Time Histories

8.5.3 Flow Mapping Tests

The flow mapping tests were performed using a laser Doppler velocimeter discussed in Section 3.9. There were three areas of investigation:

- A volume below the inlet
- The velocity profile in the nozzle just prior to exit
- The velocity profile in the vena contracta or other areas in the free jet stream

Measurements in the inlet area required the probe to be set at a slight angle as discussed in Section 8.4.3 and shown in Figure 8.23. The probe traversed a three dimensional array of measurement points. The size and density of this array was variable: a tight array to focus on a given area of interest, or broad to determine general velocity information in the region. The probe was 2-D, measuring velocities vertically and longitudinally relative to the waterjet. For full 3-D measurements, a third LDV probe set an angle relative to the present probe but measuring the same points would be required. These tests were primarily used to evaluate LDV testing methods so the third component was not essential.

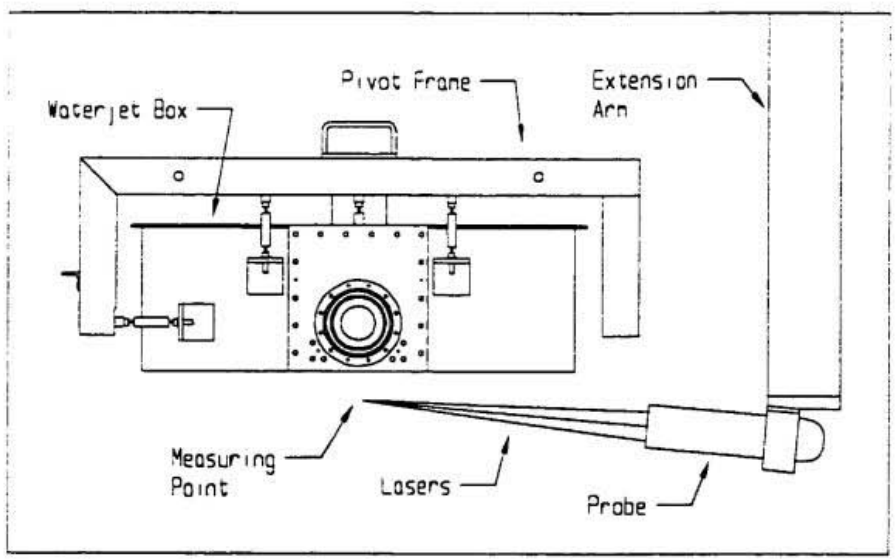

Figure 8.23 - Probe Orientation for Inlet Tests

Mapping tests in the nozzle were made through a small lens built into the side of the nozzle as described in Section 8.3.8. The laser probe was mounted horizontally and traveled in only one direction to measure velocities across the nozzle diameter. These measurements represented the axial and tangential components of the flow in this region. This method of determining nozzle velocities was not intrusive as compared with the pitot tubes discussed in Chapter 7. These velocity measurements are necessary in order to determine jet performance parameters with the use of the momentum flux method discussed in Chapter 5.

Tests in the vena contracta or other areas in the free jet were performed in a similar manner but with a greater range since there was no lens restricting the lasers' position. This velocity information is also useful in momentum flux calculations.

8.6 Experimental Results

The results from the experiments are presented in the following sections. These include:

- Thrust
- Torque
- Flow Rate
- Pressure
- Motor Current
- Flow Mapping

8.6.1 Thrust

Thrust measurements were made by the load cell fitted between the thruster box (see Section 8.4.1) and the pivot frame (see Section 8.4.2). These results are shown in Figure

8.24. The force measurements from the load cell are plotted against the impeller speed. A second order polynomial was fitted through the data points from the five test series discussed in Section 8.5. The high R^2 value shows a tight fit between the trend line and the experimental data.

It should be noted that the regression curves for this and other results do not go through the origin. This was due to the nature of the testing arrangement. There was a minimum impeller speed at which the flow could be maintained after priming, below which there was insufficient power to overcome gravity. As mentioned with full scale vessels, the waterjet units are at least partially submerged at low speeds, so overcoming gravity is not a problem. For the model tested in the platform, the minimum impeller speed was not much below 20 rps, so trends cannot be accurately extended below this value. Figure 8.25 illustrates how the thrust might have behaved at low impeller speeds. Since flow could not be established until about 1200 rpm, the measured thrust was therefore zero. Once flow was established there would be an immediate thrust jump at that impeller speed. The thrust readings would then follow the experimental regression curve with increasing impeller speed.

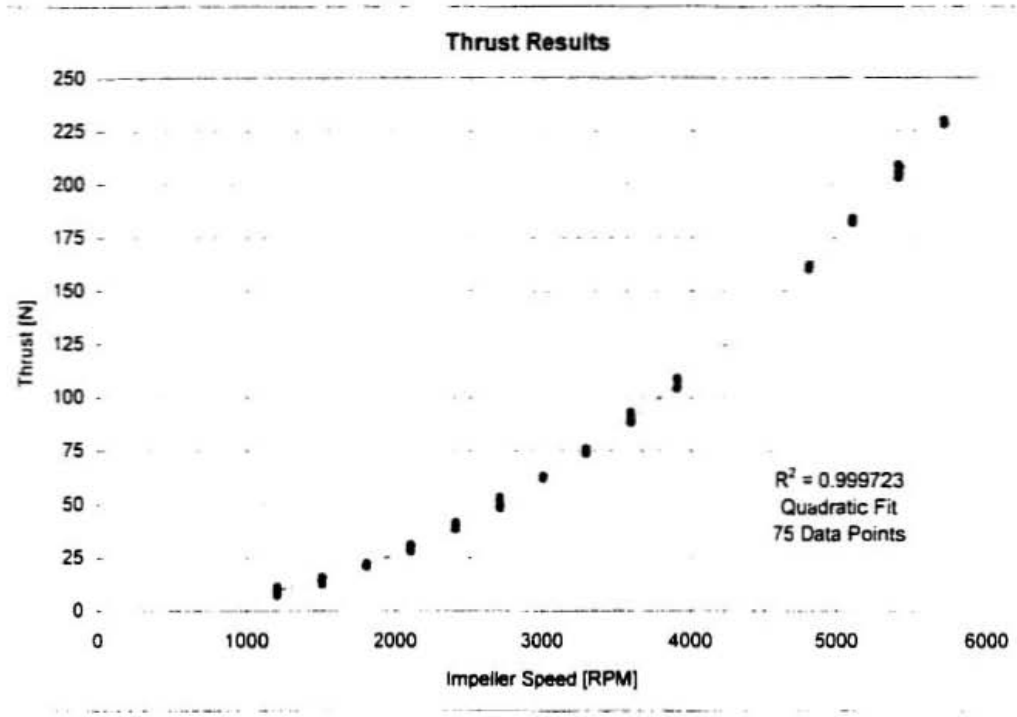

Figure 8.24 – Thrust Results

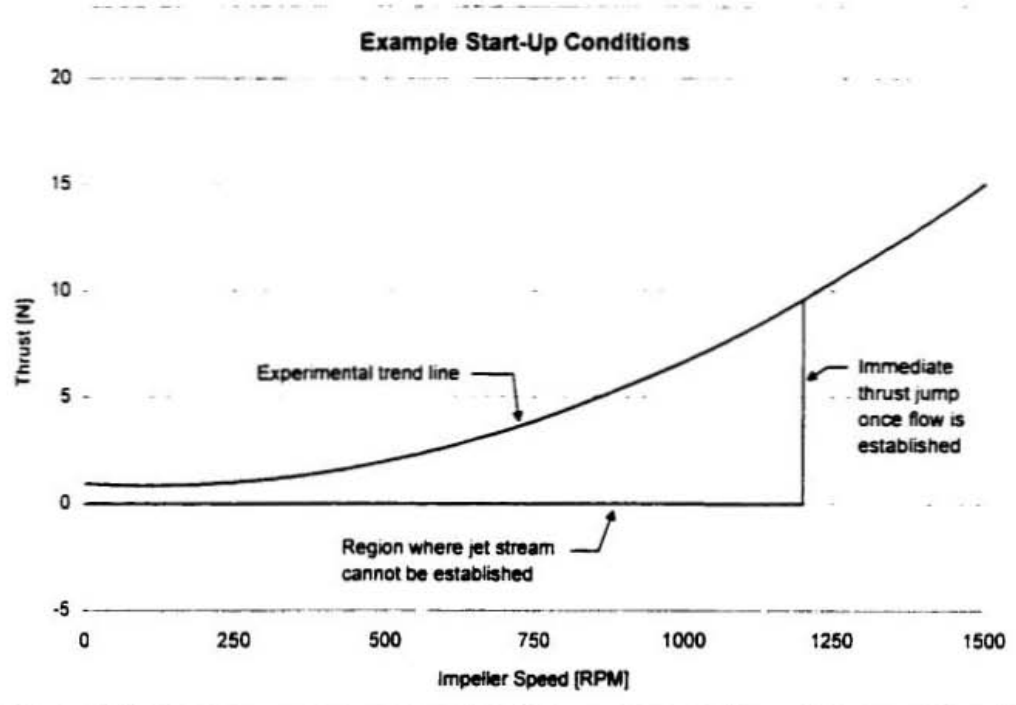

Figure 8.25 – Example Start-Up Conditions

8.6.2 Torque

Figure 8.26 shows the results from the torque transducer (see Section 3.5) which measured the reaction torque of the motor and hence the shaft torque during tests. These results were only for the flow tests since the transducer was not yet installed at the time the water collection tests were performed. This data, also fitted with a quadratic regression line, shows a higher degree of deviation from the fitted curve than the thrust results. This was attributed to both noise levels and sensitivity. The torque transducer was directly exposed to the mechanical vibrations of the system which appeared in the output signal as noise. Although the system ran relatively smoothly with the bellows coupling, there was a certain amount of vibration that could not be prevented. The transducer was also in close proximity to a high voltage motor produced electronic noise in the signal. A long sampling time was used to help lessen the effect of noise by providing many points for an average, but this was only moderately effective.

Another issue was the sensitivity of the transducer. The transducer was designed specifically for this motor and it was decided for safety to use the peak torque rating of the motor as an upper limit for the transducer. The webs and strain gauges were therefore designed for applied moments in the range of about 20 Nm. As can be seen in the figure, the upper range measured during tests was about 2.5 Nm. Only about 1/8 of the transducer range was used, decreasing the resolution of the output signal. It is possible to change the gain of the signal conditioner to increase the resolution and sensitivity of the transducer, but noise levels would increase as well. The gauged webs of the transducer would have to be smaller to truly increase sensitivity, but they are already close to the limit on how small they can be while still supporting the weight of the motor.

One other possibility for the spread in the data was that there may have been small changes in torque from test to test. This could have been caused from the shaft seal exerting more or less pressure on the shaft during a given series, or changes in the level of lubrication on various parts. When curves were fitted to each test series, as opposed to combining the data as was done in Figure 8.26, the individual curves had similar values of R^2 and spread as when they were combined. Since a test series was performed more or less continuously under the same conditions, it was concluded that the spread was more likely caused by the noise and sensitivity issues discussed above.

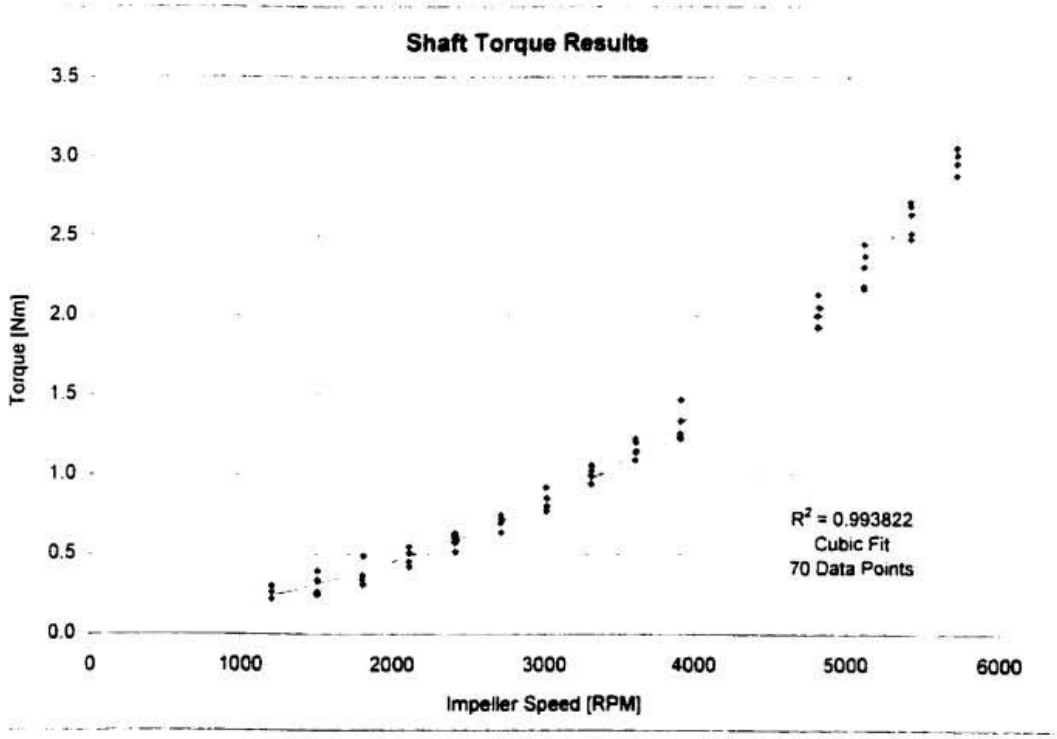

Figure 8.26 – Shaft Torque Results

8.6.3 Flow Rate

The flow rate results from the water collection tests can be seen in Figure 8.27. As discussed in Section 8.5.2, each test involved three separate measurements: pre-weight of collection tank, collection time, and post-weight of collection tank. The combined results of flow rate follow a linear trend with a high degree of consistency as indicated by an R^2 value of 0.9999. A high degree of confidence was therefore achieved in this method of measuring flow rate.

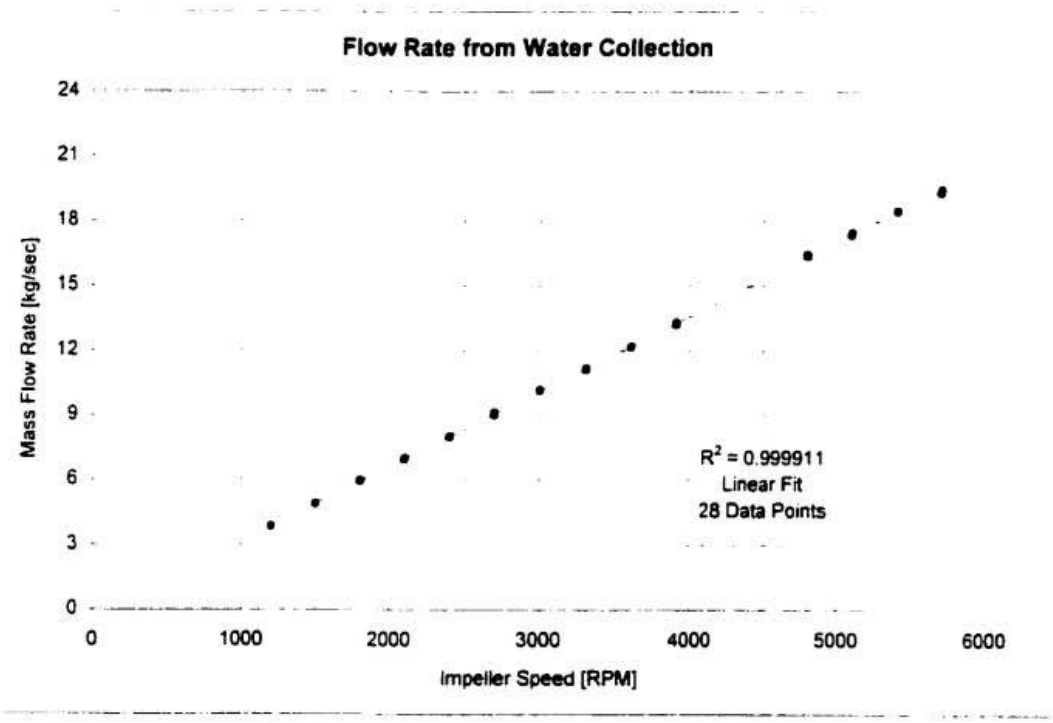

Figure 8.27 – Flow Rate Results

8.6.4 Pressure

The results from the pressure transducers are shown in Figure 8.28. The figure shows the averages of the four transducers in each of the three locations: impeller section, nozzle forward and nozzle aft. The results fit closely to quadratic regression lines with R^2 values

of better than 0.999 for the impeller section and forward nozzle transducers, and a 0.97 value for the aft nozzle transducers.

The average of the impeller section transducers excluded the bottom transducer since it was damaged during the shakedown tests. Due to its location, it was not possible to replace this particular transducer without complete disassembly of the waterjet unit. Also for these tests, the impeller section transducers were located directly over the impeller shown as 'Position 2' in Figure 8.29 as opposed to just ahead of the impeller ('Position 1') as previously discussed.

The data from the aft nozzle transducers showed slightly more deviation from its regression line than the other readings. This was largely due to the low pressures experienced in this region, which led to the same resolution and sensitivity errors for the 15 psi (100 kPa) transducers as were discussed for the torque transducer in Section 8.6.2. Future tests should employ more sensitive transducers in this area

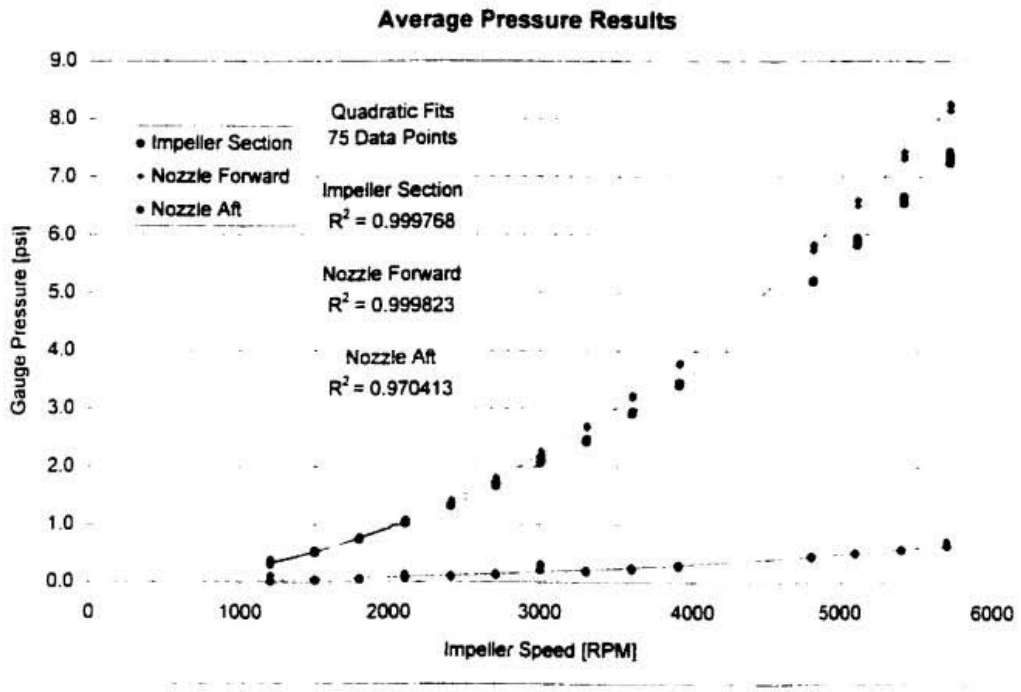

Figure 8.28 – Average Pressure Results

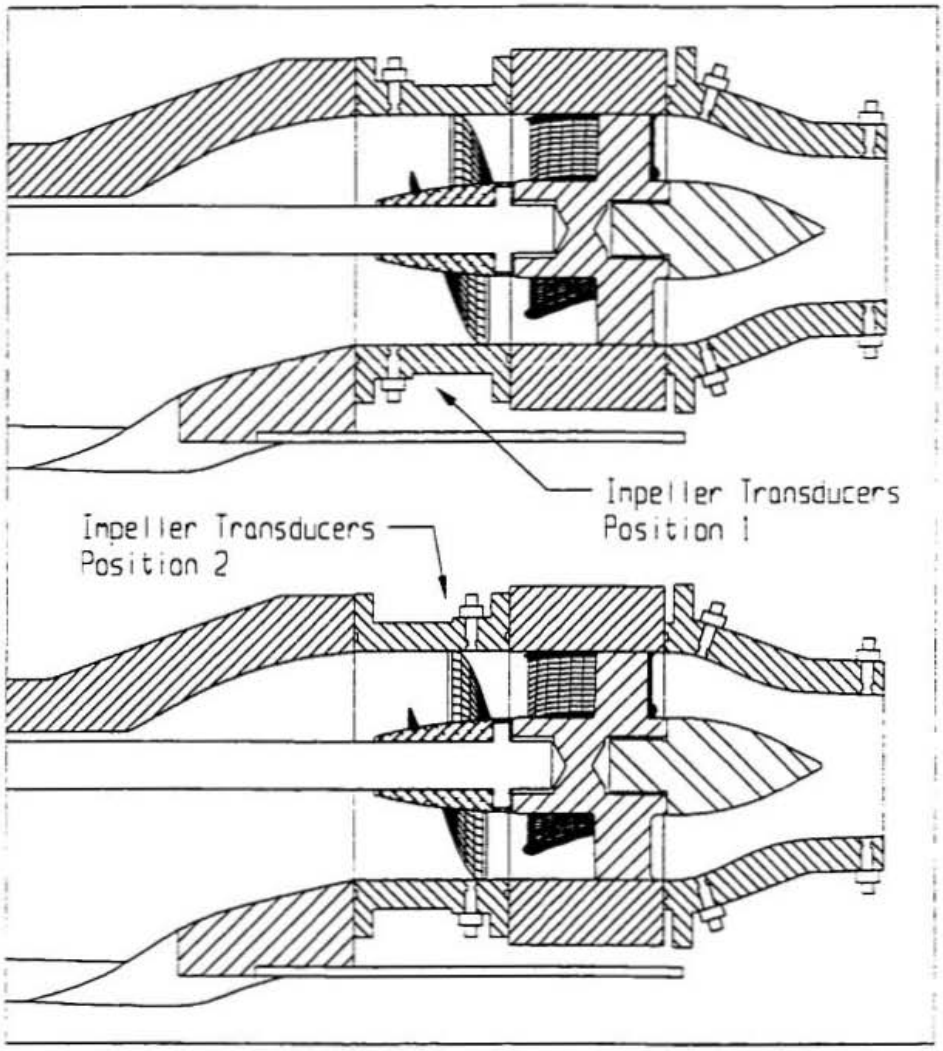

Figure 8.29 – Impeller Pressure Transducer Positions

8.6.5 Motor Current

The results for the motor current were the least consistent of the measured data. It should be noted that motor current measurements were not measured directly, but determined from the motor controller. There were electrical connections on the controller which produced a voltage proportional to the current draw of the motor (a manufacturers calibration was used of 5 amps/volt). This data was primarily used as a guide to the

power consumption of the motor, but it was also hoped that a relationship between motor current and torque could have been developed. If there had been consistent results between the two data sets, it may have been possible, in future arrangements, to use the current data to estimate shaft torque.

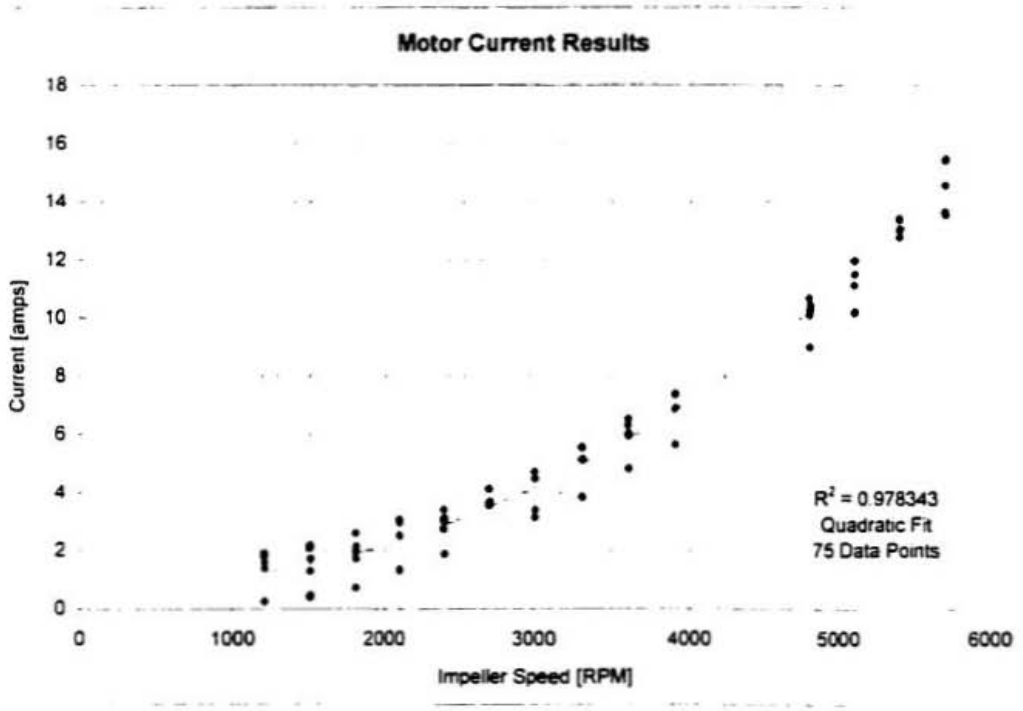

Figure 8.30 – Motor Current Results

8.6.6 Flow Mapping

Detailed flow mapping was not completed at the time of this thesis. Difficulties with the LDV and the optics of the test set up made velocity measurements difficult or impossible in the designated regions discussed in Section 8.5.3. Although data was not collected, much experience was gained in using the LDV system.

In working with variations of the test set up to accommodate the LDV, one set of measurements were made inside the jet unit, just aft of the stator. Originally, measurements were to be made in the nozzle through a small window (see Figure 8.9), but reflections inside the smooth aluminum nozzle made detection of particles impossible. In order to prevent this optical noise, a clear section was positioned between the stator and the nozzle (this clear section was a spare impeller housing described in Section 8.3.4). A window similar to the one in the nozzle was included in the section to prevent distortion of the lasers. The tail cone (see Figure 8.2 and Figure 8.7) was removed due to its interference with the lasers' measurement line.

This new arrangement, which allowed the lasers to pass through the jet unit with minimal reflection, was successful in permitting the LDV to detect particle signals. Measurements were made in a straight line across the horizontal diameter of the added section in 1 mm increments. Figure 8.31 shows the results from these tests with the impeller operating at 60 rps. Both the axial and tangential velocities are given in the figure. Positive tangential flow on the negative x-axis in the figure was in the same direction as the impeller motion. Positive tangential flow on the positive x-axis in the figure was in the opposite direction as the impeller motion. The figure shows only half of the measured data which was then mirrored across the center of the test line. The actual data on the positive side of the x-axis in the figure followed the trends shown, but with much more scatter. Noise levels increased considerably past the halfway mark in the test section and consequently affected the velocity measurements.

Figure 8.32 presents the same results as Figure 8.31, but in context of the geometry of the test arrangement. The axial velocity, shown at the top of the figure, shows boundary layers near the section's walls which quickly level off to a nearly steady flow. At the center of the section, a well defined dip in the velocity is shown. This corresponds to the stagnation region produced behind the stator hub as the tail cone was removed for these tests. The tangential velocity, shown at the bottom of the figure, also shows small boundary layers near the section's walls. There were two regions of tangential flow measured in the test section. The outer region near the walls consisted of flow rotating with the impeller. Inside of this, the flow was reversed and rotated in the opposite direction. This flow condition could have been caused by the stator blades near the hub over compensating for the impellers rotational affects. This flow would be forced to rotate opposite the impeller, which then affected the flow in the hubs stagnation region. It is unlikely that this type of flow would exist in a unit which included a tail cone.

Additional LDV measurements in other regions of the jet system would require modifications to both the test set up and the LDV probe. These modifications could be made in future based on the experience gained from these and other tests performed on the platform.

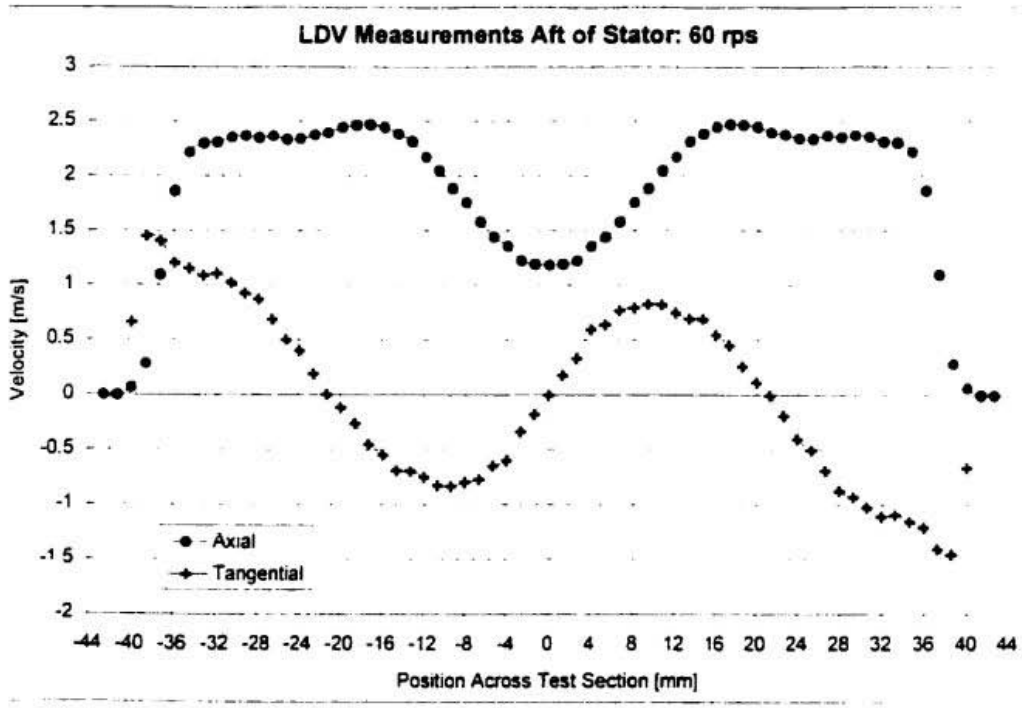

Figure 8.31 – LDV Measurements Aft of Stator: 60 rps

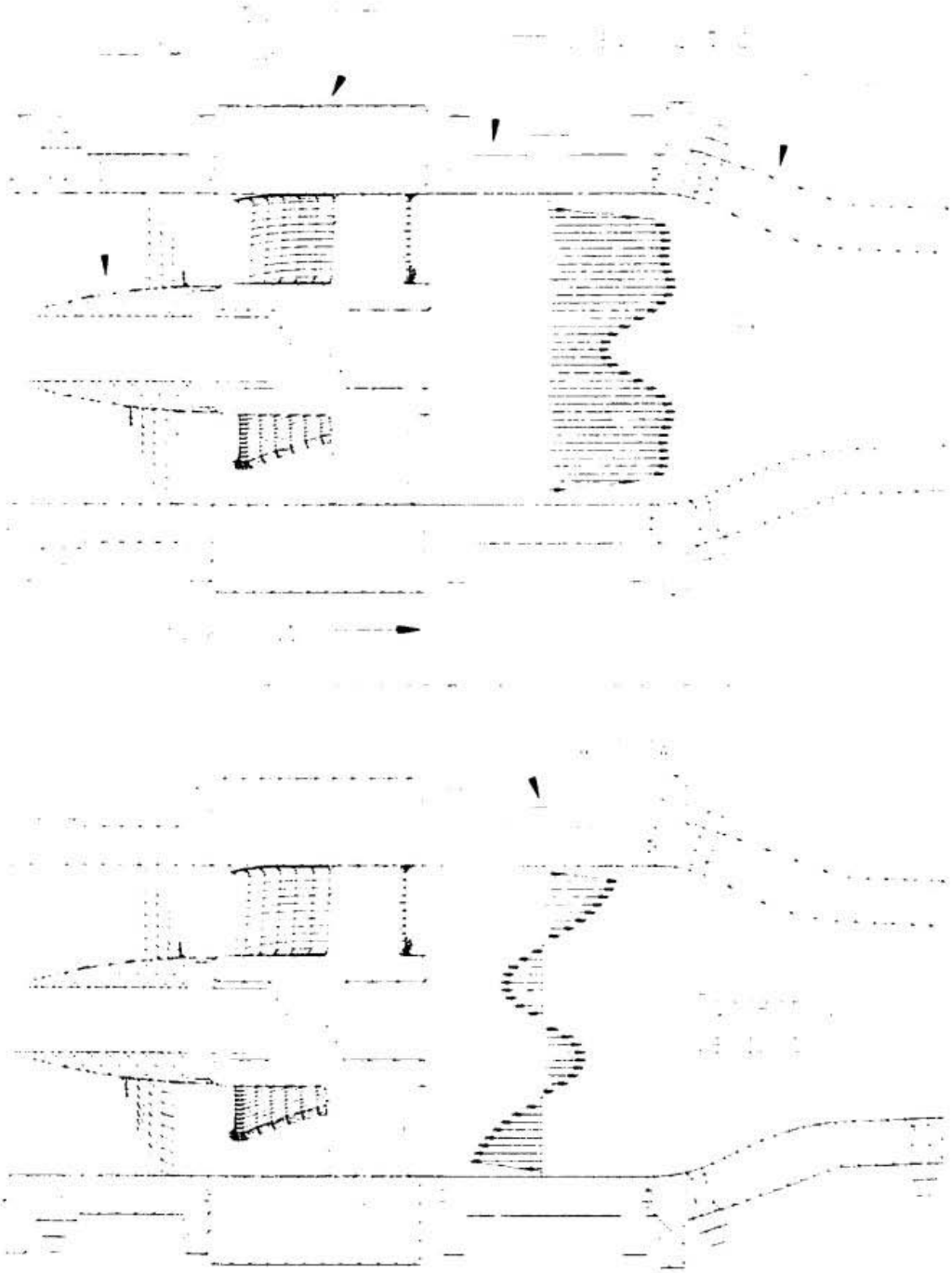

Figure 8.32 – LDV Results

8.7 Analysis of Experimental Results

The experimental results were used for several purposes:

- to evaluate the effectiveness of the various measurement techniques used in the platform;
- to obtain characteristics of the model waterjet that could be used to determine items such as thrust and flow rate during a self-propulsion test;
- to make observations about the model and platform that could be used to improve the equipment and testing methodology.

8.7.1 Flow Rate Calibration

Accurate determination of the jet flow rate, as discussed in Chapter 5, is crucial for applying the momentum flux method. One of the key functions of the test platform was to determine the relationship between mass flow rate through the jet and the pressure drop across the nozzle as measured by pressure transducers. This relationship could then be used to calculate flow rate during a self propulsion test or cavitation tunnel test where water collection measurements would be difficult or impractical.

This method of flow rate determination was based on the assumption that the velocity distribution of the flow in the nozzle is independent of the inflow conditions at the inlet. Otherwise, the nozzle flow at the bollard condition as measured on the test platform would be incompatible with the nozzle flow with different flow conditions at the inlet such as during operation in a towed model. This assumption was considered reasonable since the effect of the impeller and stator at high shaft speeds would conceivably overwhelm any incoming flow characteristics. However, it does need to be investigated

through comparison of nozzle velocity profiles of tests with differing inflow conditions. An investigation of this type was beyond the scope of this thesis.

Figure 8.33 shows measured flow rate plotted against the pressure drop across the nozzle. The pressure drop was the difference in the average values of the forward and aft nozzle pressure transducers. The theoretical value for flow rate can be determined from the nozzle pressure drop by applying Bernoulli's energy equation and the principle of continuity.

Bernoulli's energy equation can be expressed as:

$$\frac{p_1}{\gamma} + \frac{v_1^2}{2 \cdot g} + z_1 = \frac{p_2}{\gamma} + \frac{v_2^2}{2 \cdot g} + z_2 \qquad [8.1]$$

where,

p_1 and p_2 are the average pressures at the forward and aft nozzle locations respectively

v_1 and v_2 are the average velocities at the forward and aft nozzle locations respectively

z_1 and z_2 are elevations forward and aft nozzle locations respectively ($z_1 = z_2$)

γ is the specific weight of water

The conservation of mass flow rate is given as:

$$Q = \rho \cdot A_1 \cdot v_1 = \rho \cdot A_2 \cdot v_2 \qquad [8.2]$$

where,

A_1 and A_2 are the sectional areas at the forward and aft nozzle locations, respectively.

Equation 8.1 and 8.2 can be combined to express flow rate in terms of the pressure drop across the nozzle as shown in Equation 8.3.

$$Q = \frac{A_1 \cdot A_2 \cdot \sqrt{2 \cdot g}}{\sqrt{\gamma \cdot (A_1^2 - A_2^2)}} \cdot \sqrt{p_1 - p_2} \qquad [8.3]$$

The flow rate calculated by the above equation was plotted along with the measured values in Figure 8.33. The equations for the calculated values and for the regression curve through the measured results are both given. As can be seen, there was a difference of about 8% between the two curves. This difference was attributed to both frictional losses and the effect of a tangential or rotational velocity component in the flow. Despite the influence of the stator, the flow leaving the nozzle still had an appreciable rotational component, which was visible during testing. This component had the effect of increasing the absolute velocity measured by the pressure differential in the nozzle without increasing the axial velocity, which accounts for the flow rate.

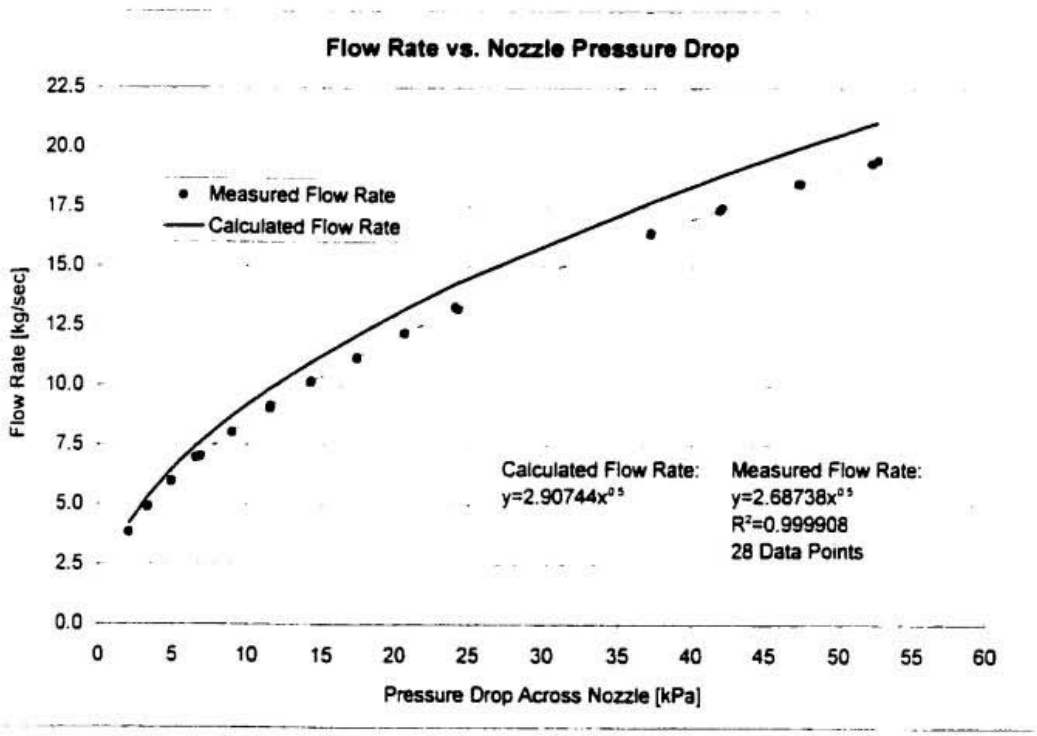

Figure 8.33 – Flow Rate vs. Nozzle Pressure Drop

8.7.2 Flow Velocities and Thrust

Although the model thruster was operating in the bollard condition, an attempt was made to apply some of the elements of the momentum flux method as a check on the test results. For the bollard condition, the momentum flux method was simplified somewhat since values of inlet momentum and energy flux become zero. Interest was therefore focused around the impeller and nozzle.

The average velocity at the nozzle exit can easily be determined from the measured flow rate. It is also possible to estimate this velocity from the pressure readings in the nozzle using Bernoulli's energy equation and the conservation of mass flow rate.

The equation for ideal average velocity at nozzle exit is:

$$V_3 = \frac{A_1 \cdot A_2 \cdot \sqrt{2 \cdot g}}{A_3 \sqrt{\gamma \cdot (A_1^2 - A_2^2)}} \cdot \sqrt{p_1 - p_2} \qquad [8.4]$$

where,

V_3 and A_3 are the average velocity and sectional area of the nozzle exit respectively.

Figure 8.34 shows the velocities calculated by the above method plotted against the nozzle velocities as determined from the flow rate. Also shown in the figure is a reference line representing 1 to 1 correspondence between the two axes. This is similar to the data plotted in Figure 8.33 but in a different form. The measured values were all slightly lower than the calculated values, which was due to tangential velocities and frictional losses as mentioned in Section 8.7.1. This effect seemed to be linear and could be accounted for with a coefficient of discharge (C_D = 1.082) used in Equation 8.3 based on the regression line in Figure 8.34.

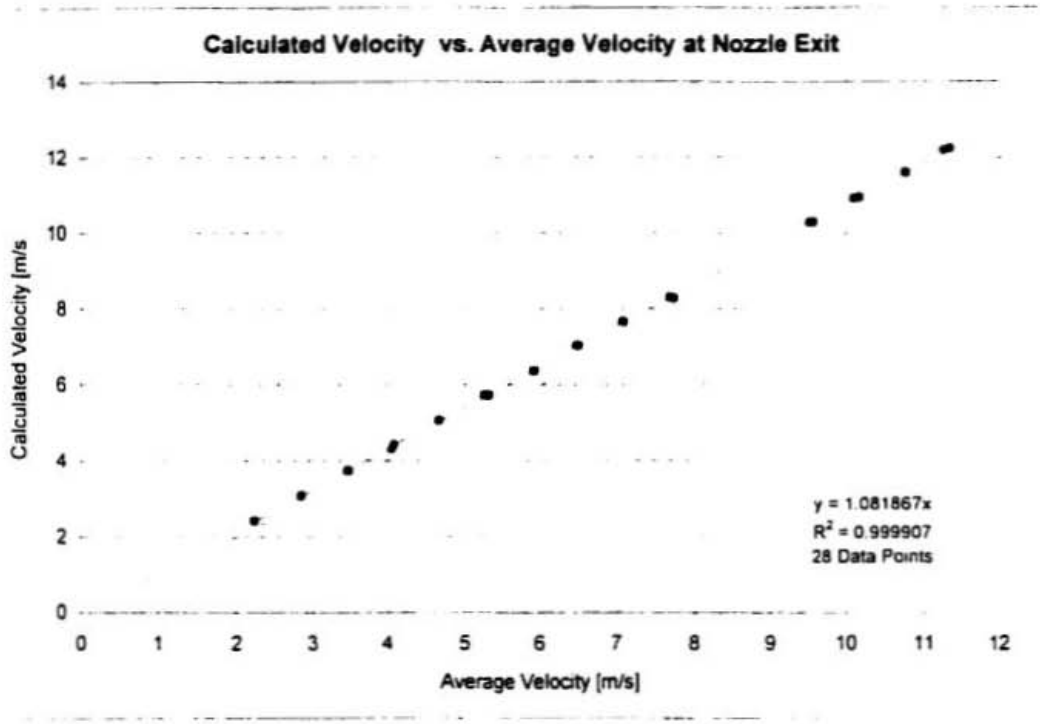

Figure 8.34 – Calculated vs. Average Velocity at Nozzle Exit

The velocity distribution in the nozzle, including the relative magnitudes of the tangential and axial velocity components, could not be determined due to problems with the LDV (see Section 8.6.6). This had an impact of the accuracy of momentum and energy flux values which depend on knowledge of velocity distributions. An example of the errors that could result from incomplete knowledge of the velocity profile in these types of calculations is given below.

Figure 8.35 shows a two dimensional example of both a constant and quadratic velocity distribution each having the same area and width. Values for flow rate, momentum flux and energy flux were calculated for each distribution and are shown in Table 8.3. It can be seen that for the same value of flow rate, there is about a 17% difference in

momentum flux and nearly a 35% difference in energy flux between the two distributions. Although this is an extreme example, as the actual distribution in the jet would likely fall somewhere in between A and B, it does demonstrate the potential impact of velocity distribution on computed results.

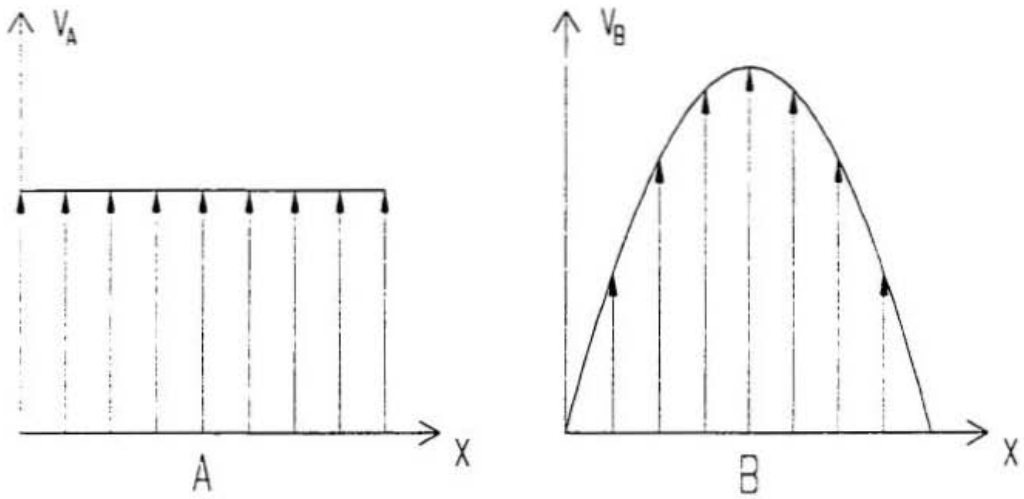

Figure 8.35 – Examples of Velocity Distributions

Parameter	Distribution A	Distribution B	Comparison
Flow Rate	$Q_A = \int v_A(x) \cdot dx$	$Q_B = \int v_B(x) \cdot dx$	$Q_A = Q_B$
Momentum Flux	$M_A = \rho \cdot \int v_A^2(x) \cdot dx$	$M_B = \rho \cdot \int v_B^2(x) \cdot dx$	$M_A = \frac{5}{6} \cdot M_B$
Energy Flux	$E_A = \rho \cdot \frac{1}{2} \cdot \int v_A^3(x) \cdot dx$	$E_B = \rho \cdot \frac{1}{2} \cdot \int v_B^3(x) \cdot dx$	$E_A = \frac{35}{54} \cdot E_B$

Table 8.3 – Example Comparison of Distribution Results

According to Equation 5.24, the thrust from a waterjet with a horizontal shaft line is the difference in the jet and inlet momentum flux. Since in this case the inlet momentum flux

was zero, the theoretical thrust was determined by the jet momentum flux. As mentioned, the velocity profile in the jet was not measured; it was assumed to be constant in further calculations. The average nozzle velocities determined from the flow collection tests were used for these values.

Figure 8.36 shows the thrust calculated according to Equation 5.19, plotted against the measured thrust from test platform's load cell. Also plotted is a reference line representing 1 to 1 correspondence between the two axes. The results were close, but the calculated results were all slightly less than the measured values. Based on the effect of the velocity distribution and the use of a constant profile, this was an expected result. The linearity of the curve suggests that the actual velocity profile in the jet did not change significantly with increasing flow rate. A flux coefficient (C_{flux} = 0.9553) could therefore be included in Equation 6.19 to correct for the use of an assumed velocity distribution in these calculations.

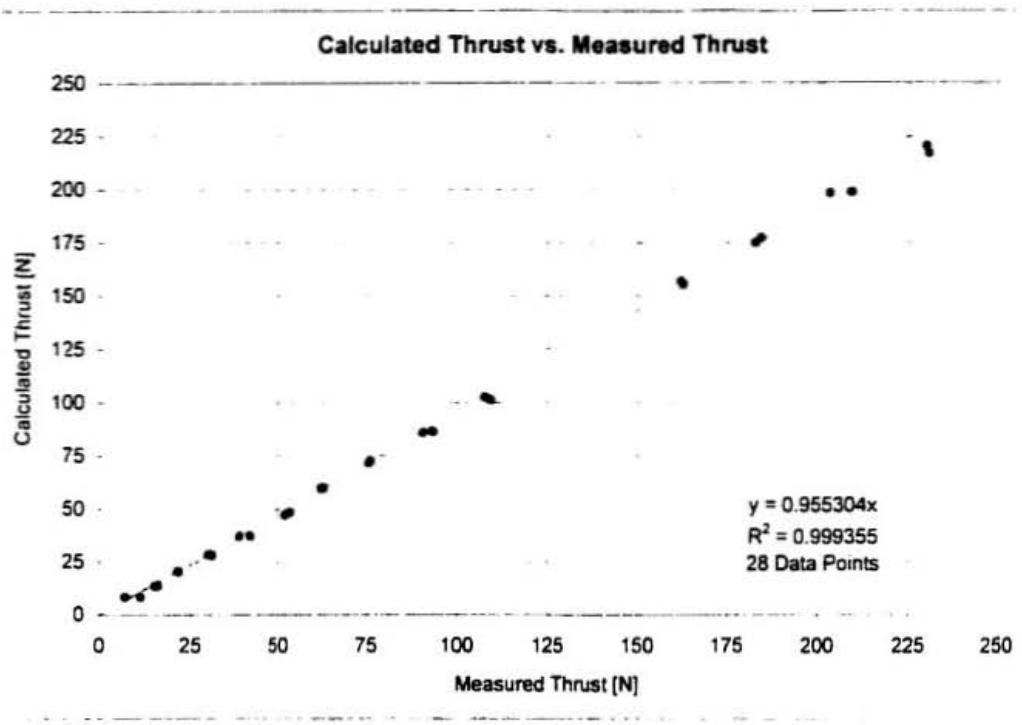

Figure 8.36 – Calculated Thrust vs. Measured Thrust

8.7.3 Torque Calibration

There was an expectation that a torque/current relationship could have been determined that could be used in testing situations where the torque transducer would be impractical. Torque would be calculated as a function of measured current. Figure 8.37 shows the torque results plotted against the motor current results. Although there was a linear trend, there was considerable spread in the data. As mentioned, efforts could help to improve torque results in future tests, but additional equipment would be required to improve current measurements. Determining torque from measured current proved to be an unreliable method.

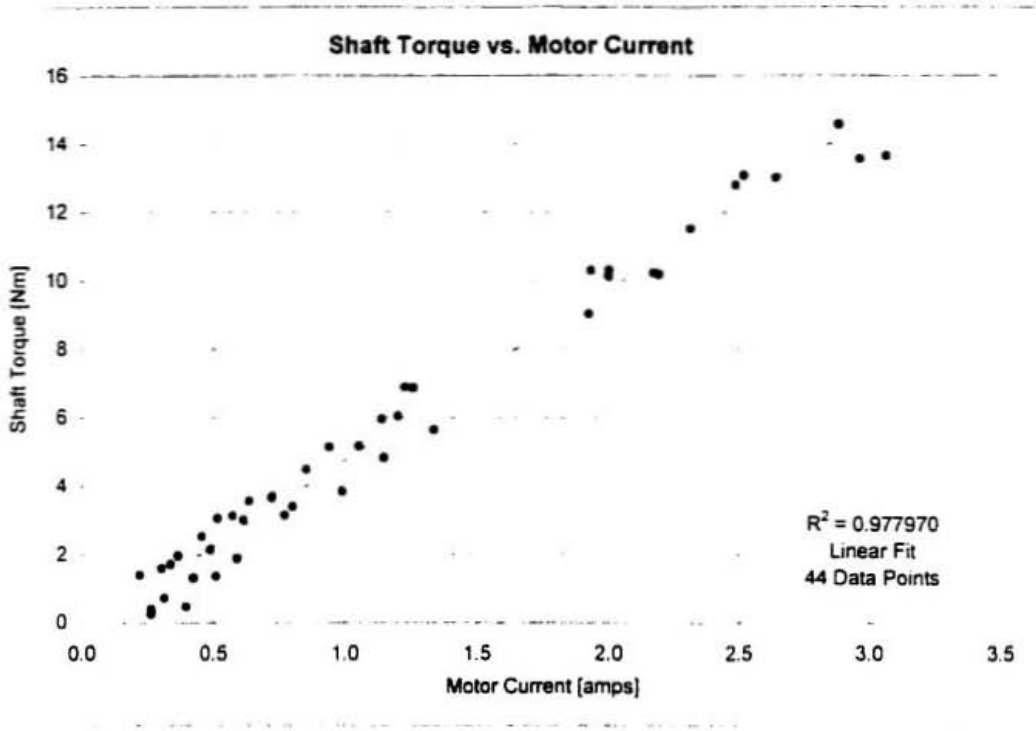

Figure 8.37 – Torque vs. Current

8.7.4 Power and Efficiency

The efficiency of the waterjet system can be expressed as the ratio of power transmitted to the shaft, to the power produced as thrust. There are other efficiencies that can be computed for various sections of the system as discussed in Chapter 5, but the focus in this section is on the available measured data.

The delivered power, or power transmitted to the shaft is given by:

$$P_{DM} = Qs_M \cdot \omega \qquad [8.5]$$

where,

Qs_M is the shaft torque at model scale

ω is the shaft speed in radians/second

Using Equations 5.21 and 5.26, the power produced as thrust, called the effective jet system power, can be simplified for the bollard pull condition as:

$$P_{JSE} = E_T = \rho \cdot \frac{1}{2} \cdot \int_{A_T} u_{xT}^{3} \cdot dA \qquad [8.6]$$

The efficiency can be expressed as:

$$\eta = \frac{P_{JSE}}{P_{SM}} \qquad [8.7]$$

Figure 8.38 shows the delivered power and effective jet system power plotted against impeller speed. Also shown in the figure is a power curve supplied by Bombardier for this waterjet. This full scale data was plotted at model scale as 'Predicted Power' for comparison. These results do not provide much quantitative insight into the model thruster's power requirements since both sets of data contain inherent inaccuracies. The effective jet system power, calculated with Equation 8.5, used the same velocity values and profile as for calculated thrust in Section 8.7.2 and would contain the same type of error. The delivered power was based on torque measurements which were not shown to be reliably consistent.

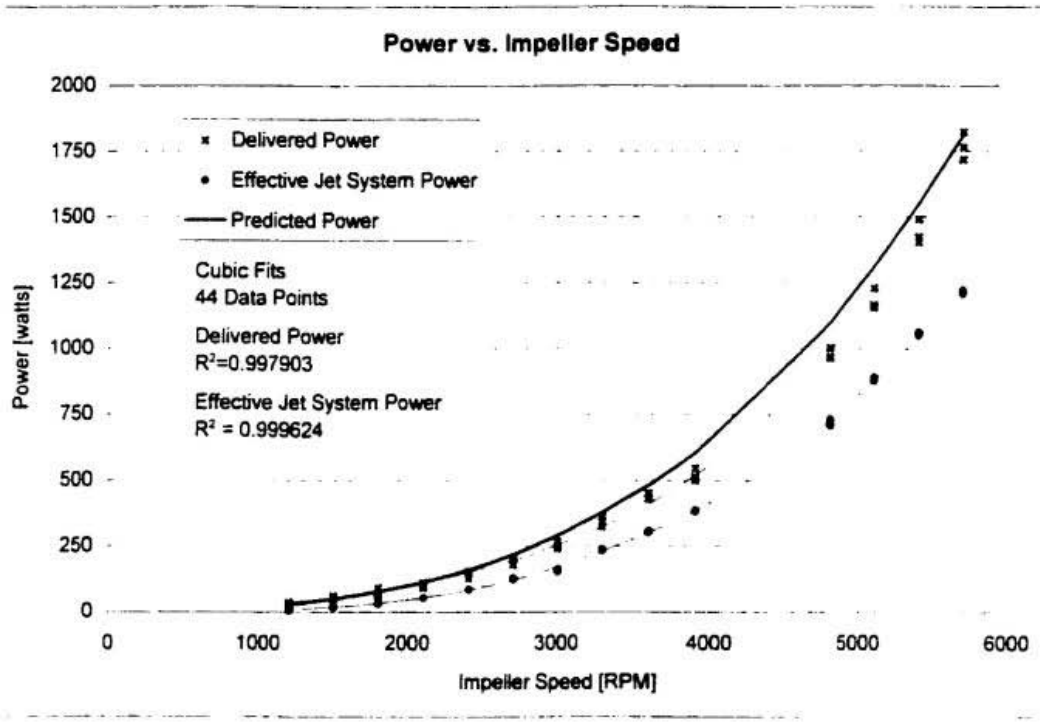

Figure 8.38 – Power vs. Impeller Speed

Figure 8.39 shows the efficiency results calculated with Equation 8.6. There was a high degree of spread in the data shown by the low R^2 value of 0.86. This figure illustrates the effects of errors in the calculated power values. The efficiency values were very high, some were even greater than one, which is impossible. This means that either the effective jet system power, based on nozzle velocities, was giving values which were too large, or the delivered power, based on shaft torque measurements, was giving values which were too low. A combination of these effects could also produce these results.

It should also be noted that these power and efficiency curves were for the bollard condition and would change significantly with the inclusion of the inlet momentum and energy flux that would accompany operation in a towed model or cavitation tunnel.

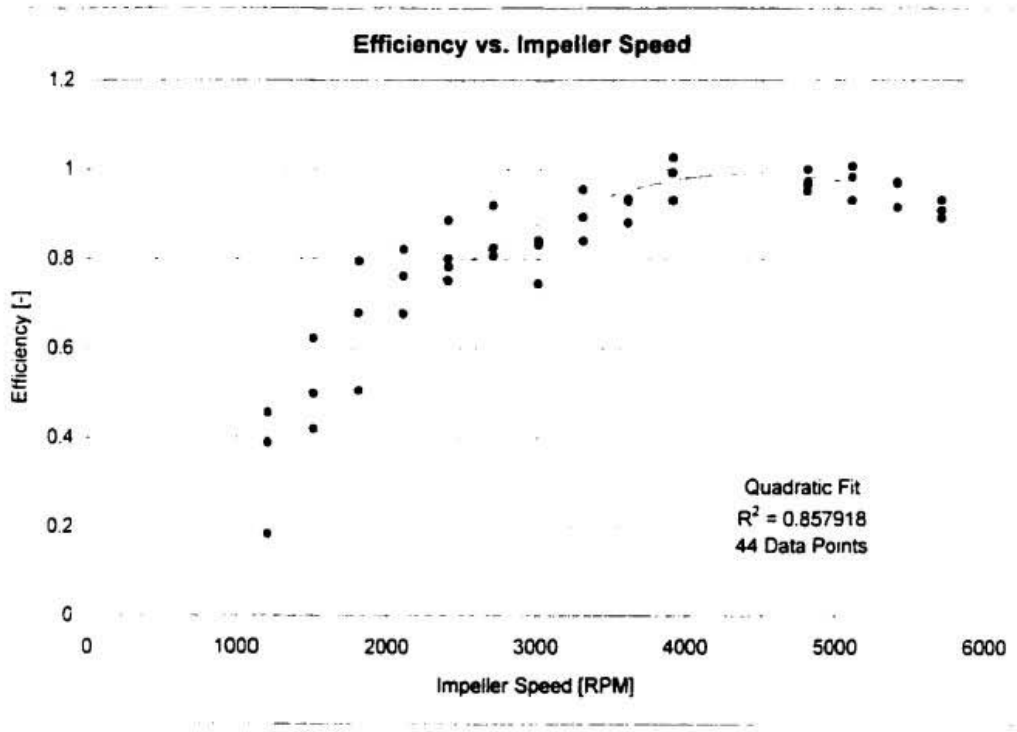

Figure 8.39 – Efficiency vs. Impeller Speed

8.8 Conclusions

The development of the waterjet test platform was intended to provide the necessary equipment to make measurements of certain characteristics of model waterjets. This data could then be used by itself for comparative evaluations of system performance, or as a basis for further experiments involving actual or simulated inflow to the jet. The design, construction, commissioning tests and results discussed in this chapter show that the platform has successfully met many of these goals.

CHAPTER 9
CONCLUSIONS AND RECOMMENDATIONS

9 CONCLUSIONS AND RECOMMENDATIONS

The aim of this project was to evaluate model testing techniques of waterjet thrusters and waterjet propelled vessels. Several conclusions and suggestions can be made from work discussed in this thesis as well as recommendations for future work.

9.1 Conclusions from Tests

The first phase of testing, the bare hull resistance tests series, was used to provide a baseline for the model at speed. These tests demonstrated that the methods used for measuring resistance, heave and trim produced consistent results. It was shown that the model's performance was sensitive to both the displacement and the position of the LCG. The tests went smoothly except for the unexpected porpoising behaviour seen at high model speeds. Flow measurements with the pitot tubes produced results consistent with

the free stream velocities but did not have the resolution needed to determine the velocity profile in the boundary layer. Measurement of the wetted surface area of the hull at speed from underwater video was effective, but as shown in Appendix B, many of the images became blurred at high model speeds. Greater resolution and shorter frame times would improve this method.

The self propulsion phase of experiments was used to gain experience in this type of test, as well as to identify areas where improvements to the instrumentation and testing methods could be made. It was found, for this model, that the pitot tubes and flow visualization tufts used to determine flow characteristics were intrusive and had a significant effect on the model's resistance (about a 10% increase). The running trim and heave profiles, however, were not sensitive to either the presence of the pitot tubes and tufts, or to the extent of operation of the model thrusters. It was found that these profiles were sensitive to ballast condition as in the bare hull resistance tests. The results from the pitot tubes at both the inlet and waterjet nozzle showed that this method for determining flow rate was ineffective. Shaft torque measurements of the toy thrusters also proved to be difficult. This was due to both the poor quality of the toy units, and to their small physical size. The experience gained from these results lead to the development of the waterjet test platform. A larger, precision-made model thruster was used, non-intrusive instrumentation was installed to determine flow rate, and a more sophisticated method was developed to measure shaft torque.

The design of the waterjet test platform was centered around requirements determined during the self propulsion tests. The stationary platform housed a waterjet model of

modular design. Instrumentation needed for measurements was integrated into the design of both the platform and model thruster. One of the primary functions of the platform was to measure the jet flow rate by means of water collection over a timed interval, in order to calibrate pressure taps in the nozzle. During a self-propulsion test with the model waterjet, jet flow rate could then be determined from these non-intrusive pressure measurements, eliminating the need for pitot tubes in the jet. The results from the water collection tests and the pressure transducers in the bollard condition were shown to produce a high degree of confidence for this method. This was emphasized by the high R^2 value (0.99991) of the regression curve fit through the experimental data.

Experience using the LDV system was gained during these tests. Several types of measurements were planned with this instrument to determine flow velocity distributions. Though the current platform and model arrangement made many of the planned LDV measurements difficult to achieve, knowledge gained from the attempts can be used in the design and planning of future work with the LDV system. One set of measurements was achieved with the LDV inside the waterjet ducting, after certain modifications, which show this instrument to be a promising method of determining velocity distributions.

Other measurements made by the platform include thrust and torque. Thrust was measured using a load cell / flexure system commonly used at IMD in force dynamometers. The thrust measurements gave consistent and repeatable results as demonstrated by the high R^2 value (0.9997) of the regression line fit through the data.

Shaft torque used to determine the power input to the thruster was measured with a specially designed reaction torque transducer. The motor mounted directly to the

transducer, so that when a load was applied to the shaft, the reaction forces from the motor could be determined from strain gauges on thin webs in the transducer's body. This method for measuring torque seemed to be a practical alternative to attaching strain gauges to a thin section of the shaft and using slip rings to maintain electrical contacts. A gauged shaft is often used for slower speed applications but is not recommended for the high shaft speeds used in these waterjet experiments. The test results for the torque transducer were less consistent than other measurements made on the platform, and showed a greater spread in the experimental data. This problem was attributed to both the sensitivity of the transducer, and to the RF interference produced by the electric motor. Future effort should be directed at resolving these problems or to developing other methods for measuring shaft torque.

The bare hull resistance and self propulsion tests provided valuable experience in the practical aspects of experimentally testing model waterjet propelled vessels. The lead to the development of a waterjet test platform which can be used to calibrate a waterjet thruster for flow rate, as well as provide a tool for evaluating some of the model's performance characteristics such as the magnitudes of the rotational velocity in the jet stream. The design and commissioning of the test platform provided valuable experience with regards to torque measurement at high shaft speeds and the use of the LDV system, which can be used in future research work at IMD.

9.2 Recommendations for Future Work

This project has only scratched the surface of possible areas of research involving waterjet propulsion. There are several areas which could directly follow the work discussed in this thesis. The first would be to make the necessary modifications to the platform and model to facilitate LDV measurements. Improvements to torque measurement techniques should also be investigated. Once reliable flow and torque measurements can be made at the test platform, the next step would be to test the model with flow to the inlet. This can be done either in a towed model or at the cavitation tunnel.

The cavitation tunnel is the logical choice for this stage since it is a stationary platform and could easily incorporate the LDV for flow measurements. Significant modifications would be required to the cavitation tunnel for tests of a waterjet model, but the end result would be tool which could easily vary the inflow conditions at the inlet (perhaps even the angle of attack). It may even be possible to take advantage of the tunnels ability to induce cavitation at model scale by lowering the ambient pressure in the water.

Tests in the cavitation tunnel could be used to investigate the flow conditions at the nozzle with various inlet flow conditions and may be used to justify or disprove the use of bollard pull results for flow calibration in self propulsion tests. Cavitation at the impeller, stator and inlet can also be studied in a cavitation tunnel. In conjunction with cavitation studies, inlet designs can be assessed in terms of drag losses. To complement towing tank tests, cavitation tunnel experiments can be useful to investigate boundary layer thickness and velocity profiles forward of the waterjet intake which cannot be

studied in the bollard condition. Similarly, internal flow investigations can be made to determine, for example, the effects of shafting and other material boundaries on the flow to the impeller.

Towed model experiments with model thrusters would be the next stage in this vein of experimental research. The characteristics of a model waterjet gained from experiments in the stationary platform and cavitation tunnel could be then used to perform self propulsion tests in a model hull. These experiments could be used to determine thrust and powering requirements of various hull types. They could also be used to investigate waterjet / hull interactions which are difficult to predict by other means.

There are also many areas of research involving computer simulations and computational fluid dynamics techniques which could be used in conjunction with experimental methods in evaluating the performance of waterjets and waterjet propelled vessels.

REFERENCES

Allison et al., "Cavitation in Model and Full-Scale Waterjet Propulsors", Preprints for Twenty-fourth American Towing Tank Conference, pp. 1 – 5, National Academy Press, Texas, U.S.A., 1995

Allison J., Member, Band, Lavis. "Marine Waterjet Propulsion", SNAME Transactions, Vol. 101, pp. 275 – 335, 1993.

Allison J.L., Stricker J.G. "Cavitation in Model and Full-Scale Waterjet Propulsors", 24th American Towing Tank Conference, pp. 27 – 32, Texas, U.S.A., 1995.

Arén P., AartoJärvi R., Croner P. "Review of test methods adopted for water jets at the KaMeWa laboratory", Supplement to the Report of the Waterjets Group; 21st International Towing Tank Conference, pp. 1 – 13, Trondheim, Norway, 1996.

Blanton J.N. "Laser Doppler Velocimetry Techniques in the Large Cavitation Channel", 24th American Towing Tank Conference, pp. 95 – 102, Texas, U.S.A., 1995.

Blount B.L., Bartee R.J. "Design of Propulsion Systems for High-Speed Craft", Marine Technology, Vol. 34, No. 4, pp. 276 – 292, October 1997.

Celano T. "The Prediction of Porpoising Inception for Modern Planing Craft", SNAME Preprints: Annual Meeting Technical Sessions 1998, pp. 10-1 – 10-22, San Diego, U.S.A., 1998.

Coop H.G., Bowen A.J. "Hull-Waterjet Interaction Mechanisms: Theory and Validation", Fast '93, International Conference on Fast Sea Transportation, pp. 1 – 12, Yokohama, Japan, 1993.

Daugherty R.L. et al. Fluid Mechanics with Engineering Applications 8th Edition. McGraw-Hill Inc., New York, 1985.

Delgado-Saldivar G. "Test Results of a Planing Hull Series", 24th American Towing Tank Conference, pp. 225 – 231, Texas, U.S.A., 1995.

Doebelin E.O. Measurement Systems Application and Design 3rd Edition. McGraw-Hill Book Company, New York, 1983.

Dyne G. and Lindell P. "Waterjet testing in the SSPA towing tank", RINA International Symposium on Waterjet Propulsion - Latest Developments, Paper No. 2, pp. 1-8, London, U.K., 1994.

Dyne G., Widmark C. "On the Efficiency of Waterjet Systems", RINA International Conference: Waterjet Propulsion – Latest Developments, pp. 1 – 21, Amsterdam, 1998.

English J.W. "Practical Considerations on Waterjets with Flush Intakes" , RINA International Symposium on Waterjet Propulsion - Latest Developments, pp. 1-11, London, U.K., 1994.

Eshbach O.W. Handbook of Engineering Fundamentals 2nd Edition. John Wile & Sons Inc., New York, 1965

Etter R.J. Krishnamoorthy V., Scherer J.O. "Model Testing of Waterjet Propelled Craft", Proceedings of the 19th General Meeting of the American Towing Tank Conference, pp. 783 – 806. Ann Arbor Science Publishers, Michigan, U.S.A., 1980.

Giancoli, D.C., Physics 3rd Edition. Prentice Hall, New Jersey, 1991

Giles D. L. "Faster ships for the future", Scientific American, Vol. 277, No. 4, pp.126-131, October 1997.

Harvald S.A. Resistance and Propulsion of Ships. John Wiley and Sons, New York, 1983.

Hoshino T., Baba E. "Determination of propulsive performance of waterjet in model and full scales", Supplement to the Report of the Waterjets Group; 21st International Towing Tank Conference, pp. 1 – 7, Trondheim, Norway, 1996.

Hothersall R.J. "Some Issues in Waterjet Design and Selection", 8th International High Speed Surface Craft Conference, pp. 1 – 19, London, England, 1992.

ITTC 1987: "Report on the High Speed Vehicles Committee", 18th International Towing Tank Conference, pp. 304 – 313, Kobe, Japan, 1987.

ITTC 1990: "Report on the High Speed Vehicles Committee", 19th International Towing Tank Conference, Madrid, Spain, 1990.

ITTC 1993: "Report on the High Speed Vehicles Committee", 20th International Towing Tank Conference 1993, pp. 363 – 413, San Francisco, U.S.A., 1993.

ITTC 1996: "Supplement to the Report of the Waterjets Group", 21st International Towing Tank Conference, Trondheim, Norway, 1996.

ITTC 1996: "Waterjets Group: Final Report and Recommendations to the 21st ITTC", 21st International Towing Tank Conference, pp.189 – 209, Trondheim, Norway, 1996.

Kruppa C.F.L. "On Pump Installation Efficiency", Supplement to the Report of the Waterjets Group; 21st International Towing Tank Conference, pp. 1 – 3, Trondheim, Norway, 1996.

Lewis, E.V. (ed.), Principles of Naval Architecture Second Revision. Society of Naval

Architects and Marine Engineers, Jersey City, 1988.

Minsaas K. J. "Exposure of Waterjet Inlets in a Seaway to Free Air", Supplement to the Report of the Waterjets Group; 21st International Towing Tank Conference, pp. 1 – 4, Trondheim, Norway, 1996a.

Minsaas K. J. "Flow studies with a pitot inlet in a cavitation tunnel", Supplement to the Report of the Waterjets Group; 21st International Towing Tank Conference, pp. 1 – 7, Trondheim, Norway, 1996b.

Moon I-S., Lee C-S., Song I-H., Kim K-S. "Prediction of performance of waterjet propulsors by surface panel method" , Propellers/Shafting '97 Symposium, pp. 2-1 – 2-13, Virginia Beach, U.S.A., 1997.

Mununga L, Huntsman I., Hothersall R. "Effects of Splitter Plate and Screen Grid on Waterjet Intake Flow". 13th Australian Fluid Mechanics Conference, pp. 1 – 4, Melbourne, Australia, 1998a.

Mununga L., Huntsman I. "Intake Studies for a Waterjet Propulsion System". IPENZ Annual Conference 1998, pp. 58 - 63, New Zealand, 1998b.

O'Neil, P.V., Advanced Engineering Mathematics 3rd Edition, PWS Publishing Company, Boston, 1993.

Pylkkänen J. V. "A test case of the application of a CFD code for predicting waterjet inlet flow", Supplement to the Report of the Waterjets Group; 21st International Towing Tank Conference, pp. 1 – 5, Trondheim, Norway, 1996.

Pylkkänen J.V. "Design of Waterjet : Selection of Main Dimensions and Two Dimensional Diffuser and Lip Selection Shape", Technical Report VALB-29, VTT Manufacturing Technology, Finland, 1994.

Rose J.C., Kruppa C.F.L. "Methodical Series of Model Test Results", FAST '91: First International Conference on Fast Sea Transportation, pp. 1129 – 1147, Trondheim, Norway, 1991.

Sasijima T., Mishima Y. "Air drawing criteria for a semi-scoop type waterjet inlet for jets", Supplement to the Report of the Waterjets Group: 21st International Towing Tank Conference, pp. 1 – 4, Trondheim, Norway, 1996.

Savitsky D. "3.3 Planing Hulls", Technical Report DTNSRDC-81/026, David Taylor Naval Research and Development Center, U.S.A., 1981.

Sharp J.J. Hydraulic Modelling, Butterworths, London, 1981.

Shaughnessy J.J. "Some Observations on Various Testing Techniques for Calm Water

Planing Boat Resistance", 24th American Towing Tank Conference, pp. 217 – 223, Texas, U.S.A., 1995.

Svensson R. "Experience with High Powered Water Jets., Water Jet Projects", Shipshape 2000; 10th International Maritime & Ship Symposium, pp. 554 – 572, Sydney, Australia, 1993.

Svensson R. "Waterjet Propulsion of High Speed Passenger Vessels", Shipbuilding Technology International '94, pp. 155 – 159, London, England, 1994.

Svensson R. "Waterjet Propulsion Operational Experience from Large Installations", Propellers/Shafting '97 Symposium, pp. 1-1 – 1-6, Virginia Beach, U.S.A., 1997.

Terwisga van T. "On the description of waterjet powering performance", Supplement to the Report of the Waterjets Group; 21st International Towing Tank Conference, pp. 1 – 9, Trondheim, Norway, 1996a.

Terwisga van T. "The Effect of Waterjet-Hull Interaction on Thrust and Propulsive Efficiency", FAST '91: First International Conference on Fast Sea Transportation, pp. 1149 – 1167, Trondheim, Norway, 1991.

Terwisga van T. Waterjet - Hull Interaction, Grafisch Bedrijf Ponsen & Looijen, Wageningen, 1996b.

Thomas J. "Studies by VSEL using Boundary Element Methods to Predict Flow Characteristics and Motion Data for a Novel Waterjet Multihull Design", CADMO '92, 4th International Conference on Computer Aided Design, Manufacture and Operation in the Marine and Offshore Industries, pp. 671 – 688, Madrid, Spain, 1992.

Törneman G. "Development of Large Waterjet Propulsion Systems", 9th International High Speed Surface Craft Conference, pp. 1 – 18, Singapore, 1993.

Vorst van de H.J.A., Verbeek R., Hendriks A.J.A.M. "Design Considerations of Waterjet Propulsion Systems", 13th Fast Ferry International Conference, pp. 1 – 34, Singapore, 1997.

Yuan, S.W. Foundations of Fluid Mechanics, Prentice Hall, London, 1967.

APPENDIX A

Model Ballasting

A.1 Model Ballasting

Proper ballasting of a model is an important part of an experimental test program. The performance of planing craft in particular is sensitive to displacement and center of gravity. The model discussed in Chapters 6 and 7 was ballasted for nine conditions: three displacements each with three positions of longitudinal center of gravity. The following outlines the procedure used for achieving these conditions, as well as for determining the model's vertical center of gravity and the inertia about the pitch axis for each condition.

The first step was to weigh all the model's components. The model is usually weighed with all permanent instrumentation and outfitting such as: the gimbal, yaw restraint mount, cover, any cabling suspended as it would when testing, and all fixed instrumentation such as the inclinometer and pitot tubes. The yaw restraint itself is counter-balanced so that it should not affect the model's ballast condition when connected (see Section 6.5). Other components, such as pressure transducers, individual ballast weights, and heave post, were weighed separately. When the model is attached to the carriage, the heave post is connected to the gimbal, (see Figure 6.6) which supports its weight. This was accounted for during ballasting by placing a dummy weight equal to the heave post weight on the gimbal.

All necessary equipment and ballast weights were added to the model until it was at a target displacement. The model was then placed in the swing frame shown in Figure A.1. The frame, made of aluminum with lightening holes not shown in the figure, was supported by knife edges on each end which rested on the smooth level surfaces of the frame supports. Since the frame supports could not apply a reacting moment to the swing

frame, the model and frame tilted until their center of gravity aligned with the knife edges. The angle of tilt was determined by an inclinometer attached to the swing frame. The swing frame alone was weighed and balanced previously so that it rested horizontally when empty.

A given model LCG was achieved by placing marks on each side of the model at the desired LCG location. The model was then supported horizontally in the swing frame and positioned so that the marks were vertically aligned with the knife edges. Alignment was ensured with the use of plumb bobs from the swing frame. The frame and model were then permitted to tilt to equilibrium. Ballast weights were re-located until the model rested horizontally in the swing frame. The ballast arrangement was then marked in the model and recorded with diagrams. The ballast weights were distributed symmetrically about the longitudinal center line of the model in order to avoid problems with model list.

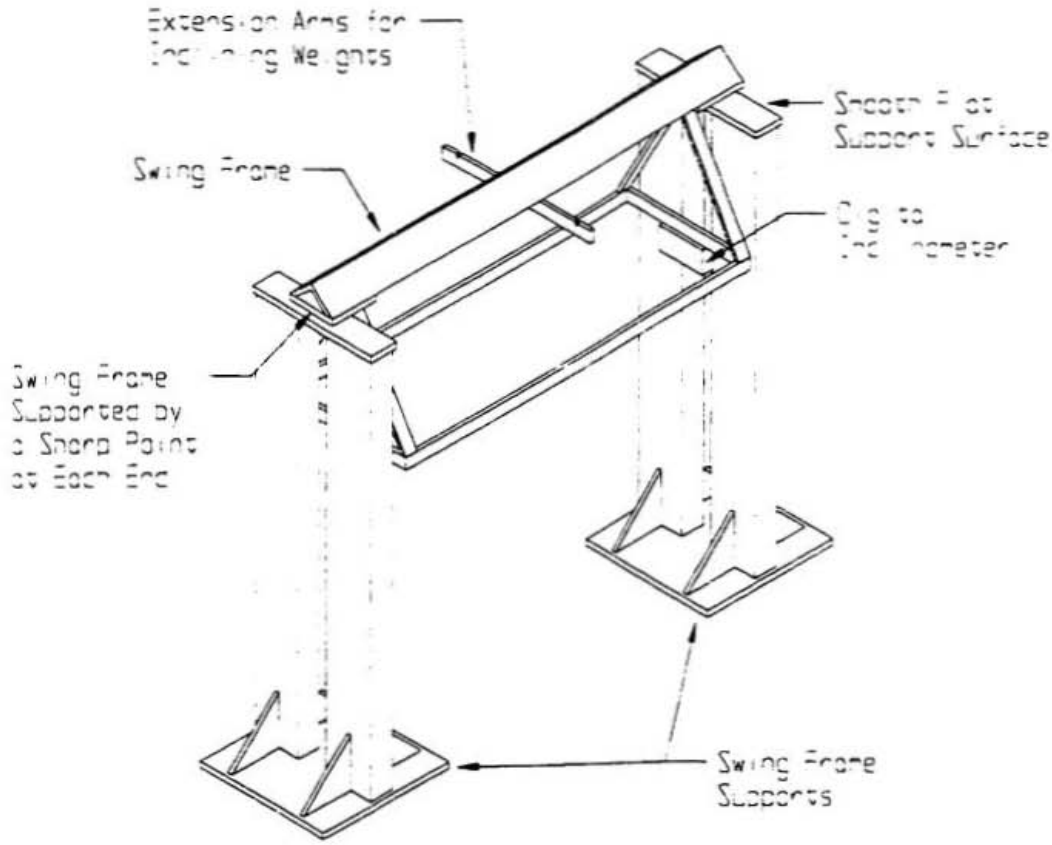

Figure A.1 – Swing Frame

A.2 Inclining Tests in Swing Frame

Once a given displacement and LCG were achieved, the VCG was determined with an inclining test. A known moment was applied to the swing frame causing it to tilt. The tilt angle was measured and the distance from the rotation point to the center of gravity of the model and swing frame were calculated. The VCG and weight of the empty swing frame. determined previously, were subtracted to give the VCG of the model. Example calculations and results from an inclining experiment are given below (see Figure A.2).

Known Values

$P = 0.996$ kg	- Applied load
$L = 0.099$ m	- Transverse distance to applied load
$Z = 0.026$ m	- Vertical distance to applied load
$H = 0.179$ m	- Distance from hull bottom to rotation point
$M_{frame} = 2.987$ kg	- Mass of swing frame
$VCG_F = 0.032$ m	- VCG of frame relative to rotation point
$M_{model} = 24.70$ kg	- Mass of model
$g = 9.807$ m/s^2	- Acceleration due to gravity

Calculated or Measured Values

θ	- Mean tilt angle
VCG_T	- VCG of model and frame relative to rotation point
VCG_M	- VCG of model relative to rotation point
VCG	- VCG of model relative to hull bottom
M_T	- Mass of frame and model
X_1	- Moment arm of applied load
X_2	- Resulting moment arm for F_T

Action	Tilt Angle	Change in Tilt Angle
Initial angle	0.00 deg.	-
Apply load	2.50 deg.	2.50 deg.
Remove load	0.05 deg.	2.45 deg.
Re-apply load	2.50 deg.	2.45 deg.
Remove load	0.00 deg.	2.50 deg.
	Mean angle =	2.475 deg.

Table A.1 – Inclining Results

Summing the moments on the tilted swing frame gives:

$$P \cdot X_1 = M_T \cdot X_2 \qquad [A.1]$$

where the moment arms are given by:

$$X_1 = Z \cdot \sin(\theta) + L \cdot \cos(\theta) \qquad [A.2]$$

$$X_2 = VCG_T \cdot \sin(\theta) \qquad [A.3]$$

Rearranging:

$$VCG_T = \frac{P}{M_T} \cdot \left(Z + \frac{L}{\tan(\theta)} \right) \qquad [A.4]$$

$VCG_T = 0.0837$ m

Subtracting the frame:

$$VCG_M = \frac{VCG_T \cdot M_T - VCG_F \cdot M_{frame}}{M_{model}} \qquad [A.5]$$

$VCG_M = 0.0934$ m

Changing reference from rotation point to hull bottom:

$$VCG = H - VCG_M \qquad [A.6]$$

$VCG = 0.0856$ m

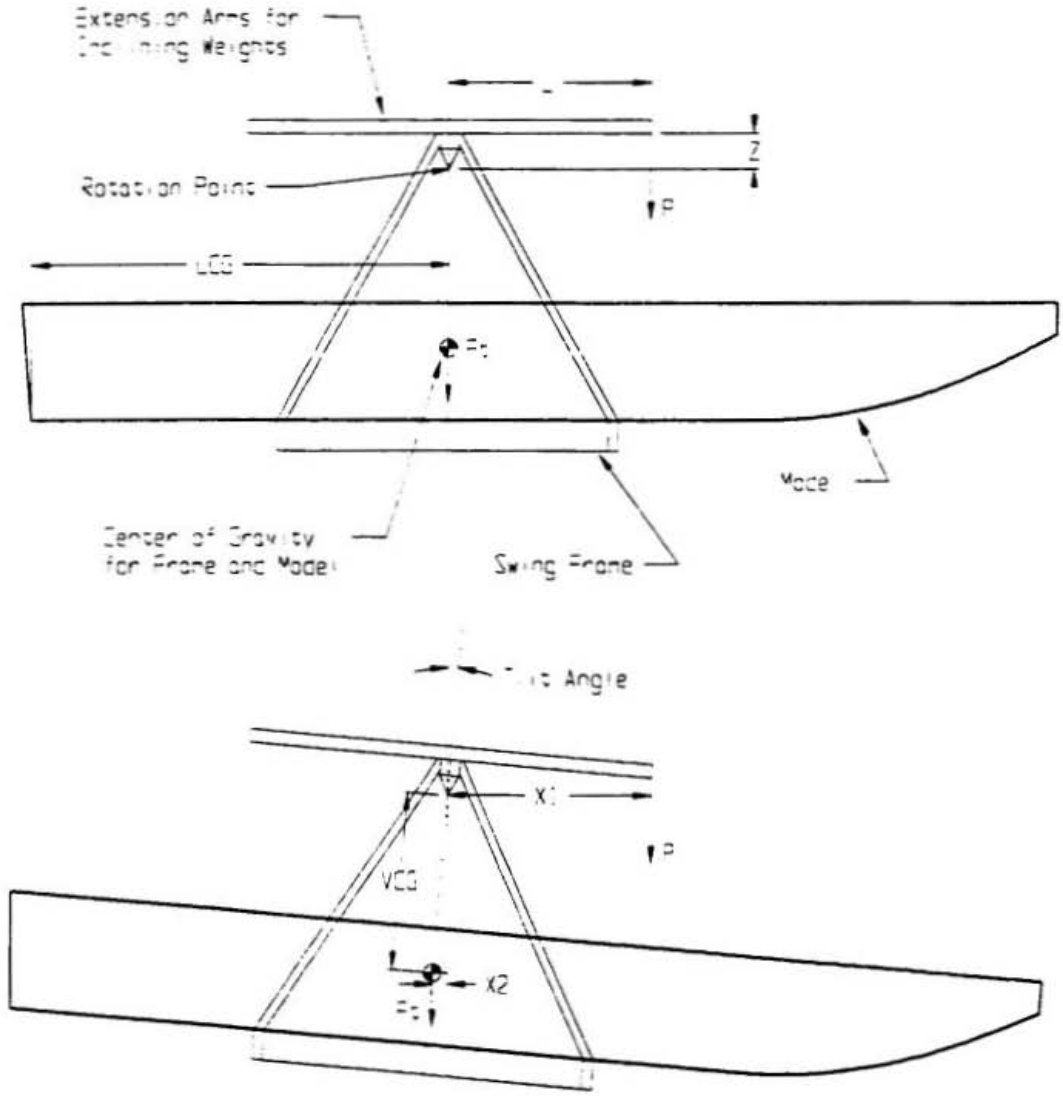

Figure A.2 – Inclining Experiment

A.3 Swing Tests

The mass moment of inertia of the model about its pitch axis was determined by a swing test which relied on the principles of a physical pendulum. A physical pendulum consists of any rigid body able to freely rotate about a horizontal axis. The swing frame and

model were given a small push to cause them to rock about the support points like a pendulum. The period of motion was determined by measuring the time the frame and model took to complete a number of swings. The inertia was then calculated using the equations based on the motion of a physical pendulum shown below.

The dynamic torsional equation for the swing frame and model is given by:

$$I_T \cdot \frac{d^2\theta}{dt^2} = -VCG_T \cdot (M_T \cdot g \cdot \sin(\theta)) \qquad [A.7]$$

where the mass moment of inertia I_T, is given by:

$$I_T = R_T^2 \cdot M_T \qquad [A.8]$$

Substituting and rearranging;

$$\frac{d^2\theta}{dt^2} + \frac{VCG_T}{R_T^2} \cdot g \cdot \sin(\theta) = 0 \qquad [A.9]$$

This is a non-linear differential equation whose solution leads to elliptic functions. An approximate solution can be made by assuming small oscillations.

$\sin(\theta) \approx \theta$ for small angles (the difference between θ and $\sin(\theta)$ is less than 1% if θ is less than 14°)

Approximating Equation A.9 gives:

$$\frac{d^2\theta}{dt^2} + \frac{VCG_T}{R_T^2} \cdot g \cdot \theta = 0 \qquad [A.10]$$

Solving yields:

$$\theta(t) = e^{i\sqrt{\frac{g \cdot VCG_T}{R_T^2}} \cdot t} = \cos\left(\sqrt{\frac{g \cdot VCG_T}{R_T^2}} \cdot t\right) + i \cdot \sin\left(\sqrt{\frac{g \cdot VCG_T}{R_T^2}} \cdot t\right) \qquad [A.11]$$

which can be expressed as:

$$\theta(t) = \cos\left(\sqrt{\frac{g \cdot VCG_T}{R_T^2}} \cdot t\right) \qquad [A.12]$$

The period of oscillation is therefore:

$$T = 2 \cdot \pi \cdot \sqrt{\frac{R_T^2}{g \cdot VCG_T}} \qquad [A.13]$$

The radius of gyration for the model and swing frame was calculated by re-arranging Equation A.13. The inertia of the frame was subtracted from the total and the model inertia was then expressed about its own VCG. Example calculations for a swing test are given below. Since the model's VCG was needed in these calculations, the inclining tests should be performed first.

Known Values

$H = 0.179$ m	- Distance from hull bottom to rotation point
$I_F = 0.048\ kg \cdot m^2$	- Inertia of frame about rotation point
$M_{model} = 24.70$ kg	- Mass of model
$g = 9.807\ m/s^2$	- Acceleration due to gravity

Calculated or Measured Values

T	- Mean swing period
VCG	- VCG of model relative to hull bottom
R_T	- Radius of gyration of model and frame about rotation points
I_T	- Inertia of frame and model about rotation points
I_{model}	- Inertia of model about rotation points
I	- Inertia of model about VCG

# of Cycles	Time (sec)	Average Period (sec)
10	21.26	2.126
10	21.59	2.159
10	21.49	2.149
10	21.71	2.171
10	21.52	2.152
10	21.61	2.161
	Mean Period =	2.153

Table A.2 – Swing Results

From Equation A.13:

$$R_T^2 = \left(\frac{T}{2 \cdot \pi}\right) \cdot g \cdot VCG_T \qquad [A.14]$$

$$R_T^2 = 0.0964 \text{ m}^2$$

$$I_T = (M_{frame} + M_{model}) \cdot R_T^2 \qquad [A.15]$$

$$I_T = 2.711 \text{ kg} \cdot \text{m}^2$$

Subtracting the inertia of swing frame:

$$I_{model} = I_T + I_{frame} \qquad [A.16]$$

$$I_{model} = R_T^2 \cdot M_T - R_{frame}^2 \cdot M_{frame} \qquad [A.17]$$

$$I_{model} = 2.663 \text{ kg} \cdot \text{m}^2$$

The inertia about the VCG of the model can then be found with:

$$I = I_{model} - M_{model} \cdot (H - VCG)^2 \qquad [A.18]$$

$$I = 2.457 \text{ kg} \cdot \text{m}^2$$

When performing swing and inclining tests, the weight and inertia of the swing frame should be made as small as possible with respect to the model. The swing frame weight should be less than about 10% of the model to ensure reasonable accuracy. There are other methods which can be used to determine the model inertia such as hanging wire methods (bifilar & trifilar).

APPENDIX B

Underwater Video Analysis

B.1 Underwater Video Analysis

In order to determine the full scale resistance from model scale measurements, the wetted surface area of the model at speed was required. This can be fairly straightforward for larger displacement vessels since, for a given ballast condition, the wetted surface area remains essentially constant through its operating speed range. However, planing vessels can undergo significant changes in wetted area with speed due to changes in its running trim and heave. Because of this, the wetted area of the model must be determined for each test.

Underwater video was taken during the bare hull resistance tests and the self propulsion tests discussed in Chapters 6 and 7 in order to determine the model's wetted surface area at speed. The cameras were located at the center of IMD's Clear Water Tank (see Section 6.4) pointing upwards at the path of the model. Two black and white cameras were used which recorded the model's passage on standard VHS tape which was then viewed frame by frame for analysis.

The model, as discussed in Section 6.1, was marked on the port side with a grid. Accurate measurements of the wetted area from video images depends on detailed information of the geometry of this grid. The grid consisted of a series of station lines and buttock lines as well as lines along the chine and centerline (see Figure 6.2). Due to the shape of the hull, grid squares approaching the bow became distorted and therefore define different areas than squares near the stern. The dimensions and areas of all grid squares were measured and recorded.

The video was examined with video equipment that enabled the model to be seen, frame by frame, as it passed through the cameras viewing area. These frames were then 'captured' as black and white digital images that could be viewed and edited by computer. The images were enhanced, where necessary, to increase the degree of definition of the grid lines and the water/air interface. The choice of black and white images over color images allowed a greater range of image enhancing options with the software. Figure B.1 shows an example digital image from the underwater video. The grid lines are enhanced for clarity and some details are identified.

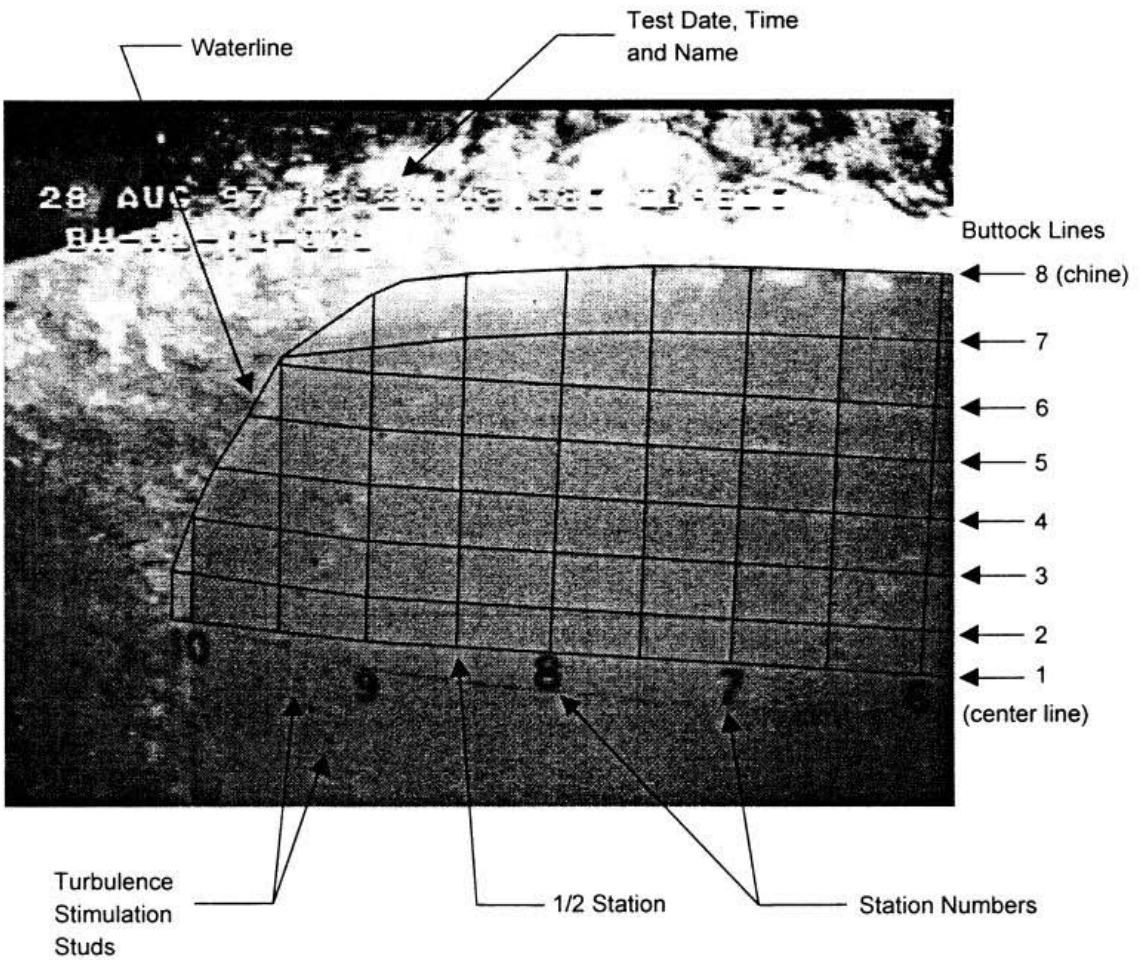

Figure B.1 – Underwater Video Image

The grid lines on the model were measured with software which can record positions and distances in units of pixels. Pixels, or picture elements, are small squares of various shades of gray which make up the black and white digital image. The wetted area of the model was mapped in pixels and then converted to physical units.

Converting from pixel units to physical length units must be done repeatedly in a given image. The two dimensional video image is of a three dimensional hull at an angle relative to the camera. Grid line measurements in the image are projected lengths which can change from position to position and from one orientation to another depending on their angle and distance from the camera. Since the true dimensions of the grid were known, many references were available for converting the pixel measurements to physical units.

The procedure for determining the wetted area from the images depends on the type of test being performed, the hull shape of the model, and the geometry of the grid markings used. The method used for these tests relied on measurements along the buttock lines. The pixel coordinates of three points were recorded for each buttock line of the grid. The first two points defined the distance between two successive station lines. The third point was located on the buttock line at the air/water interface. The number of whole stations before the air/water interface along that buttock line was also recorded. An example of this is given in Figure B.2 which shows the three points taken per buttock line.

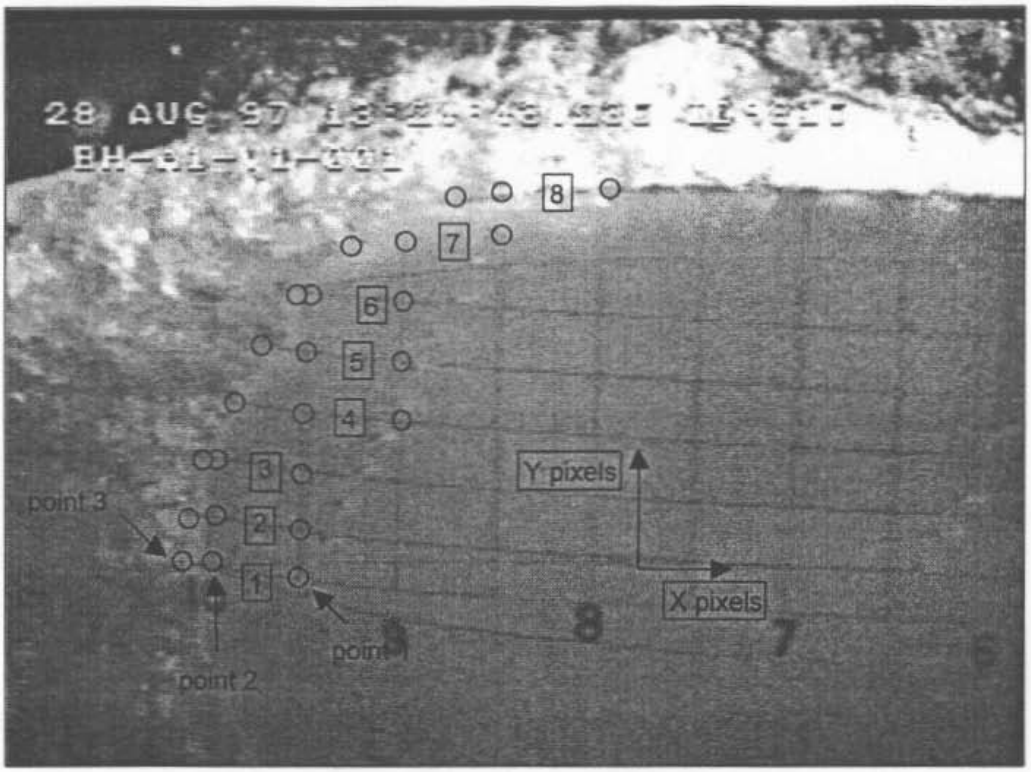

Figure B.2 – Reference Points on Underwater Video Image

The distances from point 1 to point 2, and from point 2 to point 3 were then calculated in pixels. Since the true distances between points 1 and 2 were known from the grid dimensions, they were used as a references for determining the true distances from points 2 and 3 as shown in Equation B.1. When converting from pixel measurements to model units, a reference should be taken as near, and as close to the same orientation as possible, to the projected line of interest.

$$\left(\text{dist}_{\,p2-p3}\right)_{\text{meters}} = \frac{\left(\text{dist}_{\,p2-p3}\right)_{\text{pixels}}}{\left(\text{dist}_{\,p1-p2}\right)_{\text{pixels}}} \cdot \left(\text{local grid spacing}\right)_{\text{meters}} \qquad \text{[B.1]}$$

This process was repeated for each buttock line. The wetted area was then calculated in two steps. First, the areas of all the whole wetted grid squares were summed. Next, the

area of the partial grid blocks were calculated based on their dimensions in model units. The areas were summed row by row as shown in Figure B.3 until the entire wetted surface was measured. Since the grid only covered one half of the model hull, the measured area was then doubled to account for the entire model. In addition to the wetted surface area, the wetted length along the center line and the wetted length along the chine (see Figure B.3) were also recorded for each test.

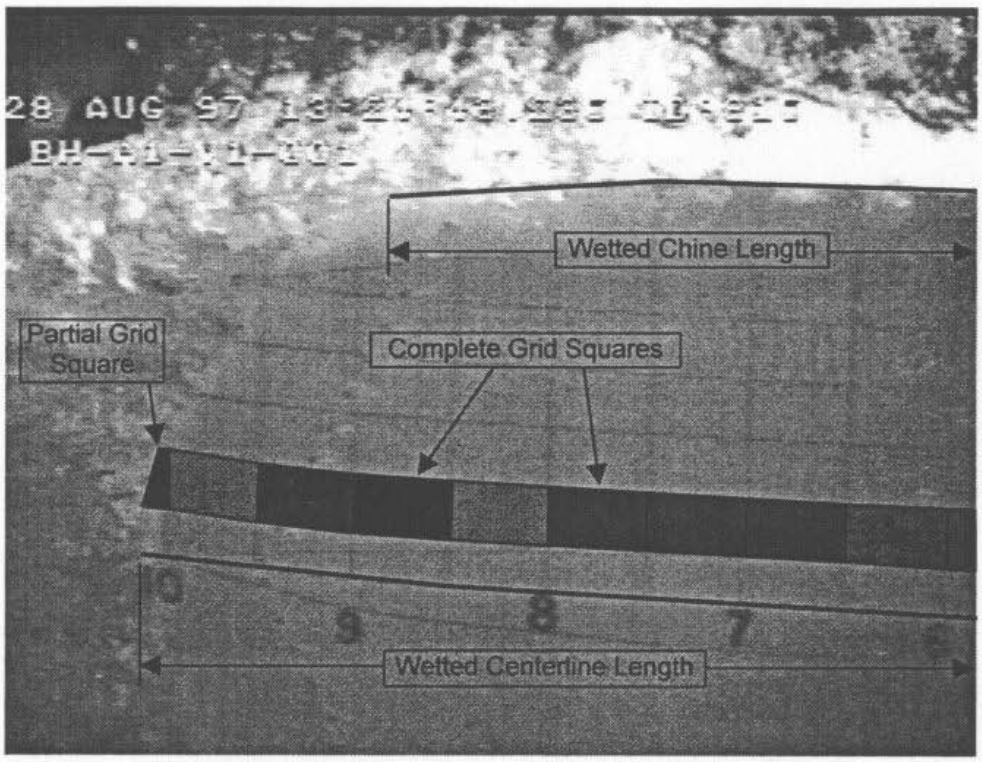

Figure B.3 – Area Measurement on Underwater Video Image

The accuracy of the video analysis is dependent on the clarity of the image, its resolution, and the proper use of references for conversions. The images were not always very clear; at high speeds the station lines tended to blur as a result of the camera's exposure time per frame. Shorter exposure times may help reduce blur, but will produce darker images since less light will reach the camera. Reference points were taken at the centers of

blurred lines for this analysis. In some cases it is possible to use a strobe as a light source which can provide instantaneous illumination of the hull bottom yielding images with virtually no blur yet high definition. This would, however, require the proper equipment and significant set-up time. Smaller grid sizes can help increase accuracy by defining the waterline with more points and by providing more references for conversions. This may require the cameras to be zoomed in closer to the hull. More cameras may then be needed to cover the hull area as well as more frames per test to analyze. This would result in a considerable increase in the time required to perform the video analysis. Higher resolution cameras, perhaps digital, could also improve the accuracy of this type of analysis.

The example still images from the bare hull resistance tests (ballast condition A2, no pitot tubes or tufts) are given in Figures B.5 to B.12. They illustrate the changes in wetted area as the vessel changes its running trim and heave with velocity. Figure B.4 shows the measured values of wetted area, wetted centerline length, and wetted chine length for that test series. Full scale values for wetted areas and lengths were calculated with simple geometric scaling as shown in Equation B.2 for areas and Equation B.3 for lengths.

$$A_S = \lambda^2 \cdot A_M \qquad [B.2]$$

$$L_S = \lambda \cdot L_M \qquad [B.3]$$

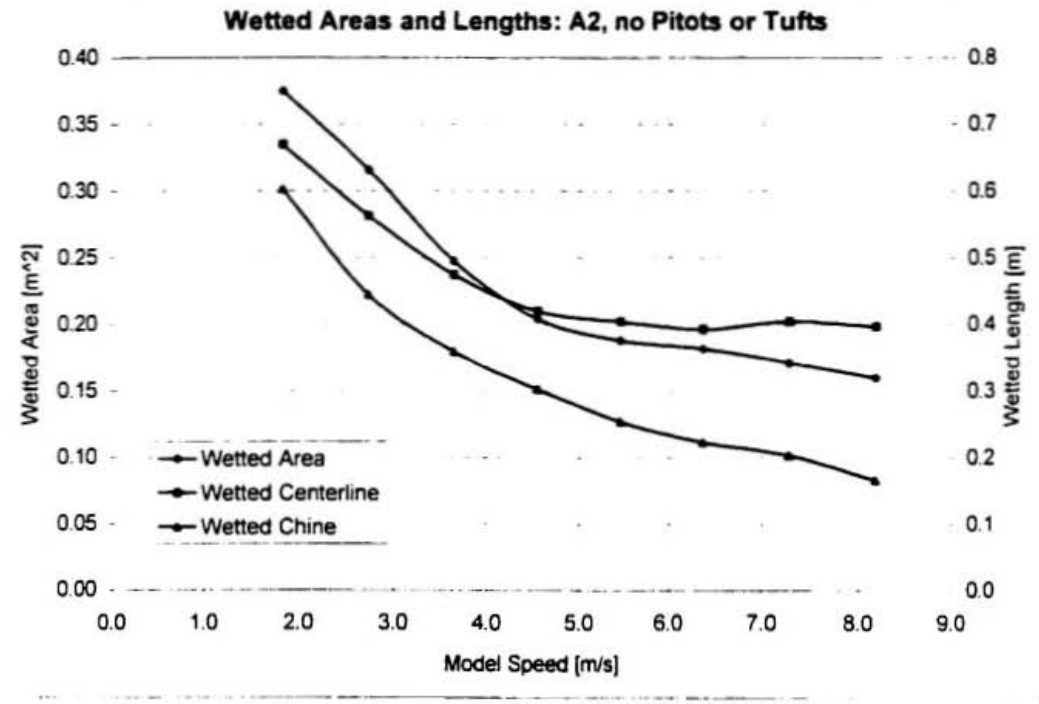

Figure B.4 – Wetted Areas and Lengths

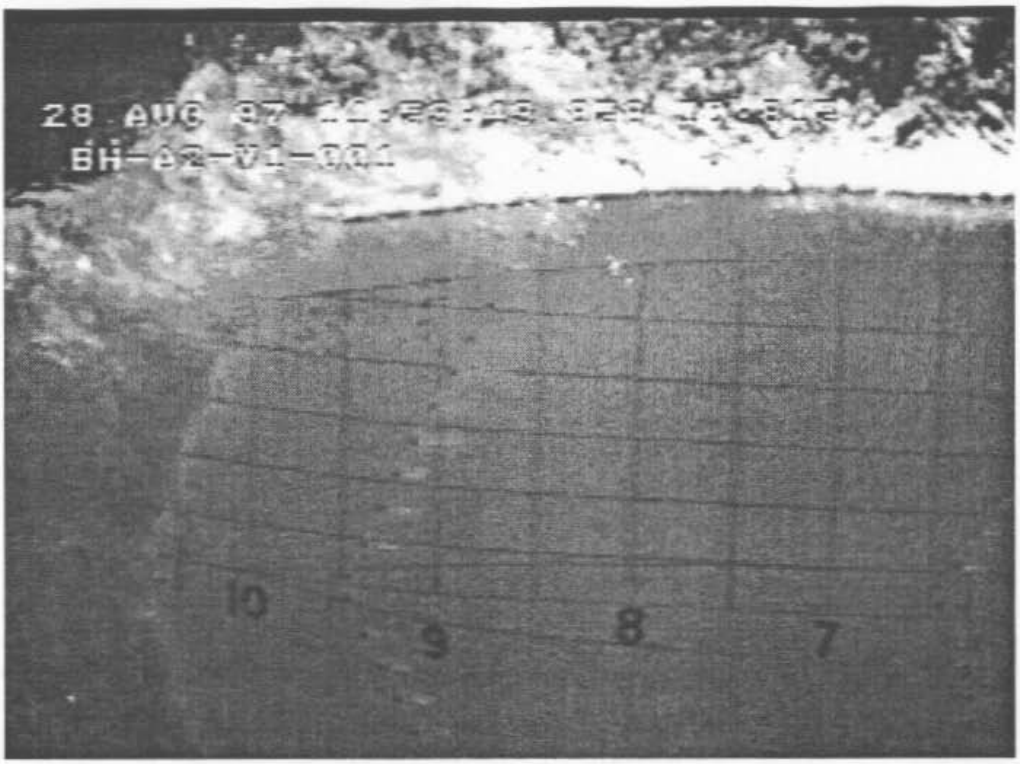

Figure B.5 – Video Image: Condition A2, 1.82 m/s

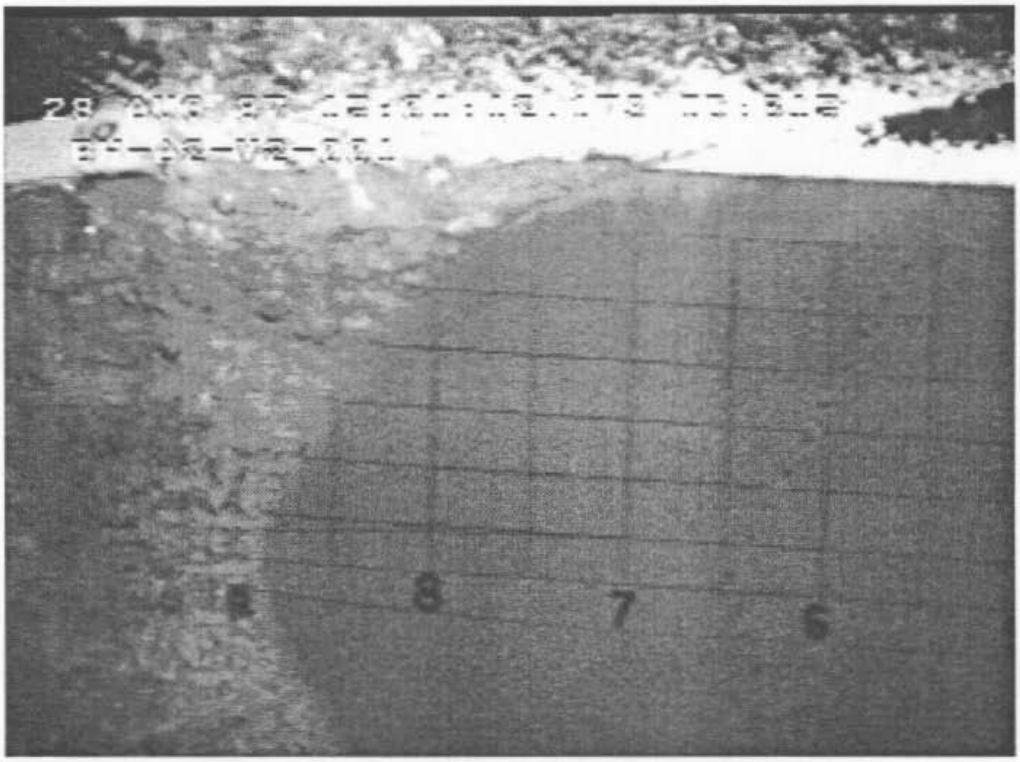

Figure B.6 – Video Image: Condition A2, 2.73 m/s

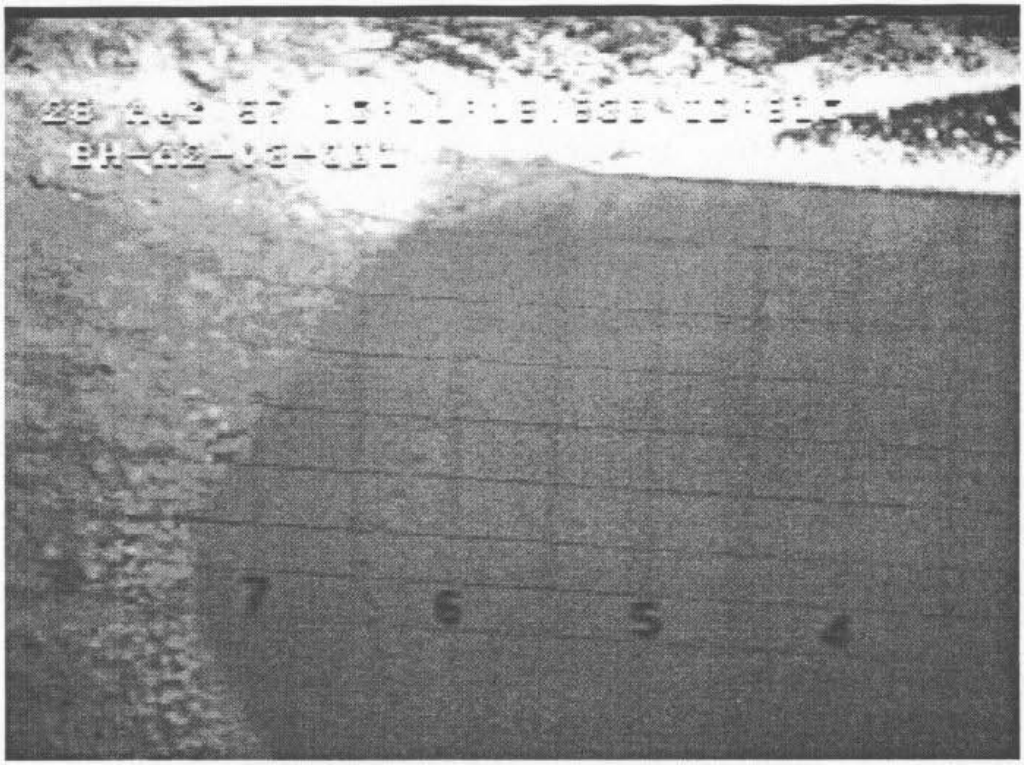

Figure B.7 – Video Image: Condition A2, 3.64 m/s

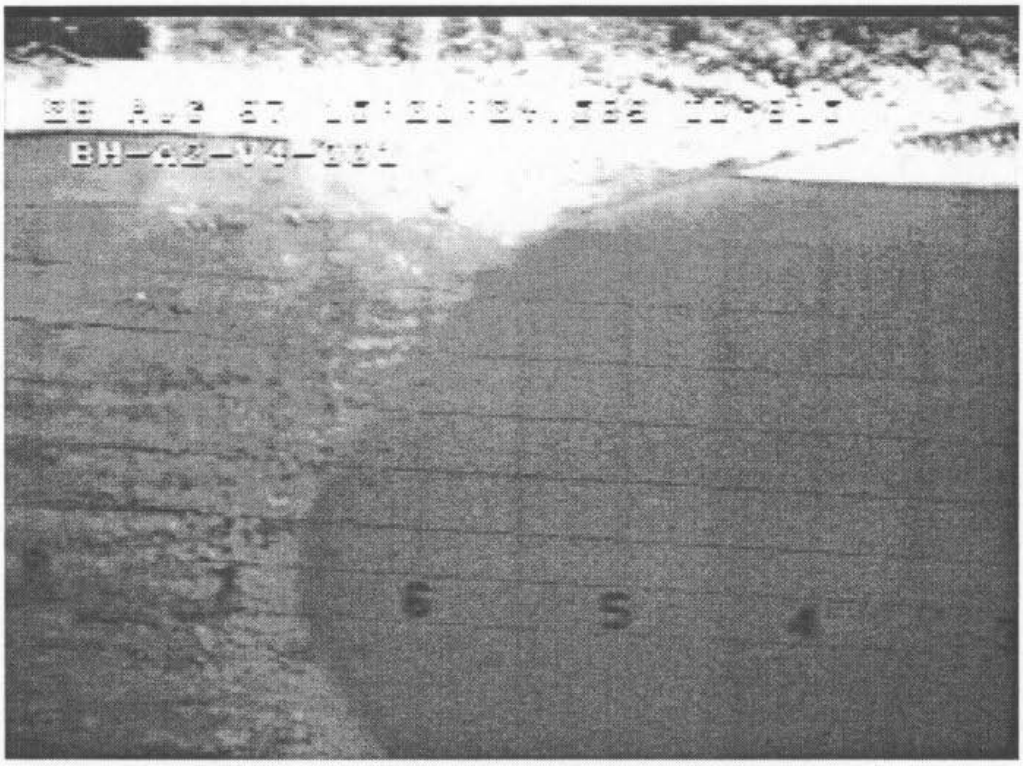

Figure B.8 – Video Image: Condition A2, 4.55 m/s

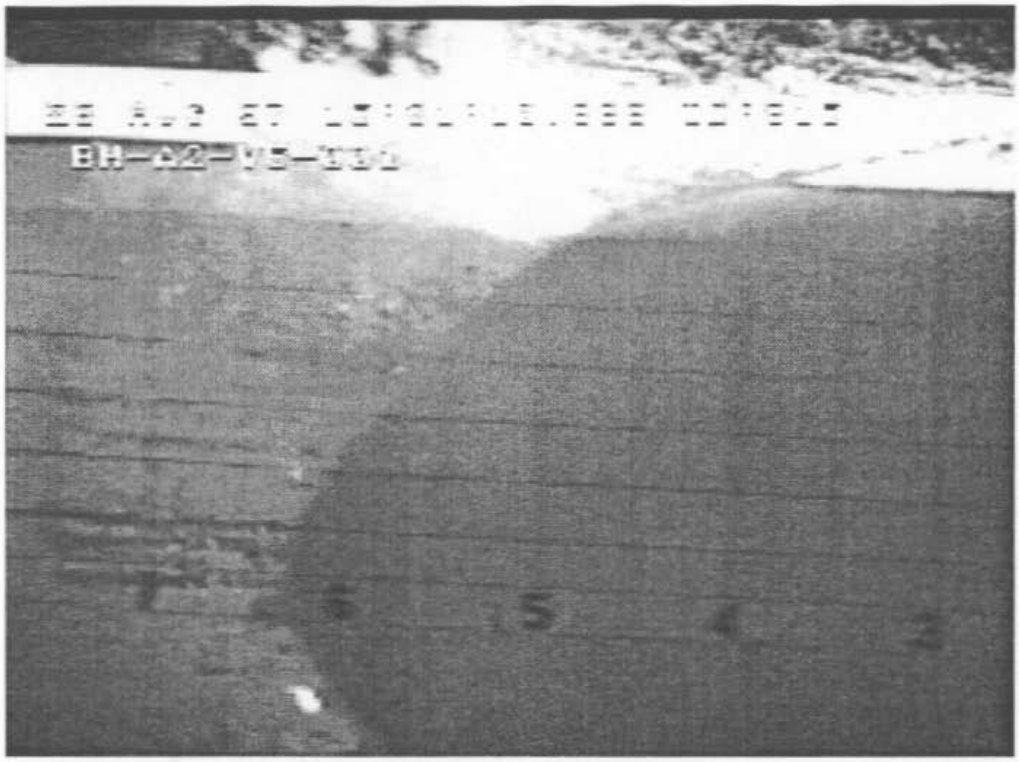

Figure B.9 – Video Image: Condition A2, 5.46 m/s

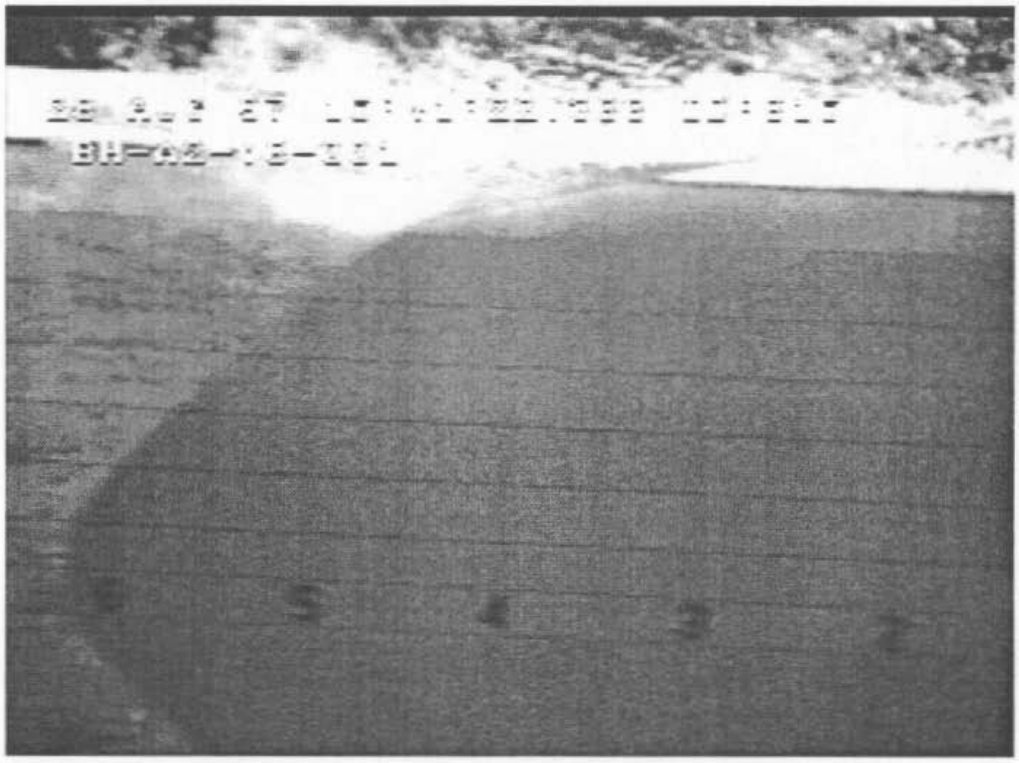

Figure B.10 – Video Image: Condition A2, 6.37 m/s

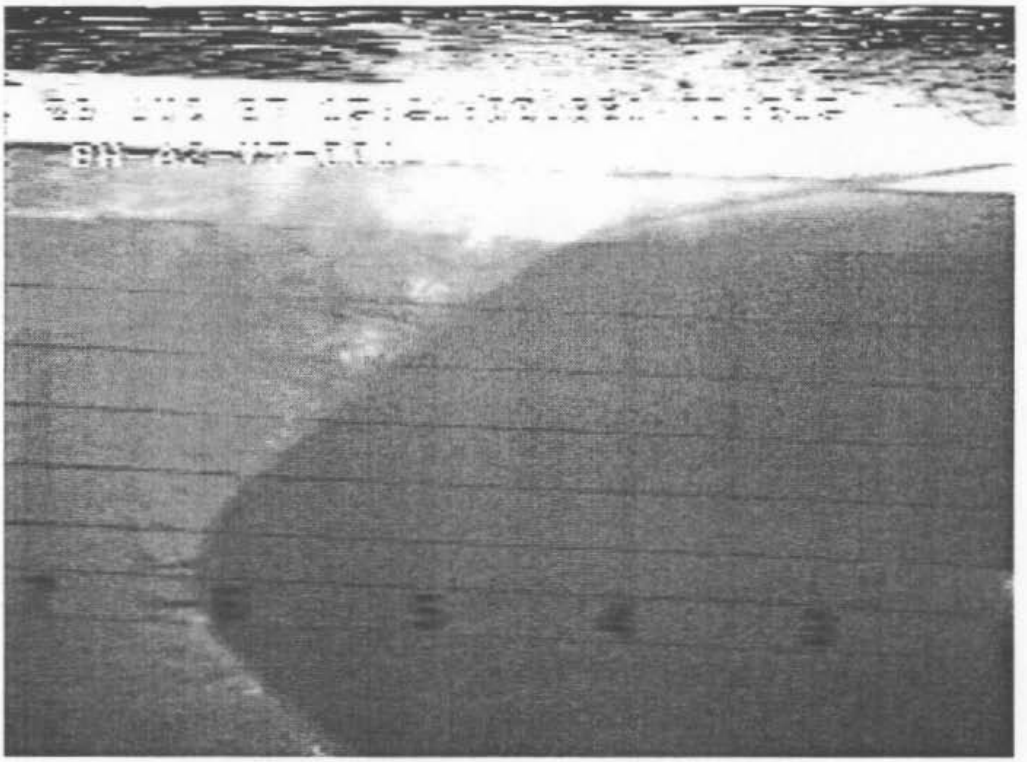

Figure B.11 – Video Image: Condition A2, 7.28 m/s

Figure B.12 – Video Image: Condition A2, 8.18 m/s

APPENDIX C

Dynamic Instability of Niagara Model

C.1 Dynamic Instability at Model Scale

During certain high speed tests with the Niagara model discussed in Chapters 6 and 7, the model experienced a form of instability called 'porpoising'. Porpoising, a phenomenon generally associated with planing craft at high speeds, is a motion where the vessel appears as if it were jumping in and out of the water. Minor cases of porpoising can be a discomfort to passengers while more severe cases can cause the vessel to leave the water entirely. This can cause stress to the hull structure at re-entry as well as extreme fluctuations of the loads on propulsion units. The porpoising behaviour seen during the tests with the Niagara model was only present at certain ballast conditions at the higher model speeds. The magnitude of the 'jumps' varied with tests from being barely noticeable, to the worst case where the heave post was travelling its full range and hitting the stops at both ends.

An illustration of this motion can be seen in Figure C.1 which shows the time history for the heave and carriage speed data of a run during the bare hull resistance tests (ballast condition C1, no pitot tubes or tufts, model speed 8.18 m/s). As the carriage reached its set speed, the oscillations began and rapidly increased to their maximum, and then decayed as the carriage decelerated.

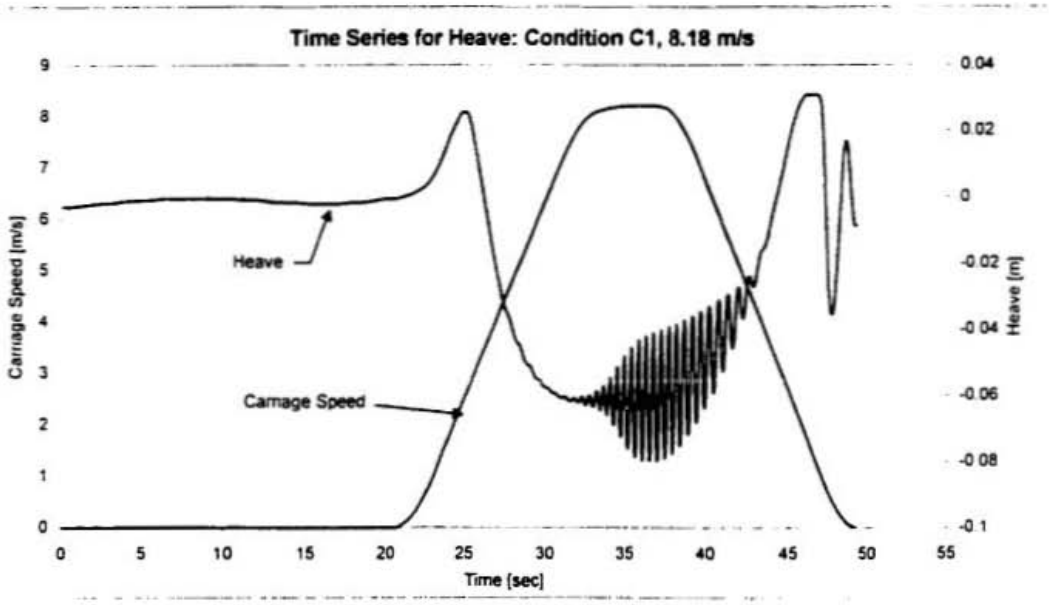

Figure C.1 – Time Series for Heave and Carriage Speed

The carriage maintained its constant velocity between 34 and 37 seconds on the time line. Focusing on this region, the oscillations of heave, trim and tow force can be seen more clearly as shown in the following figures.

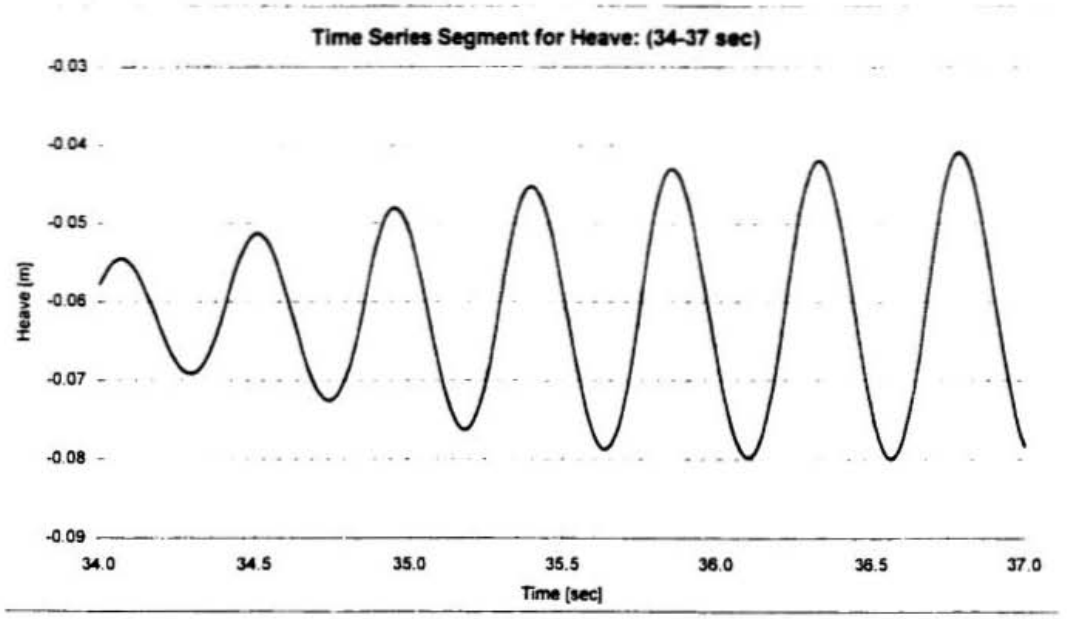

Figure C.2 – Time Series Segment for Heave

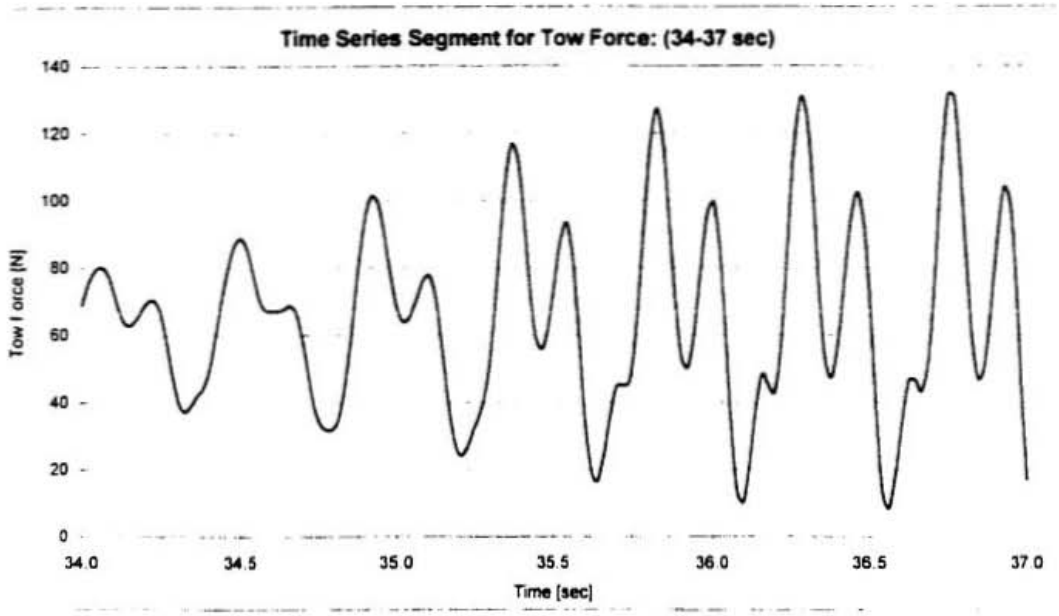

Figure C.3 – Time Series Segment for Tow Force

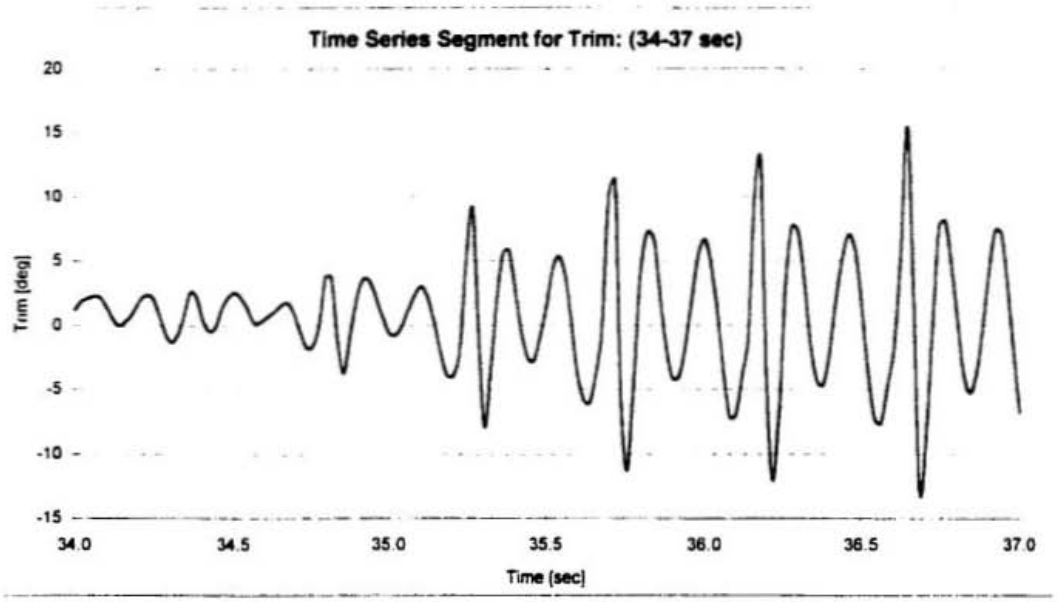

Figure C.4 – Time Series Segment for Trim

This time frame may be short, a function of the carriage run length, but was of sufficient length to distinguish the pattern of oscillation. Heave fluctuated at a single frequency

while trim and tow force contained several frequencies. These frequencies were identified by creating variance spectral density (VSD) plots of the time series segments, transforming the time domain data into the frequency domain by using fast Fourier transforms (FFT). The following figures show the VSD plots for heave, tow force and running trim of the time series segments plotted above.

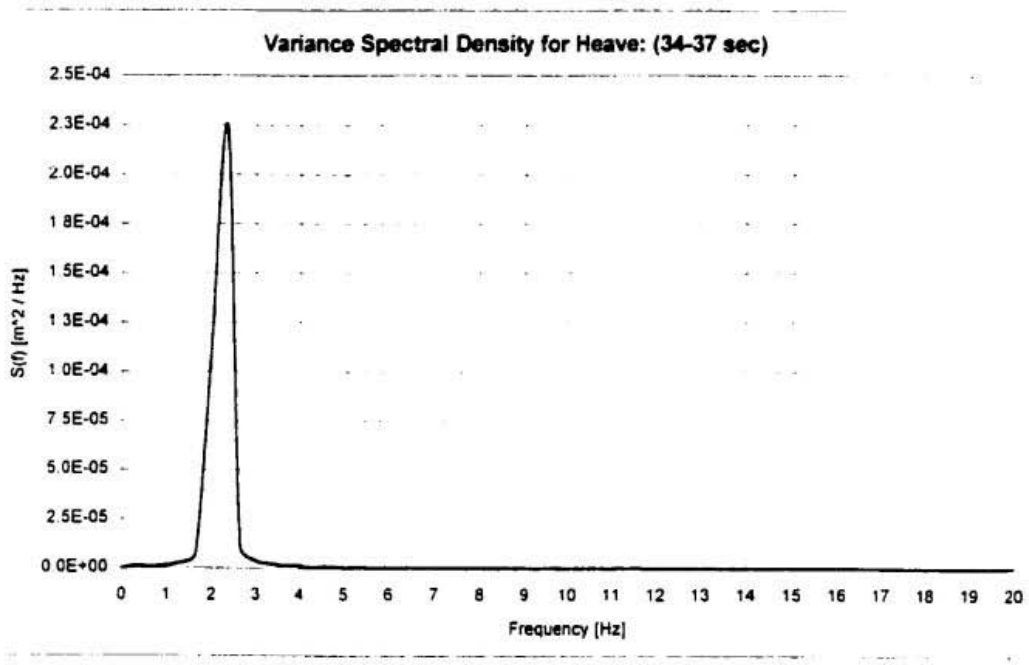

Figure C.5 – VSD for Heave

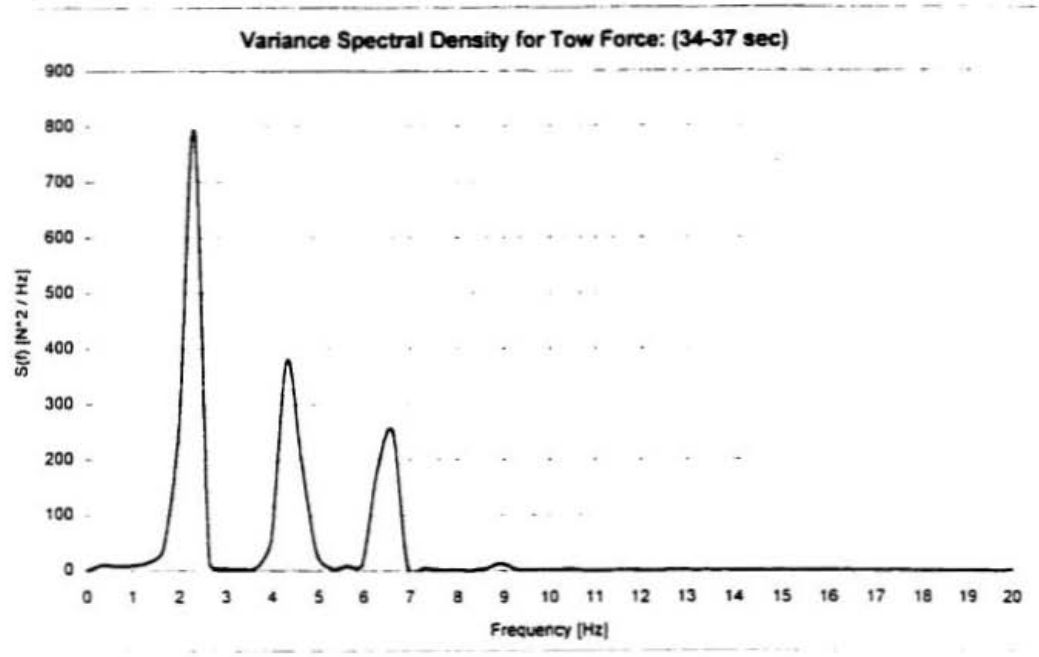

Figure C.6 – VSD for Tow Force

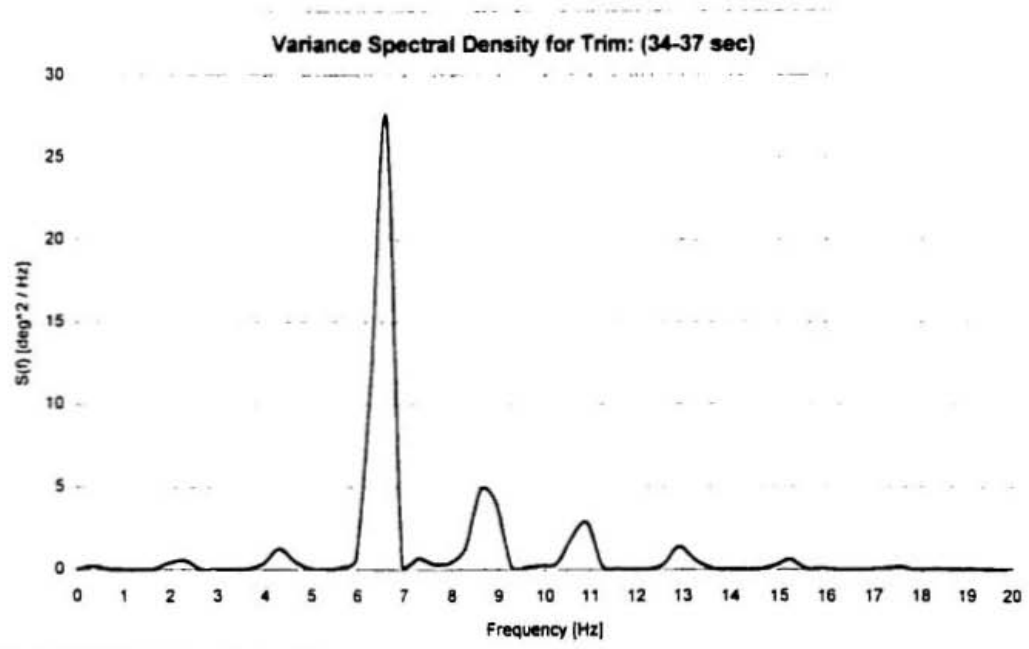

Figure C.7 – VSD for Trim

These plots show the dominant frequencies associated with the time series segments. The heave plot shows a single spike at about 2.2 Hz. The tow force VSD plot shows three distinct frequencies at 2.2 Hz, 4.4 Hz and 6.6 Hz, while the VSD plot for trim shows elements of several frequencies the dominant being at about 6.6 Hz. Information from the VSD plot can be used to derive an equation of the signal's behaviour. An example of this is shown in Equation C.17.

$$F(t) = F_0 + F_1 \cdot \sin(\phi_1 + \omega \cdot t) + F_2 \cdot \sin(\phi_2 + 2 \cdot \omega \cdot t) + F_3 \cdot \sin(\phi_3 + 3 \cdot \omega \cdot t) + \ldots \qquad [C.1]$$

where,

F_0 is a constant offset

ω_n are the frequencies determined by the VSD

F_n are the amplitudes associated with frequencies ω_n

ϕ_n are phase shifts

This porpoising phenomena was only present at model scale. The full scale vessels of this type have not reported problems with this type of instability. It is possible that this behaviour is sensitive to elements of the system which were not scaled. These would include flow effects related to Reynolds number and physical parameters such as the model's inertia. The model's weight and longitudinal center of gravity were scaled but the various rotational inertias were not as these tests did not consider accelerations due to motions. The yaw restraint and heave post were accounted for in the ballasting but would have a large effect (not measured) on the model's inertia. The vertical center of gravity was not precisely matched either due to physical restrictions in the model. The porpoising of the model was shown to be sensitive to ballast condition which had an effect on the onset and intensity of the motions, though the instability was most sensitive to model speed.

APPENDIX D

Resistance Scaling of Niagara Model

D.1 Resistance at Model and Full Scale

As discussed in Chapter 4, full scale resistance cannot be determined directly from model scale data since not all components of the resistance were scaled properly. The model resistance was instead separated into components that were scaled or calculated individually and then re-combined to form the full scale result. The following outlines this procedure.

The velocity of the model was calculated from full scale speeds using equivalent Froude numbers as discussed in Chapter 4. Froude numbers for full and model scale are shown below in Equation D.1.

$$Fn \equiv \frac{V_M}{\sqrt{g \cdot L_M}} = \frac{V_S}{\sqrt{g \cdot L_S}} \qquad [D.1]$$

where L_M and L_S are the characteristic lengths for the model and ship respectively.

For displacement ships, the characteristic length is conventionally taken as the length of the waterline, considered independent of vessel speed. Planing vessels, however, experience considerable changes in running trim and draft at speed, resulting in variations of waterline length. The ITTC recommends that the characteristic length, L_M, of planing vessels be instead defined as an average of the wetted keel length and the wetted chine length as shown in Equation D.2. These lengths were determined from underwater video of the hull during tests (see Appendix B).

$$L_M = \frac{L_K + L_C}{2} \qquad [D.2]$$

where L_K and L_C are the wetted lengths for the keel and chine respectively.

During the bare hull resistance tests, the model was propelled by the carriage. The force needed to tow the model, as measured by the load cell in the gimbal, was equal to the total resistance of the model at the test speed. The differences in resistance at model and full scale were accounted for by separating the model resistance into components. These components, shown in Equation D.3, were then analyzed independently.

$$R_{MT} = R_{MF} + R_{MW} + R_{MA} + R_{MP} \qquad [D.3]$$

where,

R_{MT} is the total model resistance

R_{MW} is the wave-making or residual resistance

R_{MF} is the frictional resistance

R_{MA} is the air resistance

R_{MP} is the parasitic resistance due to turbulence studs, flow visualization tufts and/or pitot tubes

It is conventional to express these components in a non-dimensional form. This was done using the equation for non-dimensional force derived in Chapter 4.

$$C_{MT} = C_{MF} + C_{MW} + C_{MA} + C_{MP} \qquad [D.4]$$

given that:

$$C_{MX} = \frac{R_{MX}}{\frac{1}{2} \cdot \rho_M \cdot A_M \cdot V_M^2} \qquad [D.5]$$

where,

C_{MX} is the non-dimensional resistance coefficient (C_{MT}, C_{MW}, C_{MF}, C_{MA} or C_{MP}) for the model resistance component with matching subscripts (R_{MX})

R_{MX} is a given model resistance component (R_{MT}, R_{MR}, R_{MF}, R_{MA} or R_{MP})

ρ_M is the density of water used in the model tests

A_M is the wetted surface area of the model at speed

V_M is the model speed

The full scale resistance can be expressed in a similar form:

$$C_{ST} = C_{SF} + C_{SW} + C_{MA} \qquad [D.6]$$

Since Froude scaling was used, the only resistance coefficient that had the same value at both model and full scale was the wave-making resistance as shown in Equation D.7. All other resistance coefficients were calculated independently at both scales.

$$C_{SW} = C_{MW} \qquad [D.7]$$

It should be noted that forms of Froude number, characteristic length, and non-dimensional force other than those given in Equations D.1 to D.3 can be derived and used in the scaling procedures. The choice would depend on the form that is most convenient for a particular application. The separation of resistance into components can also take other forms. Depending on the specific application, more components may be used, or some components may be combined for convenience.

D.1.1 Resistance due to Instrumentation

It is apparent that R_{MP}, the parasitic resistance due to instrumentation on the model, is not present at full scale. This component of resistance is usually small relative to the total and was estimated by the following:

$$R_{MP} = \sum_{i=1}^{n} \frac{1}{2} \cdot C_{Di} \cdot A_{Pi} \cdot V_M^{\,2} \qquad [D.8]$$

where,

n is the number of types of instrumentation whose parasitic resistance makes up R_{MP} such as pitot tubes, turbulence studs, or flow visualization tufts

C_{Di} is the coefficient of drag assigned to each type of instrumentation

A_{Pi} is the projected areas for each type of instrumentation

C_{MP} was then determined using Equation D.5. The projected areas and coefficients of drag used for calculating this approximation of R_{MP} for the Niagara model are given in Table D.1.

Type	Projected Area	C_D
Turbulence stud	10.1 mm^2	0.6
Flow visualization tuft	4.0 mm^2	0.8
Pitot-1, position 1	22.1 mm^2	0.7
Pitot-2, position 1	40.5 mm^2	0.7
Pitot-3, position 1	58.9 mm^2	0.7
Pitot-1, position 2	6.9 mm^2	0.7
Pitot-2, position 2	16.1 mm^2	0.7
Pitot-3, position 2	20.7 mm^2	0.7

Table D.1 – Projected Areas and Coefficients of Drag for Instrumentation

D.1.2 Air Resistance

The air resistance was also slightly different at model scale than at full scale. Firstly, the model did not include any superstructure, which meant that the projected areas of the model and the full scale vessel did not match. Also, the head wind faced by the model towed by the carriage was greater than that faced by the full scale vessel moving in calm air (if scaled directly). The carriage moving along the tank pushes a large volume of air which is forced around it. The air speeds up under the carriage, effectively increasing the head wind seen by the model. Figure D.1 shows the air speed data measured during the bare hull resistance tests (see Chapter 6). It can be seen that the relative air speed near the model was approximately 31% higher than the carriage speed.

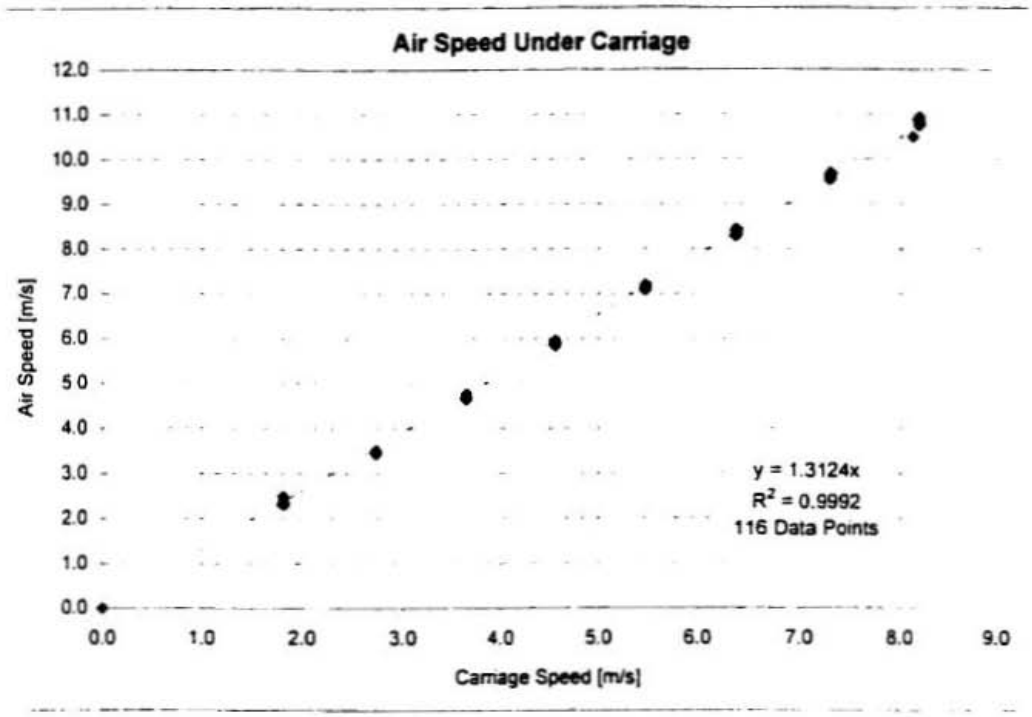

Figure D.1 – Air Speed vs. Carriage Speed

The method for estimating air resistance was similar to that for parasitic drag. It was an approximation which assigned a coefficient of drag to the hull shape and used the vessel's projected area, air speed, and air density as shown in Equations D.9 and D.10. The projected area of both the model and full scale vessel were calculated as functions of trim and heave for the purposes of this estimation. This method was found to be sufficiently accurate as air resistance constituted only a small portion of the overall resistance.

$$R_{MA} = \frac{1}{2} \cdot C_{DM} \cdot A_{MP} \cdot V_M^{\,2} \qquad [D.9]$$

$$R_{SA} = \frac{1}{2} \cdot C_{DS} \cdot A_{SP} \cdot V_S^{\,2} \qquad [D.10]$$

The non-dimensional coefficients C_{MA} and C_{SA}, for R_{MA} and R_{SA} respectively, can be determined from Equation D.5.

D.1.3 Frictional Resistance

The frictional resistance caused by water flowing over the surface of a hull has been found to be related to the Reynolds number of that flow. As mentioned, these experiments used Froude scaling, so the Reynolds number at model and full scale were equivalent. The corresponding skin friction coefficients were therefore different as well. Considerable experimental work has gone into determining the relationship between skin friction and Reynolds number to the point where several empirical equations have been derived. These relationships were used to estimate the skin friction coefficients at both model scale and full scale.

However, as discussed in Section 4.3, the skin friction is also dependent on flow regime. Figure D.2 (Lewis, 1988) shows an empirical relationship between friction coefficient and Reynolds number for both turbulent and laminar flow. Laminar flow favors lower Reynolds numbers while turbulent flow is predominant at higher Reynolds numbers. The transitional lines shown in the figure are typical but the exact nature of the transition depends on the specific characteristics of that flow.

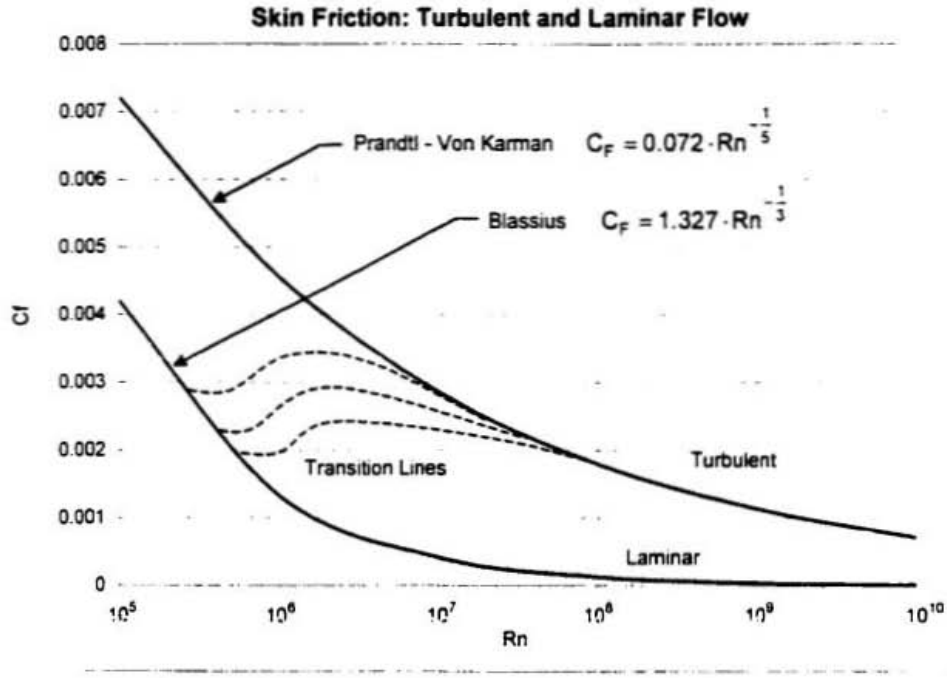

Figure D.2 – Skin Friction: Turbulent and Laminar Flow

The frictional resistance coefficients at model (C_{FM}) and full scale (C_{FS}) for the bare hull resistance tests were calculated according to the Schoenherr or 1947 ATTC (American Towing Tank Conference) line, given in Equation D.11, which is based on the results of towing flat plates with turbulent flow (Lewis, 1988).

$$\frac{0.242}{\sqrt{C_F}} = \log_{10}(Rn \cdot C_F) \qquad [D.11]$$

with Reynolds numbers expressed as:

$$Rn_M = \frac{V_M \cdot L_M}{\upsilon_M} \qquad [D.12]$$

for model scale and for full scale shown below.

$$Rn_S = \frac{V_S \cdot L_S}{\upsilon_S} \qquad [D.13]$$

D.2 Bare Hull Resistance Test Results

The results for resistance from the bare hull resistance tests were analyzed as described in the preceding sections. The full scale resistance was calculated by combining the appropriate resistance coefficients.

Rearranging Equation D.4 yields:

$$C_{MW} = C_{MT} - C_{MA} - C_{MP} - C_{MF} \qquad [D.14]$$

Using Equations D.5 and D.6, the expression for the full scale resistance coefficient becomes:

$$C_{ST} = C_{SF} + C_{MW} + C_{SA} \qquad [D.15]$$

The full scale form of Equation D.15 is then used to determine the full scale resistance:

$$R_{ST} = \frac{1}{2} \cdot \rho_S \cdot A_S \cdot V_S^2 \cdot C_{ST} \qquad [D.16]$$

Example results from the bare hull resistance tests (ballast condition B1, no pitot tubes or tufts) are listed in Tables D.5 to D.6. Also shown are the intermediate calculations based on the equations discussed. Resistance components determined from the calculations are plotted in Figures D.3 to D.5.

The characteristic resistance curve of a planing craft is clearly seen in the plots of resistance at model scale (Figure D.3) and at full scale (Figure D.5). These plots also show the relative contributions to the overall resistance made by the separate components. The wave making resistance was the primary component and drives the shape of the total resistance curves. The frictional resistance increased fairly steadily with

increasing speed. It can be seen in both plots that the air resistance components are small and could be considered negligible. The resistance due to turbulence studs (R_{SM}), which is the abbreviated from of the parasitic resistance due to instrumentation (R_{PM}), goes to zero after the third point. This was a problem in many of the tests. The running trim was greater than expected, lifting the model high enough to clear both rows of turbulence studs. The model scale Reynolds numbers at these speeds were high enough to ensure turbulence without the studs. Figure D.4 is a plot of the resistance coefficients at model and full scale and clearly shows the difference in the total resistance coefficients due to the frictional components.

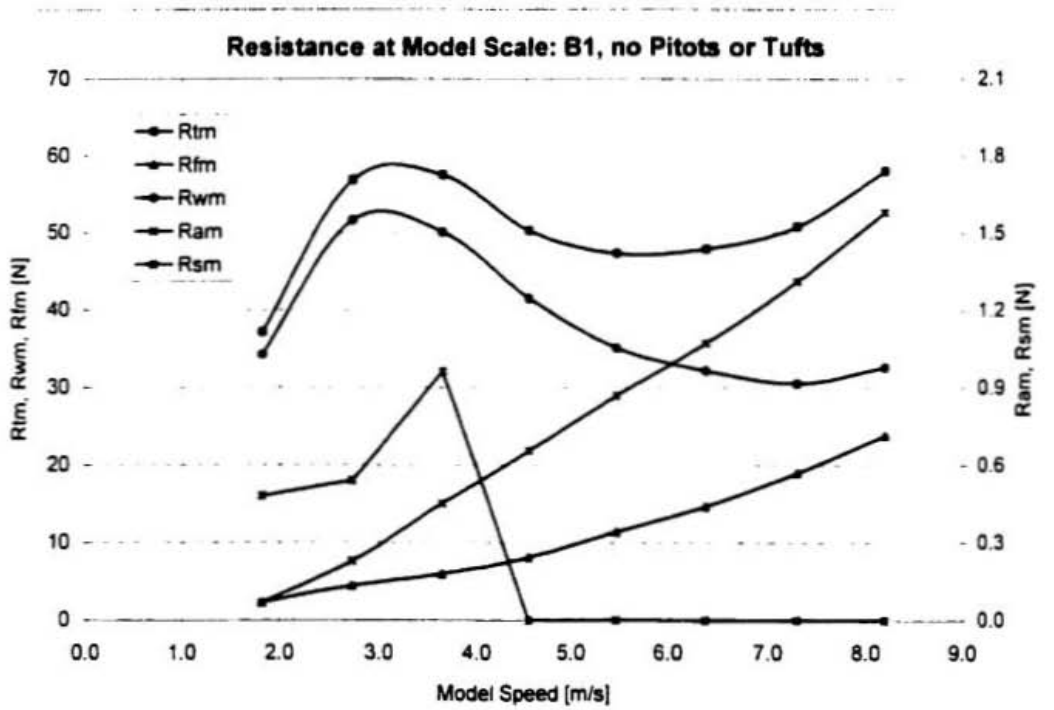

Figure D.3 – Resistance at Model Scale

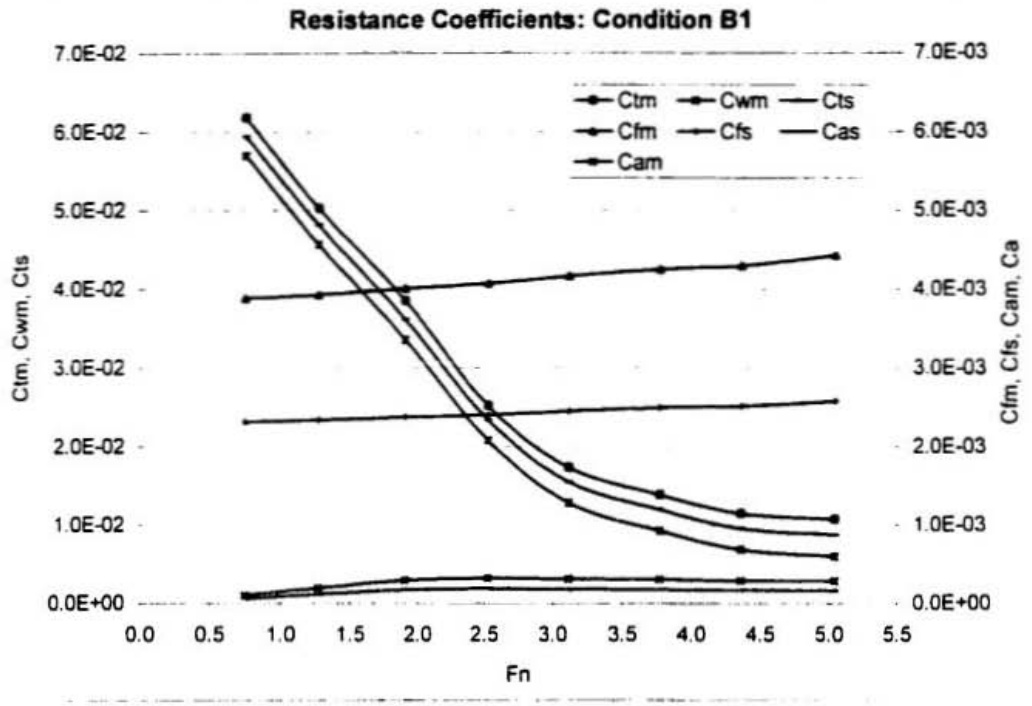

Figure D.4 – Resistance Coefficients

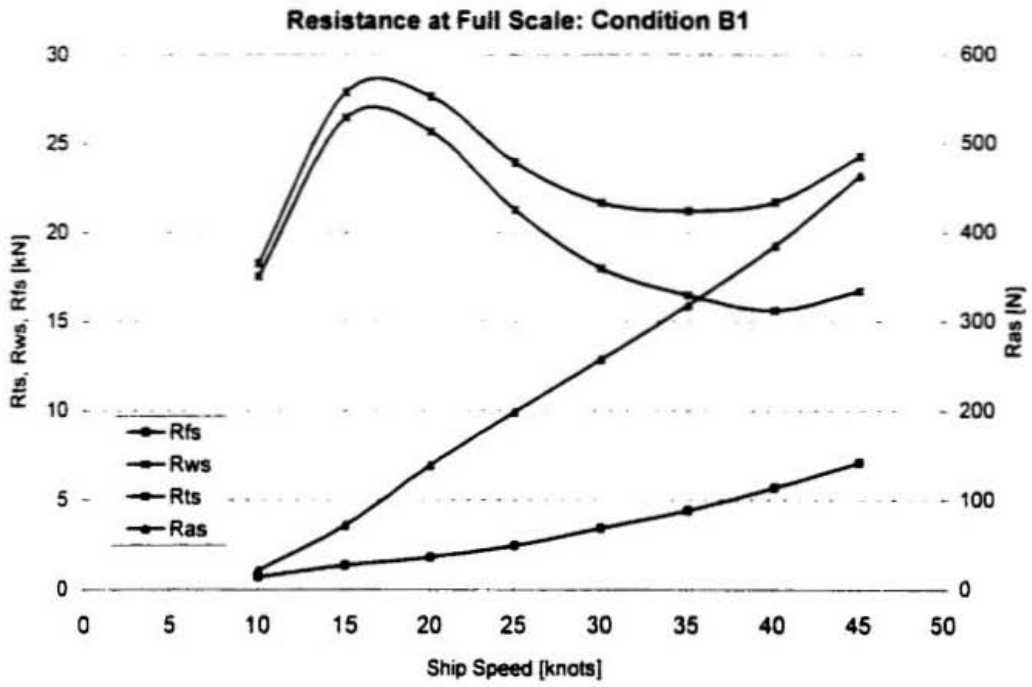

Figure D.5 – Resistance at Full Scale

Test Results

Run Name	Speed [m/s] [m/s]	Tow Force [N]	Δ Trim [deg]	Δ Heave [mm]	Wind [m/s]	Wetted Area [m^2]	Wetted Keel [m]	Wetted Chine [m]	L_M [m]	Proj Area [m^2]	# of Studs [-]
BH_B1_V1_001	1 82	37 14	3 48	28 0	2 33	0 36	0 66	0 54	0 603	0 094	48
BH_B1_V2_001	2 73	56 91	6 92	18 9	3 48	0 30	0 52	0 42	0 471	0 142	24
BH_B1_V3_001	3 64	57 56	6 74	-8 6	4 70	0 23	0 42	0 33	0 373	0 155	24
BH_B1_V4_001	4 55	50 32	4 75	-30 9	5 92	0 19	0 38	0 28	0 332	0 141	0
BH_B1_V5_001	5 46	47 35	3 19	-41 9	7 18	0 18	0 38	0 25	0 314	0 127	0
BH_B1_V6_001	6 38	47 99	2 13	-45 3	8 38	0 17	0 37	0 21	0 292	0 115	0
BH_B1_V7_001	7 29	50 86	1 41	-46 6	9 63	0 17	0 37	0 20	0 285	0 107	0
BH_B1_V8_001	8 19	58 06	0 79	-52 1	10 83	0 16	0 35	0 19	0 269	0 102	0

Table D.2 – Resistance Calculations Part 1

Calculations at Model Scale

Run Name	Fn [-]	C_{TM} [-]	Rn_M [-]	C_{FM} [-]	R_{FM} [N]	R_{AM} [N]	R_{SM} [N]	R_{WM} [N]	C_{AM} [-]	C_{SM} [-]	C_{WM} [-]
BH_B1_V1_001	0 75	6 18E-02	9 70E+05	3 89E-03	2 34	0 07	0 48	34 26	1 12E-04	7 99E-04	5 70E-02
BH_B1_V2_001	1 27	5 03E-02	1 14E+06	3 93E-03	4 45	0 23	0 54	51 69	2 02E-04	4 78E-04	4 57E-02
BH_B1_V3_001	1 90	3 86E-02	1 20E+06	4 01E-03	5 99	0 45	0 96	50 16	3 03E-04	6 45E-04	3 36E-02
BH_B1_V4_001	2 53	2 52E-02	1 34E+06	4 07E-03	8 12	0 66	0 00	41 54	3 29E-04	0 00E+00	2 08E-02
BH_B1_V5_001	3 11	1 74E-02	1 52E+06	4 17E-03	11 37	0 87	0 00	35 11	3 19E-04	0 00E+00	1 29E-02
BH_B1_V6_001	3 77	1 39E-02	1 65E+06	4 26E-03	14 70	1 07	0 00	32 22	3 11E-04	0 00E+00	9 33E-03
BH_B1_V7_001	4 36	1 15E-02	1 84E+06	4 30E-03	19 00	1 31	0 00	30 55	2 98E-04	0 00E+00	6 92E-03
BH_B1_V8_001	5 04	1 08E-02	1 95E+06	4 44E-03	23 84	1 58	0 00	32 64	2 94E-04	0 00E+00	6 07E-03

Table D.3 – Resistance Calculations Part 2

Calculations at Full Scale

Run Name	Ship Speed [m/s]	Ship Speed [knots]	Δ Trim [deg]	Δ Heave [m]	Wind [m/s]	Wetted Area [m^2]	Wetted Keel [m]	Wetted Chine [m]	L_S [m]	Proj Area [m^2]
BH_B1_V1_001	5 1	10	3 48	0 224	5 1	23 25	5 30	4 34	4 82	7 08
BH_B1_V2_001	7 7	15	6 92	0 151	7 7	19 46	4 19	3 34	3 77	7 39
BH_B1_V3_001	10 3	20	6 74	-0 069	10 3	14 40	3 35	2 62	2 98	8 33
BH_B1_V4_001	12 9	25	4 75	-0 247	12 9	12 30	3 04	2 27	2 65	9 09
BH_B1_V5_001	15 5	30	3 19	-0 335	15 5	11 68	3 02	2 00	2 51	9 46
BH_B1_V6_001	18 0	35	2 13	-0 362	18 0	10 86	2 96	1 72	2 34	9 58
BH_B1_V7_001	20 6	40	1 41	-0 373	20 6	10 63	2 95	1 61	2 28	9 62
BH_B1_V8_001	23 2	45	0 79	-0 417	23 2	10 25	2 77	1 54	2 15	9 81

Table D.4 – Resistance Calculations Part 3

Calculations at Full Scale

Run Name	Fn [-]	Rn_S [-]	C_{FS} [-]	R_{FS} [kN]	R_{AS} [kN]	C_{AS} [-]	C_{WS} [-]	R_{WS} [kN]	R_{TS} [kN]	C_{TS} [-]
BH_B1_V1_001	0 75	2 25E+07	2 32E-03	0 71	21 02	6 83E-05	5 70E-02	17 54	18 28	5 94E-02
BH_B1_V2_001	1 27	2 64E+07	2 34E-03	1 36	71 91	1 24E-04	4 57E-02	26 47	27 90	4 82E-02
BH_B1_V3_001	1 90	2 79E+07	2 38E-03	1 82	139 15	1 82E-04	3 36E-02	25 68	27 64	3 62E-02
BH_B1_V4_001	2 53	3 10E+07	2 41E-03	2 46	198 54	1 95E-04	2 08E-02	21 27	23 93	2 34E-02
BH_B1_V5_001	3 11	3 52E+07	2 46E-03	3 43	257 37	1 84E-04	1 29E-02	17 98	21 66	1 55E-02
BH_B1_V6_001	3 77	3 82E+07	2 50E-03	4 42	318 38	1 80E-04	9 33E-03	16 49	21 23	1 20E-02
BH_B1_V7_001	4 36	4 26E+07	2 52E-03	5 70	385 40	1 70E-04	6 92E-03	15 64	21 72	9 61E-03
BH_B1_V8_001	5 04	4 52E+07	2 58E-03	7 10	463 91	1 69E-04	6 07E-03	16 71	24 26	8 82E-03

Table D.5 – Resistance Calculations Part 4